

DEPARTMENT OF PHYSICS  
UNIVERSITY OF JYVÄSKYLÄ  
RESEARCH REPORT No. 1/2010

**ELECTRON HEATING, TIME EVOLUTION OF BREMSSTRAHLUNG AND  
ION BEAM CURRENT IN ELECTRON CYCLOTRON RESONANCE ION  
SOURCES**

**BY  
TOMMI ROPPONEN**

Academic Dissertation  
for the Degree of  
Doctor of Philosophy

*To be presented, by permission of the  
Faculty of Mathematics and Natural Sciences  
of the University of Jyväskylä,  
for public examination in Auditorium FYS-1 of the  
University of Jyväskylä on January 22, 2010  
at 12 o'clock noon*



Jyväskylä, Finland  
January 2010



## Preface

The work that has been done during the years 2006–2009 in the ECR ion source groups of the University of Jyväskylä and Lawrence Berkeley National Laboratory is summarised in this thesis. I sincerely want to thank my supervisor Dr. Hannu Koivisto for all his guidance and his efforts in order to transfer some of the “ion sourcery” knowledge to me. I want also to thank Dr. Olli Tarvainen for very fruitful collaboration in the ion source field and all the tips and tricks I have received from him since 2004. I wish to thank Dr. Daniela Leitner for giving me the opportunity to work in close collaboration with the LBNL ion source group and Dr. Yuan Liu and Dr. Marc Loiselet for reviewing my thesis.

I want to thank Dr. Juha Ärje for many discussions and Dr. Pekka Suominen for years of collaboration, especially providing the magnetic field profiles. I am in gratitude to Mr. Taneli Kalvas for his guidance in programming and civilization regarding light ion sources and to Dr. Timo Koponen for programming education, collaboration and off-duty activities. I would like to thank Dr. Pete Jones and Mr. Pauli Peura for their invaluable help on spectroscopy related issues and I want also to thank Mr. Janne Ropponen for his GEANT simulations which shed light on the topic of ECRIS bremsstrahlung.

At the times of some issues with the ECR ion sources I have been running back and forth between the electrical and the mechanical workshops and the ion source room sometimes asking for almost miracles. Thus, I want to thank all the personnel of the workshops for their help. I would also like to thank Mr. Veikko Nieminen for mechanical design and the cyclotron operators (Mr. Jani Hyvönen and Mr. Anssi Ikonen) for their help especially in vacuum related topics.

The executive committee of *Mörriklubi* — Mr. Juha-Matti Heikkala, Mr. Tero Salminen, Mr. Antti Valkeinen and Mr. Juho Vanhakartano — is gratefully acknowledged. Mr. Kari Moilanen has also deserved my thanks for many reasons. The always-so-joyful company of Ms. Merja Honkanen, Mr. Antti Kurko, Mr. Elias Markkanen and Mr. Jouko Perkkiö is also acknowledged.

I would like to thank my parents and my grandparents for giving every support that I ever needed. Almost last, but not least, I would like to thank Noora-Mari Nevalainen for pretty much everything.

Support from the Graduate School in Particle and Nuclear Physics (GRASPANP),

the Jenny and Antti Wihuri foundation and the Magnus Ehrnrooth foundation is gratefully acknowledged.

Jyväskylä, December 2009

Tommi Ropponen

**Author** Tommi Ropponen  
Department of Physics  
University of Jyväskylä  
Finland

**Supervisor** Dr. Hannu Koivisto  
Department of Physics  
University of Jyväskylä  
Finland

**Reviewers** Dr. Yuan Liu  
Physics Division  
Oak Ridge National Laboratory  
USA

Dr. Marc Loiselet  
Centre de Recherches du Cyclotron  
Université catholique de Louvain  
Louvain-la-Neuve  
Belgium

**Opponent** Dr. Denis Hitz  
Atomic Energy Commission (CEA)  
Institute for Nanoscience and Cryogenics  
Low Temperature Division  
Grenoble  
France



## Abstract

Ropponen, Tommi, 1981–

Electron heating, time evolution of bremsstrahlung and ion beam current in electron cyclotron resonance ion sources

Jyväskylä, University of Jyväskylä, 2010

Research Report 1/2010 / Department of Physics, University of Jyväskylä

ISBN paper copy: 978-951-39-3783-6

ISBN PDF: 978-951-39-3784-3

ISSN: 0075-465X

This thesis is a study of Electron Cyclotron Resonance Ion Source (ECRIS) plasmas and their properties. The focus has been on time evolution studies of bremsstrahlung emission, ion beam current production and numerical studies of electron heating in ECRIS plasmas. The time scales for reaching steady state bremsstrahlung production at electron energies greater than 30 keV is shown to be on the order of several hundreds of milliseconds. The ion beam currents of different elements are shown to reach steady state before the bremsstrahlung production. It is also demonstrated that by tuning the RF pulse patterns, the so-called preglow transient ion beam currents can be utilized while the amount of bremsstrahlung radiation can be significantly reduced. In numerical work it has been found, for example, that the number of high energy electrons decreases when the microwave power absorption has been modeled.

The thesis is divided in the following way: Chapter 1 is a short introduction to the ECR ion source field including motivation to electron heating studies; Chapter 2 contains basic properties of plasma physics that are needed to understand the behaviour of plasmas; Chapter 3 introduces the reader to ECR ion sources, operational principles and mechanisms dictating the production of highly-charged ions; Chapter 4 concentrates on electron heating via microwaves, describing limitations in the heating processes. The model for the electromagnetic (EM) wave absorption and the description of the simulation code developed in this thesis work are presented. In addition, properties of some of the existing electron heating / ECRIS codes are discussed. Chapter 5 deals with the bremsstrahlung production, discusses some of the previous bremsstrahlung measurements and presents the experimental apparatus. Chapter 6 contains the summary of the numerical and experimental results,

and Chapter 7 concludes the thesis.

**Keywords** ECRIS, bremsstrahlung time evolution, microwave power absorption

## List of publications

This thesis consists of the following publications and some results that have not yet been published.

- A.I** T. ROPPONEN, O. TARVAINEN, P. SUOMINEN, T. K. KOPONEN, T. KALVAS AND H. KOIVISTO. *Hybrid simulation of electron cyclotron resonance heating*. Nucl. Instr. and Meth. A **587**, 115 (2008).
- A.II** D. LEITNER, J. Y. BENITEZ, C. LYNEIS, D. S. TODD, T. ROPPONEN, J. ROPPONEN, H. KOIVISTO AND S. GAMMINO. *Measurement of the high energy component of the X-ray spectra in the VENUS electron cyclotron resonance ion source*. Rev. Sci. Instr. **79**, 033302 (2008).
- A.III** T. ROPPONEN, P. JONES, T. KALVAS, H. KOIVISTO, P. PEURA, O. TARVAINEN AND P. SUOMINEN. *Time evolution of endpoint energy of bremsstrahlung spectra and ion production from an electron cyclotron resonance ion source*. In *Proceedings of the 18<sup>th</sup> International Workshop on ECR Ion Sources*, pages TUCO–D01, 148. JACoW.org (2008).
- A.IV** T. ROPPONEN, O. TARVAINEN, P. JONES, P. PEURA, T. KALVAS, P. SUOMINEN, H. KOIVISTO AND J. ÄRJE. *The effect of magnetic field strength on the time evolution of high energy bremsstrahlung radiation created by an electron cyclotron resonance ion source*. Nucl. Instr. and Meth. A **600**, 525 (2009).
- A.V** O. TARVAINEN, T. ROPPONEN, V. TOIVANEN, J. ÄRJE AND H. KOIVISTO. *Plasma breakdown diagnostics with the biased disc of electron cyclotron resonance ion source*. Plasma Sources Sci. Technol. **18**, 035018 (2009).
- A.VI** T. ROPPONEN, O. TARVAINEN, P. JONES, P. PEURA, T. KALVAS, P. SUOMINEN AND H. KOIVISTO. *Time evolution of high energy bremsstrahlung and argon ion production in electron cyclotron resonance ion source plasma*. IEEE Trans. Plasma Sci. **37**, 2146 (2009).
- A.VII** T. ROPPONEN, O. TARVAINEN, V. TOIVANEN, P. PEURA, P. JONES, H. KOIVISTO, J. NOLAND AND D. LEITNER. *The effect of RF pulse pattern on bremsstrahlung and ion current time evolution of an ECRIS*. Accepted to be published in the Proceedings of the 13<sup>th</sup> international conference on ion sources (Rev. Sci. Instr.).

The author has performed all the numerical analysis for publications A.I, A.III and A.IV and major part of the numerical analysis of publication A.VI. The data analysis

and shielding geometry used in publication A.II is based on the ground work done by the author of the thesis and he also played an integral role on conducting the experiments for publication A.V.

# Contents

<b>1</b>	<b>Introduction</b>	<b>1</b>
<b>2</b>	<b>Basic properties of plasmas</b>	<b>3</b>
2.1	Criteria of plasmas . . . . .	3
2.1.1	Macroscopic neutrality . . . . .	4
2.1.2	Debye shielding . . . . .	4
2.1.3	The plasma frequency . . . . .	5
2.2	Collisions in plasmas . . . . .	5
2.2.1	Weakly ionized plasmas . . . . .	6
2.2.2	Fully ionized plasmas . . . . .	6
<b>3</b>	<b>ECR ion source and relevant plasma physics aspects</b>	<b>9</b>
3.1	The operational principle of an ECR ion source . . . . .	10
3.1.1	Magnetic mirror, mirror ratio and loss cone . . . . .	12
3.1.2	Ambipolar diffusion and plasma potential . . . . .	15
3.2	Scaling laws of an ECR ion source . . . . .	16
3.3	Ionization and charge exchange . . . . .	18
<b>4</b>	<b>Electron heating in ECRIS</b>	<b>23</b>
4.1	Stochastic and adiabatic heating limits . . . . .	24
4.2	Microwave power absorption in the ECR heated plasma . . . . .	27
4.3	Simulations of ECR ion source plasmas . . . . .	32
4.3.1	Examples of existing ECR codes . . . . .	33
4.3.2	Hybrid simulation code for ECR heating . . . . .	34
<b>5</b>	<b>Bremsstrahlung radiation from an ECRIS</b>	<b>39</b>
5.1	Intensity distributions and material properties . . . . .	39
5.2	Previous results of high energy bremsstrahlung measurements . . . . .	42
5.3	Experimental apparatus and measurement setup . . . . .	43
5.3.1	VENUS 28 GHz ECRIS . . . . .	43
5.3.2	JYFL 14 GHz ECRIS . . . . .	44
5.3.3	Measurement setups . . . . .	45
<b>6</b>	<b>Results from the simulations and the measurements</b>	<b>47</b>
6.1	Simulation of electron heating in JYFL 14 GHz ECR ion source . . . . .	47

6.2	Steady state bremsstrahlung measurements . . . . .	53
6.3	Time-resolved bremsstrahlung and ion current measurements . . . . .	55
<b>7</b>	<b>Discussion and conclusions</b>	<b>63</b>
<b>A</b>	<b>Publications</b>	<b>77</b>

# Chapter 1

## Introduction

Electron Cyclotron Resonance plasma heating has been widely adapted to many applications during the last decades. Several industrial applications, such as plasma sputtering, take advantage of accelerating electrons in a magnetic field under resonance condition with a GHz range radio frequency (RF) microwave in order to produce ions. Electron cyclotron resonance heating (ECRH) has been used as a heating method in fusion plasma devices and as a diagnostic tool for plasma physics investigations [1]. The electron cyclotron resonance ion source [2] was developed as a result of the fusion plasma experiments.

After the early 1930's when the first cyclotron accelerators were designed [3], the demand for charged particles of different elements increased. Because the extracted ion beam energy is proportional to the ion charge state (e.g. RFQ, synchrotrons) or to the square of the charge state (e.g. cyclotrons) it is clear that high charge state ion beams are required.

While many different types of ion sources have been used as injectors to accelerators, today mainly two different ion source types are used for highly charged heavy ions — Electron Cyclotron Resonance Ion Source (ECRIS) and Electron Beam Ion Source (EBIS). While the highly charged ion beams from an ECRIS can be continuous or pulsed, the ion beams from an EBIS are pulsed and atoms can be even fully stripped. ECR and EB ion sources are also used as charge breeders in many accelerator laboratories.

Well known ECRIS scaling laws state that the ion beam current of highly charged ions is proportional to the square of the microwave frequency. In order to satisfy electron cyclotron resonance conditions, the magnetic field strength needs to be increased in parallel with the frequency. Because of the ever increasing demands for higher ion beam currents and higher ion charge states in the field of nuclear and particle physics, the most powerful ECR ion sources today utilize superconducting magnets, high RF frequencies and high RF powers. These ion sources, such as VENUS (Versatile Ecr ion source for NUclear Science) [4], produce vast amounts of unwanted bremsstrahlung radiation which can significantly increase the heat load to the cryostat resulting in a magnet quench if the cooling power is not sufficient. In

order to design high performance superconducting ECR ion sources operating at high RF power levels the heat load from bremsstrahlung emission to the plasma chamber walls needs to be taken into account.

Both theoretical and experimental approaches are needed to understand the electron energy distribution. Uncertainties arise from many typical (ECR) plasma phenomena such as stochastic heating and plasma instabilities meaning that plasma simulations easily become very demanding. Some ECRIS simulation codes focus on electron heating (see e.g. [5, 6, 7]) while some try to solve the ion production and transport (see e.g. [8]). In addition to these code types, more complimentary plasma simulation codes also exist (see e.g. [9, 10]). In order to get information about the validity of heating codes the electron energy distribution function (EEDF) and the time evolution of electron energies in the ECRIS plasmas have to be known experimentally. Thus, bremsstrahlung measurements, which have widely been used as one of the standard plasma diagnostic tools for almost as long as laboratory plasma devices have been built, are needed. The first bremsstrahlung measurements with ECR heated plasmas took place in the 1960's (see e.g. [11]). With modern ECR ion sources utilizing both radial and axial magnetic confinement the bremsstrahlung diagnostics is probably the most common tool to obtain information about the electron energy distribution in the plasma.

Motivation to electron heating studies lies in the field of developing the next generation ECRIS, which can utilize microwave frequencies up to 56 GHz and uses RF power levels in excess of 10 kW. In order to build such a device, the electron heating process needs to be understood more accurately and the amount of heat load has to be taken into account while designing the cryostat systems and the plasma chambers. Using pulsed RF power the time scales of the electron heating processes and ion beam production can be connected. With the aid of measurements the simulation codes corresponding to more realistic electron heating time scales can then be developed. However, more research is needed in order to meet the goal to understand the electron heating processes in such a way that controlling the electron energy distribution would become possible. In this manner, the problems arising from very energetic electrons can be solved.

## Chapter 2

### Basic properties of plasmas

The word *plasma* was originally used to describe the inner region of a glowing ionized gaseous material generated in laboratory conditions. Plasma is an electrically neutral collection of ions, electrons and neutral particles. In order to classify some media as a plasma it has to satisfy certain criteria, discussed in the next section. The states of matter can be classified as solid, liquid, gaseous and plasma, thus plasma is also known as the fourth state of matter. The main difference between the states of matter are the binding strengths between molecules or particles. When the state of matter changes from solid to liquid and from liquid to gas, the phase transition occurs at a certain temperature for a given pressure requiring an amount of energy known as latent heat. However, the transition from gas to ionized gas i.e. plasma, is not a phase transition because it occurs gradually as the temperature increases.

Most of the universe is in the plasma state and many interesting naturally occurring phenomena can be explained with the aid of plasma physics. The Sun and its atmosphere and the solar wind are probably the most widely known examples of plasma in nature. Northern lights, for example, are a result of the interaction between the magnetized solar wind and the magnetic field around the Earth. Low frequency radio waves used in communication are reflected between the Earth and the ionosphere allowing radio waves to travel around the world, and part of the high energy cosmic radiation can be a result of charged particle interaction with fast moving magnetic fields known as Fermi acceleration [12], and so on. Because plasma contains charged particles, it is possible to control and confine plasma by electric and magnetic fields, and their combinations. Plasmas are used in a large variety of applications such as semiconductor manufacturing processes, ion sources, fusion research devices and plasma propulsion engines.

#### 2.1 Criteria of plasmas

In order to define a collection of particles as a plasma four conditions must be fulfilled: 1) the system is macroscopically neutral, 2) so-called Debye length is smaller than the dimensions of the particle system, 3) number of particles in the Debye

## Chapter 2. Basic properties of plasmas

sphere is large and 4) the collective motion of charged particles must dominate over the movement of the neutral particles.

### 2.1.1 Macroscopic neutrality

When external disturbances are absent a plasma is macroscopically neutral i.e.

$$n_e = \sum_i z_i n_i, \quad (2.1)$$

where  $n_e$  denotes the electron density,  $z_i$  the charge state of the ion species and  $n_i$  the ion density. The net resulting electric charge is zero when a plasma is sufficiently large to contain a high number of particles and yet small enough compared to e.g. density and temperature variation lengths. In this case the microscopic space charge fields are able to cancel each other out and macroscopically the net space charge remains zero.

Without macroscopic neutrality a plasma temperature of millions of degrees of Kelvin would be required in order to balance the electric potential and thermal potential energies [13]. Usually the requirement of the macroscopic neutrality is denoted as one of the plasma criteria although it arises from the Debye shielding (see equation 2.3).

### 2.1.2 Debye shielding

The fragile balance between perturbations of thermal particle energy and electrostatic potential energy can create departures from macroscopic electrical neutrality within a certain distance. This distance, known as the Debye length, provides a length scale within which a charged particle can feel the influence of the electric field of another charged particle or electric potential.

Generally, the Debye length  $\lambda_D$  is very small. Calculating  $\lambda_D$  for electrons from

$$\lambda_D = \left( \frac{\epsilon_0 kT}{n_e e^2} \right)^{1/2} \quad (2.2)$$

using typical values of ECRIS plasma ( $kT = 20$  eV, and electron density  $n_e = 10^{17} \text{ m}^{-3}$ ) the Debye length becomes about 0.1 mm. In the ionosphere of the Earth ( $kT \approx 0.9$  eV,  $n_e \approx 10^{12} \text{ m}^{-3}$ )  $\lambda_D$  is around 7 millimeters while in the interstellar plasma the Debye length is close to ten meters. In equation 2.2 the vacuum permittivity is marked with  $\epsilon_0$  and the elementary charge with  $e$ .

If the characteristic plasma dimension (length of the plasma) is denoted as  $L$ , the criterion of

$$L \gg \lambda_D \quad (2.3)$$

## 2.2. Collisions in plasmas

must be fulfilled, meaning that the physical dimensions of the plasma substantially exceed the Debye (screening) length. This ensures that there is enough space in the system for the collective shielding to take place.

The number of electrons inside the so-called Debye sphere is given by

$$N_D = \frac{4}{3}\pi\lambda_D^3 n_e = \frac{4}{3}\pi \left( \frac{\epsilon_0 kT}{n_e^{1/3} e^2} \right)^{3/2}. \quad (2.4)$$

Because the Debye shielding effect arises from the collective behaviour of the charged particles inside the plasma, it is required that the number of electrons in the sphere is large. Thus, a criterion of

$$n_e \lambda_D \gg 1 \quad (2.5)$$

is required. In other words, it is necessary that the average distance between electrons in the system is much smaller than the screening distance i.e. Debye length.

### 2.1.3 The plasma frequency

When a disturbance is generated in an equilibrium state plasma the macroscopic space charge neutrality is destroyed locally, and space charge fields are generated. This results in a collective charged particle motion trying to restore the equilibrium state via oscillation. Due to the large difference in electron and ion masses, the electrons react to the electric fields very fast while the ions remain, to a first approximation, stationary and are unable to follow the motion of the light electrons. Therefore, the oscillation of electrons depends on the electron-ion attraction forces, and the (angular) plasma frequency can be expressed as

$$\omega_{pe} = \left( \frac{n_e e^2}{m_e \epsilon_0} \right)^{1/2}, \quad (2.6)$$

where  $m_e$  is the electron mass.

Damping of the plasma oscillations arises from the collisions between neutral particles and electrons. Eventually this leads to a complete neutrality and the system contains no more plasma but neutral gas. Therefore, the last plasma criterion states that the collision frequency between electrons and neutral particles ( $\nu_{en}$ ) is less than the plasma oscillation frequency ( $\nu_{pe} = \omega_{pe}/2\pi$ )

$$\nu_{pe} > \nu_{en}. \quad (2.7)$$

## 2.2 Collisions in plasmas

For (mathematical) simplicity, certain plasmas are assumed to be collisionless. This approximation is valid in the case of sparse plasmas, although strictly speaking a

## Chapter 2. Basic properties of plasmas

collisionless plasma does not exist. Typically hot space plasmas can be described without collisions, but for example ionosphere plasmas tend to have such a high collision frequency that the collisions must be included in the analysis.

Collisional plasmas can be divided into two categories depending on the degree of ionization. This distinction arises from the nature of the particle interactions. Charged particles feel the Coulomb force while the mechanisms for charge-neutral or neutral-neutral collisions are different. A weakly ionized plasma is dominated by charge-neutral interactions, while in a fully ionized plasma the Coulomb collisions are dominating the particle interactions. If the ionization degree of the plasma exceeds 10 % the charged particles in the plasma start to behave in a way that resembles a fully ionized plasma, and above this threshold plasmas are usually considered to be strongly ionized [14].

### 2.2.1 Weakly ionized plasmas

In a weakly ionized plasma the particles interact through direct collisions — a neutral or charged particle collides with a neutral particle. In an elastic collision the total kinetic energy of the colliding particles is equal before and after the collision, while in inelastic collisions charged particles can be created or destroyed, molecules can be broken, charge exchange reactions become possible or atom bound electrons may be excited. In a weakly ionized plasma the number of Coulomb interactions is suppressed, thus, multiple simultaneous interactions can be ignored.

If neutral particles are assumed to be very slow compared to electrons, the collision frequency between neutrals and charged particles (e.g. electrons),  $\langle \nu_{nq} \rangle$  can be expressed as

$$\langle \nu_{nq} \rangle = n_n \sigma_{nq} \langle v_q \rangle, \quad (2.8)$$

where  $n_n$  is the density of neutrals,  $\sigma_{nq}$  is the collision cross-section between neutrals and charged particles and  $\langle v_q \rangle$  is the average velocity of the charged particles. By definition, the mean free path of the charged particle is given by

$$\lambda_{\text{mfp}} = \frac{\langle v_q \rangle}{\langle \nu_{nq} \rangle} = \frac{1}{n_n \sigma_{nq}}. \quad (2.9)$$

For example, using  $n_n = 10^{17} \text{ m}^{-3}$  and  $\sigma_{nq} = \pi r_n^2 \approx \pi(66 \cdot 10^{-12})^2 \text{ m}^2$  (oxygen atom) the mean free path is about 730 m.

### 2.2.2 Fully ionized plasmas

While collisions in weakly ionized plasmas can be understood via consecutive separate collisions, in fully ionized plasmas a charged particle feels the influence of the other charged particles located inside the Debye sphere simultaneously. The Coulomb force extends over long distances compared to the size of a particle, thus,

## 2.2. Collisions in plasmas

the path of a charged particle usually differs only a little from the original particle trajectory after so-called small angle Coulomb scattering. Although the Coulomb interaction is a so-called long distance interaction, in the case of plasma physics the diameter of the Debye sphere sets the maximum interaction length.

While the electron-ion collision frequency can be expressed similarly as that of the charged-neutral collision frequency, the difficulty arises from the derivation of the Coulomb cross-section. The average electron-ion collision frequency can be approximated as [15]

$$\langle \nu_{ei} \rangle = \frac{\sqrt{2} n_i z^2 e^4 \ln \Lambda}{12 \pi^{3/2} \epsilon_0^2 \sqrt{m_e} (kT_e)^{3/2}}, \quad (2.10)$$

where  $\Lambda = n_e \lambda_D^3$  is the so-called plasma parameter. In addition to electron-ion collisions, electron-electron and ion-ion collisions are present. The collision frequency between electrons can be evaluated as [15]

$$\langle \nu_{ee} \rangle \approx \frac{\langle \nu_{ei} \rangle}{n_i z^2 / n_e} \quad (2.11)$$

and the ion-ion collision frequency is given by [15]

$$\langle \nu_{ii} \rangle = \frac{n_i z^4 e^4 \ln \Lambda}{12 \pi^{3/2} \epsilon_0^2 \sqrt{M} (kT_{ion})^{3/2}}, \quad (2.12)$$

where  $M$  is the reduced mass yielding  $m_{ion}/2$  in the case of similar mass ions colliding.

In a singly-charged plasma,  $z = 1$ , thus electron-electron and electron-ion collision frequencies are similar. However, if the plasma contains many different charge states the effective electron-ion collision rate will exceed the collision rate between electrons by a factor of about  $z_{\text{eff}} = \sum_i n_i z_i^2 / n_e$  [15]. Frequencies for different collision processes in a fully ionized plasma can be calculated by using the same parameter values as before in addition to  $kT_{ion} = 1$  eV. Assuming oxygen plasma with an average charge state of 4, we get

$$\langle \nu_{ii} \rangle \approx 600 \text{ kHz} > \langle \nu_{ei} \rangle \approx 150 \text{ kHz} > \langle \nu_{ee} \rangle \approx 30 \text{ kHz}. \quad (2.13)$$



## Chapter 3

### ECR ion source and relevant plasma physics aspects

In the late 1960's fusion plasma research was taking its first steps and in the 1970's electron cyclotron resonance heating was proposed for production of highly-charged ions in fusion plasma devices. Herbert and Wiesemann first proposed the use of a sextupole structure to confine the plasma in 1971 [16] and the first ECR ion source (ECRIS) was built by Geller [17] in 1972. Since then remarkable research and development has taken place, and today the electron cyclotron resonance technique has been widely adapted for production of ions for commercial and scientific purposes.

Electron cyclotron resonance ion sources can be divided into different generations according to the microwave frequency used to produce the plasma. The first generation of ECR ion sources utilize a microwave frequency of 6.4 GHz or lower, the second generation uses 14 GHz and for the third generation the frequency is increased to 28 GHz. As a transition phase between the 2<sup>nd</sup> and the 3<sup>rd</sup> generation a microwave frequency of 18 GHz is sometimes used. Room temperature magnets can be used up to 18 GHz devices, but when going towards the higher RF frequencies superconducting magnets are needed in order to meet the demands of the so-called semi-empirical scaling laws [2] (see equation 3.12). According to these scaling laws, the electron density in the ECRIS plasma increases as the microwave frequency is increased resulting in higher ion beam currents. To fulfill the resonance condition inside the plasma chamber the magnetic field needs to be scaled up proportionally to the microwave frequency. Today, the fourth generation of ECR ion sources are considered to require microwave frequencies up to 56 GHz, creating challenges in the superconducting magnet design. While the needed maximum magnetic fields of the solenoids (8 T) are easily obtained, it remains to be seen if the construction of the superconducting 4 T sextupole, situated inside the solenoid field, is feasible with the limitations set by, for example, very high magnetic fields in the superconducting wires. In addition, the clamping needed to keep the magnet coils stationary under very high forces between the magnets has to be designed carefully.

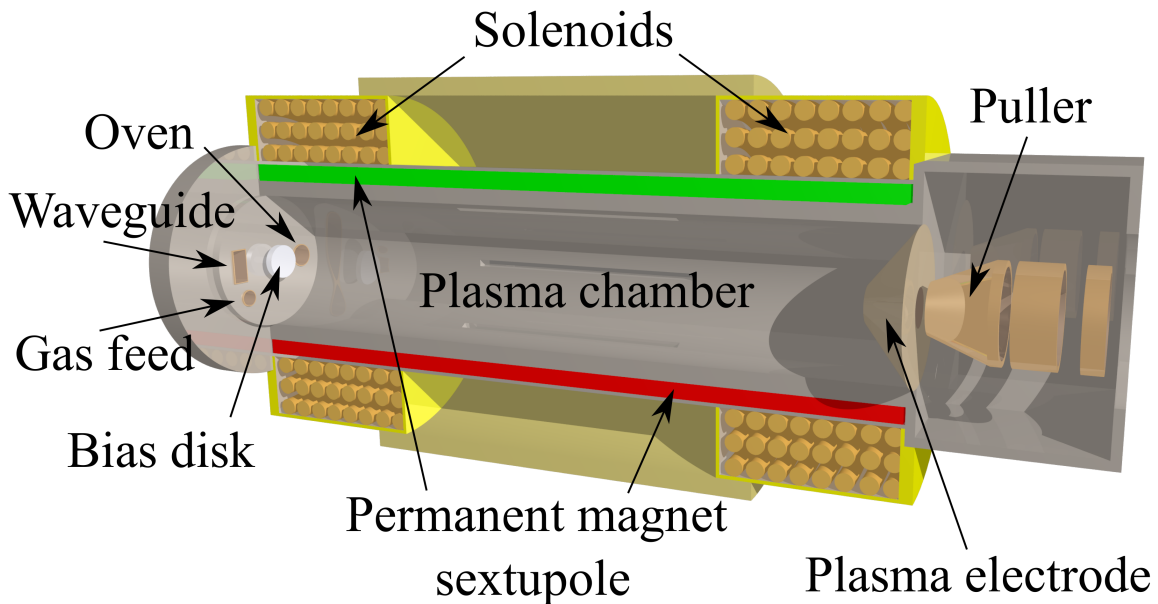


Figure 3.1: A layout of a typical room temperature ECR ion source.

### 3.1 The operational principle of an ECR ion source

An ECR ion source needs five basic elements in order to be able to produce ions: 1) sufficient vacuum conditions, 2) a magnetic bottle to confine the plasma, 3) element of interest in gaseous phase to be ionized, 4) radio frequency (RF) power to heat the electrons and 5) an extraction system to extract the ion beam from the plasma chamber using high voltage (HV). Typical tuning parameters that affect the production of highly charged ions are magnetic field profile, gas pressure and gas mixture, microwave power and bias disk voltage.

A schematic layout of a modern room temperature electron cyclotron resonance ion source is presented in figure 3.1 and the simple sextupole structure is shown in figure 3.2. In the injection part (left side of the figure 3.1) the feed-through for microwave power, gas, oven and biased disk can be seen. Solenoids and permanent magnets generating the magnetic field confining the plasma are located around the plasma chamber. The extraction region (on the right side of the figure) contains typical electrodes to extract and focus the ion beam.

In order to produce highly charged ion beams the background vacuum in the plasma chamber should be on the order of  $10^{-8}$  mbar. During the operation of an ECRIS the pressure in the plasma chamber is usually varied between high  $10^{-8}$  mbar and low  $10^{-6}$  mbar, to make the production of highly charged ions possible.

The magnetic bottle to confine the plasma is generated with solenoid and sextupole magnetic fields. In room temperature ECR ion sources the axial magnetic field is generated using room temperature copper solenoids at the injection and extraction

### 3.1. The operational principle of an ECR ion source

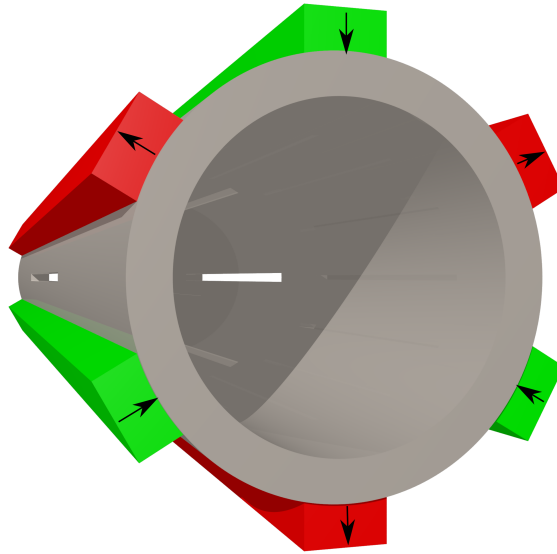


Figure 3.2: A simple sextupole structure. The arrows mark the direction of magnetization.

sides of the ion source and the radial sextupole magnetic field is created with permanent magnets. The radial multipole field is usually a Halbach-type [18] sextupole field although other multipole types have also been tested (see e.g. [19]). Hybrid-type ECR ion sources utilize a permanent magnet multipole and superconducting solenoids while fully superconducting ECRISs take advantage of a superconducting sextupole and superconducting solenoids. Typical magnetic field values for the JYFL 14 GHz ECRIS are 2.2 T at the injection, 0.9 T at the extraction, 0.4 T at the  $B_{\min}$  and 0.85 T at the magnetic field pole of the sextupole [20] (see also section 5.3.2). From these the sextupole field and the extraction field do not fulfill the magnetic field scaling laws discussed in section 3.2.

Material to be ionized can be delivered into the plasma chamber in several ways. The most straightforward approach is to use gas, such as oxygen, which can be injected into the plasma chamber via high precision leak valves. Metal ions can be produced with low and high temperature resistively and inductively heated evaporation ovens [21, 22, 23, 24, 25, 26], MIVOC method [27], sputtering of a metal sample by the plasma [28] or with laser ablation [29].

In many occasions it is useful to maintain the plasma with an inexpensive buffer gas. This method is known as gas mixing [30, 31]. When the ion of interest is heavier than the buffer (or mixing) gas ion or atom, the momentum of the ion of interest is transferred to the lighter particle via ion-ion collisions. This cools down the heavier ions and increases the confinement time resulting in higher charge states. When expensive isotopes are ionized the use of the buffer gas makes it possible to decrease the consumption of the expensive element.

## Chapter 3. ECR ion source and relevant plasma physics aspects

Ionization in an ECRIS plasma is based on collisions between electrons and neutral atoms or ions. Radio frequency microwaves in the GHz range are used to provide energy for the electrons at the resonance zone where the angular orbiting frequency at a certain magnetic field strength value corresponds to the angular frequency of the RF microwave as seen in equation:

$$\omega_{ce} = \frac{eB}{m_e\gamma}, \quad (3.1)$$

where  $\omega_{ce}$  is the electron cyclotron resonance frequency,  $B$  the magnetic field and  $\gamma = (E_{kin} + E_0)/E_0$  the relativistic gamma factor. The microwaves originating from an RF oscillator are fed into a microwave amplifier and from the amplifier into the plasma chamber of an ECRIS via a microwave guide. On the resonance zone, the energy of the electron will be increased or decreased depending on the phase between the electron entering the resonance zone and the microwave. Electrons having an energy that is equal or over the ionization threshold of a certain ion can remove an electron from the electron shell of the atom. In the ECR ion source the ionization is a stepwise process meaning that numerous ionization steps will be needed in order to produce high charge states. In the case of highly charged ions typical ionization times are on the order of milliseconds (see e.g. [32, 33]).

The plasma chamber and the plasma electrode of an ECR ion source are biased to a positive voltage (typically several kilovolts) and the positively charged ions are then accelerated into the beam line by the electric field between the plasma electrode and puller electrode. In order to control the ion beam dynamics different types of ion optical elements, such as Einzel lenses, are used at the extraction region of an ECRIS.

The ion beam extracted from an ECR ion source contains several different charge states. The distribution, which depends on the ionization potentials and charge exchange cross-sections, is almost Gaussian around the charge state having the largest ion beam current. A typical xenon charge state distribution of the VENUS ECR ion source with oxygen as a buffer gas is presented in Figure 3.3.

### 3.1.1 Magnetic mirror, mirror ratio and loss cone

Plasma confinement is probably one of the most important aspect in ECRIS operation. Charged particles feel the force of both magnetic and electric fields thus, either one can be used to control the movement of the charged particles. Usually magnetic confinement is favored over electrical confinement. Using magnetic fields, so-called magnetic mirrors can be built in order to, for example, reflect charged particles between the magnetic mirrors analogically to photons reflecting between two parallel optical mirrors. Magnetic confinement can be achieved with a simple solenoid configuration or by more complex geometry. Geometries for these confinement fields range from two parallel solenoids to different combinations of axial

### 3.1. The operational principle of an ECR ion source

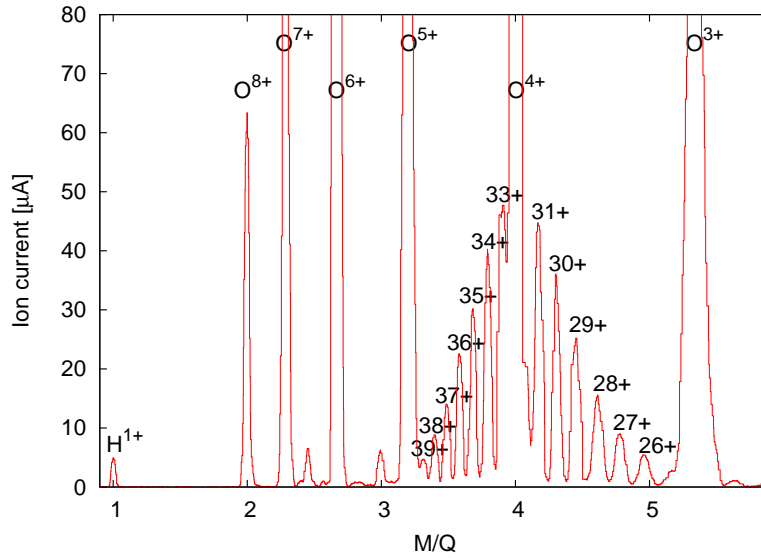


Figure 3.3: A typical xenon charge state distribution produced with the VENUS ECR ion source using oxygen as a mixing gas.

and radial magnetic fields, toroidal, poloidal and helical fields typically found in tokamaks.

The magnetic field of an electron cyclotron resonance ion source is a superposition of solenoid and sextupole magnetic fields. The solenoid field is basically a magnetic bottle generated between two, or more, solenoids. The sextupole field is used to provide more strength in the radial direction, thus, providing enhanced magnetic confinement of charged particles in the plasma. This magnetic field forms the so-called  $B_{\min}$  structure where the strength of the magnetic field increases in all directions when moving away from the center of the plasma chamber. The configuration also generates magnetic field equipotential surfaces inside the chamber, thus creating a large electron cyclotron resonance surface. Figure 3.4 presents the solenoid and sextupole field profiles in a typical 14 GHz ECRIS and in figure 3.5 the structure of the magnetic bottle consisting of solenoid and sextupole magnetic fields and a sketch of the plasma inside an ECR ion source is presented.

In order to understand the principles of the magnetic confinement, a quantity called the magnetic moment needs to be introduced. It can be shown that the magnetic moment of a charged particle can be expressed as

$$|\mathbf{m}| = \frac{0.5mv_{\perp}^2}{B} = \frac{W_{\perp}}{B}, \quad (3.2)$$

where  $m$  is the mass of the particle,  $v_{\perp}$  is the perpendicular velocity component with respect to the magnetic field and  $W_{\perp}$  is the kinetic energy of the particle transverse to the external magnetic field. In a magnetostatic field the sum of parallel

### Chapter 3. ECR ion source and relevant plasma physics aspects

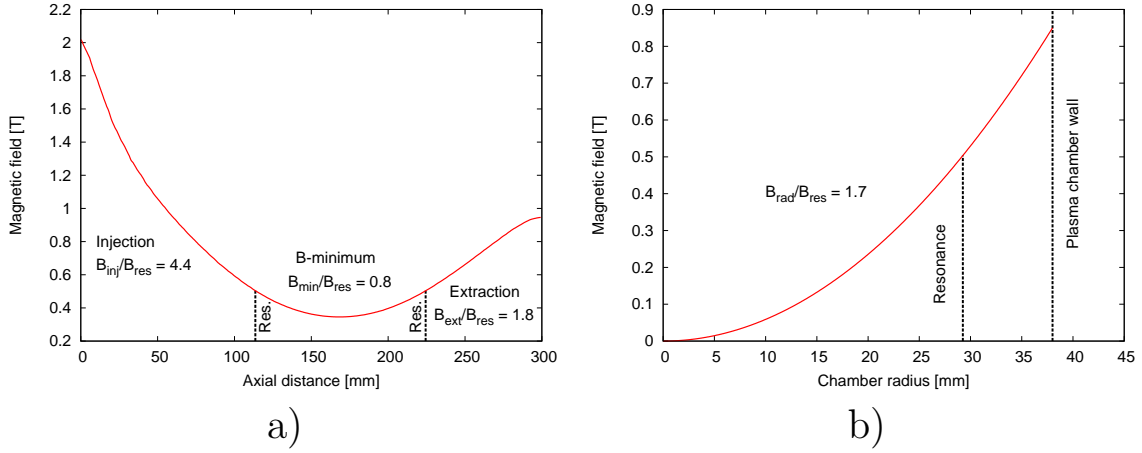


Figure 3.4: Magnetic field profiles of a typical 14 GHz ECRIS: a) solenoid field profile from injection to extraction, b) sextupole field profile from the center of the plasma chamber towards a magnetic field pole. In both a) and b) the locations of the resonances at 14.1 GHz are shown.

and transverse kinetic energies, i.e. the total energy, is constant implying that the magnitude of the magnetic moment remains constant if the spatial variation of the magnetic field inside the orbit of the particle is small enough compared to the magnitude of the magnetic field [13]. As the particle moves towards a higher magnetic field (converging field) the particle orbit radius will decrease in order to conserve the magnetic flux enclosed by the particle orbit. Also, the total kinetic energy  $W_{\text{tot}} = W_{\parallel} + W_{\perp}$  components will interchange as the particle is moving towards the converging magnetic field. Moving along the converging field results in a decrease of the parallel kinetic energy component  $W_{\parallel}$  and an increase of  $W_{\perp}$  in order to keep  $|\mathbf{m}|$  and the total energy as constants. If the magnetic field  $\mathbf{B}$  becomes strong enough, the parallel kinetic energy will decrease to zero and all the kinetic energy of the particle is within the transverse kinetic energy. The force

$$F_{\parallel} = -\mathbf{m}\nabla B_{\parallel}, \quad (3.3)$$

acting on the charged particle, produces an accelerating force parallel to the magnetic field. If the parallel kinetic energy is zero the particle starts to move towards the lower magnetic field region. This phenomenon is known as the magnetic mirror effect and is the basis of magnetically confined plasmas.

Despite the confinement, particle losses are evident. Due to collisions particles can, for example, diffuse outside the plasma or collide with the vacuum chamber walls. The effectiveness of a magnetic confinement system can be characterized by a parameter called the mirror ratio, expressed as  $B_{\text{m}}/B_0$ . However, it is common in the ECR ion source field to write the magnetic mirror ratio  $R$  in a form of

$$R = \frac{B_{\text{max}}}{B_{\text{ECR}}}, \quad (3.4)$$

### 3.1. The operational principle of an ECR ion source

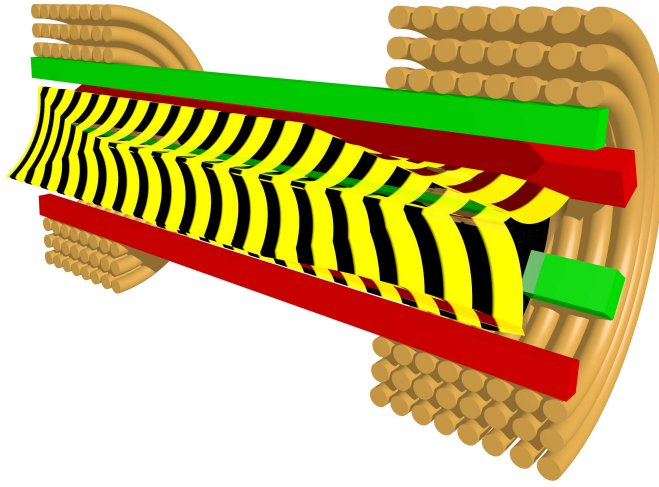


Figure 3.5: Magnetic bottle of an ECR ion source consisting of the solenoid field (light brown coils) and the sextupole field (red and green bars). A false-color plasma is presented in order to highlight the complex shape of an ECRIS plasma.

where  $B_{\text{ECR}}$  is the magnetic field at the electron cyclotron resonance. The use of  $B_{\text{ECR}}$  is justifiable because the pitch angle, as will be seen, is closely related to the particle confinement and is defined at the resonance zone due to wave-particle interaction. An expression for the pitch angle can be derived by using the invariance of the magnetic moment and by dividing the velocity vector of an electron into transverse and parallel components. Using the aforementioned magnetic field notations at the ECR surface and at the maximum of the magnetic bottle, the pitch angle can be written in the form of

$$\alpha_0 = \sin^{-1} \left( \sqrt{B_{\text{ECR}}/B_{\text{max}}} \right). \quad (3.5)$$

In an ECR plasma, electrons are strongly confined due to the heating process responsible for increasing the transverse velocity component and thus leading to a reflection point well within the space between the magnetic mirror structure. However, deceleration of an electron at the resonance zone or particle collisions can change the ratio of the transverse and parallel velocity in such a way that an electron drifts into the so-called loss cone. A schematic figure of the electron loss cone in an ECRIS is presented in figure 3.6. Ions, which can not be heated by microwaves in the GHz range, are magnetically weakly confined compared to the hot electron population and can diffuse in the plasma relatively freely.

#### 3.1.2 Ambipolar diffusion and plasma potential

In a plasma, the electrons and the ions diffuse with different velocities. While the mobility of the electrons is higher than the mobility of the ions, the requirement

## Chapter 3. ECR ion source and relevant plasma physics aspects

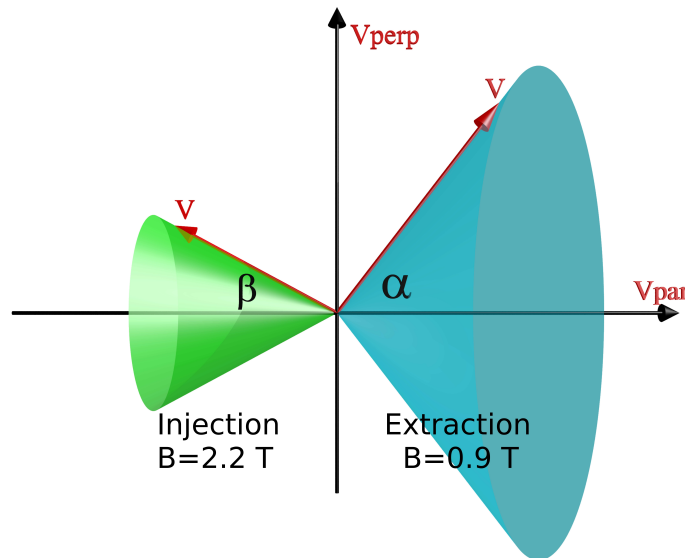


Figure 3.6: Loss cone with different magnetic field strengths. The angle of the loss cone is larger in the lower magnetic field (right-hand side of the figure, extraction of an ECRIS) than in the higher magnetic field (left-hand side of the figure, injection of an ECRIS).

of local neutrality of the plasma slows the electrons down. Thus, both electrons and ions diffuse at the same velocities. When this process occurs in a magnetized plasma, it is called ambipolar diffusion.

The higher mobility of electrons compared to the ions also makes it possible that the electrons can reach the plasma chamber walls faster than ions. Again, in order to meet the neutrality conditions, the negative charge lost from the plasma via the electrons needs to be compensated by a loss of positive charge, i.e. ions. In order to balance the charge losses the plasma develops a positive potential which will retard electrons and repel positive ions. This potential between the plasma and the plasma chamber walls is known as the plasma potential. Typical plasma potential values for the JYFL 14 GHz ECRIS with a clean plasma chamber are around 20 V, being much higher (over 50 V) if the plasma chamber surface is contaminated by e.g. carbon [20]. It has also been observed that the plasma potential is affected by the mass of the ions, RF power, gas feed rate and gas mixing effect (see e.g [20, 34]). The effect of positive plasma potential to the electron loss cone is presented schematically in figure 3.7.

### 3.2 Scaling laws of an ECR ion source

Electron cyclotron resonance ion sources have been developed to produce high ion beam intensities of highly charged ions. In order to understand and point out the

### 3.2. Scaling laws of an ECR ion source

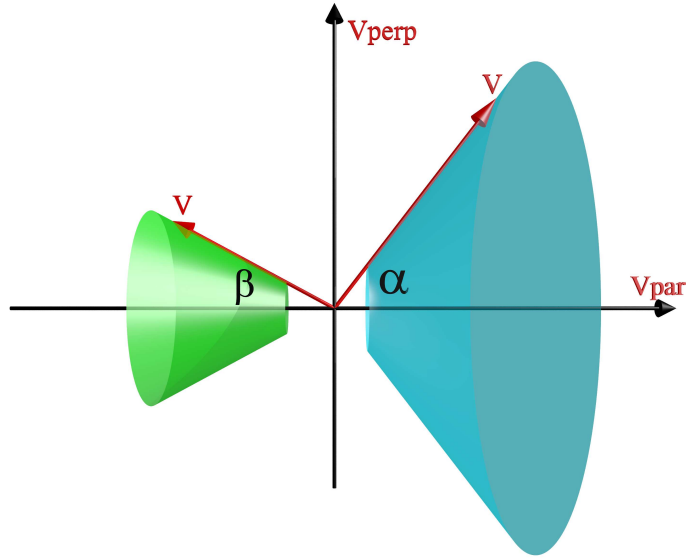


Figure 3.7: The effect of plasma potential to the electron loss cone of positively charged plasma. The cones are cut due to positive plasma potential attracting negatively charged electrons. Compare with figure 3.6.

effects of different parameters on the performance of ECR ion sources semi-empirical scaling laws have been formulated [35]. The laws can be expressed as

$$n_e v_e \tau \propto B^{3/2} \quad (3.6)$$

$$n_e v_e \tau \propto \omega_{rf}^{7/2} \quad (3.7)$$

$$q_{peak} \propto \ln B^{3/2} \quad (3.8)$$

$$q_{peak} \propto \ln \omega_{rf}^{7/2} \quad (3.9)$$

$$q_{peak} \propto P_{rf}^{1/3} \quad (3.10)$$

$$I_{peak} \propto \omega_{rf}^2 m_{ion}^{-1} \quad (3.11)$$

Here,  $v_e$  is the speed of electrons,  $\tau$  is the confinement time of ions in the plasma,  $B$  is the average magnetic field,  $\omega_{rf}$  is the microwave (angular) frequency,  $q_{peak}$  is the charge state that produces the highest ion beam current,  $P_{rf}$  is the microwave power and  $I_{peak}$  is the ion beam current of charge state  $q_{peak}$ . From these equations it can be seen that the ion current is proportional to the square of the microwave frequency. Remembering that the required magnetic field strength is proportional to the microwave frequency (see equation 3.1), higher magnetic field strengths are needed in order to maintain the magnetic mirror ratio. According to equation 3.6, increasing the average magnetic field strength also increases the confinement time which enables the production of higher charge states. When it is required that the charge state distribution should shift towards higher charge states, values of  $B$ ,  $\omega_{rf}$  and  $P_{rf}$  need to be increased.

## Chapter 3. ECR ion source and relevant plasma physics aspects

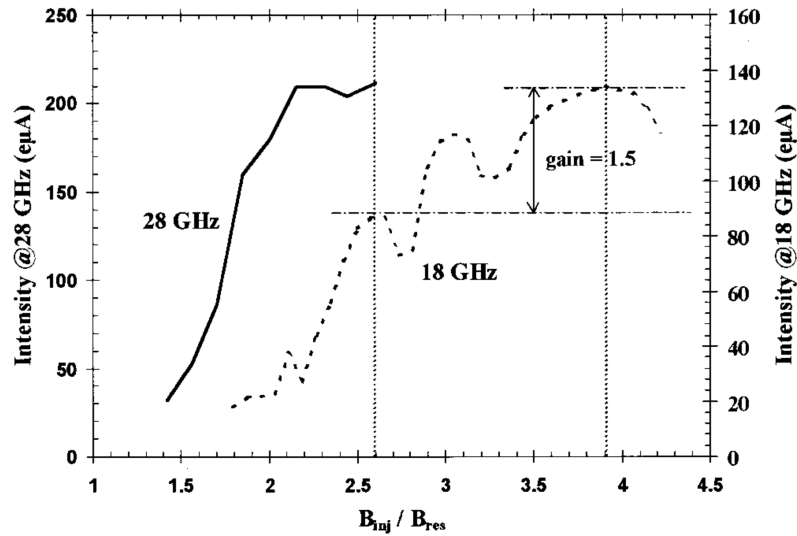


Figure 3.8: The ion beam currents of  $\text{Xe}^{20+}$  as a function of injection mirror ratio with 18 GHz and 28 GHz microwave frequencies. Figure from [39].

Comprehensive experiments to define the optimum magnetic field configuration for the production of highly charged ion beams have been performed by Gammino *et al.* [36, 37, 38] and others [39, 40, 41]. According to these measurements, equations, or scaling laws, for the mirror ratios in an ECRIS can be expressed as (see also reference [42])

$$\frac{B_{\text{inj}}}{B_{\text{ecr}}} \geq 4, \quad \frac{B_{\text{ext}}}{B_{\text{ecr}}} \geq 2, \quad \frac{B_{\text{rad}}}{B_{\text{ecr}}} \geq 2, \quad \frac{B_{\text{min}}}{B_{\text{ecr}}} \approx 0.8. \quad (3.12)$$

If the mirror ratios are below these values, only a slight increase in the mirror ratios will increase the performance of an ECR ion source significantly. The correct mirror ratios are crucial in the production of highly charged heavy ions as can be seen from figure 3.8. The figure also shows how the higher microwave frequency enhances the ion beam current.

### 3.3 Ionization and charge exchange

While collisional processes in plasmas involve collisions between all the particles present in a plasma, the collision between electrons and ions are the ones responsible for producing multiply charged ions. On the other hand, charge exchange can occur in ion-neutral, electron-ion (recombination) or ion-ion collisions or reactions. For low charge state ions the balance between the gain by ionization and loss by charge exchange reactions is such that the pressure in the plasma chamber of an ion source can be in the range of  $10^{-3}$  mbar. However, as the charge state increases the charge

### 3.3. Ionization and charge exchange

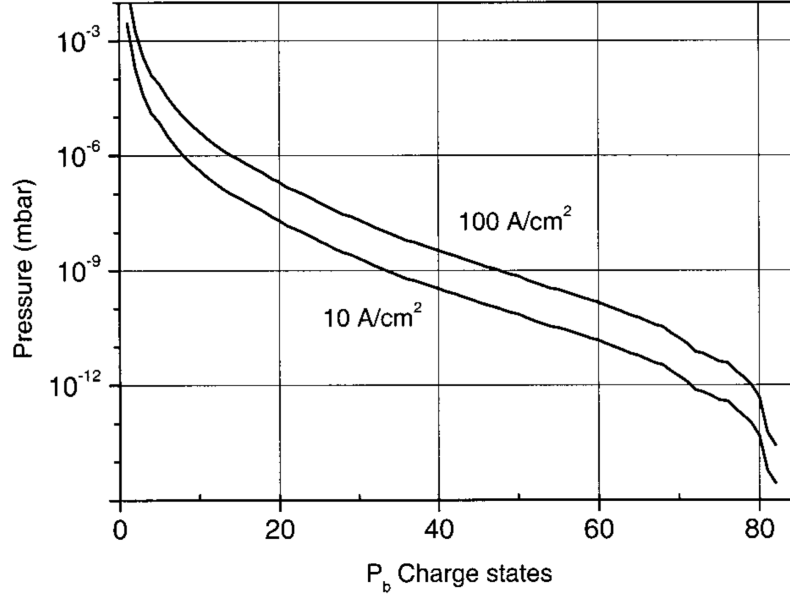


Figure 3.9: Pressure dependence of the electron impact ionization and charge exchange balance as a function of different charge states of lead ions. Curves presented with two electron current densities implying different electron densities in the plasmas. Figure from [43].

exchange cross section becomes more pronounced and lower pressures are needed. This implies that in order to produce highly charged ions in an electron heated plasma low neutral gas pressure and high electron density is favourable. Figure 3.9 shows the pressure dependence of the balance between the gain by ionization and loss by charge exchange reactions for different charge states of lead ions. Typically an ECR ion source is operated with pressures around  $10^{-7}$ – $10^{-8}$  mbar for which the figure suggests charge states lower than 40+. VENUS has been producing ions from bismuth, which is quite close to lead, up to charge states of 50+ with an ion beam current of  $0.5 \mu\text{A}$ .

The ion density time evolution of a certain charge state can be described with three separate processes in the ECR plasma: step-by-step ionization by electron bombardment, charge exchange reactions and diffusion. The time evolution of the ion density of a charge state  $q$  of ion species  $i$  can be written as [44]:

$$\frac{dn_i^q}{dt} = n_e \langle \sigma v \rangle_{q-1 \rightarrow q}^{\text{ion}} n_i^{q-1} - n_e \langle \sigma v \rangle_{q \rightarrow q+1}^{\text{ion}} n_i^q + n_{0i} \langle \sigma v \rangle_{q+1 \rightarrow q}^{\text{cx}} n_i^{q+1} - n_{0i} \langle \sigma v \rangle_{q \rightarrow q-1}^{\text{cx}} n_i^q - \frac{n_i^q}{\tau_i^q}, \quad (3.13)$$

where  $\sigma$  is the collision cross section,  $v$  is the speed of a particle,  $n_{0i}$  is the neutral density of atoms of species  $i$  and  $\tau_i^q$  is the confinement time of charge state  $q$  and ion

### Chapter 3. ECR ion source and relevant plasma physics aspects

species  $i$ . Superscript  $ion$  refers to ionization and superscript  $cx$  to charge exchange reaction. The first term on the right side of the equation describes the production rate of charge state  $q$  from charge state  $q - 1$  by electron bombardment, and the second term describes ionization by electron impact from charge state  $q$  to charge state  $q + 1$ . The third and fourth terms describe charge exchange reactions from charge state  $q + 1$  to charge state  $q$  and from charge state  $q$  to charge state  $q - 1$ , respectively. The last term, which is inversely proportional to the confinement time of ions, relates to diffusive processes responsible for ion losses to the ion source plasma chamber walls. According to the equation the densities of highly charged ion species depend on both electron and ion densities as well as cross sections of different reactions and confinement time of ions.

Ionization cross sections can be calculated with a semiempirical formula by Lotz [45, 46], however, more accurate results are obtained e.g. with the ATOM code [47] which uses the Coulomb-Born approximation with exchange (CBE) in the partial-wave representation. Charge exchange reactions, first reported by Henderson [48], have also been studied theoretically, for example, in references [49, 50].

Maximum cross section, ionization threshold and energy at the maximum cross section for electron impact ionization for oxygen, argon, krypton and xenon is presented in figure 3.10 according to ATOM simulation data [51, 52]. From the figure it can be seen how the cross section drops several orders of magnitude while increasing the charge state: with xenon the cross section varies from  $4.0 \cdot 10^{-16} \text{ cm}^2$  ( $\text{Xe}^{1+}$ ) to  $9.6 \cdot 10^{-24} \text{ cm}^2$  ( $\text{Xe}^{54+}$ ). Oxygen  $7+$ , which is one of the most common ions used to indicate the performance of an ECR ion source, has an ionization threshold of 739 eV and the maximum cross section for  $\text{O}^{6+} \rightarrow \text{O}^{7+}$  ionization is reached with an electron energy of about 2.0 keV. Xenon  $35+$ , which is the highest charge state of Xe regularly accelerated in JYFL, has an ionization threshold of almost 2.2 keV while the maximum of the cross section curve for  $\text{Xe}^{34+} \rightarrow \text{Xe}^{35+}$  lies around 4.4 keV. The values of cross sections for the aforementioned ionization processes are  $6.1 \cdot 10^{-20} \text{ cm}^2$  (oxygen) and  $3.2 \cdot 10^{-20} \text{ cm}^2$  (xenon). The ionization threshold for  $^{40}\text{Ar}^{8+}$  is 153 eV, the cross section for  $\text{Ar}^{7+} \rightarrow \text{Ar}^{8+}$  is around  $3.4 \cdot 10^{-18} \text{ cm}^2$  and the maximum ionization cross section is reached with an electron energy of 800 eV. By looking at the cross section values it is clear that producing medium charge states, such as  $\text{Ar}^{8+}$ , is much easier than the production of  $\text{O}^{7+}$  or  $\text{Xe}^{35+}$ .

Reaching electron energies capable of ionizing even the highest charge states of xenon is however not the limiting process in ECR ion sources. The problem of highly charged heavy ion production lies in the charge exchange cross sections. The charge exchange cross section (electron capture) with molecular hydrogen for  $\text{Xe}^{35+}$  has been measured to be  $4.6 \cdot 10^{-14} \text{ cm}^2$  [53]. This value is six orders of magnitude larger than the ionization cross section meaning that in order to produce highly charged heavy ions by electron bombardment, the process should take place in a very low vacuum.

### 3.3. Ionization and charge exchange

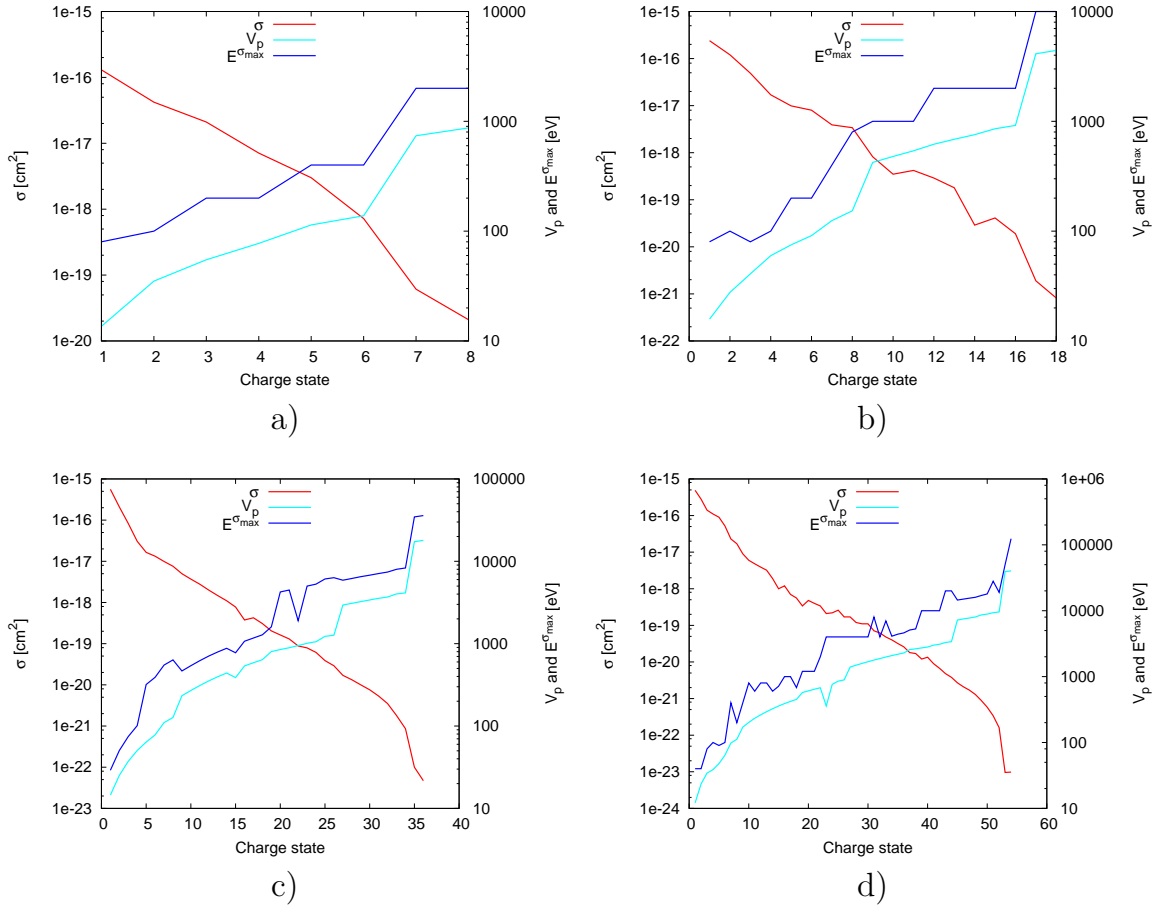


Figure 3.10: Maximum cross section  $\sigma$ , ionization potential  $V_p$  and energy at the maximum cross section  $E^{\sigma_{\max}}$  for a) oxygen, b) argon, c) krypton and d) xenon.

In addition to Coulomb interaction based ionization, several other processes are responsible for removing electrons from atoms and ions [54]. These processes become more pronounced when the charge state of an ion increases, and some of these processes contribute significantly to the total ionization [55, 56]. It has been noticed that these processes are important especially in the case of heavy alkali-like (Li, Na, K, Rb, Cs, Fr) and alkaline-earth-like (Be, Mg, Ca, Sr, Ba, Ra) ions.



## Chapter 4

### Electron heating in ECRIS

Electron cyclotron resonance heating can be used to produce continuous beams of highly charged ions. From equation 3.1 it can be seen that while the electrons are heated their resonance magnetic field will shift according to the value of  $\gamma$ . Therefore, thermal electrons have resonance zones in lower magnetic field values than the energetic electrons. It can be approximated that the shift of the resonance “point” on the axis of the JYFL 14 GHz ECRIS between a thermal electron and a 511 keV electron is roughly 4.5 cm (resonance field increases from 0.5 T to 1.0 T). Thus, it becomes clear that instead of talking about the resonance point a term resonance volume should be used.

In addition, multiple microwave frequencies can be launched into the plasma chamber to increase the heating volume in order to improve the production of highly charged heavy ions extracted from an ECR ion source [57, 58]. The use of multiple frequency heating in ECR ion sources has been studied extensively. It has been found that the second resonance can shift the charge state distribution towards higher charge states if the frequency gap between the microwave frequencies launched into the plasma chamber is adequate [59]. Production times of highly charged ions can also be decreased with multiple frequency heating [60] and slightly lower plasma potentials have been measured with double frequency heating compared to single frequency heating [61, 62]. It has also been demonstrated that using three different microwave frequencies can further improve the highly charged ion beam production compared to double frequency heating [63]. It has also been demonstrated that broadband microwave can improve the production of highly charged ions [64, 65].

The resonance volume can also be adjusted with the gradient of the magnetic field. A lower field gradient at the resonance region allows the electron to remain in the close proximity of the resonance longer than in the case of a high magnetic field gradient (see e.g. reference [66]). This so-called volume heating [67, 68, 69] (“low gradB-mode”) allows the electrons to absorb energy from the microwaves more efficiently during single resonance crossing. Increased heating efficiency has been observed with increased bremsstrahlung radiation levels during the plasma breakdown [70] and steady state [71].

## Chapter 4. Electron heating in ECRIS

Besides electron heating volume increase, there are also other techniques to increase the high charge state ion currents. ECR ion source plasma chambers are multimode cavities which means that the plasma chamber dimensions are larger than the wave length [72]. By tuning the source or microwave frequency within a relatively narrow frequency range it is possible to excite different discrete modes or combinations of overlapping modes. It has been observed numerically that the absorption rate of microwave power increases rapidly as the electron density increases [7]. This means that the plasma chamber quality factor [73],

$$Q = \omega \frac{\text{stored energy}}{\text{dissipated power}} = \frac{\text{stored energy}}{\text{dissipated energy per cycle}}, \quad (4.1)$$

can change significantly between different operation points of an ECR ion source. The effect of frequency tuning has been observed to be very significant for the ion beam currents of highly charged ions and Q-values exceeding 1000 have been proposed [72, 74]. This is considerably higher than the generally used value of about 3 [66, 75]. It is clear that the quality factor of an empty plasma chamber, which basically is a non-ideal resonant cavity, is much higher and can be even around hundreds of thousands [76]. It is likely that modern ECR ion sources built for highly charged ion production would probably benefit from the possibility of tuning the microwave frequency. However, this method of fine tuning ECR ion sources, despite promising results, is still quite rarely exploited and the effect of the frequency tuning to the ion beam production and the radiation levels has not yet been studied systematically.

### 4.1 Stochastic and adiabatic heating limits

Electron cyclotron resonance heated plasmas are governed by stochastic heating. While the electron exhibits periodic motion in the magnetic bottle and crosses the resonance the net energy change is positive as long as the phase change of the microwave electric field is much more than  $2\pi$  during the bounce period between resonances. When this condition is satisfied the phase of the wave is random each time the electron enters the resonance [77]. The time that an electron takes to travel between two resonance points is a function of energy. When the energy is increased, the time-of-flight (TOF) between the resonances decreases if collisions are neglected. At high energies the TOF becomes small and leads to a decreased phase variation experienced by the electron. As a result the stochastic electron heating is disturbed and the interaction between a hot electron and microwave becomes superadiabatic [78]. As a consequence the energy of an electron is limited in the electron cyclotron resonance heating process.

It has been shown [79], that for a given value of the electric field of the microwave, the velocity space for particles is divided into three regions: (1.) low velocities

#### 4.1. Stochastic and adiabatic heating limits

( $E_{e^-} < W_s$ ) for which particles are heated stochastically, (2.) intermediate velocities ( $W_s < E_{e^-} < W_a$ ) which are accessible from the lower velocities, but where the assumption of the random phase is not valid anymore and (3.) higher adiabatic velocities ( $E_{e^-} > W_a$ ) for which the motion in velocity space oscillates in time. Here, the energy of an electron is marked with  $E_{e^-}$ . The equations for stochastic ( $W_s$ ) and adiabatic energy limits ( $W_a$ ) can be expressed as [80]

$$W_s = 0.2 \left[ m_e L \left( 1 + \frac{l^2}{L^2} \right) \right]^{1/4} l \omega^{1/2} (eE)^{3/4} \quad (4.2)$$

and

$$W_a = 5W_s. \quad (4.3)$$

In equation 4.2,  $E$  is the electric field of the microwave and parameter  $L$  can be calculated from the axial magnetic field profile ( $B = B_0(1 + z^2/L^2)$ ) of the mirror system, where the resonances are at  $z = \pm l$ . The (angular) microwave frequency is denoted with  $\omega$ . Because the electric field in the ECRIS plasma chamber is assumed to be proportional to the plasma chamber quality factor (see e.g. [75]), it can be written that  $E_{\text{tot}} \approx QE$ . Using this assumption and substituting the axial magnetic field profile of the JYFL 14 GHz ECRIS with coil currents of 500/500 A (see magnetic field details from reference [70]), a microwave frequency of 14.1 GHz, resonance location  $l \approx 0.042$  m and  $L^2 \approx 0.0038$  m<sup>-2</sup>, the stochastic and adiabatic heating limits can be calculated. The limits are presented, as a function of electric field amplitude, microwave frequency, magnetic field gradient at the resonance and distance between axial resonances, in figure 4.1. In fig. 4.1 b)  $L$  is determined by artificially fixing  $l$  and  $B_{\text{min}}/B_{\text{ecr}}$ . Due to the magnetic field structure, it has to be noted that in fig. 4.1 c)  $B_{\text{min}}$  is changed and the distance between axial resonances ( $d_{\text{res}}$ ) is fixed while in fig. 4.1 d) the magnetic field gradient is changed while keeping  $B_{\text{min}}$  as constant.

It is observed from fig. 4.1 a) that the limit for both stochastic and adiabatic heating is very low if the electric field amplitude is low. In the bremsstrahlung measurements conducted with the JYFL 14 GHz ECRIS it has been observed that typical maximum energies of the bremsstrahlung spectra lie around 500 keV, thus, from figure 4.1 it can be approximated that the electric field amplitude is in the range from 1700 kV/m to about 14 000 kV/m. In reference [80] the measured electron energies at an electric field amplitude of about 250 kV/m were observed to be roughly 13–55 % higher than the theoretical stochastic heating limit predicts but significantly lower than the adiabatic limit suggests. From fig 4.1. b), where the heating limits are presented as a function of the microwave frequency, it is observed that the higher the frequency the higher the energy limits. The effect of the magnetic field gradient at the resonance zone is very pronounced when the gradient decreases, as can be seen from fig. 4.1 c). It has been observed on several occasions that the lower magnetic field gradient at the resonance zone allows electrons to absorb energy from the microwave more

## Chapter 4. Electron heating in ECRIS

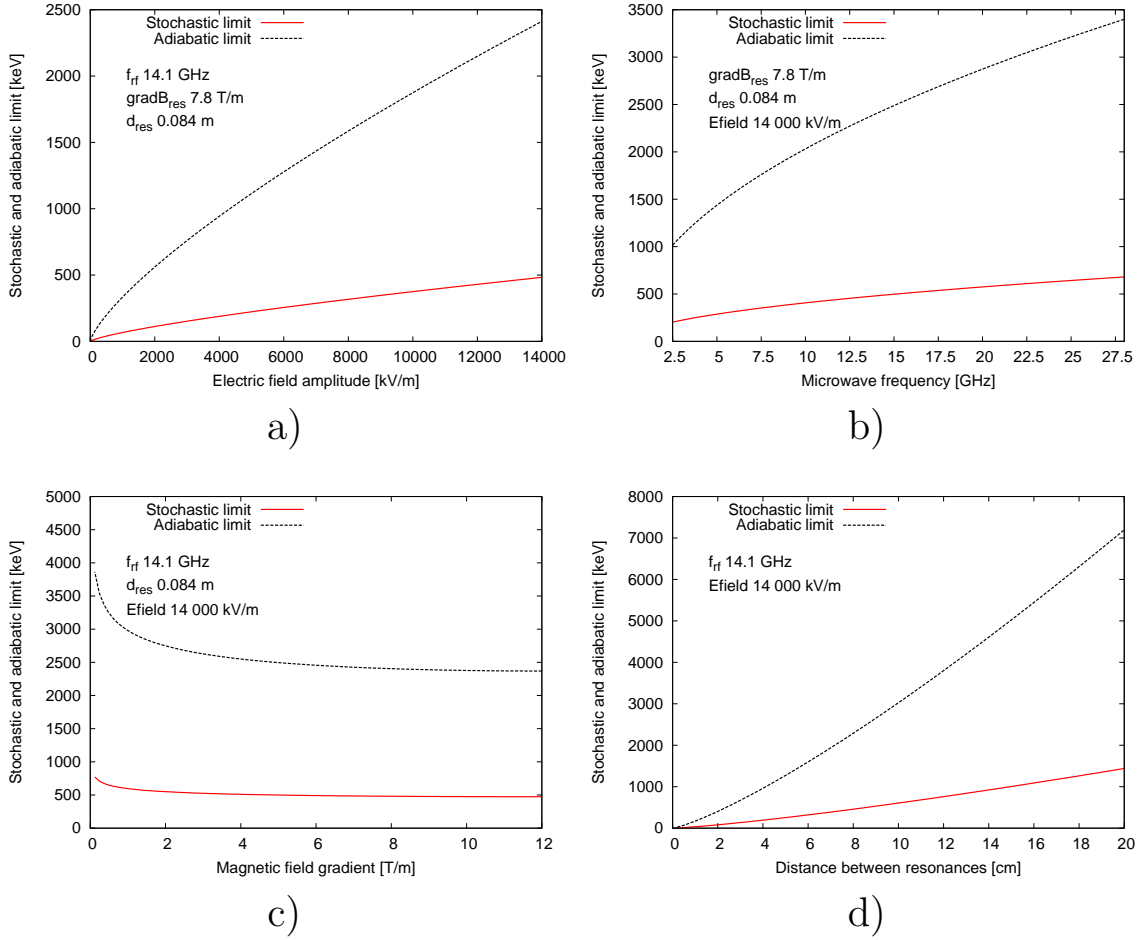


Figure 4.1: Stochastic and adiabatic heating limits according to equations 4.2 and 4.3 as a function of a) electric field amplitude, b) microwave frequency, c) magnetic field gradient at the resonance and d) distance between axial resonances. Magnetic field characteristics calculated from the magnetic field profile used in the simulation code presented in section 4.3.2.

## 4.2. Microwave power absorption in the ECR heated plasma

efficiently. The axial distance between the resonance point also clearly affects the stochastic and adiabatic heating limits, as shown in fig. 4.1 d).

### 4.2 Microwave power absorption in the ECR heated plasma

The electron heating simulations play a crucial role in this work and gave motivation to experimentally study the evolution of electron energies. In the code used in this thesis work, the behaviour of the electromagnetic wave absorption in the resonance region has been calculated by using the cold plasma dispersion relation with a collisional term. A similar approach for modeling the absorption has also been used e.g. in reference [81]. In this section the relevant mathematical formulation needed for the absorption modeling is presented. In electron cyclotron resonance the frequency of the electron orbiting the magnetic field line and external microwave, moving parallel to the magnetic field, are matched resulting in an energy transfer from the wave to the electrons. This phenomenon, known as cyclotron damping (see e.g. [13]) will decrease the amplitude of the external electromagnetic wave.

Any electromagnetic wave can be expressed in a form of

$$\mathbf{E} = E_0 e^{i(kz - \omega t)} = E_0 e^{ikz} e^{-i\omega t} = E_0 e^{-k_i z} e^{ik_r z} e^{-i\omega t}, \quad (4.4)$$

where  $E_0$  is the amplitude of the wave,  $\omega$  the angular frequency of the wave and the wave number  $k$  has been divided into imaginary and real parts. If the system (in this case the plasma) is in a state where the imaginary part of the wave number differs from zero, cyclotron damping takes place. In an ECR plasma this happens at the resonance region and the term  $e^{-k_i z}$  determines the rate of energy absorption as the wave penetrates into the electron cyclotron resonance zone. In the following, expressions for the wave numbers will be derived using cold plasma theory.

Macroscopic quantities for a cold electron plasma are electron density  $n_e$  and velocity  $v_e$  which are coupled via continuity equation of the particle density

$$\frac{\partial n_e}{\partial t} + \nabla \cdot (n_e \mathbf{v}_e) = 0 \quad (4.5)$$

and the Langevin equation

$$m_e \frac{dv_e}{dt} = -e (\mathbf{E} + \mathbf{v}_e \times \mathbf{B}) - m_e \nu_{\text{col}} \mathbf{v}_e, \quad (4.6)$$

where  $\nu_{\text{col}}$  is the collision frequency,  $\mathbf{E}$  the electric field and  $\mathbf{B}$  the magnetic field. If small perturbations around the average (constant) values are assumed, density, velocity and magnetic field can be written with linear approximations

$$n_e(\mathbf{r}, t) = n_0 + \delta n_e(\mathbf{r}, t) \quad (4.7)$$

$$\mathbf{v}_e(\mathbf{r}, t) = \delta \mathbf{v}_e(\mathbf{r}, t) \quad (4.8)$$

$$\mathbf{B}(\mathbf{r}, t) = \mathbf{B}_0 + \delta \mathbf{B}(\mathbf{r}, t). \quad (4.9)$$

## Chapter 4. Electron heating in ECRIS

Using the harmonic wave approximation

$$\delta n_e, \delta \mathbf{v}_e \propto e^{i(kz - \omega t)} \quad (4.10)$$

and rejecting all higher order perturbations, equations 4.7 and 4.8 can be written in linearized form as

$$-i\omega\delta n_e + i\mathbf{k} \cdot (n_0\delta \mathbf{v}_e) = 0 \quad (4.11)$$

$$-i\omega m_e \delta \mathbf{v}_e = -e(\mathbf{E} + \delta \mathbf{v}_e \times \mathbf{B}_0) - m_e \nu_{\text{col}} \delta \mathbf{v}_e. \quad (4.12)$$

Next, two of Maxwell's equations need to be introduced; Faraday's law

$$\nabla \times \mathbf{E} = -\frac{\partial \mathbf{B}}{\partial t} \quad (4.13)$$

and Ampère's law

$$\nabla \times \mathbf{B} = \mu_0 \left( \mathbf{J} + \epsilon_0 \frac{\partial \mathbf{E}}{\partial t} \right), \quad (4.14)$$

where current density

$$\mathbf{J} = -en_e \mathbf{v}_e = -en_0 \delta \mathbf{v}_e \quad (4.15)$$

and material permeability  $\mu$  and permittivity  $\epsilon$  are set equal to one. Again, using harmonic approximations equations 4.13 and 4.14 take forms of

$$\mathbf{k} \times \mathbf{E} = \omega \delta \mathbf{B} \quad (4.16)$$

and

$$i\mathbf{k} \times \delta \mathbf{B} = \mu_0 (-en_0 \delta \mathbf{v}_e - i\omega \epsilon_0 \mathbf{E}). \quad (4.17)$$

If the angle between  $\mathbf{B}_0$  and  $\mathbf{k}$  is marked with  $\theta$  and a Cartesian coordinate system is chosen in a way that  $\hat{z}$  is in the direction of  $\mathbf{B}_0$  and  $\hat{y}$  is perpendicular to the plane formed by  $\mathbf{B}_0$  and  $\mathbf{k}$  we have

$$\mathbf{B}_0 = B_0 \hat{z} \quad (4.18)$$

$$\mathbf{k} = k_{\perp} \hat{x} + k_{\parallel} \hat{z} = k(\sin \theta \hat{x} + \cos \theta \hat{z}). \quad (4.19)$$

Now it is possible to derive an equation pair for  $\mathbf{v}_e$  and  $\mathbf{E}$ . To do this we need to solve  $\delta \mathbf{B}$  from 4.16 and insert this into 4.17 while remembering that  $c^{-2} = \mu_0 \epsilon_0$ , and rewrite equation 4.12 in a different form. Thus,

$$\mathbf{k} \times (\mathbf{k} \times \mathbf{E}) + \frac{\omega^2}{c^2} \mathbf{E} = \frac{i\omega en_0}{c^2 \epsilon_0} \mathbf{v}_e \quad (4.20)$$

$$\left( 1 + \frac{i\nu_{\text{col}}}{\omega} \right) \mathbf{v}_e + \frac{ie}{\omega m_e} \mathbf{v}_e \times \mathbf{B}_0 = -\frac{ie}{\omega m_e} \mathbf{E}. \quad (4.21)$$

In order to express equation 4.20 in a convenient matrix form the equation is multiplied by  $c^2/\omega^2$  and by using

$$\mathbf{k} \times (\mathbf{k} \times \mathbf{E}) = (\mathbf{k} \cdot \mathbf{E}) \mathbf{k} - k^2 \mathbf{E} = (k \sin \theta E_x + k \cos \theta E_z) \mathbf{k} - k^2 \mathbf{E} \quad (4.22)$$

## 4.2. Microwave power absorption in the ECR heated plasma

we can write

$$\begin{pmatrix} 1 - \frac{k^2 c^2}{\omega^2} \cos^2 \theta & 0 & \frac{k^2 c^2}{\omega^2} \sin \theta \cos \theta \\ 0 & 1 - \frac{k^2 c^2}{\omega^2} & 0 \\ \frac{k^2 c^2}{\omega^2} \sin \theta \cos \theta & 0 & 1 - \frac{k^2 c^2}{\omega^2} \sin^2 \theta \end{pmatrix} \begin{pmatrix} E_x \\ E_y \\ E_z \end{pmatrix} = \frac{ie n_0}{\omega \epsilon_0} \begin{pmatrix} v_x \\ v_y \\ v_z \end{pmatrix}. \quad (4.23)$$

The matrix form of 4.21 is obtained after realizing that

$$\mathbf{v} \times \mathbf{B}_0 = B_0 \mathbf{v} \times \hat{z} = B_0 (v_y \hat{x} - v_x \hat{y}), \quad (4.24)$$

resulting in

$$\begin{pmatrix} 1 + \frac{i\nu_{col}}{\omega} & \frac{i\omega_{ce}}{\omega} & 0 \\ -\frac{i\omega_{ce}}{\omega} & 1 + \frac{i\nu_{col}}{\omega} & 0 \\ 0 & 0 & 1 + \frac{i\nu_{col}}{\omega} \end{pmatrix} \begin{pmatrix} v_x \\ v_y \\ v_z \end{pmatrix} = -\frac{ie}{\omega m} \begin{pmatrix} E_x \\ E_y \\ E_z \end{pmatrix}. \quad (4.25)$$

In order to eliminate  $\mathbf{v}$  from equation 4.23 the left hand side matrix of 4.25 can be inverted and used to multiply both sides of equation 4.23. This results in a matrix form consisting only of components of the electric field  $\mathbf{E}$ :

$$\begin{pmatrix} D - \frac{k^2 c^2}{\omega^2} \cos^2 \theta & -iE & \frac{k^2 c^2}{\omega^2} \sin \theta \cos \theta \\ iE & D - \frac{k^2 c^2}{\omega^2} & 0 \\ \frac{k^2 c^2}{\omega^2} \sin \theta \cos \theta & 0 & F - \frac{k^2 c^2}{\omega^2} \sin^2 \theta \end{pmatrix} \begin{pmatrix} E_x \\ E_y \\ E_z \end{pmatrix} = 0, \quad (4.26)$$

where

$$\begin{aligned} A &= 1 + \frac{i\nu_{col}}{\omega}, & B &= \omega_{ce}/\omega \\ C &= \omega_{pe}^2/\omega, & D &= 1 - \frac{CA}{A^2 - B^2} \\ E &= -\frac{CB}{A^2 - B^2}, & F &= 1 - \frac{C}{A}. \end{aligned}$$

If we then consider microwave propagation parallel to the magnetic field the angle  $\theta$  between the wave vector  $\mathbf{k}$  and  $\mathbf{B}_0$  becomes zero and equation 4.26 simplifies into a form of

$$\begin{pmatrix} D - \frac{k^2 c^2}{\omega^2} & -iE & 0 \\ iE & D - \frac{k^2 c^2}{\omega^2} & 0 \\ 0 & 0 & F \end{pmatrix} \begin{pmatrix} E_x \\ E_y \\ E_z \end{pmatrix} = 0. \quad (4.27)$$

The longitudinal component gives a dispersion relation

$$F = 1 - \frac{C}{A} = 0, \quad (4.28)$$

from which, at the limit of  $\nu_{col} \rightarrow 0$ , arises the familiar plasma oscillation  $\omega^2 = \omega_{pe}^2$ . In the transverse plane the dispersion relation is expressed by

$$\frac{k^2 c^2}{\omega^2} = D + E = 1 - \frac{C}{A + B} \quad (4.29)$$

$$\frac{k^2 c^2}{\omega^2} = D - E = 1 - \frac{C}{A - B'} \quad (4.30)$$

## Chapter 4. Electron heating in ECRIS

where the first equation is related to a right-handed circularly polarized (RHCP) wave and the latter a left-handed circularly polarized (LHCP) wave. Because an electron follows the right-handed rotation around the magnetic field line, we are mainly interested in the RHCP wave. Hence, the dispersion relation in a cold plasma with collisions included in the case of an electron cyclotron resonance can be expressed as

$$N^2 = \frac{k^2 c^2}{\omega^2} = 1 - \frac{\omega_{pe}^2}{\omega(\omega - \omega_{ce} + i\nu_{col})}, \quad (4.31)$$

where  $N$  is the refractive index. In some contexts the sign of the collisional term  $i\nu_{col}$  is negative (see for example [81]). However, this only switches the roots of equation 4.31 while solving it for wave number  $k$ . In figure 4.2, the real and imaginary parts of the square of the refractive index are presented as a function of magnetic field strength. As can be seen, the real part and the imaginary peaks sharply at the resonance. The region between the resonance and the cut-off ( $N = 0$ ) is known as the evanescent region. The behavior of the real and imaginary parts of the wave numbers (see equation 4.34) are shown in figure 4.3. When the microwave is coming from the higher magnetic field side ( $\omega_{ce} > \omega_{rf}$ ) towards the lower magnetic field (the so-called magnetic beach) the wave enters the evanescent region after crossing the resonance. According to Budden [82] transmission and absorption of the wave occurs without reflection. If the wave travels into the resonance from the lower magnetic field side ( $\omega_{ce} < \omega_{rf}$ ) towards the increasing magnetic field, both transmission and reflection can occur. Also in this case absorption of the wave occurs [81].

In order to model the cyclotron damping in the resonance region the real and the imaginary parts of the wave number must be solved from equation 4.31 which can first be divided into real and imaginary parts. Using notations

$$k^2 = \frac{\omega^2}{c^2} \left[ 1 - \frac{\omega_{pe}^2(\omega - \omega_{ce})}{\omega[(\omega - \omega_{ce})^2 + \nu_{col}^2]} + i \frac{\omega_{pe}^2 \nu_{col}}{\omega[(\omega - \omega_{ce})^2 + \nu_{col}^2]} \right] = G + iH \quad (4.32)$$

and

$$k^2 = (k_{real} + ik_{imag})^2 \quad (4.33)$$

four roots are found for both real and imaginary parts. Two of these are opposite numbers to the first two solutions, thus, we can write

$$\begin{aligned} k_{real,1} &= \frac{H}{\sqrt{2}(-G + \sqrt{G^2 + H^2})^{1/2}}, & k_{imag,1} &= \left( \frac{-G + \sqrt{G^2 + H^2}}{2} \right)^{1/2} \\ k_{real,2} &= \frac{H}{\sqrt{2}(-G - \sqrt{G^2 + H^2})^{1/2}}, & k_{imag,2} &= \left( \frac{-G - \sqrt{G^2 + H^2}}{2} \right)^{1/2} \\ k_{real,3} &= -k_{real,1}, & k_{imag,3} &= -k_{imag,1} \\ k_{real,4} &= -k_{real,2}, & k_{imag,4} &= -k_{imag,2}. \end{aligned} \quad (4.34)$$

From these equations a pair of solutions where both the real and the imaginary part of the wave number are non-negative is selected. The real part of the wave number

## 4.2. Microwave power absorption in the ECR heated plasma

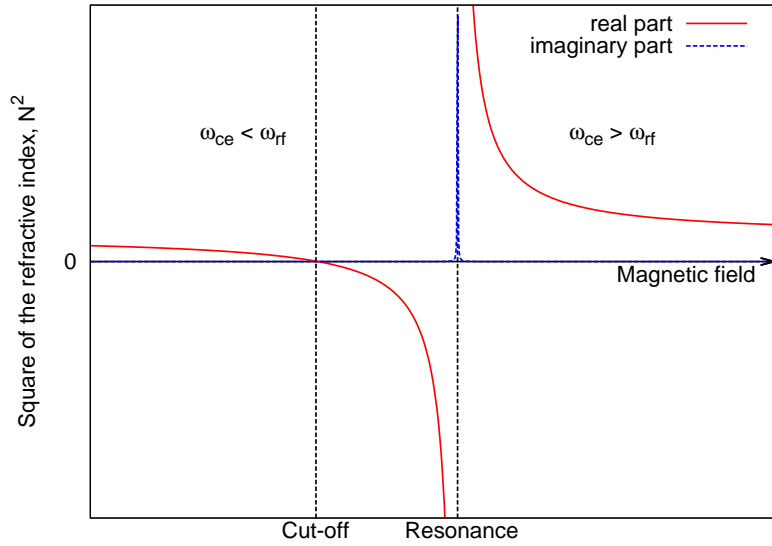


Figure 4.2: Schematic representation of the square of the refractive index  $N^2$  of the right-hand circularly polarized wave as a function of magnetic field. Both real and imaginary parts are shown.

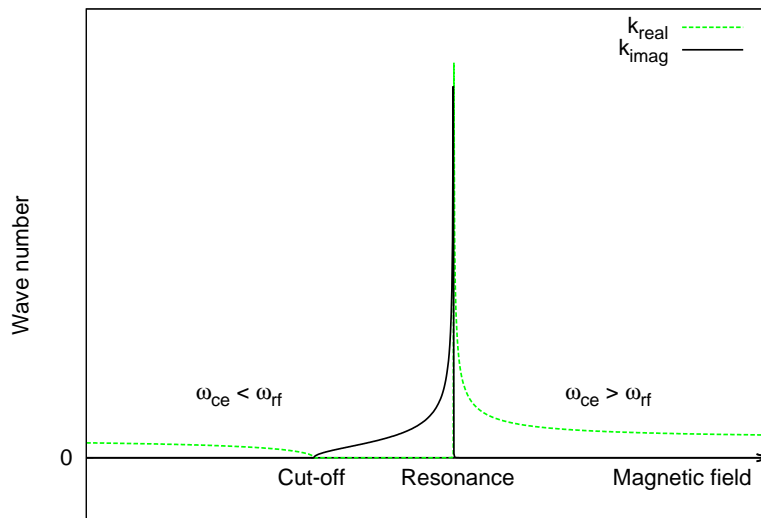


Figure 4.3: Schematic representation of the wave number  $k$  in the vicinity of the resonance region. Both real and imaginary parts are shown.

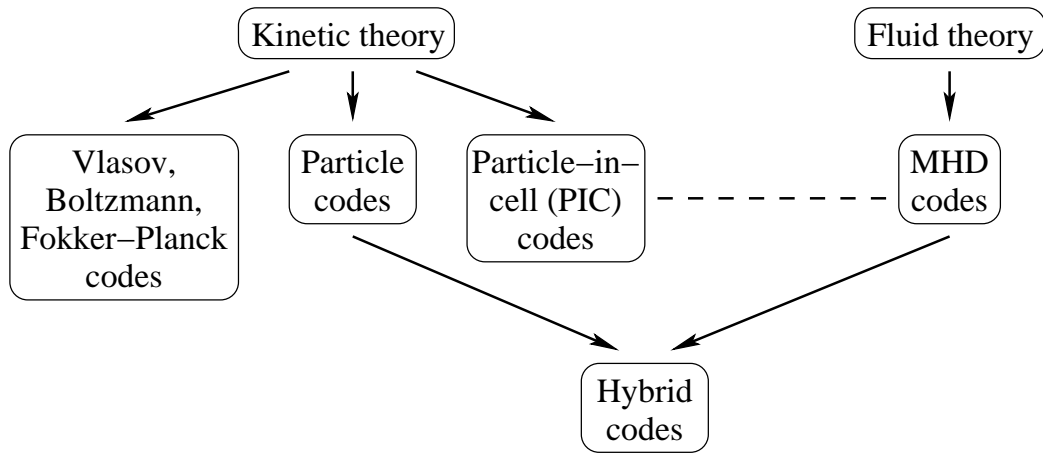


Figure 4.4: A rough classification of plasma simulation models.

can be utilized in the RHCP wave (see equation 4.36) launched into the plasma chamber and the imaginary part can be used to model the cyclotron damping. This approach is adopted in the numerical part of this thesis.

### 4.3 Simulations of ECR ion source plasmas

Numerical modeling has been an important tool in physics almost as long as computers have been available. Analytical solutions can be obtained usually for only a limited number of physical problems, thus, in many cases a numerical solution is needed in order to solve the problem. Today, as more and more complicated phenomena are studied, the use of numerical methods is one of the key elements in theoretical studies. In plasma physics numerical simulations are typically based on two theories — fluid and kinetic theories. Fluid description utilizes magnetohydrodynamic equations assuming approximate transport coefficients while a kinetic approach is more accurate by taking into account detailed models of plasmas including particle interactions via electromagnetic fields. In kinetic simulations the problem is approached by solving Vlasov, Boltzmann and Fokker-Planck equations or using particle simulation taking into account a collection of charged particles affected by electromagnetic fields. However, the classification of different types of plasma simulations is not so simple because so-called “hybrid” simulations are extensively used. These hybrid codes utilize both kinetic and fluid theories in combination. Widely adapted particle-in-cell (PIC) codes are fundamentally kinetic but with certain assumptions they can be classified as fluid codes (see e.g. FLIP MHD [83]). Figure 4.4 presents a very general overview of the usual plasma simulation types, and a comprehensive discussion of different kind of plasma simulations can be found for example in references [84, 85].

### 4.3. Simulations of ECR ion source plasmas

Total electron densities and cold electron population energies have been measured e.g. with VUV (vacuum ultra violet) techniques (see e.g. reference [42]), however there are several parameters which are not known for ECR plasmas and need to be guessed in simulation studies if self-consistent PIC codes are not used. Such parameters are e.g. electron and ion density profiles, average electron energy in the plasma and plasma chamber quality factor. From the time-resolved measurements of bremsstrahlung it is noticed that it takes at least a couple of hundred of milliseconds to reach steady state of integrated total count rate [70, 33] suggesting that same time span is needed to saturate the electron energy distribution function. This means, that electron heating codes capable of simulating hundreds of milliseconds in a reasonable time are needed to link the experimental observations tightly to theoretical understanding. Problems in the simulations also arise from the numerical instabilities related to different solver algorithms. Electron cyclotron resonance heating is prone to these instabilities due to the resonance where the velocity components of electrons change rapidly in time and space. Therefore a phenomenon known as “numerical heating” where the stochastic behaviour is not observed is not unfamiliar. In one-particle simulations there is always the issue of statistics, or lack of it. Very small changes in the initial conditions will create a very different time-resolved behaviour of the electron and the system might be described as chaotic. However, even with single particle simulations, without coupled equations of motion between a vast number of particles, the knowledge of ECR plasmas and trapping of electrons can be increased significantly by running the simulations with randomized initial values repeatedly.

#### 4.3.1 Examples of existing ECR codes

The TrapCAD code [5, 86] is a good example of a single particle simulation which is typically used to simulate 30–60 thousand electrons one by one for a period of several hundreds of nanoseconds [87]. During this time the highest electron energies are in the range of 10 keV using typical parameters of the SUPERSHyPIE 14 GHz ECRIS [88]. Extensive electron heating and trapping simulations have also been conducted by Heinen *et al.* [6, 89] who studied both conventional  $B_{\min}$  structure as well as the so-called flat-B [67] structure. The electron density profiles simulated by Heinen have also been observed experimentally with VUV techniques [90]. Unlike TrapCAD, Heinen *et al.* are using standing wave modes in the electron heating and report electron energies up to tens of keV after 1  $\mu\text{s}$ .

In addition to pure electron heating codes, there are several other general plasma or ECRIS plasma simulation codes available. The GEM code by Far-tech [9, 91] simulates the electron distribution function using a bounce-averaged Fokker-Planck method, the ion dynamics are modeled with fluid equations and the DC electric field in the plasma (plasma potential) is calculated self-consistently from force balance. In GEM it is assumed that the microwave is fully absorbed at the resonance and the propagation of the microwave is not modeled. the code is capable of simulating

## Chapter 4. Electron heating in ECRIS

millisecond time scales [92]. The VORPAL code, by the University of Colorado and Tech-X corporation, is a general plasma simulation code containing both PIC and fluid models for the plasma [10]. The kinetic ionization model in the VORPAL plasma simulation framework is based on the so-called Monte Carlo Collisions (MCC) algorithm which determines at each time step the probability that a collection of particles undergoes a certain process [93]. VORPAL has been used to study how the different locations for injecting the neutral gas into an ECRIS change the abundances of different ion charge states [93]. The ion production in an ECRIS has also been modeled by Mironov and Beijers [8]. In this code the PIC MCC method is used in a three dimensional geometry, heavier particles (ions and atoms) are tracked while the electrons are represented using a Maxwell-Boltzmann energy distribution and collisional and diffusive processes have been taken into account. The code has been used to obtain spatial distributions of ions and to study charge state distributions.

### 4.3.2 Hybrid simulation code for ECR heating

In this thesis work a single particle hybrid code was developed in order to simulate the time evolution of electron energies in an electron cyclotron resonance ion source plasma. Propagating RHCP electromagnetic wave is launched into the plasma chamber and the effect of microwave power absorption (cyclotron damping), which is the key point of the code, is calculated from the magnetohydrodynamics by solving the cold plasma dispersion relation with collisional term (see section 4.2). The magnetic field consists of superposition of two solenoid fields and the electron trajectory is calculated by numerically integrating the relativistic equations of motion.

The calculation of the microwave absorption can be divided into two steps. First the initial average electric field amplitude of the electromagnetic wave launched into the plasma chamber is evaluated by using Poynting vector, plasma chamber radius, plasma chamber quality factor and microwave power. The initial electric field amplitude in vacuum  $E_0$ , derived from the Poynting vector  $\mathbf{N} = \mathbf{E} \times \mathbf{H}$ , can be expressed as

$$E_0 = \frac{Q}{r} \sqrt{\frac{P}{\pi}} \left( \frac{4\mu_0}{\epsilon_0} \right)^{1/4}, \quad (4.35)$$

where  $r$  is the plasma chamber radius,  $P$  the microwave power,  $\mu_0$  the vacuum permeability and  $\epsilon_0$  the vacuum permittivity. Plasma chamber quality factor  $Q$  is used to multiply the initial electric field amplitude. The second step is the calculation of the microwave absorption (damping of the electromagnetic wave) at the resonance region from the dispersion relation of the EM wave, which is a function of plasma density. In the vicinity of the resonance region, where  $k_{\text{imag}} > 0$ , the amplitude of the electromagnetic wave propagating into the plasma is attenuated according to  $E = E_0 e^{-k_{\text{imag}}(z)z}$ . The resulting electric field amplitude is thus modeled in 1D. The

### 4.3. Simulations of ECR ion source plasmas

RHCP electromagnetic wave of the form of

$$\mathbf{E} = E_0 \sin(\omega t - k_{\text{real}}z) \hat{e}_x - E_0 \cos(\omega t - k_{\text{real}}z) \hat{e}_y \quad (4.36)$$

is used. The wave number  $k_{\text{real}}$  is calculated from the dispersion relation (see section 4.2).

Recent frequency tuning experiments suggest that EM wave modes exist in the loaded ECRIS plasma chamber. In the simulations a propagating EM wave is used. This approach is chosen because even small changes in the ECRIS operating parameters can affect the wave modes inside the plasma chamber and make the comparison between different simulation parameters very difficult. The wave modes existing in an empty plasma chamber (resonance cavity) with given dimensions can be calculated straightforwardly. However, according to theoretical plasma models transmission, reflection and mode conversion, caused by for example density gradients, can occur in the plasma. Thus, it is difficult to obtain wave modes for the loaded ECRIS plasma chamber.

The solenoid magnetic field is calculated using magnetic field profiles obtained with RADIA [94] simulations corresponding to the JYFL 14 GHz ECRIS. A second order polynomial of the form of  $B(z) = Az^2 + C$ , where  $A$  and  $C$  are constants, is fitted to the simulated axial magnetic field profile and the final magnetic field expressions used in the simulation code,  $B_z(r, z)$  and  $B_r(r, z)$ , can be obtained with the aid of the so-called solenoid field approximation equations or B field off-axis expansion equations [95]:

$$B_z(r, z) = \sum_{n=0}^{\infty} \frac{(-1)^n}{(n!)^2} B^{(2n)}(z) \left(\frac{r}{2}\right)^{2n} \quad (4.37)$$

$$B_r(r, z) = \sum_{n=0}^{\infty} \frac{(-1)^{n+1}}{n!(n+1)!} B^{(2n+1)}(z) \left(\frac{r}{2}\right)^{2n+1}. \quad (4.38)$$

Here  $B^{(2n)}(z)$  means  $2n^{\text{th}}$  derivative of  $B_z$  respect to  $z$ . The magnetic field is thus calculated in 3D.

The equations of motion are derived from

$$\frac{d\mathbf{p}}{dt} = \frac{d}{dt}(\gamma m_e \mathbf{v}_e) = \mathbf{F} \quad (4.39)$$

and they are presented in detail in reference [7]. In the force term the Lorentz force  $\mathbf{F} = e(\mathbf{E} + \mathbf{v}_e \times \mathbf{B})$  is used. The sextupole field can be considered as a small perturbation of the solenoid field near the symmetry axis of the ion source and is therefore omitted. Furthermore, the static magnetic field generated by the solenoids is typically several orders of magnitude higher than the RF magnetic field of the RHCP EM wave. Thus, in the simulation the magnetic term consists only of the

## Chapter 4. Electron heating in ECRIS

solenoid field. The equations of motion are integrated using an 8<sup>th</sup> order Prince-Dormand Runge-Kutta method [96]. This integration scheme uses adaptive step size control and it can be used e.g. from the Gnu Scientific Library (GSL) [97]. The integrator returns position and velocity coordinates of an electron in 3D on each iteration step.

The electron density profile that is used for the simulations presented in this thesis is Gaussian along the source axis with minimum density of  $10^{16} \text{ m}^{-3}$  (at both ends of the plasma chamber) and maximum density of  $10^{17} \text{ m}^{-3}$  (at the center of the plasma chamber). In order to calculate the ion density needed for the electron-ion collision frequency, an average ion charge state of 8+, which can be typical for example with Ar plasma, is assumed. In addition, the average electron energy of the plasma is set to 100 eV. For the JYFL 14 GHz ECRIS the plasma chamber radius is 38 mm and the total length of the plasma chamber is 280 mm. Simulation is stopped if the electron is no longer contained in the volume of the plasma chamber. The second order polynomial magnetic field profile in the simulations is of form of  $B(z) = 93.24z^2 + 0.35$  which implies that the magnetic field at the end plates of the plasma chamber ( $z = \pm 0.14 \text{ m}$ ) is roughly 2.2 T and the magnetic field at the center of the plasma chamber is 0.35 T. The magnetic field gradient at the resonance  $\nabla B_{\text{res}} = 7.8 \text{ T}$ . Microwave power of 500 W with the frequency of 14.1 GHz is used. At the beginning of a simulation the electron is shifted (in xy-plane) according to its Larmor radius in a way that it rotates around the source axis (z-axis) while bouncing in the magnetic bottle. The initial energy of the electron is randomized between 1 meV and 1 keV and the initial pitch angle is between  $-89^\circ$  and  $+89^\circ$  with respect to the source axis. The electrons are launched from the resonance region towards increasing magnetic field. The code does not take into account collisions between plasma particles (ionization and charge exchange reactions) during electron tracing. Thus, the secondary electron emission from ionizing processes or collisions between plasma particles and plasma chamber walls is not calculated.

Usually ECR plasmas are treated as collisionless if the electron density is less than  $10^{18} \text{ m}^{-3}$  [6]. Electron-ion collision times can be calculated for example using an electron density of  $10^{17} \text{ m}^{-3}$ . Using these values the times between the electron-ion collisions can be approximated to be around 6  $\mu\text{s}$  and 160  $\mu\text{s}$  with electron energies of 100 eV and 1 keV, respectively. This means that while the simulation times of 20  $\mu\text{s}$  or less are presented in this thesis it is reasonable to exclude the effects arising from particle collisions while the trajectory of the electron is calculated. However, in longer simulations the collisional effects between electrons and other plasma particles should be calculated during the electron tracing.

The philosophy behind the simulation development has been trying to simulate electron heating in an ECRIS plasma by taking into account relevant aspects of plasma physics related to ECRH but to keep the calculation time as low as possible. Single particle hybrid simulation in a simplified magnetic mirror structure (no

### 4.3. Simulations of ECR ion source plasmas

sextupole), which simulates electron heating under steady state background, is thus used. Usually, the exponential damping of the microwave power is not included in the simulations of ECR ion source plasmas which easily results in very energetic electrons in short heating times. If cyclotron damping is not modeled, it is assumed that the electron density is negligible and the ionization degree of the plasma is low, thus the power absorption in the resonance zone is low. This means that electrons are heated with a full EM wave amplitude rapidly into high energies. Using the cyclotron damping model in the code non-zero electron and ion densities are assumed leading to increased power absorption in the resonance zone. Steady state modeling was chosen instead of including the plasma breakdown due to a simpler approach — the time evolution of electron density and the loaded plasma chamber Q-value and the energy of the average electron energy population are currently not known. However, time evolution information about the plasma breakdown is crucial in order to successfully model the first moments of plasma after it has been ignited.

With typical accuracy requirements (absolute and relative accuracies of  $10^{-9}$ ) for the particle integrator simulating 20 000 electrons for a period of 1  $\mu$ s takes roughly 48 hours of CPU time at the minimum while the same simulation without cyclotron damping modeling takes less than 7 CPU hours. Decreasing the simulation times significantly by lowering the accuracy demands is not reasonable due to possible numerical instabilities. Modeling plasma breakdown by changing average electron energy, electron density profile and plasma chamber quality factor as a function of time will increase the needed CPU time, however, it is one of the future goals in the code development. In order to realize this, the time evolution of the quality factor of an operational ECR ion source needs to be measured.



## Chapter 5

### Bremsstrahlung radiation from an ECRIS

In magnetized plasmas charged particles are orbiting the magnetic field lines, thus, emitting radiation. This type of radiation is known as cyclotron or synchrotron radiation, depending on the energy of the radiation. Plasma bremsstrahlung is emitted when charged particles are colliding in the plasma and external radiation fields interacting with a plasma give rise to scattered radiation [98]. The so-called wall-bremsstrahlung radiation occurs when energetic particles are stopped in a solid material. This happens for example in ECR ion sources where the plasma flux hits the plasma chamber wall. The bremsstrahlung spectrum is continuous although a wall-bremsstrahlung spectrum usually contains characteristic “line” radiation (x-rays) caused by the wall material. The maximum energy of the bremsstrahlung is defined by the energy of the charged particle, contradictory to the energy of characteristic radiation depending on the electron shell structure of the material. Bremsstrahlung emission from electron cyclotron resonance heated plasmas has been studied using charge-coupled device (CCD) cameras [99], vacuum ultraviolet (VUV) techniques [90, 100, 101], scintillator [71, 102] and semiconductor detectors [33, 70, 103, 104]. Both CCD and VUV methods are used for probing the ion species and low energy electrons directly in the plasma but are limited to low energies. CdTe detectors can be used to observe photon energies inside the vacuum due to their small sizes while the highest energy photons are usually observed by measuring wall-bremsstrahlung radiation outside the ion source with different scintillator and semiconductor detectors.

#### 5.1 Intensity distributions and material properties

While a charged particle accelerates or decelerates it produces angular radiation distributions (see references [105, 106]). The direction of the maximum radiation intensity can be described with  $\theta_{\max}$  which is the angle between the direction of motion of the charged particle and the maximum intensity radiation cone. The angle, at which the particle emits radiation, and the intensity of the radiation depend strongly on the energy of the particle. This is presented in figure 5.1.

## Chapter 5. Bremsstrahlung radiation from an ECRIS

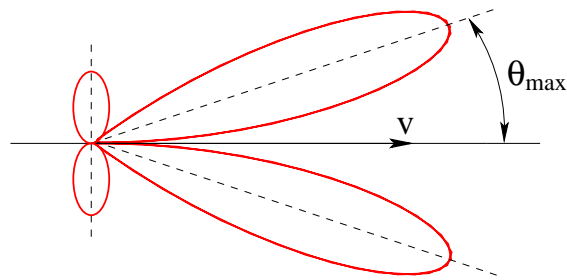


Figure 5.1: Schematic radiation intensity pattern for a charge accelerated in its direction of motion. The two small cones in the vertical position correspond to low energy particles and the two stretched cones at angle  $\theta_{\max}$  correspond to a case of energetic relativistic electrons. The two patterns are not in scale, and the radiation intensity of the forward tilted cones exceeds the intensity of the small cones roughly by a factor of 100 [105].

However, bremsstrahlung radiation measured outside the ECRIS plasma chamber, as well as from all thick targets, can be characterized by different angular distributions. ECRIS bremsstrahlung is a coarse example of bremsstrahlung at non-relativistic energies i.e. energies that are smaller or comparable to the rest energy of the electron [107]. Absorption of the bremsstrahlung photons becomes important with thick targets, such as the plasma chamber of an ECR ion source. The angular distribution and the intensity of the bremsstrahlung depend on both the target i.e. plasma chamber material and the geometry of the target. In this discussion, a target is denoted thick if the scattering and energy loss processes have an appreciable influence on the bremsstrahlung production. The angular distribution of bremsstrahlung radiation intensity is widely spread at non-relativistic energies being about the same order of magnitude at zero and ninety degrees, compared to the trajectory of the incident electron causing bremsstrahlung radiation [107]. This is different compared to the radiation emitted by an accelerated charge, as shown in figure 5.1. Aluminum and copper as well as stainless steel have been used as plasma chamber materials in ECR ion sources. Figure 5.2 shows thick target bremsstrahlung intensity distributions with different electron energies as a function of angle between the original trajectory of the electron and observed radiation. It can be observed that using a thick aluminum target and incident electron energy of 1.25 MeV the bremsstrahlung intensity ratio ( $I_{0^\circ}/I_{90^\circ}$ ) is measured to be approximately 6, while with copper the same ratio is about 4. This means that the angular distribution of bremsstrahlung emission is very similar for both Al and Cu targets. From figure 5.3 it is noted that the integrated total bremsstrahlung intensity is quite linear with the atomic number of the thick target. With 1.25 MeV incident electrons a thick copper target produces more than twice the amount of bremsstrahlung radiation generated by an aluminum target.

## 5.1. Intensity distributions and material properties

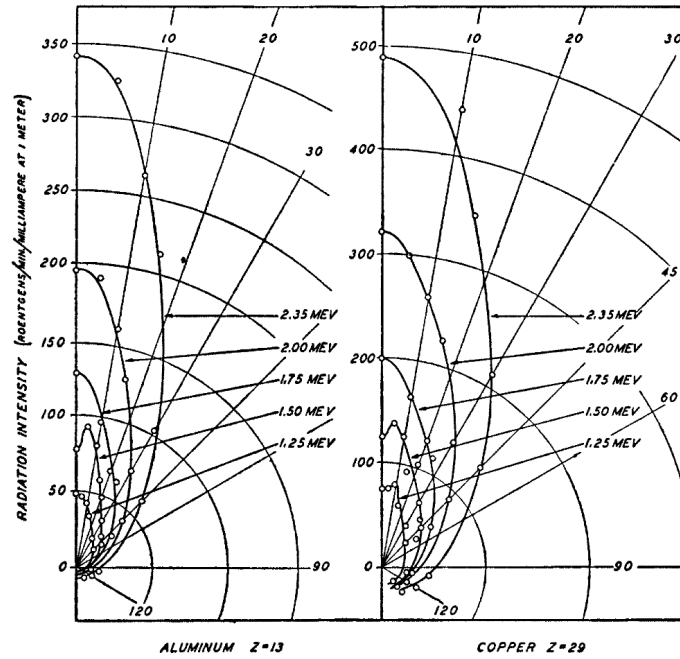


Figure 5.2: Bremsstrahlung intensity at various energies as a function of angle for Al and Cu targets. Figure reproduced from reference [108].

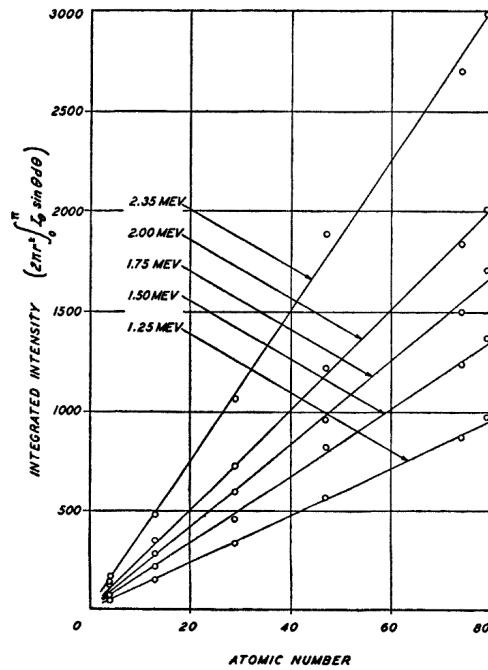


Figure 5.3: Integrated bremsstrahlung intensity as a function of atomic number of target material. Figure from reference [108].

## Chapter 5. Bremsstrahlung radiation from an ECRIS

In a typical ECR ion source the total material thickness in the radial direction is several tens of millimeters and consists of different elements. Due to the material thickness the lower energy part of the bremsstrahlung spectrum is largely damped as the radiation penetrates into the structure and interacts with the ion source materials (see e.g. GEANT4 simulations from reference [109]). Attenuation of the wall-bremsstrahlung is difficult to correct due to complex geometry of the ECRIS plasma chamber, cooling systems, magnets and outer casing. In addition, the plasma and electrons hitting the chamber walls can not be considered a point source, and the bremsstrahlung emission flux is higher at the radial magnetic field poles than between the poles. This makes the absolute efficiency calibration of the detector system very difficult. Compton tails from bremsstrahlung events have a distinct effect on the shape of the bremsstrahlung spectrum, and it is well known that unless the Compton continuum, arising from Compton scattering, is removed from the spectra (unfolding) the lower energy part of the measured radiation spectrum is over-emphasized. However, time evolution of the spectrum around the highest observed photon energies is less dominated by the Compton scattering and information about the time evolution of the highest electron energies can be obtained without unfolding the spectrum data.

### 5.2 Previous results of high energy bremsstrahlung measurements

Several ECR ion source groups have studied the ECRIS plasma with the aid of steady state bremsstrahlung measurements. In some measurements the radiation is measured from the injection and in some cases measurements through the diagnostic port of the bending magnet have been carried out. The radial ports of the AECR-U [110] type ion source have also been utilized for bremsstrahlung measurements. High energy bremsstrahlung from ECR ion sources have been measured with Ge, NaI and CdTe detectors.

Zhao *et al.* have studied the ECRIS bremsstrahlung in an axial measurement geometry where a HPGe detector was located in the injection of the Lanzhou ECR ion source No. 3 (LECR3) (see [111]) at Lanzhou institute of modern physics (IMP). The effect of gas mixing on the bremsstrahlung energy spectra has been reported [104], and it was found out that adding oxygen to an argon plasma resulted in higher electron energies and increased bremsstrahlung production throughout the energy range. They also observed that increasing the extraction voltage of the ion source increased the bremsstrahlung energies and intensities. The reason for this behaviour has not been given. During the measurements the maximum electron energies were in the range of 1 MeV using microwave power of 600 W at 14.5 GHz.

Bremsstrahlung pinhole studies have been reported by Xie [112] with the AECR-U ion source. Using single and double frequency heating modes at 14 and 10 GHz

### 5.3. Experimental apparatus and measurement setup

microwave frequencies it was seen that the axial bremsstrahlung intensity observed at the dipole magnet downstream from the ion source was essentially linear with the input microwave power. Electron energies over 600 keV were observed and it was found out that the slope of the bremsstrahlung spectra (spectral temperature) was not changed as a function of microwave power.

The effect of different ion source parameters on the spectral temperature has been studied with VENUS [102]. It was found out that the value of  $B_{\min}$  affects the spectral temperatures significantly. By changing the  $B_{\min}$  at 18 GHz from 0.37 T to 0.6 T changes the spectral temperature from 54 keV to 99 keV quite linearly.

Plasma bremsstrahlung from the ECR-II ion source [113] in the ATLAS facility at Argonne National Laboratory (ANL) has been studied with a CdTe detector [103]. It was observed that the radiation power of the bremsstrahlung emission decreased with increasing pressure of argon feeding gas. At the same time the intensity of argon  $K_{\alpha/\beta}$  lines increased. This is explained by decreased electron energies due to increased partial pressure of argon which, on the other hand, results in a higher amount of low charge state argon ions. It was also confirmed that increasing the  $B_{\min}$  resulted in increased spectral temperature. In addition, using double frequency heating it was observed that the total bremsstrahlung power decreases by a factor of 7 when the total RF power is kept constant and the fraction of 11.1 GHz microwave power is varied from 0 % to 100 % (primary microwave frequency was 14 GHz). In the same measurement the spectral temperature remained relatively constant until the fraction of 50 % in the frequencies was reached. After this, the spectral temperature decreased roughly from 30 keV to 20 keV.

### 5.3 Experimental apparatus and measurement setup

The measurements presented in this thesis (see references [33, 70, 71, 114, 115, 116]) were mainly performed with two ECR ion sources. One of the ion sources, VENUS (28 GHz and 18 GHz), is operated in Lawrence Berkeley National Laboratory (LBNL) and the other, 14 GHz ECRIS, in the department of Physics at the University of Jyväskylä (JYFL). These two ion sources represent different generations of ECR ion sources. The main differences arise from the microwave frequency which dictates the characteristics of the magnetic confinement. While VENUS utilizes superconducting solenoids and sextupole, the JYFL 14 GHz ECRIS is based on room temperature solenoids and permanent magnets.

#### 5.3.1 VENUS 28 GHz ECRIS

The superconducting ECRIS VENUS is an example of a third generation ECR ion source. In addition to the primary microwave frequency at 28 GHz a secondary microwave frequency of 18 GHz can be used. The maximum magnetic field strength

## Chapter 5. Bremsstrahlung radiation from an ECRIS

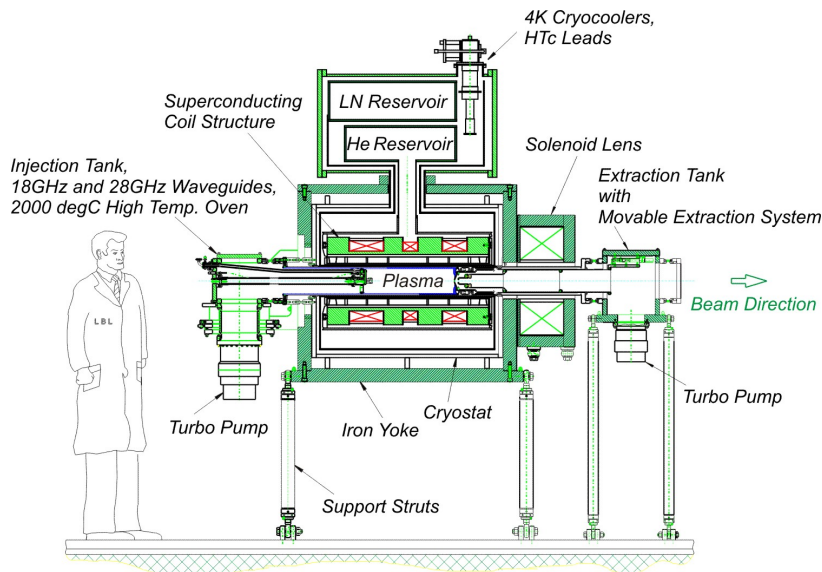


Figure 5.4: Mechanical layout of the superconducting VENUS 28 GHz ECRIS at LBNL [117].

at the injection is 4 T while the extraction field is 3 T and the sextupole generates a maximum field of 2.1 T. The plasma chamber volume is about 9 litres and VENUS is designed to operate with 2 kW at 18 GHz and/or up to 10 kW at 28 GHz resulting in maximum microwave power densities of 1.3 kW/l in the plasma chamber volume [117]. In terms of ion beam currents VENUS can produce around 270  $\mu\text{A}$  of  $\text{Ar}^{16+}$ , 86  $\mu\text{A}$  of  $\text{Xe}^{31+}$ , 28.5  $\mu\text{A}$  of  $\text{Xe}^{35+}$ , 202  $\mu\text{A}$  of  $\text{U}^{34+}$  and 1.9  $\mu\text{A}$  of  $\text{U}^{50+}$ . Figure 5.4 presents the mechanical layout of the VENUS ECR ion source.

### 5.3.2 JYFL 14 GHz ECRIS

The JYFL 14 GHz ECRIS is used several thousands of hours per year for the medium and high charge state heavy ion production. The source is a modified version of the AECR-U ion source [110] at LBNL with some ideas adopted also from a similar source operated in Michigan State University, National Superconducting Cyclotron Laboratory (MSU/NSCL) [118]. In addition to the 14.1 GHz primary frequency a tunable signal generator and Travelling Wave Tube Amplifier (TWTA) is used to launch a secondary microwave frequency into the plasma chamber. The secondary microwave frequency is between 10.75 GHz and 12.40 GHz and the TWTA can amplify several simultaneous microwave frequencies. The maximum magnetic field strength is 2.2 T at the injection, 0.9 T at the extraction and the radial magnetic field at the pole is 0.85 T. The plasma chamber volume is around 1.3 litres and the maximum microwave power density with double frequency heating is about 0.9 kW/l (900 W at 14.1 GHz, 300 W from TWTA). In terms of ion beam currents, the JYFL 14 GHz ECRIS can produce around 10  $\mu\text{A}$  of  $\text{Ar}^{16+}$  and 7.6  $\mu\text{A}$  of  $\text{Xe}^{31+}$ .

### 5.3. Experimental apparatus and measurement setup

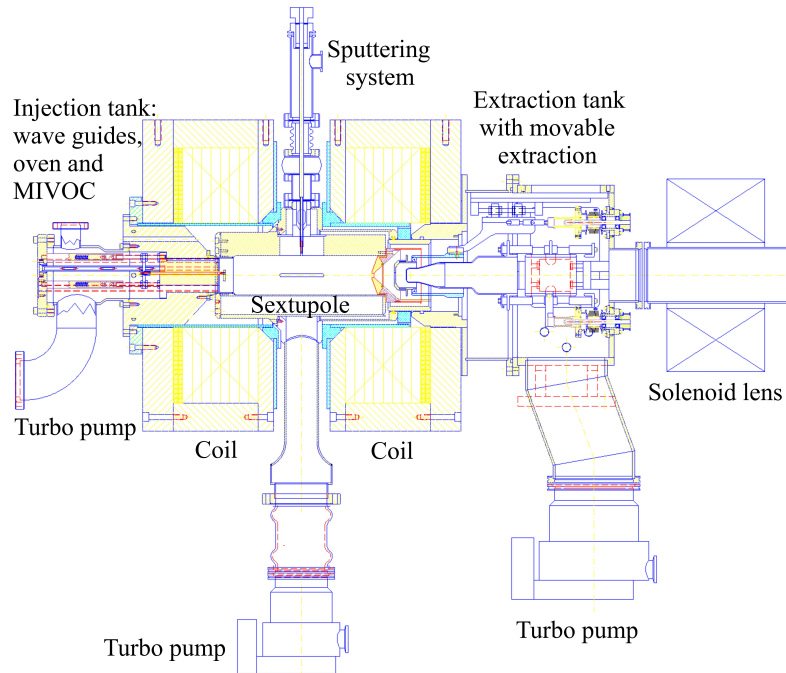


Figure 5.5: Mechanical layout of the 14 GHz ECRIS at JYFL.

The mechanical layout of the JYFL 14 GHz ECRIS is presented in figure 5.5.

#### 5.3.3 Measurement setups

Bremsstrahlung can be measured axially or radially from an ECR ion source. In the axial direction it is possible to “see” the plasma and plasma electrode through a diagnostic port of the bending magnet located downstream from the ion source. In a radial measurement the plasma can be observed directly from a radial diagnostic port if one is available or indirectly observing photons through the plasma chamber walls. In radial measurements between the radial ports the structure of an ECR ion source will attenuate the bremsstrahlung radiation. It has been simulated that the angular distribution of the bremsstrahlung radiation outside the ECRIS at the radial magnetic field pole is mainly concentrated within a 15 degree angle around the normal of the ECRIS surface [109]. In radial measurements the detector can be positioned towards one of the radial magnetic field poles in order to maximize the photons emitted by electrons colliding with the chamber wall.

Motivation for the measurements was to find out the parameters of ECR ion sources affecting the bremsstrahlung production and how the amount of radiation affects the heat load to the cryostat. The motivation for the pulsed microwave power measurements was to find out parameters for the electron heating simulation codes in order to validate them against the measurements, and also to find out how the pulsing of the microwave power could be utilized in order to decrease the amount of

## Chapter 5. Bremsstrahlung radiation from an ECRIS

bremsstrahlung emission without compromising the intensity of the highly charged ion beams.

The measurement setup used in CW bremsstrahlung measurements with VENUS is described in detail in reference [71]. The effect of magnetic field, RF power and microwave frequency on the bremsstrahlung production under steady state conditions were studied using a NaI detector in the axial direction. The heat load to the cryostat was also studied during the measurements. Bremsstrahlung emission was recorded for several minutes in order to obtain reasonable statistics. During the commissioning of the measurement setup some problems had to be solved. For example, the shifting in energy calibration due to the external magnetic field of the LBNL 88-inch cyclotron was unravelled by shielding the photomultiplier tube with iron casing. Bremsstrahlung count rate and calibration drifting as a function of time were settled by performing an energy calibration for each measurement. It was also noticed that a bump in the bremsstrahlung spectra was present when the other LBNL ECR ion sources were operated. The bump was suppressed by adding more lead shielding around the detector.

The measurement setup that was used during the time evolution bremsstrahlung measurements with the JYFL 14 GHz ECRIS is described thoroughly in references [33, 70]. Time evolution measurements of bremsstrahlung production in the radial direction and ion beam currents as a function of magnetic field, RF power, neutral gas pressure, plasma species and different RF pulse duty factors were measured with a germanium detector [33, 70, 114, 115]. The RF on times ranged from less than 5 ms to 1760 ms while the RF off time was varied between 10 ms and 5920 ms. A similar type of bump, as with VENUS, in the bremsstrahlung spectra was observed. The bump was decreased after additional lead shielding was placed around the original collimator structure (see reference [114]). It was noticed that the time scales of reaching a steady state of bremsstrahlung production were not altered by the amount of shielding, and the measurements conducted with different shielding were comparable [70] from the time evolution point of view. The time scales of both bremsstrahlung and ion beam current were measured as a function of typical ECRIS operating settings in order to get an idea about the time scales involved in electron heating and ion beam current production. The effect of the RF pulse pattern to both bremsstrahlung emission and to the ion beam preglow transient were studied and the JYFL 6.4 GHz ECRIS was used in order to find out the electron heating and ion beam current production time scales with an ECRIS operating at a lower microwave frequency than the 14 GHz ECRIS.

## Chapter 6

### Results from the simulations and the measurements

In this chapter both numerical and experimental work is summarized. The simulation code is presented in reference [7] (see appendix A.1) but results presented in section 6.1 have been simulated with an improved version of the code. These results have not yet been published. Simulation work and code development is still a work in progress and more extensive results will be published later. Experimental work presented in sections 6.2 and 6.3 is documented in references [33, 71, 70, 114, 115, 116] (see appendixes A.2–A.7) excluding the data obtained with the JYFL 6.4 GHz ECRIS which have not yet been published.

#### 6.1 Simulation of electron heating in JYFL 14 GHz ECR ion source

The development of the simulation code was started in order to improve the understanding of heating processes inside the ECR ion source plasma. The code is able to model the behaviour of electric field amplitude in the vicinity of the resonance region and takes into account several plasma-related parameters. The same behavior cannot be obtained by linear scaling of the Q-value, because the absorption of the microwave is strongly nonlinear. The first results indicated that the energy evolution of the electron is too slow compared to earlier results obtained with the TrapCAD code [5] and by Heinen *et al.* [6]. This gave us a motivation for the experimental studies of different plasma processes and parameters like the evolution of electron energy by measuring the time evolution of bremsstrahlung in pulsed operation mode.

The time-resolved bremsstrahlung experiments [33, 70, 114, 115] together with the bias disk experiments [116] showed that the plasma breakdown process is a very complicated phenomenon and cannot be handled with the present capabilities of the simulation code. According to the measurements the progression of the breakdown process is very sensitive to the electron and neutral densities at the moment the microwave field is launched into the plasma chamber. Consequently,

## Chapter 6. Results from the simulations and the measurements

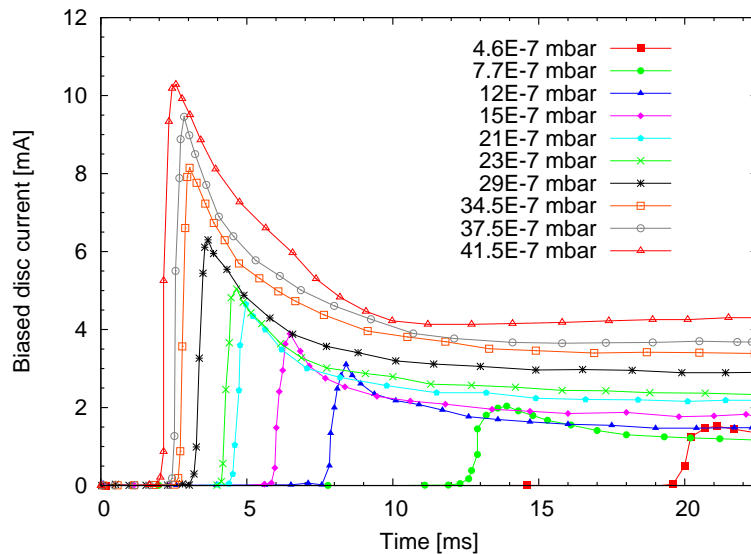


Figure 6.1: Time-resolved bias disc current of neon plasma as a function of neutral gas pressure during the first 22 ms of the applied microwave pulse. Figure from reference [116].

the time to observe the first bremsstrahlung photons can vary from several hundreds of microseconds to several tens of milliseconds. As an example, typical measured plasma breakdown times as a function of neutral gas pressure of neon are shown in figure 6.1. In this chapter the focus is however on the electron heating simulations and on the bremsstrahlung measurements. More detailed explanations concerning the breakdown process is given in reference [116] included also in this thesis.

During the breakdown process the quality factor  $Q$  of the system rapidly changes from the value of an empty chamber to the value of a loaded chamber. The  $Q$  value for the loaded chamber is presently under active experimental research investigation. When the development of this simulation code was started a  $Q$ -value of 3 was frequently used. Since then more information has been received and the results obtained by L. Celona *et al.* indicate that the  $Q$ -value of a loaded plasma chamber is of the order of thousands.

The effect of the microwave power absorption near the electron cyclotron resonance zone is presented and discussed in reference [7]. When the amount of absorption is studied it is evident that the electron density of the plasma affects the absorption processes. Changing the average electron energy of the plasma affects the absorption also, but the effect is more or less insignificant compared to the effect caused by the electron density. The most recent development version of the hybrid simulation code enables statistical analysis with varying input parameters. Simulations using 20 000 electrons with varying initial conditions (initial electron energy and pitch angle) were used to study the effect of microwave absorption and plasma chamber

## 6.1. Simulation of electron heating in JYFL 14 GHz ECR ion source

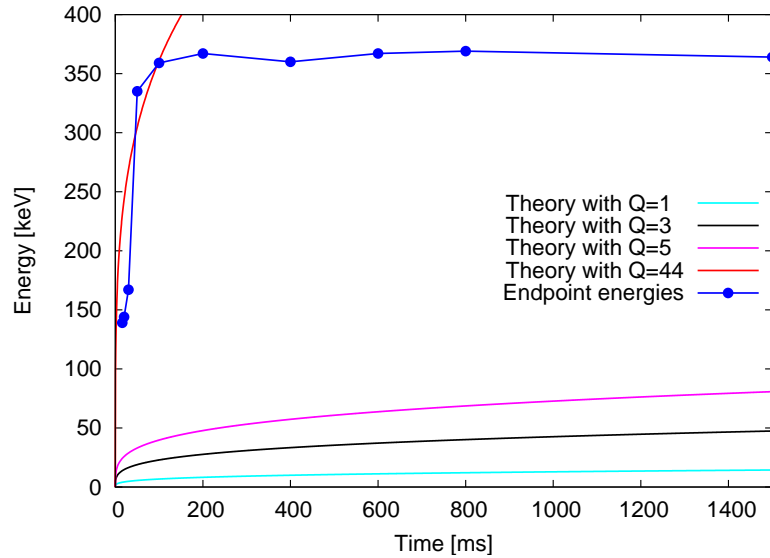


Figure 6.2: Modified stochastic heating theory by Sergeichev *et al.* with different plasma chamber quality factors and approximated bremsstrahlung endpoint energies from argon plasma. Figure from reference [114].

quality factor on the electron energy spectrum.

As an example, plasma chamber quality factors of 3 and 44 were used. The latter value is based on a approximation calculated with modified stochastic heating theory by Sergeichev *et al.* [119] using parameters corresponding to the 14 GHz ECRIS at JYFL. From the measurement data it was found that a plasma chamber quality factor of 44 was needed to match the first 100 ms of the measured maximum energy time evolution as can be seen from figure 6.2. In the most recent RF measurements (see section 6.3) it was discovered that with the aid of a proper RF pulse pattern it is possible to reach high photon energies in very short time scales. This means that the Q-value approximated from the measurement data depends significantly on the plasma breakdown time scales. However, due to a lack of bremsstrahlung statistics with very short RF pulses we haven't been able to approximate the time evolution of the highest photon energies from the energy spectra, and the value of  $Q = 44$  is used in these simulations. Simulated electron energy spectra using 20 000 electrons with and without the microwave power absorption (cyclotron damping) are presented in figures 6.3 and 6.4 with various heating times. Both the electrons that escaped the chamber during the simulation time and the electrons that remained in the chamber for the whole heating time have been taken into account in the data.

From figure 6.3 it is seen that after 1  $\mu$ s of heating time the electron energy spectra reach energies in order of a few keV when the plasma chamber quality factor Q is set to 3. The lowest energy part of the spectra (energies less than 1 keV) corresponding to simulations with and without cyclotron damping are quite similar. The differences

## Chapter 6. Results from the simulations and the measurements

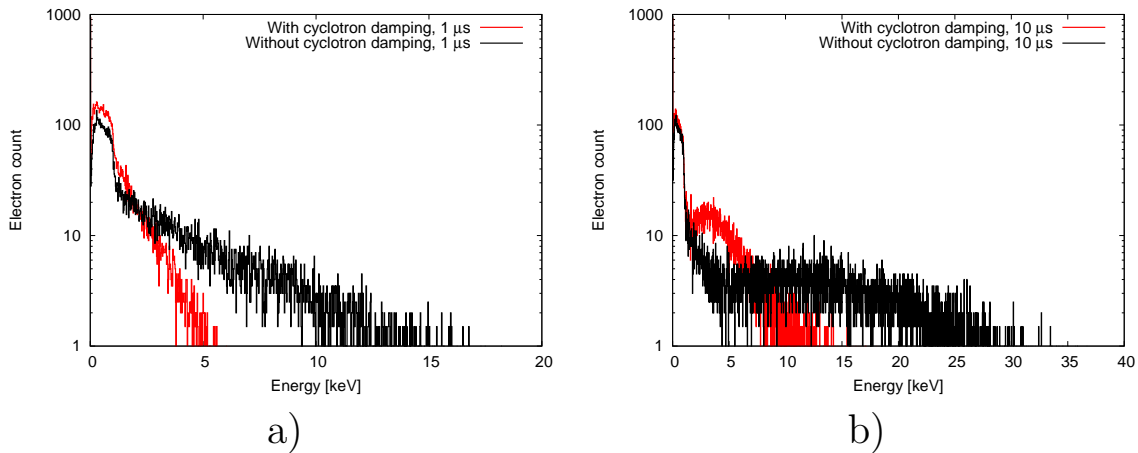


Figure 6.3: Simulated electron energy with a plasma chamber Q-value of 3. Data is presented with and without the cyclotron damping after a) 1  $\mu\text{s}$  and b) 10  $\mu\text{s}$  of heating time.

start to emerge above electron energies of 1 keV, and the simulation done without EM wave absorption results in maximum electron energies that are roughly three times higher (15 keV) compared to the simulation where the damping of the wave has been included (5 keV). After 10  $\mu\text{s}$  of heating time the highest energies simulated with the microwave power absorption (cyclotron damping) are between 7 keV and 14 keV while electron energies ranging from roughly 20 keV to 33 keV are observed without the microwave power absorption model. It can also be seen that a larger number of electrons are concentrated at higher energies after 10  $\mu\text{s}$  than after 1  $\mu\text{s}$ . By using linear extrapolation it could be expected to observe electrons with energies around 500 keV after 500  $\mu\text{s}$  of simulation with absorption model if no saturation of electron energies would take place. However, in order to confirm this, longer simulation times are required.

When the quality factor is increased to 44, the electrons are heated into an energy range of hundreds of keV in the microsecond time scales. From figure 6.4 a) it is seen that using the so-called “traditional” electron heating, where the absorption is not taken into account, the highest energies are between 360 keV and 450 keV while taking the absorption into account the maximum energies range from 320 keV to 360 keV after 1  $\mu\text{s}$ . Electrons with energies exceeding 190 keV are more abundant in the simulation data where the absorption has not been modeled. After 5  $\mu\text{s}$  of heating (fig. 6.4 b)) the highest electron energies are about the same with both heating models. At this point maximum electron energies of 345–430 keV are observed. Electron energies between 190 keV and 320 keV seem to be more abundant in the case where the microwave absorption has not been calculated. Same behavior is observed after 10  $\mu\text{s}$  and 20  $\mu\text{s}$  of heating time as can be seen from figures c) and d). In fig. c) the highest electron energies with the absorption model are observed at 560 keV while it

## 6.1. Simulation of electron heating in JYFL 14 GHz ECR ion source

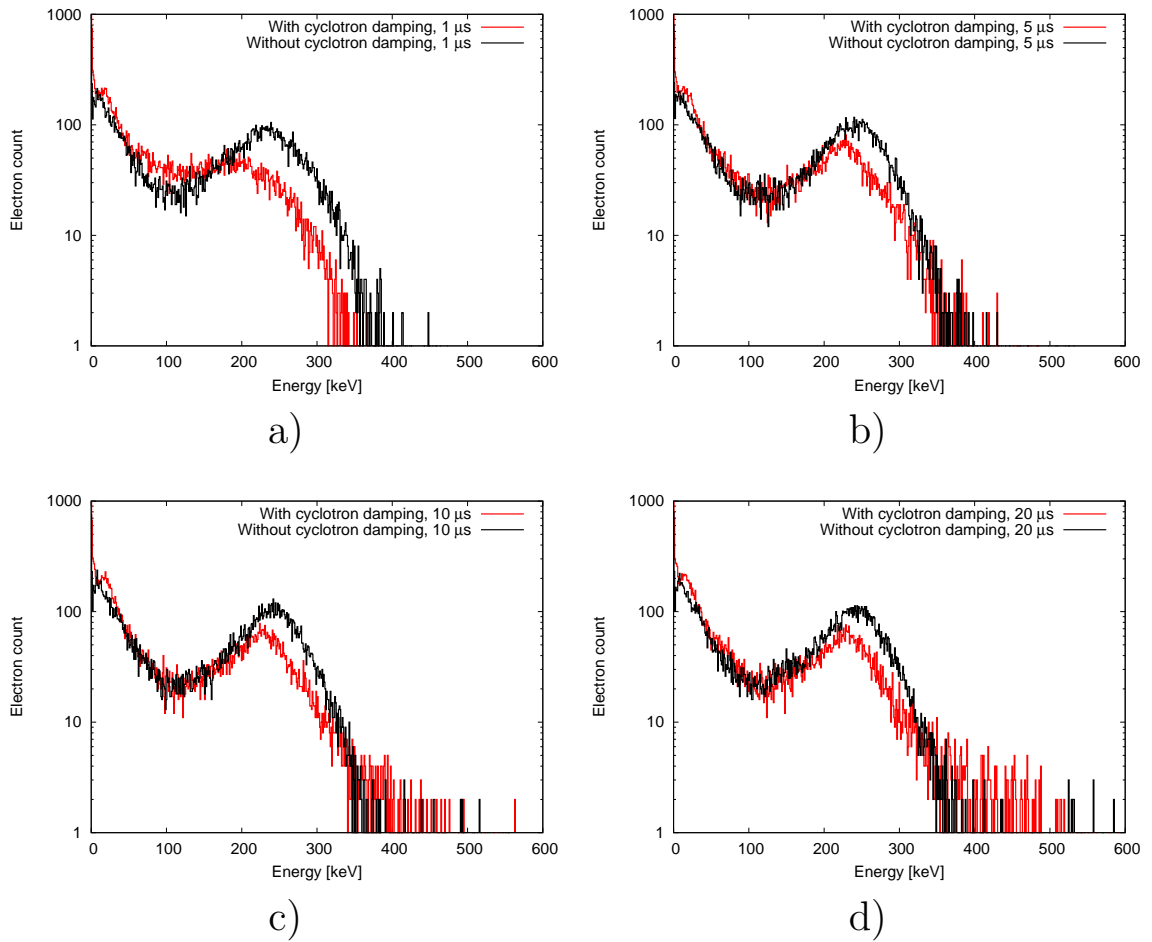


Figure 6.4: Simulated electron energy with a plasma chamber Q-value of 44. Data is presented with and without the cyclotron damping after a) 1  $\mu\text{s}$ , b) 5  $\mu\text{s}$ , c) 10  $\mu\text{s}$  and d) 20  $\mu\text{s}$  of heating time.

## Chapter 6. Results from the simulations and the measurements

Table 6.1: The number of electrons observed and the ratio of electrons between the absorption model and without the model at the energies  $E \geq 110$  keV. Data corresponds to that of figure 6.4 at different time steps.

	1 $\mu$ s	5 $\mu$ s	10 $\mu$ s	20 $\mu$ s
With absorption	6532	7492	7471	7368
Without absorption	11251	11303	11349	11405
with abs. / without abs	0.58	0.66	0.66	0.65

seems that usually electron energies below 500 keV are seen. Without the model the maximum electron energies seem to be below 520 keV. It is also observed that the microwave absorption modeling produces slightly more highest energy electrons than the traditional heating model. In fig. d) this difference is more pronounced. The maximum electron energies with absorption modeling are roughly around 520 keV while the data without the model extends up to 580 keV. From figures 6.4 a)–d) it can be seen that the energies where the electron count drops down to around 1 (at energies exceeding 300 keV) are not increasing very much when the simulation time is increased from 5  $\mu$ s to 20  $\mu$ s. This could indicate that the electron energies start to be around the stochastic heating limit, but to be sure longer simulations are needed to confirm this.

From all of the spectra presented in figure 6.4 it can be seen that there is a bump developing at energies over 110 keV. With the absorption model the bump is not yet fully developed after 1  $\mu$ s although the bump is clearly seen in the data without the absorption modeling. While the simulation time is increased the bump observed without the absorption modeling remains always above the bump obtained with the model. The number of electrons and the ratio of electrons with and without the absorption model at energies equal or greater than 110 keV are presented in table 6.1. It is observed that after 5  $\mu$ s the ratio of electrons observed in the bumps remains relatively constant at around 0.66 and that there clearly are more electrons in the simulation data corresponding energies over 110 keV without the absorption model than with it. It is assumed that as the heating time increases a larger part of the remaining electron population is heated into higher energies. It has been observed, in both steady state measurements with the VENUS and time evolution measurements with the JYFL 14 GHz ECRIS, that bumps in the measured spectra can sometimes be seen. However, it has been found that this could be an issue with the measurement setup. It could be that the electron heating in the simulation code, where a lot of assumptions have been made, is too efficient which can lead to increased amount of higher energy electrons. This effect can cause the bump to appear soon after starting the simulations. One should also remember that the the code is not modeling secondary electrons released from collisional processes, which can have a clear effect on the shape of the spectra. On the other hand the

## 6.2. Steady state bremsstrahlung measurements

simulated data is suggesting that the electron energy distribution under ECR heating is “double Maxwellian” as presented for example in reference [2]. This means that the electron energy spectra contain two electron intensity maximums. One at the lower energies (thermal population) and one at the higher energies (hot population). This type of electron distribution is known to be unstable as the positive slope of the electron velocity function makes the distribution prone to instabilities [120].

### 6.2 Steady state bremsstrahlung measurements

In these measurements (see appendix A.2) the magnetic field of VENUS was scaled such, that the magnetic field gradient at the resonance zone for both 28 GHz and 18 GHz microwave frequencies was roughly the same. As expected, the amount of microwave power had a significant effect on the amount of emitted bremsstrahlung radiation. Measurements conducted with 28 GHz (single frequency heating) using a  $B_{\min}$  of 0.7 T stated that the slope of the bremsstrahlung spectrum (spectral temperature) remains relatively unchanged while varying the RF power from 500 W to 7000 W. Similar behaviour was observed with  $B_{\min} = 0.45$  T. In this case, the observed electron energies were lower than with  $B_{\min} = 0.7$  T due to decreased heating efficiency of the electrons caused by the steeper gradient of the magnetic field in the resonance zone and possibly by increased plasma volume (decreased microwave power density). The effect of the microwave frequency was also studied. Higher total bremsstrahlung count rates, maximum photon energies and spectral temperatures were obtained with 28 GHz compared to 18 GHz. Changing the  $B_{\min}$  affects again the highest photon energies and the spectral temperatures: the higher the  $B_{\min}$  the higher the maximum energies and spectral temperatures.

Operating VENUS with 6000 W of microwave power at 28 GHz ( $B_{\min} = 0.67$  T) or with 7500 W + 1300 W at 28 GHz and 18 GHz ( $B_{\min} = 0.45$  T), respectively, produced the same ion beam current of  $\text{Xe}^{35+}$ . With a double frequency mode the total microwave power was 2.8 kW higher than in single frequency operation. By comparing the bremsstrahlung spectra measured at these RF power settings it was observed that using two frequency heating results in decreased high energy bremsstrahlung radiation compared to the single frequency operation (see figure 6.5). This is due to the increased magnetic field gradient at the resonance of 28 GHz decreasing the heating efficiency. Higher total microwave power is needed to compensate the decrease of the heating efficiency. It was also observed that the power to be absorbed by the cold mass of the cryostat was significantly different at single frequency heating ( $B_{\min} = 0.64$  T) compared to double frequency heating ( $B_{\min} = 0.45$  T) as can be seen from figure 6.6. With the higher  $B_{\min}$  value the heating rate was found to be around 1 W for each kilowatt of injected RF power while with the lower  $B_{\min}$  value the slope was roughly one order of magnitude smaller i.e. 0.1 W/ kW.

## Chapter 6. Results from the simulations and the measurements

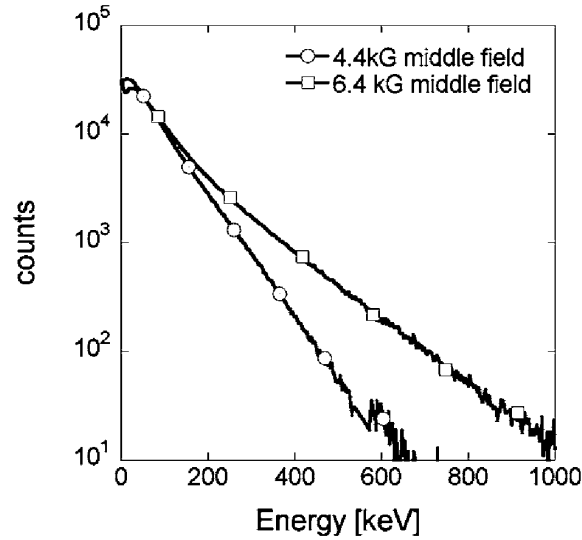


Figure 6.5: The axial bremsstrahlung spectra for a  $B_{\min}$  of 0.44 T (double frequency, 8.8 kW of total RF power) in comparison to a  $B_{\min}$  of 0.64 T (single frequency, 6 kW of total RF power). Figure from reference [71].

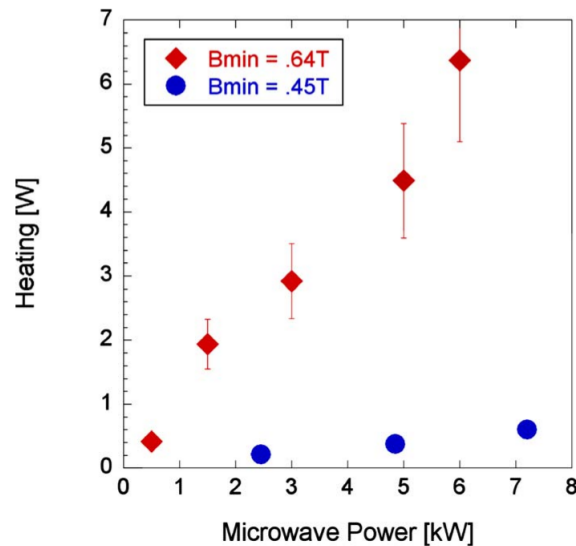


Figure 6.6: Heat load into the cryostat of VENUS at  $B_{\min}$  fields of 0.64 T and 0.45 T as a function of the injected microwave power. The error bar indicates the range of heat load depending on the discharge pressure and the accuracy of the measurement. Figure from reference [71].

### 6.3. Time-resolved bremsstrahlung and ion current measurements

The high energy tail of the bremsstrahlung emission can be suppressed significantly by operating VENUS in double frequency heating mode with a steep magnetic field gradient for the main heating frequency (28 GHz) and a gentle magnetic field gradient for the secondary heating frequency (e.g. 18 GHz). In double frequency heating mode the amount of total microwave power needs to be increased compared to single frequency operation, but the ion source performance (ion beam current) can be matched to single frequency operation with a significantly decreased heat load to the cryostat.

### 6.3 Time-resolved bremsstrahlung and ion current measurements

By studying the total count rate curves as a function of time with the JYFL 14 GHz ECRIS (see appendix A.4)) it was observed that the magnetic field gradient in the vicinity of the electron cyclotron resonance zone affects the total count rate slopes, and thus the heating rate, significantly. The lower the magnetic field gradient the steeper the total count rate slope during the first tens of milliseconds. Lower gradients also resulted in higher steady state count rates (see figure 6.7). It is well known that ECR ion source plasmas can become very unstable at certain source settings. Severe instabilities in total count rates were observed with the highest  $B_{\min}$  that was used during the measurements as can be seen in figure 6.8. Similar behaviour were observed with both oxygen and argon plasmas while the steady state was obtained faster with argon (200 ms) than with oxygen (600 ms).

As a function of neutral gas pressure of argon (appendix A.6) it was observed that the lower the pressure the longer it takes before the bremsstrahlung count rate starts to build up after the microwave power is injected into the ECRIS plasma chamber (see figure 6.9). This result is also confirmed with the biased disk measurements [116] (see appendix A.5). The simple theory presented in the same reference predicts that the plasma breakdown time is inversely proportional to the neutral particle density. However, the slopes of the total count rate curves were quite similar with the different gas pressures of argon and oxygen. The plasma breakdown times ranged typically from a few milliseconds to a few tens of milliseconds and the time scales to reach steady state plasma were around 200–300 ms with argon and 600 ms with oxygen. Steady state was not always observed with oxygen plasma during the RF pulse, though. It is believed that this behaviour is due to outgasing of oxygen molecules and atoms which are deposited on the plasma chamber walls during the RF off period. When the microwave power is launched into the chamber again, the plasma heating will gradually remove the oxygen from the chamber walls which adds an uncontrollable source of neutral oxygen into the plasma.

Using higher microwave powers (appendix A.6) led to higher total count rates, as expected. Steady state bremsstrahlung emission from argon plasmas is reached between 200 ms and 600 ms. The plasma breakdown times are almost independent

## Chapter 6. Results from the simulations and the measurements

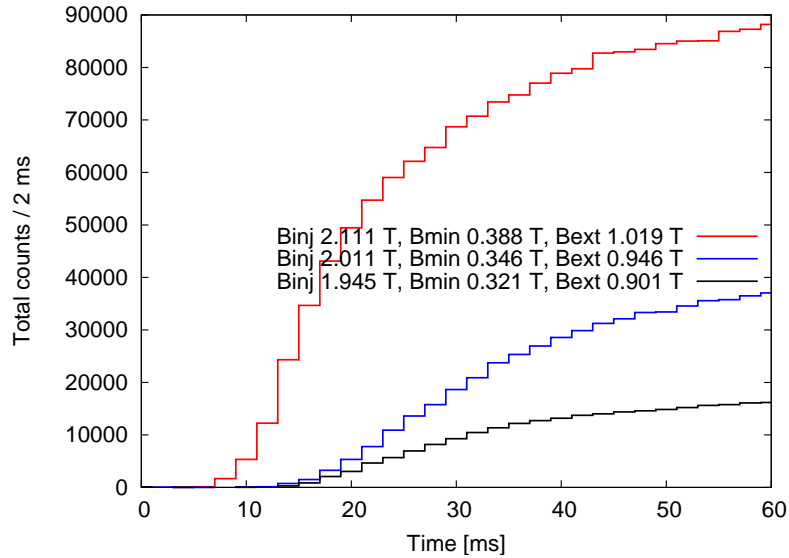


Figure 6.7: Comparison of total count rates during the first 60 ms from the leading edge of the microwave pulse with different magnetic field strengths. Measured with the JYFL 14 GHz ECRIS. Figure from reference [70].

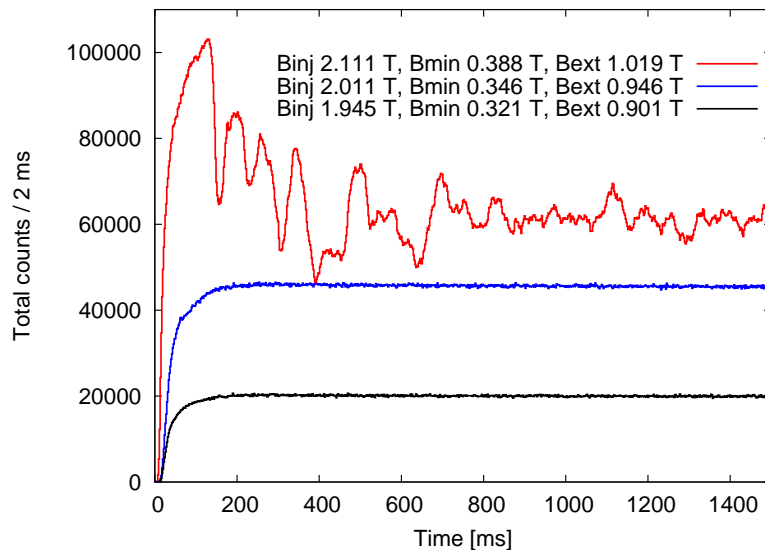


Figure 6.8: Comparison of total count rates during the first 1500 ms from the leading edge of the microwave pulse with different magnetic field strengths. Note the instabilities with the highest  $B_{\min}$  corresponding to the lowest magnetic field gradient in the resonance zone. Measured with the JYFL 14 GHz ECRIS. Figure from reference [70].

### 6.3. Time-resolved bremsstrahlung and ion current measurements

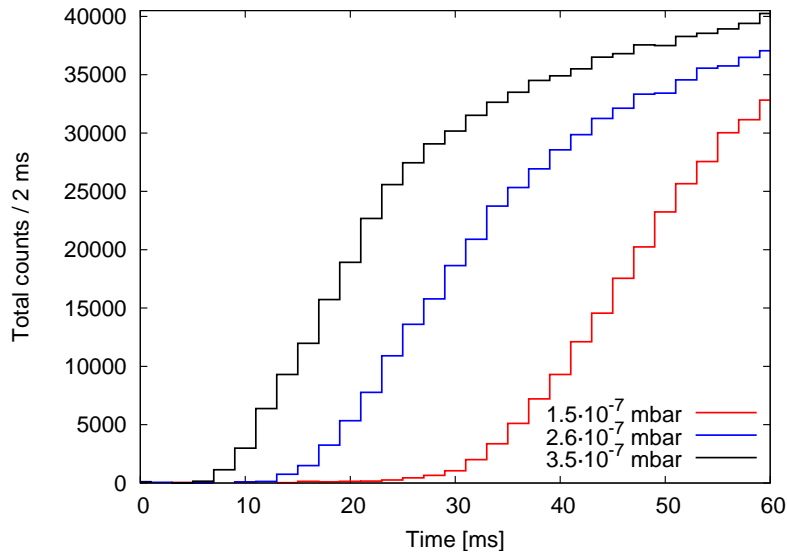


Figure 6.9: Comparison of total count rates during the first 60 ms from the leading edge of the microwave pulse with different neutral gas pressures of argon. Measured with the JYFL 14 GHz ECRIS. Figure from reference [33].

of the microwave power. There is, however, a clear difference of the count rate slopes with different microwave powers: the higher the power, the steeper the slope i.e. faster electron heating (see figure 6.10). This is expected due to higher electric fields when a higher microwave power is used. Similar behaviour was observed with oxygen plasma.

It was also found out (appendix A.6) that the ion current of low and medium charge states of argon saturated in less than 65 ms while the bremsstrahlung count rate reached steady state after several hundreds of milliseconds (see figure 6.11). Ion beam currents of different charge states of oxygen also tend to saturate before the bremsstrahlung emission (appendix A.3). During the plasma breakdown process a so-called preglow transient [121] was observed. Concurrently with this transit time the ion beam currents of different charge states peaked and steady state currents were exceeded by several factors for a period of a couple of milliseconds.

Independent of the source settings, the normalized total integrated count rate of bremsstrahlung radiation decreased to 10 % of the maximum count rate in about 100 ms after the microwave power was shut down. So-called afterglow instabilities [2] were observed in many measurement sets during the plasma decay as sudden bursts in the total count rate data. The ion beam currents and the bremsstrahlung emission during the afterglow [122, 123, 124, 125] has been studied more thoroughly in reference [126].

The preglow regime was studied more thoroughly with helium plasmas using different RF pulse patterns (appendix A.7). It was found out that the plasma breakdown

## Chapter 6. Results from the simulations and the measurements

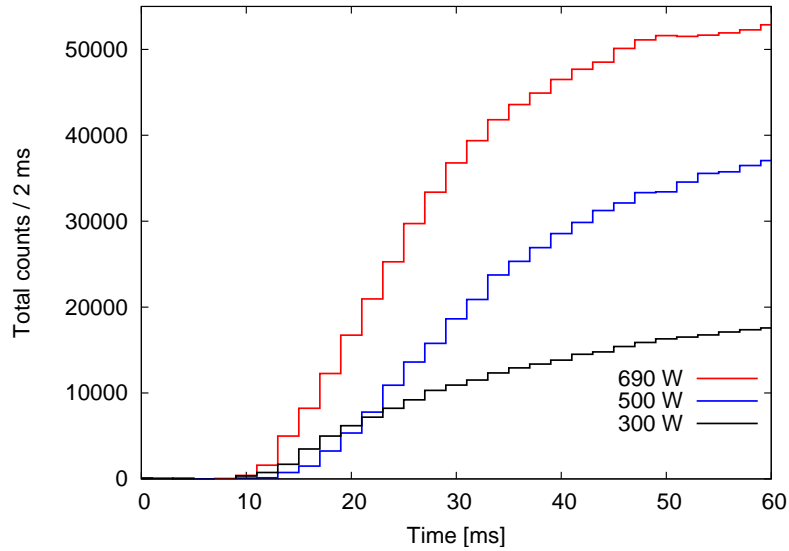


Figure 6.10: Comparison of total count rates during the first 60 ms from the leading edge of the microwave pulse with different microwave powers. Measured with the JYFL 14 GHz ECRIS. Figure from reference [33].

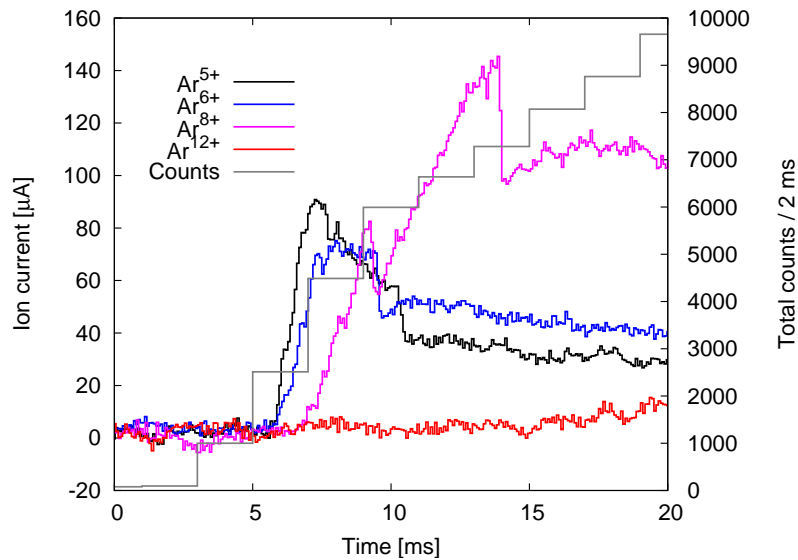


Figure 6.11: Ion beam currents of argon and total count rate of bremsstrahlung emission during the first 20 ms from the leading edge of the RF pulse. Measured with the JYFL 14 GHz ECRIS. Figure from reference [33].

### 6.3. Time-resolved bremsstrahlung and ion current measurements

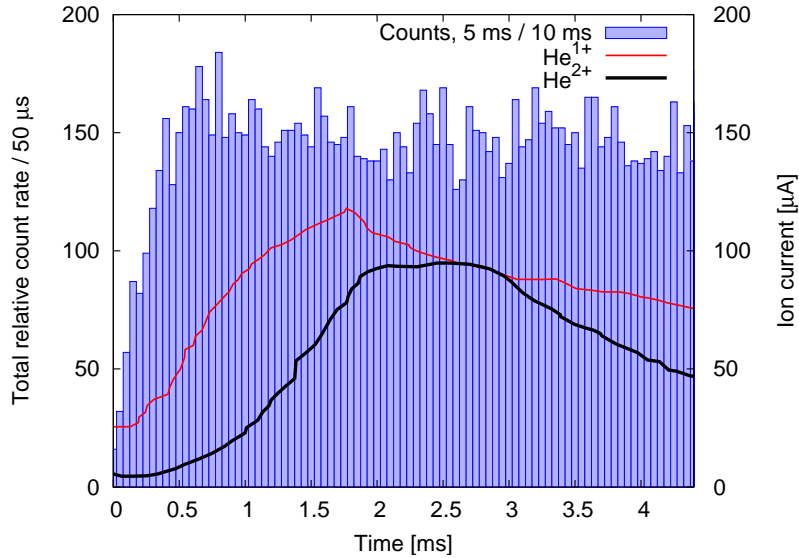


Figure 6.12: Ion beam currents of helium and total count rate of bremsstrahlung emission with an RF pulse pattern of 5 ms/10 ms (on/off). Measured with the JYFL 14 GHz ECRIS. Figure from reference [115].

time can be decreased significantly when the time between the consecutive microwave pulses is decreased. It is understood that if the microwave pulse separation is kept short the number of electrons remaining in the magnetic confinement system, the seed electrons, is higher than with longer pulse separation and when the microwave power is launched again into the plasma chamber the plasma breakdown takes place almost immediately. By tuning the RF pulse separation, i.e. changing the initial conditions for the plasma breakdown, it was observed that the plasma breakdown time is increased when the time between the RF pulses is increased. However, the highest ion beam currents of  $\text{He}^{1+}$  and  $\text{He}^{2+}$  remained about the same while the amount of bremsstrahlung radiation was decreased to one third of the original as can be seen from figures 6.12 and 6.13.

The time scales of bremsstrahlung emission and ion beam current production were measured with the JYFL 6.4 GHz ECR ion source using the same RF pulse times as with the JYFL 14 GHz ECRIS (RF on/off: 1760 ms/5920 ms). Measurements were performed as a function of magnetic field strength, RF power and neutral gas pressure of argon. It was discovered that typical times to reach a steady state of bremsstrahlung emission were in the range of hundreds of milliseconds, corresponding to the time scales measured with the 14.1 GHz ECRIS. In figure 6.14 the ion beam currents of different charge states of argon and the bremsstrahlung emission is presented as a function of time. During the measurements the ion source was tuned to  $\text{Ar}^{9+}$ . It can be observed that the ion beam currents of  $\text{Ar}^{3+}$  and  $\text{Ar}^{5+}$  appear after 5 ms,  $\text{Ar}^{7+}$  takes around 6 ms to appear and after 8 ms the ion beam

## Chapter 6. Results from the simulations and the measurements

current of  $\text{Ar}^{9+}$  starts to rise. Ion beam currents saturate roughly after 70 ms. The total count rate of bremsstrahlung starts to increase after 5 ms has elapsed from the leading edge of the RF pulse, and it continues to rise until the steady state is reached after 150 ms (not shown in the figure). The ion beam currents saturate much faster than the bremsstrahlung emission, as was earlier observed with the JYFL 14 GHz ECRIS. Normalized total count rates during the plasma decay take typically 50–70 ms, and as in the case of JYFL 14 GHz ECRIS, afterglow instabilities were observed.

### 6.3. Time-resolved bremsstrahlung and ion current measurements

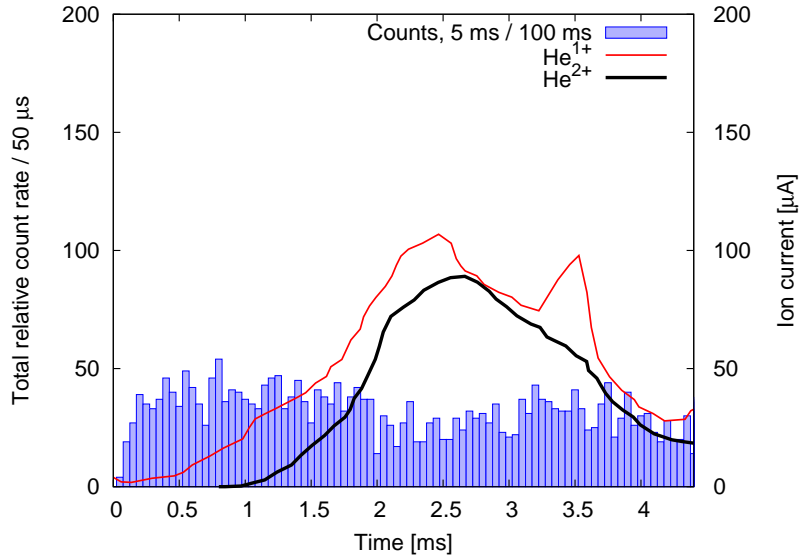


Figure 6.13: Ion beam currents of helium and total count rate of bremsstrahlung emission with an RF pulse pattern of 5 ms/100 ms (on/off). Measured with the JYFL 14 GHz ECRIS. Figure from reference [115].

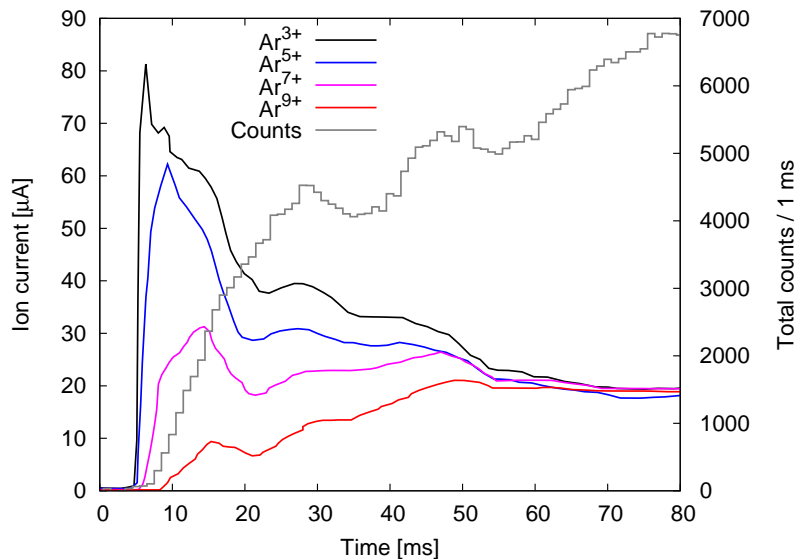


Figure 6.14: Ion beam currents of argon and total count rate of bremsstrahlung emission during the first 80 ms from the leading edge of the RF pulse. Measured with the JYFL 6.4 GHz ECRIS.



## Chapter 7

### Discussion and conclusions

The demand to produce ever increasing ion charge states and ion beam intensities from heavy elements with ECR ion sources has led the ECRIS community to utilize increasing microwave frequencies, magnetic fields, microwave powers and plasma volumes. The development has been following the well-known semi-empirical scaling laws proposed by Dr. Geller. While the charge states of the ion beams and ion beam intensities have been increased significantly since the first ECR ion sources, problems have started to appear with the third generation of ECR ion sources due to this brute force method of “making everything larger”. Increased electron heating efficiency by increased microwave frequency and large plasma volumes requiring high microwave power levels, increase the production of high energy electrons. These electrons shouldn't be responsible for the ionization processes due to cross sections and they tend to generate problems in the form of extra heat load to the plasma chamber walls and cryostat system of superconducting ECR ion sources. However, it might be that these very high energy electrons could increase the confinement of ions but more research is needed in this area. Therefore, in order to design and construct high performance electron cyclotron resonance ion sources, more information about the electron heating would be beneficial. In this thesis work different ECRIS parameters affecting the bremsstrahlung emission have been studied, numerical work in order to understand the heating characteristics has been performed and ways to decrease the bremsstrahlung production while maintaining high ion beam currents have been investigated.

During this thesis work it was observed that the time evolution of maximum photon energies from the bremsstrahlung spectra coincided with one of the stochastic heating theories if the plasma chamber quality factor is increased roughly by one order of magnitude from the previously used value. However, according to recent bremsstrahlung measurements, Q-values over 1000 could be plausible [72].

In the 10  $\mu\text{s}$  simulations, using a Q-value of 3, the highest electron energies were in the order of less than 14 keV with the microwave power absorption model and less than 33 keV without the absorption model, respectively. By a rough extrapolation, maximum electron energies of around 500 keV could be expected after 500  $\mu\text{s}$  of

## Chapter 7. Discussion and conclusions

heating if the microwave absorption model is used. With a quality factor of 44 the maximum electron energies are between 320 keV and 580 keV, depending on the simulation time. These energies are quite close to the measured maximum photon energies from the JYFL 14 GHz ECRIS. However, comparing the simulations with measurements is somewhat problematic because the simulation assumes a steady state background plasma and in measurements we will have to go through the plasma breakdown before reaching the steady state plasma. The best comparison is reached when the simulation results are compared to measurements in which the time between the RF pulses is very short and the amount of seed electrons that are remaining in the magnetic bottle between the RF pulses remains high. This ensures almost negligible plasma breakdown time in some cases. From the measurement data it was noticed that when the microwave power was launched in to the ECRIS plasma chamber photons with energies in the range of 100–300 keV appeared in the spectra in less than 300 microseconds when an RF pulse pattern of (on/off) 5 ms/5 ms was used. With the RF pulse pattern of 1760 ms/5920 ms it took millisecond time scales before high energy photons were observed.

It is also observed from the simulation data that electrons with energies over 110 keV are more abundant without the absorption model compared to the simulation data where the model is used. This can be seen as a height difference of the bumps in the simulated spectra. The shape of the spectra have the appearance of the so-called “double Maxwellian” electron energy distribution. In this case the spectra consists of one electron intensity maximum at the low energies (thermal electron population) and one maximum at the higher energies (hot electron population). After 5  $\mu$ s of heating time the ratio of electrons observed at energies equal or greater than 100 keV remains relatively constant at 0.66.

With VENUS it was observed that double frequency heating can play a remarkable role in decreasing the heating of the cryostat. Ion beam currents of high charge states can be matched with single and double frequency operation while double frequency operation requires more microwave power to reach the same ion beam currents. However, due to different magnetic field gradients used in the double frequency heating mode (18 GHz/28 GHz) compared to the single frequency heating, the electron heating is less efficient and the number of high energy electrons is significantly suppressed. In order to optimize the heating efficiency in terms of required input microwave power one should presumably decrease the gap between the two frequencies allowing the optimization of the magnetic field profile for the primary frequency. In the experiments with two frequency heating the heat load to the cryostat was decreased by one order of magnitude compared to single frequency heating. The effect of more than two simultaneous microwave frequencies to bremsstrahlung production could also be studied together with the effect of the frequency separation.

In the time evolution measurements with the JYFL 14 Hz ECRIS it was observed

that the magnetic field gradient at the resonance clearly affects the bremsstrahlung production. This has previously been observed also with e.g. VENUS. It was found that the gentler the magnetic field gradient the faster the steeper the bremsstrahlung count rate during the plasma breakdown. Typical times to reach steady state plasmas were in the order of hundreds of milliseconds. In the case of Ar plasma significant instabilities were also observed. The effect of neutral gas pressure on the bremsstrahlung production was also studied and it was found that the higher the pressure the faster the plasma breakdown. A simple theoretical model for the plasma breakdown time and the performed measurements presented in reference [116] confirm the effect of neutrals observed during the bremsstrahlung measurements. The bremsstrahlung count rate slopes with different neutral gas pressures were, however, quite similar after the counts started to appear. As a function of microwave power it was observed that the plasma breakdown times were roughly the same for all the measured RF powers, but again, the slopes are different. The highest microwave power corresponds to the steepest slope. By studying the behavior of extracted ion beams and bremsstrahlung production it was found that the ion beam currents of low and medium charge states tend to reach steady state well before the bremsstrahlung emission. Thus, the electron energy distribution function shifts towards higher energies for a significant time after the ion beam production has saturated. This is a clear sign of unoptimized electron heating processes in an ECRIS plasma.

During the measurements with the JYFL 14 GHz ECRIS it was also noticed that the plasma breakdown times are significantly affected by the time between the RF pulses. When the time between the pulses decreases the amount of seed electrons that remain in the plasma chamber during the pulses increases. When the microwave power is applied again at the beginning of the next RF pulse the amount of free electrons is sufficient to cause a fast ionizing avalanche. In addition, the amount of bremsstrahlung radiation was decreased into one third of the original by tuning the microwave pulse pattern while almost equal amounts of helium ion beams could be produced during the preglow transient. From these time-resolved measurements it is now understood that in order to decrease the amount of bremsstrahlung radiation from an ECRIS one can try to find RF pulse patterns that enable the production of sufficient ion beam currents but do not allow electrons to be heated into very high energies. In pulsed operating mode the preglow transient can also be used to produce high ion beam currents. To find optimum RF pulse patterns, extensive studies are still needed.

In order to get a more realistic picture of the electron heating and plasma breakdown processes, the Q-value of the loaded plasma chamber and its time evolution together with the time evolution of the plasma potential should be measured. This would also help to develop more reasonable ECRIS simulation codes. The simulation code used in this thesis work will be further developed. More extensive studies for example as a function of magnetic field, Q-value and density profiles will be

## Chapter 7. Discussion and conclusions

carried out. The use of standing wave modes and plasma breakdown modeling via time-dependent Q-values and density profiles are considered, and means to include plasma breakdown modeling should be studied. To simulate electron heating from the plasma breakdown into steady state simulation times ranging from hundreds of microseconds to hundreds of milliseconds are needed. This is a very difficult task and significant improvement in the ECR heating codes are needed to meet these demands. Some of these requirements can be achieved by parallelization of the calculations and restraining using e.g. sextupole modeling. In addition, the time-averaged ion beam current from an ECRIS in pulsed mode utilizing preglow transient should be compared to the steady state operation in order to find out if the pulsed mode would produce required amounts of ion beam into various applications including cyclotron injection.

## Bibliography

- [1] V. ERCKMANN AND U. GASPARINO. *Electron cyclotron resonance heating and current drive in toroidal fusion plasmas*. Plasma Phys. Control. Fusion **36**, 1869 (1994).
- [2] R. GELLER. *Electron Cyclotron Resonance Ion Sources and ECR Plasmas*. Taylor & Francis (1996). ISBN 0750301074.
- [3] E. O. LAWRENCE AND M. S. LIVINGSTON. *The production of high speed light ions without the use of high voltages*. Plasma Rev. **40**, 19 (1932).
- [4] D. LEITNER, C. M. LYNEIS, T. LOEW, D. S. TODD, S. VIROSTEK AND O. TARVAINEN. *Status report of the 28 GHz superconducting electron cyclotron resonance ion source VENUS*. Rev. Sci. Instr. **77**, 03A302 (2006).
- [5] J. VÁMOSI AND S. BIRI. *TrapCAD - a tool to design and study magnetic traps of ECR ion sources*. Nucl. Instr. Meth. B **94**, 297 (1994).
- [6] A. HEINEN, M. RÜTHER, J. DUCRÉE, J. LEUKER, J. MROGENDA, H. W. ORTJOHANN, E. RECKELS, C. VITT AND H. J. ANDRÄ. *Successful modeling, design, and test of electron cyclotron resonance ion sources*. Rev. Sci. Instr. **69**, 729 (1998).
- [7] T. ROPPONEN, O. TARVAINEN, P. SUOMINEN, T. K. KOPONEN, T. KALVAS AND H. KOIVISTO. *Hybrid simulation of electron cyclotron resonance heating*. Nucl. Instr. and Meth. A **587**, 115 (2008).
- [8] V. MIRONOV AND J. P. M. BEIJERS. *Three-dimensional simulations of ion dynamics in the plasma of an electron cyclotron resonance ion source*. Phys. Rev. ST Accel. Beams **12**, 073501 (2009).
- [9] D. H. EDGELL, J. S. KIM, S. K. WONG, R. C. PARDO AND R. VONDRASEK. *Model of charge-state distributions for electron cyclotron resonance ion source plasmas*. Phys. Rev. ST Accel. Beams **2**, 123502 (1999).
- [10] C. NIETER AND J. R. GARY. *VORPAL: a versatile plasma simulation code*. J. Comput. Phys **194**, 448 (2004).
- [11] T. J. FESSENDEN. *Pulsed electron-cyclotron resonance discharge experiment*. Technical Report MIT-3221-19, Massachusetts Institute of Technology (1966).
- [12] E. FERMI. *On the Origin of the Cosmic Radiation*. Phys. Rev. **75**, 1169 (1949).
- [13] J. A. BITTENCOURT. *Fundamentals of Plasma Physics*. Springer (2004). ISBN 075030183X.
- [14] H. KOSKINEN. *Johdatus plasmafysiikkaan ja sen avaruussovelluksiin*. Limes Ry (2001). ISBN 951-745-191-1.

## BIBLIOGRAPHY

- [15] R. J. GOLDSTON AND P. H. RUTHERFORD. *Introduction to Plasma Physics*. Institute of Physics Publishing (1995). ISBN 0387209751.
- [16] H. C. HERBERT AND K. WIESEMANN. *Production of highly charged ions in plasmas with high electron temperature (in german)*. GSI-Bericht **71**, 171 (1971).
- [17] R. GELLER. *Electron cyclotron resonance multiply charged ion sources*. IEEE Trans. Nucl. Sci **23**, 904 (1972).
- [18] K. HALBACH. *Design of permanent multipole magnets with oriented rare earth cobalt material*. Nucl. Instr. Meth. **169**, 1 (1980).
- [19] Y. JONGEN AND C. M. LYNEIS. *Experimental results from an ECR source using an octupole*. Nucl. Instr. Meth. B **9**, 529 (1985).
- [20] O. TARVAINEN. *Studies of electron cyclotron resonance ion source plasma physics*. Ph.D. thesis, University of Jyväskylä (2005).
- [21] D. J. CLARK AND C. M. LYNEIS. *The production of beams from solid materials at LBL ECR source*. In *Proceedings of the international conference on the physics of multiply charged ion and international workshop on ECR ion sources*, pages 759–766. Grenoble (1988).
- [22] C. M. LYNEIS. *Operational performance of the LBL 88-inch cyclotron with an ECR ion source*. In *Proceedings of the 11<sup>th</sup> international conference on cyclotrons and their applications*, page 707. Tokyo (1987).
- [23] D. HITZ, G. MELIN, M. PONTONNIER AND T. K. NGUYEN. *New results and evolution of the CAPRICE ECR ion source concept*. In *Proceedings of the 11<sup>th</sup> International Workshop on ECR Ion Sources*, pages 91–96. Groningen (1993).
- [24] R. HARKIEWICZ. *Efficient production of a <sup>48</sup>Ca beam from oxide material in an electron cyclotron resonance ion source using a low power miniature oven*. Rev. Sci. Instr. **67**, 2176 (1996).
- [25] P. A. ZAVODSZKY, B. AREND, D. COLE, J. DEKAMP, G. MACHICOANE, F. MARTI, P. MILLER, J. MOSKALIK, J. OTTARSON, J. VINCENT, A. ZELLER AND N. Y. KAZARINOV. *Status report on the design and construction of the superconducting source for ions at the National Superconducting Cyclotron Laboratory/Michigan State University*. In *Proceedings of the 11<sup>th</sup> international conference on ion sources*, page 03A334. Rev. Sci. Instr. (2006).
- [26] D. BULGIN, J. DYKE, F. GOODFELLOW, N. JONATHAN, E. LEE AND A. MORRIS. *A high temperature furnace for use in photoelectron spectroscopy*. J. Electron Spectrosc. Relat. Phenom. **12** (1977).
- [27] H. KOIVISTO, J. ÄRJE AND M. NURMIA. *Metal ion beams from an ECR ion source using volatile compounds*. Nucl. Instr. Meth. B **94**, 291 (1994).
- [28] R. HARKIEWICZ, P. J. BILLQUIST, J. P. GREENE, J. J. A. NOLEN AND R. C. PARDO. *Ion plasma sputtering as a method of introducing solid material into an electron cyclotron resonance ion source*. Rev. Sci. Instr. **66**, 2883 (1995).
- [29] R. HARKIEWICZ, J. STACY, J. GREENE AND R. C. PARDO. *Solid material evaporation into an electron cyclotron resonance source by laser ablation*. Rev. Sci. Instr. **65**, 1104 (1994).

## BIBLIOGRAPHY

- [30] B. JACQUOT. *French patent No. 83 10862* (1983).
- [31] A. G. DRENTJE. *The ECR ion source and associated equipment at the KVI*. Nucl. Instr. and Meth. B **9**, 526 (1985).
- [32] R. C. VONDRASEK, R. H. SCOTT, R. C. PARDO AND D. EDGELL. *Techniques for the measurement of ionization times in ECR ion sources using a fast sputter sample and fast gas valve*. Rev. Sci. Instr. **73**, 548 (2002).
- [33] T. ROPPONEN, O. TARVAINEN, P. JONES, P. PEURA, T. KALVAS, P. SUOMINEN AND H. KOIVISTO. *Time evolution of high-energy bremsstrahlung and argon ion production in electron cyclotron resonance ion source plasma*. IEEE Trans. Plasma Sci. **37**, 2146 (2009).
- [34] T. ROPPONEN. *ECR-ionilähteiden plasmapotentiaali ja ambipolaarinen diffuusio*. Master's thesis, University of Jyväskylä (2005).
- [35] R. GELLER. *ECRIS: the electron cyclotron resonance ion sources*. Annu. Rev. Nucl. Sci. **40**, 15 (1990).
- [36] S. GAMMINO, G. CIAVOLA, T. ANTAYA AND K. HARRISON. *Volume scaling and magnetic field scaling on SC-ECRIS at MSU-NSCL*. Rev. Sci. Instr. **67**, 155 (1996).
- [37] S. GAMMINO, G. CIAVOLA, R. HARKEWICZ, K. HARRISON, A. SRIVASTAVA AND P. BRIAND. *Effects of frequency and magnetic field scaling on the superconducting electron cyclotron resonance ion source at MSU-NSCL*. Rev. Sci. Instr. **67**, 4109 (1996).
- [38] S. GAMMINO, L. CELONA, G. CIAVOLA, M. CASTRO, F. CHINES, S. MARLETTA, G. MELIN, P. BRIAND, A. GIRARD, P. LUDWIG, P. SEYFERT AND D. GUILLAUME. *Production of intense highly charged ion beams with SERSE*. In *Proceedings of the 14<sup>th</sup> international workshop on ECR ion sources*, pages 5–8. Geneva (1999).
- [39] D. HITZ, A. GIRARD, G. MELIN, S. GAMMINO, G. CIAVOLA AND L. CELONA. *Results and interpretation of high frequency experiments at 28 GHz in ECR ion sources, future prospects*. Rev. Sci. Instr. **73**, 509 (2002).
- [40] D. HITZ, A. GIRARD, K. SEREBRENNIKOV, G. MELIN, D. CORMIER, J. M. MATHONNET, J. CHARTIER, L. SUN, J. P. BRIAND AND M. BENHACHOUM. *Production of highly charged ion beams with the Grenoble test electron cyclotron resonance ion source*. In *Proceedings of the 10<sup>th</sup> international conference on ion sources*, pages 1403–1406. Rev. Sci. Instr. (2004).
- [41] D. LEITNER, C. M. LYNEIS, T. LOEW, D. S. TODD, S. VIROSTEK AND O. TARVAINEN. *Status report of the 28 GHz superconducting electron cyclotron resonance ion source VENUS*. In *Proceedings of the 11<sup>th</sup> international conference on ion sources*, page 03A302. Rev. Sci. Instr., Caen (2006).
- [42] D. HITZ. *Recent progress in high frequency electron cyclotron resonance ion sources*. Advances in imaging and electron physics **144**, 1 (2006).
- [43] R. BECKER. *Collision physics in ECR and EBIS/T*. Rev. Sci. Instr. **73**, 693 (2002).
- [44] G. MELIN, A. G. DRENTJE, A. GIRARD AND D. HITZ. *Ion behavior and gas*

## BIBLIOGRAPHY

- mixing in electron resonance plasmas as sources for highly charged ions.* J. Appl. Phys. **86**, 4772 (1999).
- [45] W. LOTZ. *An empirical formula for the electron-impact ionization cross-section.* Z. Phys. **206**, 205 (1967).
- [46] W. LOTZ. *Electron-impact ionization cross-sections and ionization rate coefficients for atoms and ions from hydrogen to calcium.* Z. Phys. **216**, 241 (1968).
- [47] V. P. SHEVELKO AND L. A. VAINSHTEIN. *Atomic physics for hot plasmas.* IOP Publishing (1993). ISBN 9780750302319.
- [48] G. H. HENDERSON. *Changes in the charge of an  $\alpha$ -particle passing through matter.* Proc. R. Soc. Lond. A **102**, 496 (1923).
- [49] D. RAPP AND W. E. FRANCIS. *Charge exchange between gaseous ions and atoms.* J. Chem. Phys **37**, 2631 (1962).
- [50] W. LICHTEN. *Resonant charge exchange in atomic collisions.* Phys. Rev. **131**, 229 (1963).
- [51] V. M. POVYSHEV, A. A. SADOVOY, V. P. SHEVELKO, G. D. SHIRKOV, E. G. VASINA AND V. V. VATULIN. *Electron-impact ionization cross sections of H, He, N, O, Ar, Xe, Au, Pb atoms and their ions in the electron energy range from the threshold up to 200 keV.* Communication of the Joint Institute for Nuclear Research pages E9–2001–148 (2001).
- [52] V. M. POVYSHEV, A. A. SADOVOY, V. P. SHEVELKO, G. D. SHIRKOV, E. G. VASINA AND V. V. VATULIN. *Electron-impact ionization cross sections of Ti, Kr, Sn, Ta, U atoms and their ions in the electron energy range from the threshold up to 200 keV.* Communication of the Joint Institute for Nuclear Research pages E9–2002–5 (2001).
- [53] G. M. WEINBERG. *Measurement of charge exchange cross sections for highly charged xenon and thorium ion with molecular hydrogen in a penning ion trap.* Ph.D. thesis, Texas A & A University (1995).
- [54] D. H. CRANDALL. *Atomic physics of highly ionized atoms.* Plenum (1983).
- [55] C. BOTTCHEER, D. C. GRIFFIN, M. S. PINDZOLA AND R. A. PHANEUF. *Indirect processes in electron-ion scattering* (1983). Oak Ridge National Laboratory Report ORNL/TM-8868.
- [56] S. M. YOUNGER. *Electron impact ionization.* Springer–Verlag (1985).
- [57] Z. Q. XIE AND C. M. LYNEIS. *Improvements on the LBL AECS source.* In *Proceedings of the 12<sup>th</sup> international workshop on ECR ion sources*, pages 24–28. Riken (1995).
- [58] G. D. ALTON, F. W. MEYER, Y. LIU, J. R. BEENE AND D. TUCKER. *Enhancing the performances of traditional electron cyclotron resonance ion sources with multiple-discrete-frequency microwave radiation.* Rev. Sci. Instr. **69**, 2305 (1998).
- [59] R. C. VONDRASEK, R. H. SCOTT AND R. C. PARDO. *Two frequency operation of the Argonne ECR ion source.* In *Proceedings of the 15<sup>th</sup> international workshop on ECR ion sources*, pages 63–66. Jyväskylä (2002).

## BIBLIOGRAPHY

- [60] R. C. VONDRASEK, R. H. SCOTT, R. C. PARDO, H. KOIVISTO, O. TARVAINEN, P. SUOMINEN AND D. H. EDGELL. *ECRIS operation with multiple frequencies*. In *Proceedings of the 16<sup>th</sup> international workshop on ECR ion sources*, pages 31–34. American institute of physics, Berkeley (2004).
- [61] O. TARVAINEN, P. SUOMINEN, T. ROPPONEN, H. KOIVISTO, R. C. VONDRASEK AND R. H. SCOTT. *Plasma potential measurements with a new instrument*. In *Proceedings of the 16<sup>th</sup> international workshop on ECR ion sources*, pages 61–66. American institute of physics, Berkeley (2004).
- [62] O. TARVAINEN, P. SUOMINEN, T. ROPPONEN AND H. KOIVISTO. *Emission and plasma potential measurements in double-frequency heating mode with the 14 GHz electron cyclotron resonance ion source at the university of jyvaskylä*. In *Proceedings of the 11<sup>th</sup> international conference on ion sources*, page 03A309. Rev. Sci. Instr., Caen (2006).
- [63] H. KOIVISTO, P. SUOMINEN, O. TARVAINEN, A. VIRTANEN AND A. PARKKINEN. *Electron cyclotron resonance ion source related development work for heavy-ion irradiation tests*. In *Proceedings of the 11<sup>th</sup> international conference on ion sources*, page 03A316. Rev. Sci. Instr., Caen (2006).
- [64] Y. KAWAI, G. D. ALTON, O. TARVAINEN, P. SUOMINEN AND H. KOIVISTO. *Effect of broadband microwave radiation on the performance of a conventional B-minimum geometry electron cyclotron resonance ion source*. In *Proceedings of the 11<sup>th</sup> international conference on ion sources*, page 03A331. Rev. Sci. Instr., Caen (2006).
- [65] L. CELONA, S. GAMMINO, G. CIAVOLA, F. CONSOLI AND A. GALATÁ. *Analysis of the SERSE ion output by using klystron-based or TWTA-based microwave generators*. In *Proceedings of the 16<sup>th</sup> international workshop on ECR ion sources*, pages 99–102. American institute of physics, Berkeley (2004).
- [66] H. KOIVISTO. *The effect of microwave frequency and grad B on the energy of electrons in an electron cyclotron resonance ion source*. Rev. Sci. Instrum. **70**, 2979 (1999).
- [67] G. D. ALTON AND D. N. SMITHE. *Design studies for an advanced ECR ion source*. Rev. Sci. Instr. **65**, 775 (1994).
- [68] G. D. ALTON. *Broadband frequency ECR ion source concepts with large resonant plasma volumes*. Nucl. Instr. and Meth. A **382**, 276 (1996).
- [69] Y. LIU, H. BILHEUX, Y. KAWAI, F. W. MEYER AND G. D. ALTON. *Performance characterization studies of a flat field volume ECR ion source*. Nucl. Instr. and Meth. B **241**, 965 (2005).
- [70] T. ROPPONEN, O. TARVAINEN, P. JONES, P. PEURA, T. KALVAS, P. SUOMINEN, H. KOIVISTO AND J. ÄRJE. *The effect of magnetic field strength on the time evolution of high energy bremsstrahlung radiation created by an electron cyclotron resonance ion source*. Nucl. Instr. and Meth. A **600**, 525 (2009).
- [71] D. LEITNER, J. Y. BENITEZ, C. LYNEIS, D. S. TODD, T. ROPPONEN, J. ROPPONEN, H. KOIVISTO AND S. GAMMINO. *Measurement of the high energy*

## BIBLIOGRAPHY

- component of the X-ray spectra in the VENUS electron cyclotron resonance on source.* Rev. Sci. Instr. **79**, 033302 (2008).
- [72] L. CELONA, G. CIAVOLA, F. CONSOLI, S. GAMMINO, F. MAIMONE, D. MASCALI, P. SPÄDTKE, K. TINCSHERT, R. LANG, J. MÄDER, J. ROSSBACH, S. BARBARINO AND R. S. CATALANO. *Observations of the frequency tuning effect in the 14 GHz CAPRICE ion source.* Rev. Sci. Instr. **79**, 023305 (2008).
- [73] C. A. BALANIS. *Advanced engineering electromagnetics.* John Wiley & Sons, inc. (1989). ISBN 0-471-62194-3.
- [74] V. TOIVANEN, H. KOIVISTO, O. STECZKIEWICZ, L. CELONA, O. TARVAINEN, T. ROPPONEN, S. GAMMINO AND G. CIAVOLA. *Effect of ECR ion source frequency tuning on ion beam intensity and quality.* To be published in the Proceedings of the 13<sup>th</sup> international conference on ion sources.
- [75] Y. JONGEN. *E.C.R. electron acceleration.* In *Workshop on the Sixth International ECR Ion Source*, pages 238–255. Lawrence Berkeley Laboratory, Berkeley, USA (1985).
- [76] F. CONSOLI, S. BARBARINO, L. CELONA, G. CIAVOLA, S. GAMMINO AND D. MASCALI. *Investigation about the modes in the cylindrical cavity of an ECR ion source.* Radiat Eff Defect S **160**, 467 (2005).
- [77] E. V. SUVOROV AND M. D. TOKMAN. *Theory of microwave breakdown of low-density gas at electron cyclotron resonance in magnetic mirror systems.* Soviet journal of Plasma Physics **15**, 540 (1989).
- [78] I. V. IZOTOV, T. LAMY, L. LATRASSEL, A. V. SIDOROV, V. A. SKALYGA, T. THUILLIER AND V. G. ZORIN. *Experimental and theoretical investigation of the preglow in ECRIS.* IEEE Trans. Plasma Sci. **36**, 1494 (2008).
- [79] F. JAEGER, A. J. LICHTENBERG AND M. A. LIEBERMAN. *Theory of electron cyclotron resonance heating — I. short time and adiabatic effects.* Plasma phys. **14**, 1073 (1972).
- [80] N. C. WYETH, A. J. LICHTENBERG AND M. A. LIEBERMAN. *Electron cyclotron resonance heating in a pulsed mirror experiment.* Plasma phys. **17**, 679 (1975).
- [81] M. C. WILLIAMSON, A. J. LICHTENBERG AND M. A. LIEBERMAN. *Self-consistent electron cyclotron resonance absorption in a plasma with varying parameters.* J. Appl. Phys **72**, 3924 (1992).
- [82] K. G. BUDDEN. *Radio waves in the Ionosphere.* Cambridge University Press (1966).
- [83] J. U. BRACKBILL. *FLIP MHD - a particle-in-cell method for magnetohydrodynamics.* Journal of Computational Physics **96**, 163 (1991).
- [84] C. K. BIRDSALL AND A. B. LANGDON. *Plasma physics via computer simulation.* McGraw-Hill, inc. (1985). ISBN 0-07-005371-5.
- [85] J. M. DAWSON. *Particle simulation of plasmas.* Rev. Mod. Phys. **55**, 403 (1983).
- [86] S. BIRI, A. DERTZSI, É. FEKETE AND I. IVÁN. *Upgraded TrapCAD code.* In *Proceedings of the 17<sup>th</sup> International Workshop on ECR Ion Sources*, number 31. High energy physics and nuclear physics - Chinese edition supplement (2007).

## BIBLIOGRAPHY

- [87] *Personal communication with Dr. S. Biri* (2009).
- [88] L. MAUNOURY, C. PIERRET, S. BIRI AND J. Y. PACQUET. *Studies of the ECR plasma using the TrapCAD code*. *Plasma Sources Sci. Technol.* **18**, 015019 (2009).
- [89] A. HEINEN, M. RÜTHER, H. W. ORTJOHANN, C. VITT, S. RHODE AND H. J. ANDRÄ. *Heating and trapping of electrons in ECRIS, from scratch to afterglow*. In *Proceedings of the 14<sup>th</sup> International Workshop on ECR Ion Sources* (1999).
- [90] P. GRÜBLING, J. HOLLANDT AND G. ULM. *Topography of an electron cyclotron resonance plasma in the vacuum-ultraviolet spectral range*. *Rev. Sci. Instr.* **73**, 614 (2001).
- [91] J. S. KIM, L. ZHAO, B. P. CLUGGISH, I. N. BOGATU, S. GALKIN AND L. GRUBERT. *Status of Far-tech's electron-cyclotron-resonance charge-breeder simulation toolset; MCBC, GEM and IONEX*. In *Proceedings of the 18<sup>th</sup> International Workshop on ECR Ion Sources*, pages TUCO–C04. JACoW.org (2008).
- [92] *Personal communication with Dr. B. Cluggish* (2009).
- [93] P. MESSMER, D. FILLMORE, A. SOBOL, P. MULLOWNEY, K. PAUL, D. BRUH-WILER, D. S. TODD AND D. LEITNER. *Simulation-driven optimization of heavy-ion production in ECR sources*. In *Proceedings of the 22<sup>nd</sup> particle accelerator conference*, page FROBAB01. JACoW.org (2007).
- [94] *RADIA, RADIA magnetic field simulation code, version 4.098, copyright of ESRF, Grenoble, France, Oxfordshire, UK* (1997). <http://www.esrf.eu/Accelerators/Groups/InsertionDevices/Software/Radia>.
- [95] M. REISER. *Theory and Design of charged particle beams*. John Wiley & Sons, inc. (1994).
- [96] P. J. PRINCE AND J. R. DORMAND. *High order embedded Runge–Kutta formulae*. *J. Comput. Appl. Math.* **7**, 67 (1981).
- [97] *GSL—GNU Scientific Library* (2009). <http://www.gnu.org/software/gsl/>.
- [98] T. J. M. BOYD AND J. J. SANDERSON. *Atomic physics for hot plasmas*. Cambridge University Press (2003). ISBN 9780521459129.
- [99] U. LEHNERT AND G. ZSCHORNACK. *X-ray imaging spectroscopy of an electron cyclotron resonance discharge*. *Rev. Sci. Instr.* **67**, 1264 (1995).
- [100] S. BIRI, A. VALEK, T. SUTA, E. TAKÁCS, C. SZABÓ, L. T. HUDSON, B. RADICS, J. IMREK, B. JUHÁSZ AND J. PÁLINKÁS. *Imaging of ECR plasmas with a pinhole X-ray camera*. *Rev. Sci. Instr.* **75**, 1420 (2004).
- [101] M. DRUETTA AND D. HITZ. *VUV diagnostic of the plasma of an E.C.R. ion source*. In *Tenth International Conference on Vacuum Ultraviolet Radiation Physics, VUV 10*, pages 259–262 (1992).
- [102] C. LYNEIS, D. LEITNER, D. TODD, S. VIROSTEK, T. LOEW, A. HEINEN AND O. TARVAINEN. *Measurements of bremsstrahlung production and x-ray cryostat heating in VENUS*. *Rev. Sci. Instr.* **77**, 03A342 (2006).
- [103] B. P. CLUGGISH, I. N. BOGATU, L. ZHAO, J. S. KIM, R. C. VONDRASEK, R. C. PARDO AND R. H. SCOTT. *Measurements of X-ray spectra on ECR-II*. In

## BIBLIOGRAPHY

- Proceedings of the 18<sup>th</sup> International Workshop on ECR Ion Sources*, pages MOPO-07. JACoW.org (2008).
- [104] H. Y. ZHAO, H. W. ZHAO, X. W. MA, S. F. ZHANG, W. T. FENG, X. L. ZHU, Z. M. ZHANG, W. HE, L. T. SUN, Y. C. FENG, Y. CAO, J. Y. LI, X. X. LI, H. WANG AND B. H. MA. *Measurements of bremsstrahlung spectra of lanzhou ECR ion source no. 3 (LECR3)*. *Rev. Sci. Instr.* **77**, 03A312 (2006).
- [105] J. D. JACKSON. *Classical electrodynamics*. John Wiley & Sons, inc. (1975). ISBN 0-471-43132-X.
- [106] N. A. DYSON. *X-rays in atomic and nuclear physics*. Cambridge University Press (2005). ISBN 978-0-521-01722-0.
- [107] H. W. KOCH AND J. W. MOTZ. *Bremsstrahlung cross-section formulas and related data*. *National bureau of standards* **31**, 920 (1959).
- [108] W. W. BUECHNER, R. J. V. DE GRAAF, E. A. BURRILL AND A. SPERDUTO. *Thick-target X-ray production in the range from 1250 to 2350 kilovolts*. *Phys. Rev.* **74**, 1348 (1948).
- [109] J. ROPPONEN. *ECR-ionilähteen tuottaman Röntgensäteilyn simulointi*. Master's thesis, University of Jyväskylä (2008).
- [110] Z. Q. XIE AND C. M. LYNEIS. *Performance of the upgraded LBNL AEER ion source*. In *Proceedings of the 13<sup>th</sup> international workshop on ECR ion sources*. College Station, USA (1997).
- [111] L. T. SUN, H. W. ZHAO, Z. M. ZHANG, B. WEI, X. Z. ZHANG, X. H. GUO, X. W. MA, Y. CAO, W. HE AND H. Y. ZHAO. *Brief review of multiple charge state ECR ion sources in Lanzhou*. *Nucl. Instr. and Meth. B* **235**, 524 (2005).
- [112] X. Q. XIE. *Production of highly charged ion beams from electron cyclotron resonance ion sources*. *Rev. Sci. Instr.* **69**, 625 (1998).
- [113] M. SCHLAPP, R. C. VONDRASEK, J. SZCZECHE, P. J. BILLQUIST, Z. Q. XIE, C. M. LYNEIS, R. HARKEWICZ AND R. C. PARDO. In *Proceedings of the 13<sup>th</sup> International Workshop on ECR Ion Sources* (1997).
- [114] T. ROPPONEN, P. JONES, T. KALVAS, H. KOIVISTO, P. PEURA, O. TARVAINEN AND P. SUOMINEN. *Time evolution of endpoint energy of bremsstrahlung spectra and ion production from an electron cyclotron resonance ion source*. In *Proceedings of the 18<sup>th</sup> International Workshop on ECR Ion Sources*, pages TUCO-D01, 148. JACoW.org (2008).
- [115] T. ROPPONEN, O. TARVAINEN, V. TOIVANEN, P. PEURA, P. JONES, H. KOIVISTO, J. NOLAND AND D. LEITNER. *The effect of rf pulse pattern on bremsstrahlung and ion current time evolution of an ECRIS*. Accepted to be published in the Proceedings of the 13<sup>th</sup> international conference on ion sources.
- [116] O. TARVAINEN, T. ROPPONEN, V. TOIVANEN, J. ÄRJE AND H. KOIVISTO. *Plasma breakdown diagnostics with the biased disc of electron cyclotron resonance ion source*. *Plasma Sources Sci. Technol.* **18**, 035018 (2009).
- [117] D. LEITNER, C. M. LYNEIS, S. R. ABBOTT, D. COLLINS, R. D. DWINELL, M. L. GALLOWAY, M. LEITNER AND D. S. TODD. *Next generation ECR ion*

## BIBLIOGRAPHY

- sources: first results of the superconducting 28 GHz ECRIS — VENUS.* Nucl. Instr. and Meth. B **235**, 486 (2005).
- [118] H. KOIVISTO, D. COLE, A. FREDELL, C. LYNEIS, P. MILLER, J. MOSKALIK, B. NURNBERGER AND J. OTTARSON. *ARTEMIS — the new ECR ion source for the coupled cyclotron facility at NSCL/MSU.* In *Proceedings of the Workshop on the Production of intense beams of highly charged ions*, 72. Italian Physical Society, Catania (2000).
- [119] K. F. SERGEICHEV, D. M. KARFIDOV AND N. A. LUKINA. *Electron cyclotron resonance acceleration of electrons to relativistic energies by a microwave field in a mirror trap.* Plasma Phys. Rep. **33**, 455 (2007).
- [120] T. H. STIX. *Waves in plasmas.* AIP Press (1992).
- [121] T. THUILLIER, T. LAMY, L. LATRASSE, I. V. IZOTOV, A. V. SIDOROV, V. A. SKALYGA, V. G. ZORIN AND M. MARIE-JEANNE. *Study of pulsed electron cyclotron resonance ion source plasma near breakdown: The preglow.* In *Proceedings of the 12<sup>th</sup> international conference on ion sources*, number 79, page 02A314. Rev. Sci. Instr. (2008).
- [122] G. MELIN, F. BOURG, P. BRIAND, J. DEBERNARDI, M. DELAUNAY, R. GELLER, B. JACQUOT, P. LUDWIG, T. K. N'GUYEN, L. PIN, J. C. ROCCO AND F. ZADWORNÝ. *Some particular aspects of the physics of the ECR sources for multi-charged ions.* Rev. Sci. Instr. **61**, 236 (1990).
- [123] P. BRIAND, R. GELLER AND G. MELIN. *A newly designed ECR source for the lead injector of CERN.* Nucl. Instr. and Meth. A **294**, 673 (1990).
- [124] P. SORTAIS. *Pulsed ECR ion source using the afterglow mode.* Rev. Sci. Instr. **63**, 2801 (1992).
- [125] C. HILL AND K. LANGBEIN. *Pulsed ECR source in afterglow operation at CERN.* Rev. Sci. Instr. **67**, 1328 (1996).
- [126] O. TARVAINEN AND T. ROPPONEN. To be submitted to Plasma Sources Sci. Technol.



## **Appendix A**

### **Publications**



# APPENDIX A.I



## Hybrid simulation of electron cyclotron resonance heating

T. Ropponen<sup>a,\*</sup>, O. Tarvainen<sup>b</sup>, P. Suominen<sup>c</sup>, T.K. Koponen<sup>d</sup>, T. Kalvas<sup>a</sup>, H. Koivisto<sup>a</sup>

<sup>a</sup>Department of Physics, University of Jyväskylä, P.O. Box 35, FI-40014, Finland

<sup>b</sup>Los Alamos National Laboratory, Los Alamos, NM 87545, USA

<sup>c</sup>CERN Genève 23, CH-1211, Switzerland

<sup>d</sup>Department of Physics, University of Jyväskylä, Nanoscience Center, P.O. Box 35, FI-40014, Finland

Received 22 November 2007; received in revised form 10 December 2007; accepted 25 December 2007

Available online 1 January 2008

### Abstract

Electron Cyclotron Resonance (ECR) heating is a fundamentally important aspect in understanding the physics of Electron Cyclotron Resonance Ion Sources (ECRIS). Absorption of the radio frequency (RF) microwave power by electron heating in the resonance zone depends on many parameters including frequency and electric field strength of the microwave, magnetic field structure and electron and ion density profiles. ECR absorption has been studied in the past by e.g. modelling electric field behaviour in the resonance zone and its near proximity. This paper introduces a new ECR heating code that implements damping of the microwave power in the vicinity of the resonance zone, utilizes electron density profiles and uses right hand circularly polarized (RHCP) electromagnetic waves to simulate electron heating in ECRIS plasma.

© 2007 Elsevier B.V. All rights reserved.

PACS: 52.50.Sw

Keywords: ECR; Electron heating simulation

### 1. Introduction

Electron cyclotron resonance ion sources (ECRISs) [1] have been used for research and industrial applications for decades. With ECRISs it is relatively easy to produce highly charged ion beams from heavy elements and therefore they are often employed in nuclear and material physics research. Future nuclear physics experiments require more intensive highly charged ion beams and thus better performing ECRISs are needed. While extensive research has been performed in order to study ECRIS plasma properties the detailed mechanisms related to electron cyclotron resonance heating (ECRH) are still not very well understood. Several simulation codes to model ECRH and resulting electron energies have been developed (see e.g. Refs. [2,3]), however, in order to understand the overall ECRH mechanism a more sophisticated program is still needed. One of the major

challenges with modern superconducting ECRISs is the extensive amount of bremsstrahlung created by high energy electrons, which is causing heat load to the plasma chamber and the cryostats. X-ray energies well over 1 MeV in high performance ECRISs like VENUS have been measured [4]. However, there are no ECRH codes capable of simulating ECRH and reaching energies around 1 MeV with typical realistic operational parameters and conditions of an ECRIS. In this paper we present a new ECRH code that is capable of modelling electric field absorption at the resonance zone using different electron density profiles and simulating several hundreds of resonance crossings with different ion source operating parameters.

This code, like many others, utilizes the average electric field amplitude calculated from plasma chamber dimensions and RF power using Poynting vector which gives the energy flux of an electromagnetic (EM) field and the direction of propagating microwave power. This approximation is needed, because calculating exact EM wave structure (modes) is challenging due to geometry of the

\*Corresponding author. Tel.: +358 142602456; fax: +358 142602351.  
E-mail address: [tommi.ropponen@phys.jyu.fi](mailto:tommi.ropponen@phys.jyu.fi) (T. Ropponen).

multi-mode cavity and spatial variation of different plasma properties yielding long calculation (CPU) times. Studying the mode structure may prove to be essential, because there might be a power density peak around the resonance area causing higher electric field amplitudes than used in this code. However, such an effort is not in the scope of the work presented in this article. Plasma chamber quality factor  $Q$  is another very important parameter affecting the efficiency of the heating process. A higher  $Q$  value corresponds to a higher amplitude of the electric field. The generally accepted value for the quality factor of an ECRIS with plasma is around 3 [5]. As will be shown in this paper, the electric field is absorbed significantly around the resonance zone resulting in the conclusion that  $Q$  is relatively small when the plasma is ignited. Reflection and mode conversion of the EM wave at the plasma boundaries are not modelled in this code. With some input parameters the amplitude of electric field in the code is close to 70% of the initial amplitude after one resonance zone crossing but for other parameters the amplitude can drop almost to zero. This implies that, although electron cyclotron resonance (ECR) plasma chamber can be considered to be a resonance chamber there seems not to be a predominant standing wave mode structure inside the chamber when the plasma is ignited.

## 2. Description of the code

Our ECRH code has been written in C++, using functions from Gnu Scientific Library (GSL). The numerical integration method is a standard eighth order Prince–Dormand Runge–Kutta. The code is a so-called hybrid simulation code, which uses magnetohydrodynamics (MHD) to calculate the behaviour of the EM wave near the resonance zone and subsequently simulates electron heating for a single particle using the aforementioned electric field (the so-called mean field calculation). Magnetic field in 3D ( $B_x$ ,  $B_y$ ,  $B_z$ ) in the simulation is based on solenoid field approximation. The hexapole field characteristic for a modern ECRIS is not included. Depending on the pitch angle the electron can drift into the loss cone of the magnetic bottle or it can be reflected and undergo further interactions with the RF electric field. If the electron moves too far in the magnetic trap i.e. it hits the plasma chamber walls, the simulation can be stopped. Radiative cyclotron energy losses are not included in our code.

We are using forced step size of  $10^{-14}$  s with adaptive step size control meaning that if smaller step size is needed, the adaptive step size control decreases the step size according to eighth order Prince–Dormand Runge–Kutta algorithms, but maximum step size is limited to be  $10^{-14}$  s. All the simulations in this paper use  $10^{-14}$  as absolute and relative accuracy. Regardless, we are still seeing numerical instabilities which begin after several resonance crossings when the electron enters yet another resonance zone

(around 200 ns). These instabilities cannot be avoided in such accuracy and step sizes that are usable in the sense of reasonable CPU time. Changing the step size (or other accuracy parameters like absolute and relative error) in the integration scheme affects the time evolution of electron energy. However, we are able to simulate tendencies in electron energy even if the simulation time is let to run beyond this limit. It should also be noted that if the simulation is run with fixed relative accuracy, absolute accuracy and step size the energy curve is always identical between different simulation runs using the same initial parameters. There are several ways to try to reduce the numerical instabilities. One could e.g. couple the time step to the position of the electron in the magnetic bottle [6]. However, it is not known whether such an implementation would help in the case of our calculations. Due to the fact that our code is a one particle simulation it is difficult to use threads in multi-processor environments to decrease the calculation time. Nonetheless, as the simulation time increases these numerical instabilities are fudged by the stochastic heating effects which randomize the phase between electron and the microwave.

### 2.1. Magnetic field

To model the solenoid field of an ECRIS, we used RADIA [7] simulation data from JYFL 14 GHz ECRIS. The axial magnetic field  $B_z$  on the source axis is, in a first approximation, a parabola

$$B_z = 91.837z^2 + 0.4 \quad (1)$$

where the magnetic field is in Teslas and  $z$  in meters. From Eq. (1) we can derive the magnetic field in axial and radial directions as a function of  $z$  and  $r$ ,  $B_z(r, z)$  and  $B_r(r, z)$ , respectively. Necessary equations for solenoid field approximations can be derived from the Maxwell equations yielding [8]

$$B_z(r, z) = \sum_{n=0}^{\infty} \frac{(-1)^n}{(n!)^2} B^{(2n)}(z) \left(\frac{r}{2}\right)^{2n} \quad (2)$$

$$B_r(r, z) = \sum_{n=0}^{\infty} \frac{(-1)^{n+1}}{n!(n+1)!} B^{(2n+1)}(z) \left(\frac{r}{2}\right)^{2n+1}. \quad (3)$$

Here  $B^{(2n)}(z)$  means second derivative of  $B_z$  respect to  $z$ , etc. Now, using Eqs. (1)–(3)  $B_z(r, z)$  and  $B_r(r, z)$  can be calculated:

$$B_z(r, z) = 91.837z^2 + 0.4 - 183.674 \left(\frac{r}{2}\right)^2 \quad (4)$$

$$B_r(r, z) = -183.674z + 0.4 \left(\frac{r}{2}\right). \quad (5)$$

We also confirmed that Eqs. (4) and (5) give a very good approximation of the solenoid field near the axis of the ion source.

## 2.2. Electric field

In the code the EM waves are launched into the plasma chamber parallel to magnetic field and the EM wave structure depends on time and axial position coordinate  $z$ . Starting from Maxwell's equations and deriving a general dispersion relation using the dielectric tensor with a collisional term, one can write the dispersion relation for RHCP EM wave propagating parallel to magnetic field in the case of cold electrons in a neutralizing ion background [9]

$$N^2 = \frac{k^2 c^2}{\omega_{rf}^2} = 1 - \frac{\omega_{pe}^2}{\omega_{rf}(\omega_{rf} - \omega_{ce} - j\nu_c)}. \quad (6)$$

Here  $N$  is the refraction index of the plasma,  $k$  the wave number,  $c$  the speed of light,  $\omega_{rf}$  the angular frequency of the microwave,  $\omega_{pe}$  the plasma oscillation (angular) frequency,  $\omega_{ce} = eB_{tot}/\gamma m_e$  electron cyclotron (angular) frequency,  $j$  the imaginary unit and  $\nu_c$  the collision frequency between electrons and ions [10]. In the ECR Ohm's law breaks and the electric field is proportional to the acceleration of the electron instead of the velocity. In the ECRH process there are several parameters such as the electron density at the resonance and plasma instabilities which are unknown while ECRIS is operational. While Eq. (6) assumes the use of Ohm's law in tensor form we are using it as the first approximation in our calculations. The relativistic gamma factor is denoted with  $\gamma$  throughout the paper. Collision frequency [10]

$$\nu_c = \frac{\sqrt{2}n_i(z)Q^2 e^4 \log \Lambda}{12\pi^{3/2}\epsilon_0^2 m_e^{1/2} (kT_e)^{3/2}} \quad (7)$$

is calculated using a Gaussian electron density distribution with maximum density reached at  $B_{min}$  ( $z = 0$ ). In Eq. (7)  $n_i(z)$  is the ion density, which can be calculated when the electron density and average charge state of the plasma are known. The Coulomb logarithm  $\log \Lambda$  is calculated from assumed average electron population energy and density. The average electron temperature  $T_e$  is also a parameter in Eq. (7). However, it is very difficult to approximate the value of  $T_e$  due to different electron populations [11]. For fixed  $\omega_{rf}$  it is possible to solve Eq. (6) for  $k$ . The real part of  $k$  is used for electric field which is proportional to  $\sin(\omega_{rf}t - k^{real}z)$ . Depending on the values of  $\omega_{rf}$ ,  $\omega_{ce}$  and  $\nu_c$  the wave number  $k$  can have imaginary part, which is related to cyclotron damping. We have assumed that electric field behaves proportionally to  $\exp(-k^{imag} dz)$ , where  $dz$  is small increment in distance and  $k^{imag}$  depends on  $z$ .

## 2.3. Equations of motion

Equations of motion for the electron can be derived denoting that force equals the time derivative of momentum:

$$\frac{d}{dt}\underbrace{\vec{p}}_{\vec{p}} = \frac{d}{dt}(\gamma m \vec{v}) = \vec{F}. \quad (8)$$

Thus

$$\dot{\gamma} m \vec{v} + \gamma m \dot{\vec{v}} = \vec{F} \quad (9)$$

where

$$\dot{\gamma} = \frac{v_i \dot{v}_i}{c^2} \gamma^3. \quad (10)$$

Now, taking into account that  $\gamma$  is calculated always from all three velocity components ( $v_x$ ,  $v_y$ ,  $v_z$ ), and by using Einstein's summation convention, equation of motion (9) can be written in form of

$$\dot{v}_j + \frac{v_i \dot{v}_i}{c^2} \gamma^2 v_j = \frac{1}{\gamma m} F_j. \quad (11)$$

For each component at the time we get the following equations:

$$\dot{v}_x + \tilde{a}\dot{v}_x + \tilde{d}\dot{v}_y + \tilde{f}\dot{v}_z = \frac{1}{\gamma m} F_x \quad (12)$$

$$\dot{v}_y + \tilde{b}\dot{v}_y + \tilde{d}\dot{v}_x + \tilde{e}\dot{v}_z = \frac{1}{\gamma m} F_y \quad (13)$$

$$\dot{v}_z + \tilde{c}\dot{v}_z + \tilde{e}\dot{v}_y + \tilde{f}\dot{v}_x = \frac{1}{\gamma m} F_z \quad (14)$$

where

$$\tilde{a} = v_x^2 \frac{\gamma^2}{c^2}, \quad \tilde{b} = v_y^2 \frac{\gamma^2}{c^2}$$

$$\tilde{c} = v_z^2 \frac{\gamma^2}{c^2}, \quad \tilde{d} = v_x v_y \frac{\gamma^2}{c^2}$$

$$\tilde{e} = v_y v_z \frac{\gamma^2}{c^2}, \quad \tilde{f} = v_x v_z \frac{\gamma^2}{c^2}.$$

Denoting  $\vec{u} = (\gamma/c)\vec{v}$  and substituting it into the matrix form of (12)–(14) we get

$$\begin{pmatrix} \tilde{A} & \tilde{D} & \tilde{F} \\ \tilde{D} & \tilde{B} & \tilde{E} \\ \tilde{F} & \tilde{E} & \tilde{C} \end{pmatrix} \begin{pmatrix} \dot{v}_x \\ \dot{v}_y \\ \dot{v}_z \end{pmatrix} = \frac{1}{\gamma m} \begin{pmatrix} F_x \\ F_y \\ F_z \end{pmatrix} \quad (15)$$

in which

$$\tilde{A} = 1 + u_x^2, \quad \tilde{B} = 1 + u_y^2$$

$$\tilde{C} = 1 + u_z^2, \quad \tilde{D} = u_x u_y$$

$$\tilde{E} = u_y u_z, \quad \tilde{F} = u_x u_z.$$

Eq. (15) can be solved for acceleration components, and finally we get

$$\begin{pmatrix} \dot{v}_x \\ \dot{v}_y \\ \dot{v}_z \end{pmatrix} = K \begin{pmatrix} \hat{A}F_x - \tilde{D}F_y - \tilde{F}F_z \\ -\tilde{D}F_x + \hat{B}F_y - \tilde{E}F_z \\ -\tilde{F}F_x - \tilde{E}F_y + \hat{C}F_z \end{pmatrix} \quad (16)$$

using notations

$$\hat{A} = 1 + u_y^2 + u_z^2, \quad \hat{B} = 1 + u_x^2 + u_z^2$$

$$\hat{C} = 1 + u_x^2 + u_y^2, \quad K = \frac{1}{m\gamma \left(1 + \frac{\gamma^2}{c^2} v^2\right)}.$$

It should be noted that these equations are written for an arbitrary force. For a charged particle in the presence of electric and magnetic field, we substitute Lorentz's force  $\vec{F} = q(\vec{E} + \vec{v} \times \vec{B})$  into Eq. (16), which, then, can be solved for space coordinates and velocity components.

#### 2.4. Input parameters

The simulation code utilizes the following input parameters: initial energy and initial pitch angle, average electron population energy, average charge state of the plasma, electron density distribution, microwave power, microwave frequency and  $Q$  value of the plasma chamber. Also the plasma chamber dimensions can be changed. Setting up a different magnetic field is possible in order to study the effect of magnetic field gradient and mirror strength. The vast number of input parameters makes systematic studies very time-consuming. However, this selection allows us to use the code to model different ECRISs with different operating conditions and RF frequencies. Because we do not have adequate information about the electron density profiles in ECRIS plasma chamber, we have decided to use Gaussian density profiles as a first approximation. It is generally stated that electron density in ECR plasma is around  $10^{17} \text{ m}^{-3}$  (see Ref. [1]), so we constructed a few density profiles around this value.

### 3. Damping of the electric field in the vicinity of the resonance zone

In this section we present the Gaussian electron density profiles used in this paper. We also discuss the imaginary part of the wave number which is related to damping of the electric field. We present how the imaginary wave number behaves as density and average electron population energy are changed. Finally, we illustrate how electric field is affected by the above-mentioned parameters.

#### 3.1. Density and absorption profiles

To simulate the behaviour of the electric field in the resonance zone we use the electron density profiles presented in Table 1 and in Fig. 1. Maximum density is located at the  $B_{\min}$  and minimum density is reached at the plasma chamber walls.  $Q$  value of 3 is used and based on the extracted beam (all charge states) we estimate the average charge of a typical argon plasma to be  $8+$ , which is used in the following calculations.

Real part of the wave number  $k$  approaches the free space wave number outside the resonance but increases on the resonance zone when entering the plasma and then drops close to zero. After the resonance crossing  $k^{\text{real}}$  can approach the free space wave number again or remain close to zero depending on the density profile and average electron population energy. Because  $k^{\text{imag}}$  is peaked on resonances and approaches zero elsewhere it is clear that after the microwave passes a resonance the electric field

Table 1  
Electron density profiles

Label	Density profile, Gaussian shape
#1	max $10^{16}$ , min $10^{15} \text{ m}^{-3}$
#2	max $10^{17}$ , min $10^{16} \text{ m}^{-3}$
#3	max $10^{17}$ , min $10^{15} \text{ m}^{-3}$
#4	max $10^{18}$ , min $10^{16} \text{ m}^{-3}$

Profiles are Gaussian shape with max corresponding to the highest density (located at the  $B_{\min}$ ) and min corresponding to minimum density (located at the plasma chamber walls).

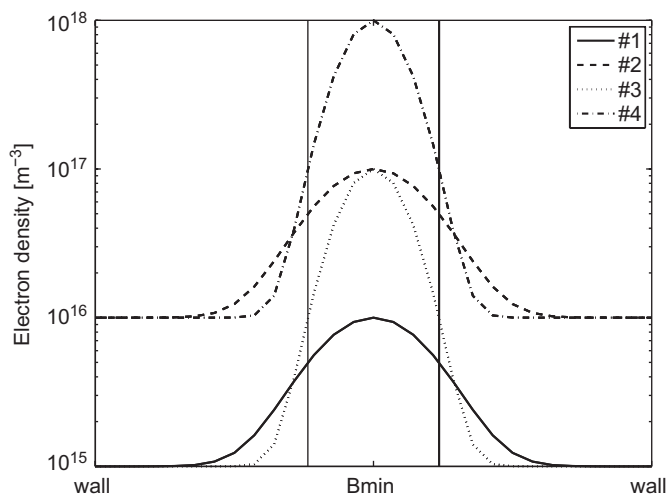


Fig. 1. Gaussian electron density profiles used in the simulation. In the horizontal axis 'Wall' denotes position of the plasma chamber wall and 'Bmin' centre of the chamber (minimum  $B$  field,  $z = 0$ ). The two vertical lines on left and right sides of Bmin are resonance points for 1 eV electron at 14 GHz.

amplitude of the propagating wave is decreased due to damping. At cut-off frequency the refraction index  $N = 0$ . The EM wave does not propagate at frequencies in which  $N^2 < 0$  implying that refraction index is imaginary. Thus the phase velocity  $v_{\text{ph}} = Nc$  of the EM wave is imaginary and the amplitude of the EM wave is decreased exponentially. Both normalized  $k^{\text{real}}$  and normalized  $k^{\text{imag}}$  close to resonance zones are presented in Fig. 2 with density profiles #1 and #4 (see Table 1). From the pictures one can see that different density profiles and average electron energies have a significant impact on the wave number behaviour thus damping the wave near the resonance zone. In subpicture (a) the wave behaviour is calculated using a 100 eV average electron population energy and density profile #1, the same parameters are 100 eV and #4 in (b), 70 keV and #1 in (c) and 70 keV and #4 in (d). The scale of the  $x$ -axis is the same in all presented subpictures. One can see the effect of the density profile i.e. with profile #1 the imaginary wave number goes to zero in resonance faster than with profile #4. This means that in #1 the damping of the wave takes place in smaller distance i.e. resonance zone is smaller than in the case of density profile #4. If one studies the effect of average electron energy one notes that

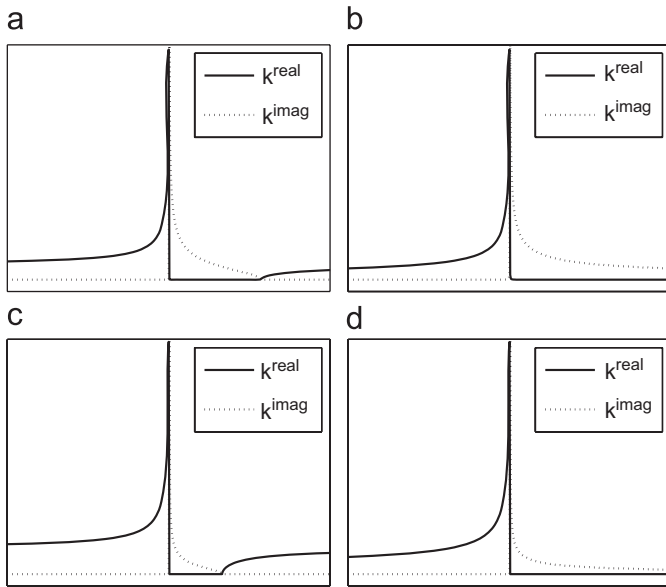


Fig. 2. Real and imaginary parts (both normalized to their maximum values) of wave number in the vicinity of resonance zone. (a) Average electron population energy 100 eV, density profile #1, (b) 100 eV, #4, (c) 70 keV, #1 and (d) 70 keV, #4. EM wave is propagating from left to right into the resonance zone and the  $k^{\text{real}}$  is approaching free space wave number on the left in all of the subpictures.

in (c) the imaginary wave number drops down to zero even faster than in (a) meaning that the width of the resonance zone is further decreased and the EM wave is absorbed in a smaller volume. With density profile #1 the real part of the wave number is approaching the free space wave number after the resonance zone. This implies that the EM wave is propagating through the resonance. However, using density profile #4 leads to almost total absorption of the wave thus  $k^{\text{real}}$  remains zero after the resonance meaning that more electric field power goes through the resonance when using 70 keV instead of 100 eV (later see Figs. 3 and 4). The average electron population energies in the pictures were chosen just to demonstrate the effect of the average energy. One hundred eV represents the lower energy population and 70 keV is based on the earlier X-ray measurements done with the JYFL 14 GHz ECRIS (the most probable energy in the measurement) [12]. However, one must remark that these measurements were done radially so the structure of the ion source is attenuating the bremsstrahlung meaning that low energy electron population cannot be seen at all in the spectrum. Therefore more accurate measurements should be made.

### 3.2. Damping of the electric field

An example of absorption of the electric field is presented in Fig. 3 using density profiles from Table 1. The upper subpicture (a) is a close-up of the first resonance crossing and the lower subpicture (b) presents the damping for two resonance crossings. In the picture the Poynting vector points from left to right representing the direction of

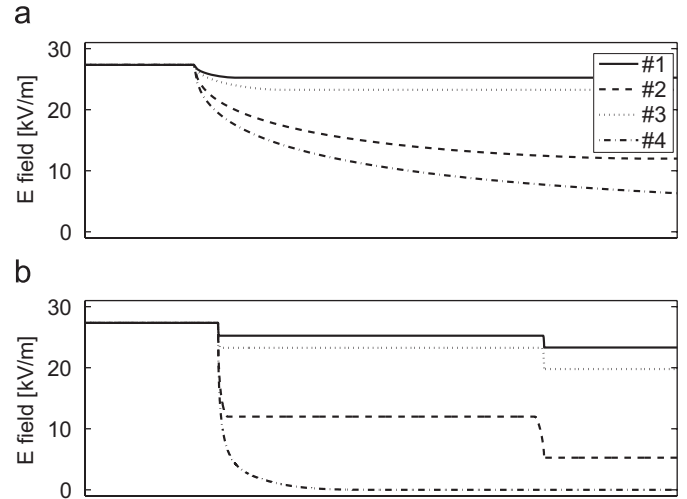


Fig. 3. Electric field damping on the resonance zone with 500 W RF power and 100 eV average electron population energy as a function of densities. (a) Damping near the first resonance, (b) damping in two resonance crossings. Distance in both pictures is arbitrary.

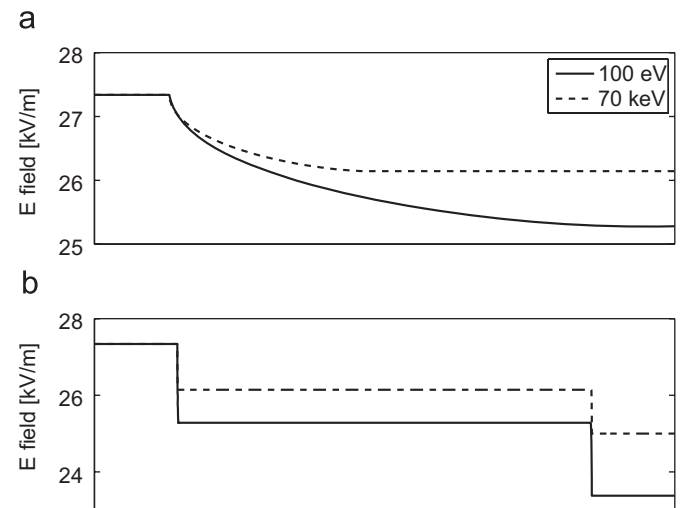


Fig. 4. Electric field damping on the resonance zone with 500 W RF power and density profile #1 as a function of average electron population energy. (a) Damping near the first resonance, (b) damping in two resonance crossings. Distance in both pictures is arbitrary and normalized to have the resonances at the same location.

RF-power propagation. It can be seen that as the maximum density gets higher the electric field absorption is increased. In the case of Gaussian density profile for which the peak value is  $10^{18} \text{ m}^{-3}$  the electric field is damped so intensively that the amplitude drops almost to zero. In the second resonance there is very little energy left to be absorbed by the electrons. However, if the maximum density is  $10^{16}$  or  $10^{17} \text{ m}^{-3}$  significant energy absorption can take place also on the second resonance. All this implies that when there is plasma in the chamber, the quality factor of the chamber is most likely very small.

We also present how the average electron population energy affects the damping of the wave in the resonance

zone. In Fig. 4 average electron population energies of 100 eV and 70 keV are compared. In subpicture (a) the first resonance is zoomed and in (b) two resonance crossings are presented. Using different average electron population energies the location of the resonance zone is shifted, so we present the  $x$ -axis of the figures scaled to have the resonances at the same location. As stated already earlier, the higher average electron population energy results in smaller resonance zone width (see Fig. 2). It is also noted that higher average electron population energy damps the EM field less (because of lower collision frequency) than lower average electron population energy as can be seen from Fig. 4.

#### 4. Simulated time evolution of electron energy with different input parameters

In this section we present simulations using different input parameters. The dependence of electron energy on different parameters like density profile,  $Q$  value and RF power is presented up to 1  $\mu$ s simulation time.

##### 4.1. The effect of density profiles

In Fig. 5 we present energy trends in 200 ns simulations using three electron density profiles. The density profile and time-averaged electron energy in the simulation is mentioned in the label of the picture. There is a clear connection between the damping of the electric field on the resonance and obtained electron energy. If we consider the density profile #2 (see Table 1) we see that electron gains less energy than using e.g. the profile #3 for which cyclotron damping is not so predominant. In the cases presented in the figure (with parameters given in the figure caption) we see that average energies differ roughly by a factor of 9 suggesting that density profile has a huge effect on the electron energy. In maximum energies there is a factor of around 5 between the simulations. In the case of #2 and #3 the energy of the electron reaches its maximum at 200 ns where we stop the simulation. However, if we use density profile #1 the maximum energy in 200 ns simulation is reached around 35 ns.

##### 4.2. The effect of average electron population energy

We have also simulated the effect of different average electron population energies. This can be seen in Fig. 6 where we have 200 ns simulations with 100 eV, 1 keV, 10 keV and 100 keV average energies. One can see that increasing the average electron population energy of the plasma the time-averaged (simulated) electron energy is increasing. This is due to smaller collision frequency as discussed earlier. It is not known what the average electron population energy actually is. However, during stable operation it is likely to be almost constant if instabilities, plasma ignition and shutdown are ignored.

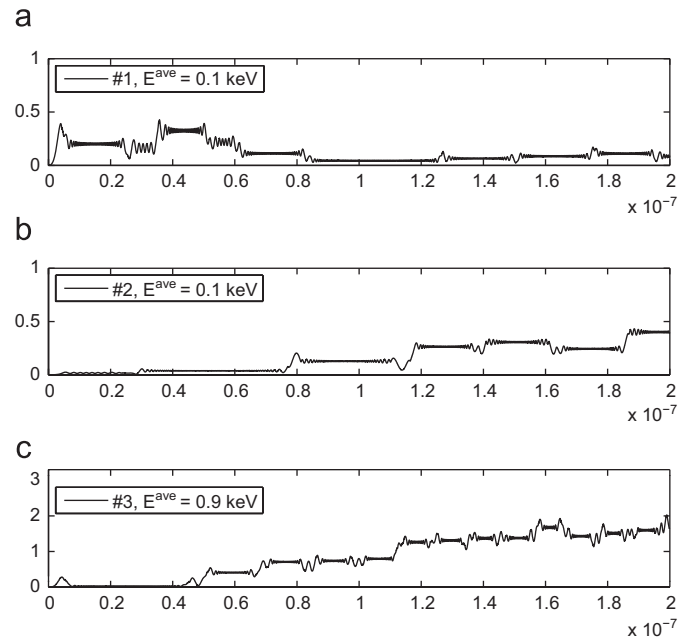


Fig. 5. Electron energy in keV in 200 ns simulation with different density profiles: (a) #1, (b) #2, (c) #3. Parameters 14 GHz, 500 W RF power,  $Q$  value 3, initial energy 1 eV, initial pitch angle  $50^\circ$ , assumed average electron population energy 100 eV.

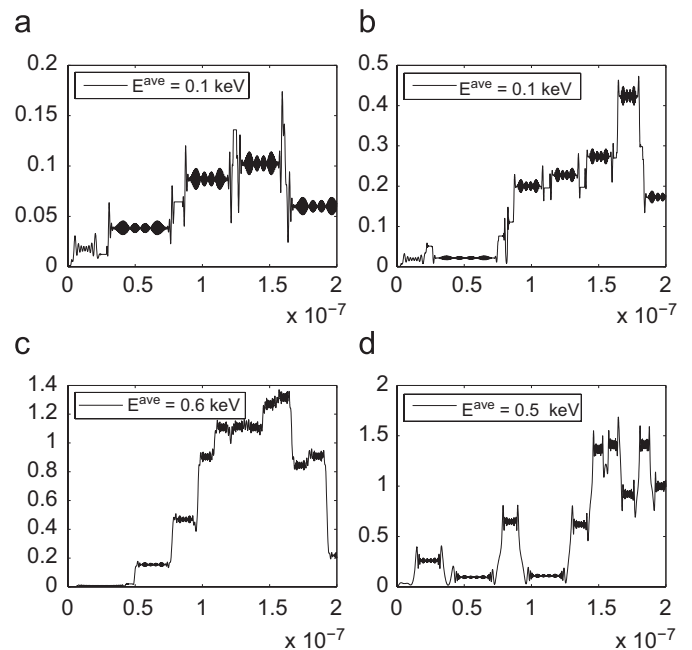


Fig. 6. Electron energy in 200 ns simulation with different assumed average electron population energies: (a) 100 eV, (b) 1 keV, (c) 10 keV, (d) 100 keV. Parameters 14 GHz, 500 W RF power,  $Q$  value 3, initial energy 1 eV, initial pitch angle  $50^\circ$ , density profile #2.

##### 4.3. The effect of plasma chamber $Q$ value

In Fig. 7 we present how the electron energy behaves as a function of the plasma chamber quality factor. We have used three values for the quality factor and average electron population energy was set to be 100 eV. It is

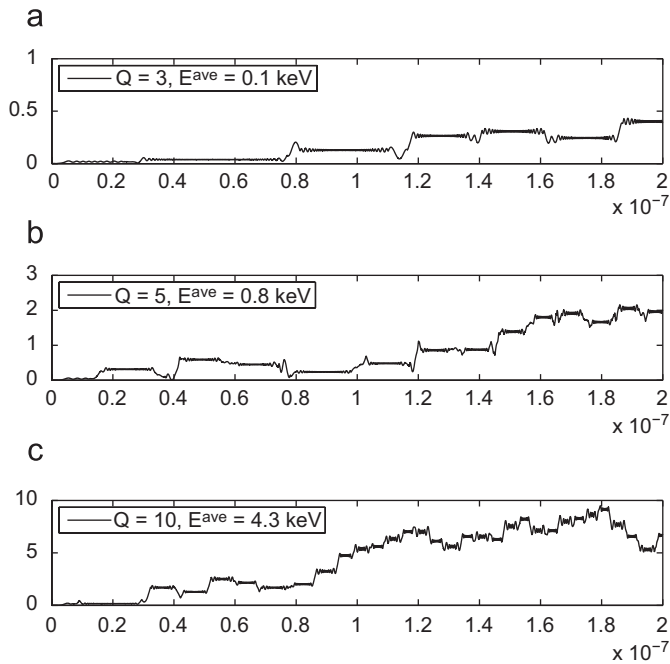


Fig. 7. Electron energy in keV in 200 ns simulation with different  $Q$  values using average electron population energy of 100 eV.  $Q$  values are (a) 3, (b) 5 and (c) 10. Parameters 14 GHz, 500 W RF power, initial energy 1 eV, initial pitch angle  $50^\circ$ , density profile #2.

observed that time-averaged electron energy is increasing with increasing  $Q$  value. This is expected because the quality factor affects the electric field amplitude inside the plasma chamber. The average energy rises from 0.1 to 0.8 keV and finally to 4.3 keV in subpictures (a), (b) and (c), respectively. Comparing (a) and (c) we have a factor of 43 in the average energy gain while the factor in maximum energies between (a) and (c) is roughly 22. We also did a simulation with the same parameters than in Fig. 7, but with 70 keV average electron population energy. This can be seen in Fig. 8. In (a) the time-averaged energy is 0.2 keV and in (b) 2.8 keV, so there is a factor of 14 between using 3 or 5 as the quality factor. In maximum energies the factor is a bit over 5. In subpicture (c) one can see a situation where the electron is heavily decelerated after about 40 ns. However, the electron was not lost to plasma chamber walls. It went approximately to 0.8 T field before it was reflected back towards the resonance. The energy of the electron after deceleration was so small (8 eV) that it took about 115 ns to go from resonance to mirror point and back to resonance where the electron starts to gain energy again (slightly before 160 ns). This behaviour also means that the time-averaged energy for the simulation in subpicture (c) is quite low. This simulation is a very nice example of stochastic heating process where the electron can drift to decelerating phase with the RHCP EM wave.

In order to have some idea of how the average electron population energies behave when the ECR is turned on we used a quality factor of 3, 500 W RF power and density profile #2 and went through an iterative process. This means that we started our 200 ns simulation with the initial

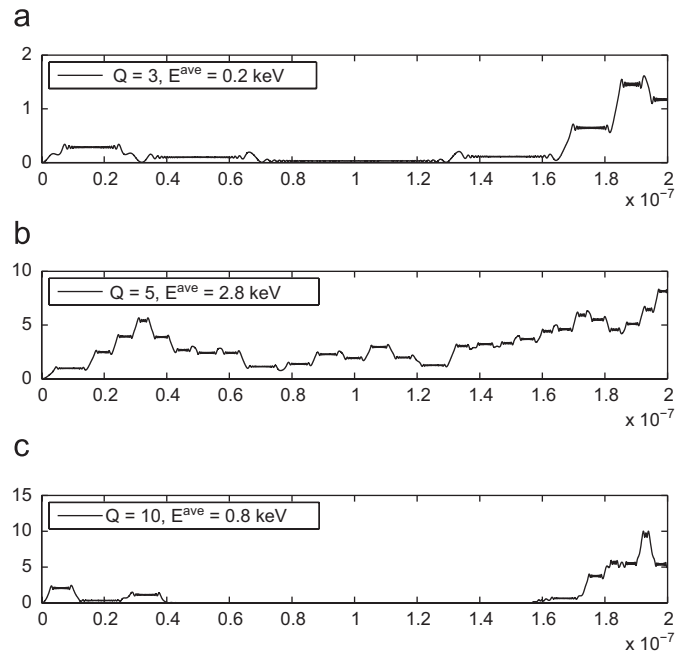


Fig. 8. Electron energy in keV in 200 ns simulation with different  $Q$  values using average electron population energy of 70 keV.  $Q$  values are (a) 3, (b) 5 and (c) 10. Parameters 14 GHz, 500 W RF power, initial energy 1 eV, initial pitch angle  $50^\circ$ , density profile #2.

electron energy of 1 eV and average electron population energy of 20 eV. After the first simulation the time-averaged energy was calculated from simulation results and it was used as an input average electron population energy in the next 200 ns simulation. We did this several times in this case until the time-averaged electron energy after the simulation was the same as the input average population energy. According to our simulations it is reasonable to use average electron population energy of 100 eV in 200 ns simulation with initial parameters of 14 GHz, quality factor 3, density profile #2, 500 W, 1 eV initial energy of the electron and  $50^\circ$  initial pitch angle. However, it must be concluded that this kind of a process is not working for all sets of initial parameters due to stochastic heating. We found several cases where the energy did not converge towards a certain value but was left to produce a different time-averaged energy in consecutive iterations. When discussing about EM wave damping we have stated that  $Q$  value cannot be very high if EM wave's energy is absorbed. This leads us to the conclusion that the amplitude of the electric field must be higher than it is by calculating the field from the Poynting vector and it could be explained by the mode structure. Therefore it is very important to measure the time evolution of the bremsstrahlung spectra from ECRIS. This would give us more information about how fast the electrons are heated and how the average electron energy inside the plasma chamber is evolved. The  $Q$  value of the loaded plasma chamber is not known exactly and it is extremely difficult to measure for the loaded chamber. Main problem of such a measurement is the high frequency

of the microwaves which corresponds to small wave lengths. In this case it is difficult to manufacture a pick-up antenna which could operate at high frequency and relatively high RF powers. High frequency also tends to average the measurement of electric field unless the measured signal is proportional to square of the EM wave amplitude, because in GHz region no available measurement technique is fast enough.

It is very clear that quality factor of the plasma chamber has a significant effect on the energy gain process. The higher the  $Q$  value the higher the average and maximum energies. In reality we have a certain propagating mode structure from the wave guide into the ECRIS plasma chamber and depending on the conditions we can have substantially higher electric fields in the resonance zone. This means that even when using 3 as a quality factor the electric field in reality could be much higher and the energies from the simulations could equal the measured energies up to 600 keV in JYFL 14 GHz ECRIS.

#### 4.4. The effect of RF power

To study the effect of RF power we decided to do 1  $\mu$ s simulations using 500 W, 1 and 2 kW RF powers with 100 eV and 70 keV [12] average electron population energies (see also Fig. 4). In Fig. 9 we have the energy gains using 100 eV as the average energy. One can see that time-averaged electron energy is increasing with RF power. However, the difference in average energy between 500 W and 1 kW is much larger than 1 and 2 kW (see Fig. 9). Between (a) and (b) we have a factor of 7 in time-averaged energy and between (b) and (c) there is only a factor of 1.3. If one looks at the maximum energies, one notes that using 500 W results in about 1.2 keV, 1 kW results roughly in 3 keV and 2 kW RF power can accelerate the electron into energy of almost 6 keV at the maximum. It is then noted that both average and maximum energy are increased with increasing microwave power using 100 eV as average electron population energy. Increasing the average electron population energy to 70 keV leads to smaller resonance width and less damped EM wave than 100 eV as presented in Fig. 4. From Fig. 10 one can immediately see that average population energy of 70 keV results in both higher average and maximum energy than 100 eV. In subpicture (a) average energy is 5.5 keV and the maximum energy is almost 15 keV. Compared to subpicture (b) where the numbers are 8.2 and roughly 20 keV we have the factors of 1.5 and 1.3 in average and maximum energies, respectively. Changing the RF power to 2 kW (subpicture (c)) results in both lower average and maximum energies compared to 1 kW simulation in this case of initial parameters. The electron has not gone into a phase where absorption of the energy from the EM wave would be most efficient resulting in energies that are lower than when using 1 kW RF power. The effects of stochastic heating are nicely seen in subpicture (b) where the energy lies quite low upto simulation time of 350 ns and after that gains energy in

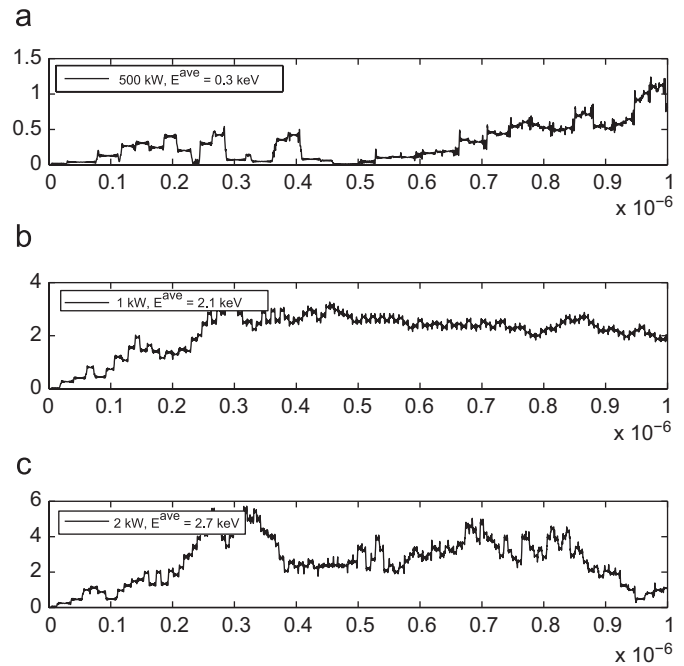


Fig. 9. Electron energy in 1  $\mu$ s simulation with different RF powers. Parameters 14 GHz, assumed average electron population energy 100 eV, initial energy 1 eV, initial pitch angle  $50^\circ$ , density profile #2.

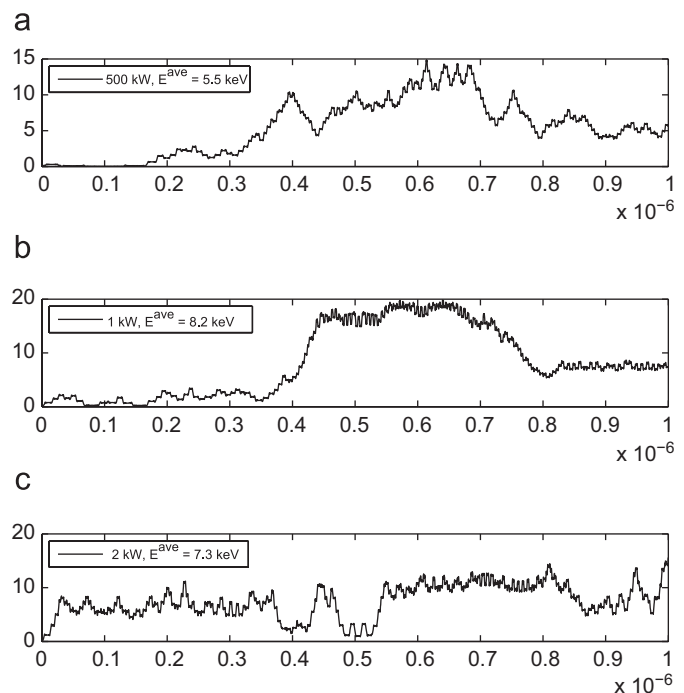


Fig. 10. Electron energy in 1  $\mu$ s simulation with different RF powers. Parameters 14 GHz, assumed average electron population energy 70 keV, initial energy 1 eV, initial pitch angle  $50^\circ$ , density profile #2.

several resonance crossings until the energy levels down into 18–19 keV region. After 700 ns the electron starts to lose its energy again. In stochastic heating the electron can gain or lose energy in consecutive resonance zone crossings or it can gain or lose energy in several consecutive

resonance zone crossings. We also did a test with 10 kW RF power (other parameters were the same than in Fig. 9) and noted that average energy was almost 30 keV while the maximum time-averaged energy was a bit over 60 keV. It has to be stated that neither a fixed average electron population energy nor the fixed electron density profile is a valid approximation while increasing the RF power. It is clear that the electron density distribution is changing with the RF power. Therefore it is suggested that electron density profiles with varying parameters would be measured in the ECRIS plasma chamber.

## 5. Discussion

In this paper we have presented an ECRH code which is then tested with typical operating settings of JYFL 14 GHz ECRIS, although we do not use higher RF powers than 1 kW. We have been using simulation times from 200 ns to 1  $\mu$ s, but also longer simulations are achievable. The calculation times for the cases presented in this paper varied typically from a few minutes to a few hours. Further development of the code is necessary to gain more understanding on the ECRH process. We have shown that the electron density and the density profile have a significant effect on the cyclotron damping of the electric field. If the density is too high the electric field strength drops rapidly almost to zero in the vicinity of the resonance zone resulting in lower electron energies achieved during the stochastic heating process. However, the reduction of the heating efficiency can be compensated by increasing the RF power and thus the amplitude of the electric field. Also the mode structure excited within the plasma can affect the electric field, at least locally. Currently we are not able to heat the electrons in the simulation to match the energies that have been measured with the JYFL 14 GHz ECRIS [12] using generally accepted values for the quality factor and the average electron density. It is possible that plasma instabilities which can cause distortion to electric field phase and amplitude can explain the discrepancy between simulated and measured maximum energies. In theory the maximum energy is limited by stochastic acceleration limit (adiabatic limit) i.e. without considering plasma instabilities maximum electron energy is limited between 10 and 270 keV [1]. On the other hand, averaging the electric field amplitude is a relatively crude approximation. It is possible that in a given EM wave mode the power density near resonance zones is very high. Due to high power density the electron can be accelerated to higher energies than the simulations of this paper imply. However, as discussed earlier the mode structure or the local electric field is nearly impossible to measure within the GHz frequency range. It has been considered that Fermi acceleration [13] could also have an impact on electron energy in ECRIS plasma. However, while this phenomenon indeed exists in ECRIS it seems to be less effective in GHz frequency range than ECRH [14]. Proposed actions to develop the code include modelling plasma instabilities by changing the phase and

amplitude of the EM wave, trying to study the mode structure in the plasma chamber and adding relativistic Doppler effect into the code. In the future versions of the code it would also be relevant to consider refining the model of electric field damping near the resonance by taking into account the break-down of Ohm's law, which causes the electric field at the resonance to be proportional to the acceleration of the electrons (instead of velocity). However, it is questionable that such a refinement would explain the discrepancy between simulated and measured electron energies and therefore we have chosen to pursue other modifications of the model at the first place. The electron densities in the plasma chamber should be studied more thoroughly, especially in the vicinity of the resonance zone. This could be made with probe measurements. We also plan to test the code with different magnetic field gradients and microwave frequencies like 28 GHz and compare our code to other ECRH codes. It is noted that different initial parameters in simulations greatly affect the heating and energy gain of the electron. More systematic study will need to be made using different initial parameters. In order to validate our simulation results we will put significant effort on measuring the time evolution of the bremsstrahlung spectra produced by the JYFL ECRIS (14 GHz klystron and 10.75–12.75 GHz TWTA).

## Acknowledgements

This work has been supported by the EU 6th Framework programme 'Integrating Infrastructure Initiative—Transnational Access', Contract Number: 506065 (EURONS) and by the Academy of Finland under the Finnish Centre of Excellence Programme 2006–2011 (Nuclear and Accelerator Based Physics Programme at JYFL). T. Ropponen would also like to acknowledge support from the Graduate School in Particle and Nuclear Physics and T.K. Koponen would like to acknowledge support from the National Graduate School in Materials Physics and Emil Aaltonen foundation.

## References

- [1] R. Geller, *Electron Cyclotron Resonance Ion Sources and ECR Plasmas*, Taylor & Francis, London, 1996.
- [2] J. Vámosi, S. Biri, *Comput. Phys. Commun.* 98 (1995) 215.
- [3] H. Koivisto, *Rev. Sci. Instr.* 70 (1999) 2979.
- [4] D. Leitner, C. Lyneis, H. Koivisto, T. Ropponen, J. Ropponen, D.~S. Todd, J.~Y. Benitez, S. Gammino, Measurement of the High Energy Component of the X-ray Spectra in the VENUS ECR Ion Source, Proceedings of International Conference of Ion Sources (ICIS) 2007, to be published.
- [5] Y. Jongen, E.C.R. electron acceleration, in: Workshop on the Sixth International ECR Ion Source, 1985, p. 238.
- [6] A.B. Petrin, *IEEE Trans. Plasma Sci.* 34 (1) (2006) 70.
- [7] RADIA, RADIA magnetic field simulation code, version 4.098, copyright of ESRF, Grenoble, France, Oxfordshire, UK, 1997 (<http://www.esrf.eu/Accelerators/Groups/InsertionDevices/Software/Radia>).
- [8] J.P. Schapira, et al., Un Spectrometre Constitue d'Un ou Deux Solenoides Cryogeniques Coaxiaux, IPN-Orsay, 1979.

- [9] M.C. Williamson, A.J. Lichtenberg, M.A. Lieberman, *J. Appl. Phys.* 72 (1991) 3924.
- [10] R.J. Goldston, P.H. Rutherford, *Introduction to Plasma Physics*, Institute of Physics Publishing, 1995.
- [11] G. Douysset, H. Khodja, A. Girard, J.P. Briand, *Phys. Rev. E* 61 (2000) 3015.
- [12] H. Koivisto, P. Heikkinen, V. Hänninen, A. Lassila, H. Leinonen, V. Nieminen, J. Pakarinen, K. Ranttila, J. Ärje, E. Liukkonen, *Nucl. Instr. and Meth. B* 174 (2001) 379.
- [13] E. Fermi, *Phys. Rev.* 75 (1949) 1169.
- [14] R.L. Dewar, C.I. Ciubotariu, *Phys. Rev. E* 60 (1999) 7400.

## APPENDIX A.II



## Measurement of the high energy component of the x-ray spectra in the VENUS electron cyclotron resonance ion source<sup>a)</sup>

D. Leitner,<sup>b)</sup> J. Y. Benitez, C. M. Lyneis, and D. S. Todd  
Lawrence Berkeley National Laboratory, One Cyclotron Road, Berkeley, CA 94720, USA

T. Ropponen, J. Ropponen, and H. Koivisto  
Accelerator Laboratory, Department of Physics, University of Jyväskylä, FIN-40014, Finland

S. Gammino  
INFN-Laboratori Nazionali del Sud, Catania 95125, Italy

(Received 24 September 2007; accepted 10 November 2007; published online 27 March 2008)

High performance electron cyclotron resonance (ECR) ion sources, such as VENUS (Versatile ECR for Nuclear Science), produce large amounts of x-rays. By studying their energy spectra, conclusions can be drawn about the electron heating process and the electron confinement. In addition, the bremsstrahlung from the plasma chamber is partly absorbed by the cold mass of the superconducting magnet, adding an extra heat load to the cryostat. Germanium or NaI detectors are generally used for x-ray measurements. Due to the high x-ray flux from the source, the experimental setup to measure bremsstrahlung spectra from ECR ion sources is somewhat different from that for the traditional nuclear physics measurements these detectors are generally used for. In particular, the collimation and background shielding can be problematic. In this paper, we will discuss the experimental setup for such a measurement, the energy calibration and background reduction, the shielding of the detector, and collimation of the x-ray flux. We will present x-ray energy spectra and cryostat heating rates depending on various ion source parameters, such as confinement fields, minimum  $B$ -field, rf power, and heating frequency. © 2008 American Institute of Physics. [DOI: 10.1063/1.2821137]

### I. INTRODUCTION

The VENUS electron cyclotron resonance (ECR) ion source at the Lawrence Berkeley National Laboratory has been designed for optimum operation using 28 GHz plasma heating frequency. The maximum axial magnetic confinement fields are 4 T at injection and 3 T at extraction, and are generated by three solenoid coils. A wide range of minimum  $B$  fields ( $B_{\min}$ ) between the magnetic mirrors can be tuned by changing the current of the middle coil. The radial field at the plasma chamber wall can be operated at fields up to 2.1 T (slightly more than twice the resonant field for 28 GHz [ $B_{\text{ECR } 28 \text{ GHz}} = 1 \text{ T}$ ]). VENUS has been operated routinely using 28 GHz as its main heating frequency since 2004 and has produced many world record beams.<sup>1,2</sup> Besides 28 GHz, 18 GHz can be injected as a second frequency for double frequency heating or used for single frequency heating at 18 GHz ( $B_{\text{ECR } 18 \text{ GHz}} = 0.64 \text{ T}$ ). The source design and its performance are described in detail in Refs. 1 and 2 and in several references within these papers. Because VENUS is a fully superconducting ECR ion source, its magnetic confinement field can be tuned over a wide range. This flexibility

makes VENUS a good tool to study frequency scaling laws and the influence of the magnetic field gradient at the resonance zone.

Bremsstrahlung spectroscopy is a standard plasma diagnostic tool and has been extensively used in fusion devices and ECR ion sources to diagnose the hot electron population.<sup>3-5</sup> Two processes in the plasma lead to the emission of bremsstrahlung. First, bremsstrahlung is created by electron-ion collisions within the plasma volume. Second, bremsstrahlung is emitted by electrons that are lost to the plasma chamber wall and that lose their energy through interaction with the wall material. The x-rays produced by these processes can penetrate through the plasma chamber wall. They cause x-ray radiation in the vicinity of ECR ion sources and can add a substantial heat load to the cryostat (see Sec. VII) when they are absorbed in the cold mass. To minimize and control this radiation, an understanding of the expected x-ray energy and flux is essential for the design and operation of superconducting sources. At the VENUS ECR ion source, measurements of the bremsstrahlung spectra have been proven to be a particularly powerful tool for the characterization and understanding of the source and minimization of the x-ray heating load from the plasma. Previous measurements of the axial bremsstrahlung spectra of the VENUS ECR ion source led to the design of a plasma chamber that incorporates a 2 mm Ta shielding wall around the chamber.<sup>6</sup> This Ta shielding reduces the effective x-ray flux by a factor of 10 and has allowed the source to operate at

<sup>a)</sup>Based on a paper presented at the 12th International Conference on Ion Sources, 26–31 August 2007 Jeju, Korea. An abstract-only version of this paper was published with the conference proceedings in Review of Scientific Instruments, in Part II of the February 2008 issue.

<sup>b)</sup>Author to whom correspondence should be addressed. Electronic mail: dleitner@lbl.gov.

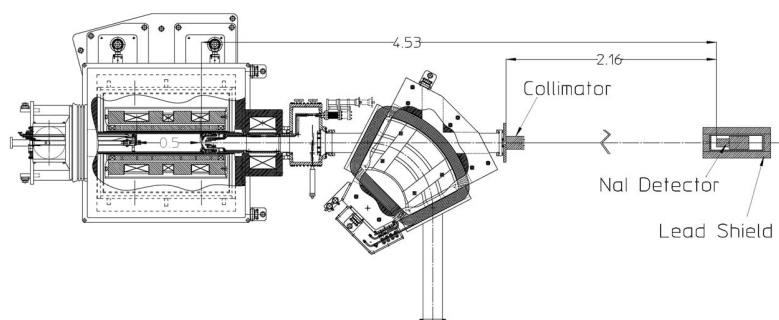


FIG. 1. Schematic of the experimental x-ray detector setup at the VENUS ECR ion source. Distances are indicated in meters.

higher rf power and a wider range of magnetic confinement fields. Similar designs are now incorporated in other superconducting ECR ion sources under construction.<sup>7,8</sup> However, as shown in Ref. 6, Ta becomes transparent for x-ray energies above 400 keV, and it is these high energy x-rays that contribute most to the cryostat heating. These “ultra-hot” electrons continue to present a challenge for the design and operation of next generation superconducting ECR ion sources using microwave heating frequencies of 28 GHz and higher and must be studied carefully to further advance the field of high field superconducting ECR ion sources.

## II. EXPERIMENTAL SETUP

Due to the high x-ray flux and the high x-ray energies produced by the ECR ion source, the experimental setup (Fig. 1) to measure bremsstrahlung spectra is somewhat different from that for the traditional nuclear physics measurements these detectors are generally used for. In particular, the collimation and background shielding have to be done carefully and are described in detail below. It is particularly important to ensure that the shielding is adequate; otherwise, unphysical high energy “bumps” appear in the x-ray spectra in the energy range where 1–2 cm of lead shielding does not provide enough attenuation (Fig. 2). These bumps disappear as more lead shielding is added around the collimator. The experimental setup used for all the measurements presented is shown in Fig. 1. The x-ray signal was collimated by a 127 mm long heavy-metal collimator composed of 95% W

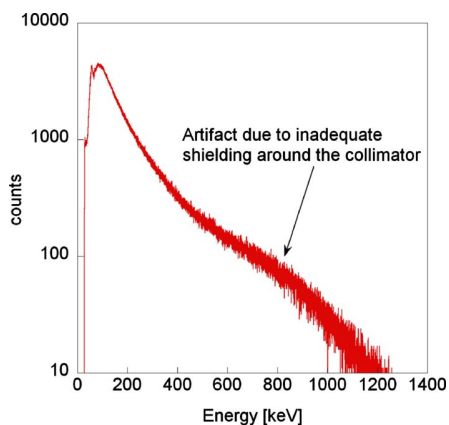


FIG. 2. (Color online) If the shielding around the collimator is insufficient, unphysical high energy “bump” appears in the x-ray spectra for the high energy region where the shielding becomes transparent. If more shielding is added, this bump disappears (see Fig. 4).

and 5% Cu located 2.37 m away from the extraction aperture. The collimator block has a 1 mm square groove along the length, which is aligned with the extraction hole of the VENUS ECR ion source. In addition, the collimator is surrounded by lead shielding blocks to minimize the detection of x-rays coming from other areas of the plasma chamber or are scattered outside the collimator from reaching the detector. The NaI phototube detector is placed about 2.16 m away to reduce the dead time of the detector. In addition, the detector is surrounded by 5 cm thick lead shielding blocks to minimize background radiation (coming from other x-ray sources in the vicinity, e.g., the AECR ion source). Finally, another entrance collimator of 12.7 mm diameter is placed before the detector. With the collimator and all the shielding in place, the x-ray leakage to signal ratio is reduced to 1:250. The energy calibration of the spectrum is done using a <sup>207</sup>Bi source, using three characteristic gamma lines at 569, 1063, and 1770 keV.

As the ECR ion sources are located directly above the cyclotron vault, the detector must be shielded from the cyclotron’s magnetic stray field. Therefore, the detector was placed into a 6 mm thick iron shield. In addition, phototube detectors can experience energy calibration drifts due to ambient temperature changes. The temperature drift of our detector was measured to be less than 2% for a temperature change of 10 deg. Finally, the change of the energy calibration due to count rate changes was found to be less than 1% when varying the count rates from 800 to 30 000 Hz. However, over several days of operation, the energy calibration of the detector can drift a few percentages, which we were unable to eliminate. Therefore, we recalibrate the detector for each measured spectrum to avoid any systematic errors. The spectra were not corrected for detector efficiency across the energy range since the detector efficiency is not flat across the energy range, but lower for higher energies. Therefore, the spectral temperatures and absolute x-ray intensity will be underestimated for higher energies. The maximum acceptance angle of the collimator system is 0.2 deg. This acceptance angle translates to a 14 mm diameter circle at the extraction plate. Since the extraction aperture of the VENUS ECR ion source has a diameter of 8 mm, the bremsstrahlung created by electrons lost to the extraction aperture wall can be detected in our setup. When the collimator geometry and the angular distribution of the bremsstrahlung were simulated with GEANT4,<sup>9</sup> it was found that changes of the shape of the energy spectrum due to scattering effects of x rays in the collimator can be neglected and that the produced brems-

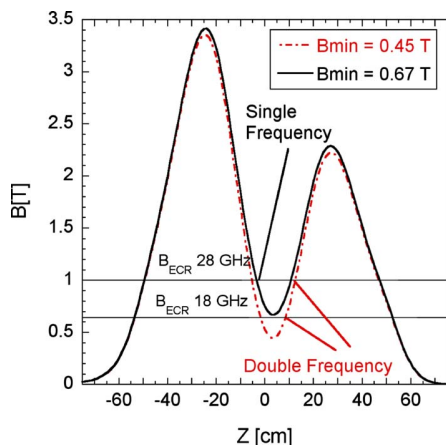


FIG. 3. (Color online) Axial field profile used for the single frequency heating at 28 GHz and double frequency heating at 18 and 28 GHz experiments. Only the middle field was changed, while all other source parameters remained unchanged.

strahlung is mainly forward directed. This also suggests that a substantial part of the x rays detected with the current experimental setup come from electrons lost on the extraction plate.

### III. EXPERIMENTAL RESULTS WITH VENUS

For this paper, we focus on a comparison of the x-ray spectra using two axial magnetic field configurations. Both are typical field configurations, which are used to achieve high intensity, high charge state ion beams. In the first configuration, we use a minimum  $B$  field of 0.44 T; in the second configuration, we use a minimum  $B$  field of 0.67–0.7 T. The sextupole field and the peak mirror fields were held nearly the same during all experiments. All other source parameters, such as gas flow and gas mixing ratio, were kept constant. The biased disk was adjusted for each configuration to optimize the stability of the ECR ion source. Figure 3 shows the magnetic field configurations used for all the measurements presented in this paper. However, changing the minimum  $B$  field of the source changes the resonance zone volume. The resonance zone volume is about 40% smaller when the minimum  $B$  field is raised from 0.44 to 0.67 T.

The following sections summarize the results of three experimental series. In Sec. IV, the influence of rf power on the electron energy distributions and on the total x-ray flux is presented. In Sec. V, the x-ray spectra obtained using 28 GHz plasma heating are compared to spectra using 18 GHz plasma heating. In Secs. VI and VII, the source performance and the x-ray heat load into the cryostat are compared for single frequency operation at 28 GHz using a minimum  $B$  field of 0.67 T to double frequency operation using 18 and 28 GHz heating and a minimum  $B$  field of 0.45 T.

### IV. INFLUENCE OF THE MICROWAVE POWER ON THE ENERGY DISTRIBUTION OF THE X-RAY SPECTRA

X-ray spectra were measured for microwave power levels from 500 up to 7000 W using single frequency heating at

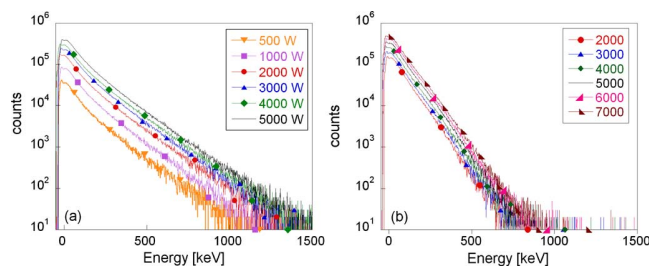


FIG. 4. (Color online) The bremsstrahlung spectra measured for a  $B_{\min}$  of 0.7 T (a) compared to a  $B_{\min}$  of 0.45 T (b).

28 GHz. The amount of x rays produced increases nearly linearly with power in both cases, but as can be seen from Figs. 4(a) and 4(b), increasing the microwave power for a given axial field configuration does not change the slope of the semilogarithmic plot. However, the x-ray spectra extend up to much higher energies for  $B_{\min}$  of 0.7 T compared to  $B_{\min}$  of 0.44 T. To compare x-ray spectra measured with different magnetic field configurations, the spectral temperatures defined in Refs. 4 and 6 have been determined [Figs. 5(a) and 5(b)]. For this purpose, a linear fit to the semilogarithmic plot is determined, and the reciprocal of the line's slope yields a spectral temperature ( $T_s$ ) in keV. This spectral temperature is a relative indication of the temperature of the hot electrons, not a direct measure of the temperature distribution of the hot electrons in the plasma.

As shown in Fig. 5, the spectral temperatures are nearly independent of the microwave power injected. This suggests that increasing the rf power mainly increases the plasma density, but does not (or very little) affect the energy distribution function. However, two or more slopes (temperatures) are needed to fit the semilogarithmic plot for higher minimum  $B$  fields, while the spectra obtained with a lower minimum  $B$  field can be fitted by one slope.

The higher spectral temperatures measured for high minimum  $B$  fields could suggest that the heating efficiency is higher for lower magnetic field gradients at the resonance zone. This finding is consistent with the simple heating models suggested by Jongen<sup>10</sup> in 1982 and by Koivisto<sup>11</sup> in 1999, which predict a more efficient acceleration process of the electrons when the resonance zone is crossed at a lower field gradient. This is also consistent with previously published results, which found that higher ion beam intensities can be extracted for higher minimum  $B$  fields.<sup>2,7</sup>

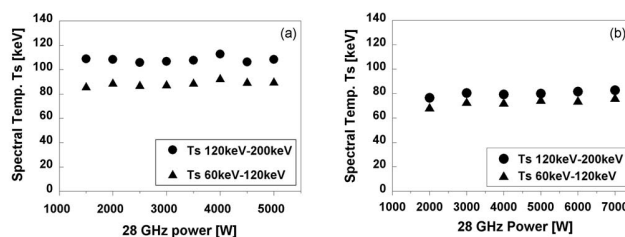


FIG. 5. The spectral temperatures (slope of the x-ray spectrum) remain nearly constant with increasing power, but are a strong function of the magnetic field gradient at the resonant zone. Shown are the spectral temperatures obtained by fitting the spectra for a  $B_{\min}=0.7$  T (a) and  $B_{\min}=0.45$  T (b).

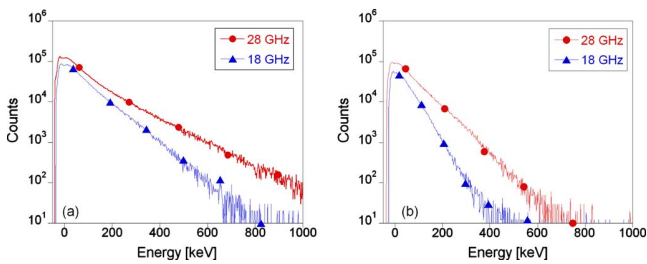


FIG. 6. (Color online) Comparison of the bremsstrahlung spectra for 28 GHz heating to 18 GHz heating at scaled fields with a  $B_{\min}/B_{\text{ECR}}$  of 0.70 (a) and 0.47 (b).

### V. COMPARISON OF 28 GHz HEATING WITH 18 GHz HEATING AT SCALED FIELDS AT $B_{\min}/B_{\text{ECR}}$ OF 0.70 AND 0.47 T

To test ECR scaling laws,<sup>12</sup> the bremsstrahlung spectra using single frequency heating at 28 GHz were compared to spectra obtained with 18 GHz. To ensure that the magnetic confinement, the magnetic field gradient, and the size of the resonance zone are identical, the magnetic fields (including the sextupole fields) were carefully scaled according to the ratio of 18/28. All other source parameters were kept constant.

For single frequency heating at 18 GHz, a similar trend in the x-ray spectra between the steep (low minimum  $B$  field) and shallow (high minimum  $B$  field) magnetic field gradients is observed. The spectrum extends to higher energies and has a higher spectral temperature for the higher  $B_{\min}$  (compare Fig. 6, blue curves). In addition, the slopes of the spectra do not change with increasing power. However, when the 18 GHz spectra are compared to the 28 GHz spectra using the same injected power and scaled magnetic fields, the latter spectra extend up to much higher energies and have higher spectral temperatures. This suggests that 28 GHz heating (or higher frequency heating, in general) is more efficient than lower frequency heating. This result is consistent with a model developed by Girard *et al.*,<sup>13</sup> which predicts higher mean electron energies for increased heating frequencies.

The development of a high energy tail in the electron energy distribution for the 28 GHz heated plasma can explain why the heated x-ray heat load from a 28 GHz heated plasma is much higher than what could be expected from the simple increase in electron density using the frequency scaling law.<sup>14</sup> Since the Ta shield and the plasma chamber walls become almost transparent for x rays above 300 keV, the high energy x rays are primarily responsible for heating the cryostat (see Sec. VII).

### VI. COMPARISON OF THE ION SOURCE PERFORMANCE AND X-RAY SPECTRA FOR AN AXIAL MAGNETIC FIELD PROFILE WITH A $B_{\min}$ OF 0.67 T AND 0.45 T

The goal of these measurements was to systematically compare the high charge state performance using a middle field of 0.45 T and a double frequency heating to single frequency heating using a middle field of 0.67 T. For the measurements presented in this paper, the source was operated

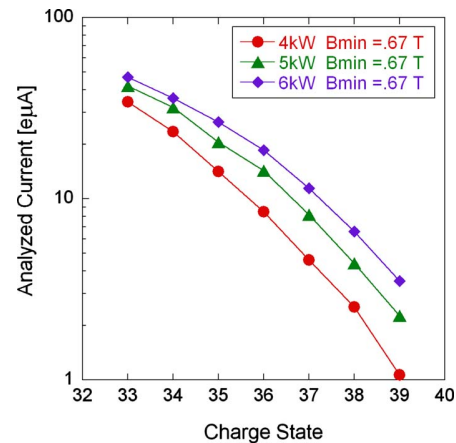


FIG. 7. (Color online) Xenon high charge state distributions for a single frequency heated plasma using a  $B_{\min}$  of 0.67 T ( $B_{\min}/B_{\text{ECR}}=0.67$ ) for 4, 5, and 6 kW of 28 GHz microwave power.

with xenon using oxygen as mixing gas, but similar trends have been found for other ion beams, such as argon, krypton, and uranium.

As shown by many authors before, for the single frequency heated plasma, the high charge state performance of the ECR ion source is strongly dependent on the minimum  $B$  field.<sup>7,14,15</sup> For VENUS, an optimum can be found for a minimum  $B$  field of 0.64–0.75 T,<sup>14</sup> which results into a magnetic field gradient at the resonant zone of about 0.08–0.07 T/cm. Good plasma stability can be achieved above microwave powers above 2 kW or a power density of 220 W/l. When the gas flow into the source is unchanged, the charge state distribution slowly shifts to higher charge states as more power is injected. For example, the peak of the xenon charge state distribution shifts from 30+ to 32+ using 4, 5, and 6 kW of 28 GHz microwave power. Figure 7 shows the increase in high charge state current for Xe<sup>33+</sup> to Xe<sup>39+</sup> for this power range.

For the double frequency heated plasma, the large frequency gap between 18 and 28 GHz requires a relatively low minimum  $B$  field to enable the coupling of 18 GHz into the plasma. A typical magnetic field profile used for a double frequency operation is shown in Fig. 3 (dashed line). For 28 GHz heating, this field profile results in a relatively steep magnetic field gradient on axis at the resonant zone (0.13 T/cm) with a  $B_{\text{ECR}}/B_{\min}$  ratio of 0.45. For 18 GHz heating, this profile results in a gentle magnetic field gradient (0.075 T/cm) with a  $B_{\text{ECR}}/B_{\min}$  ratio of 0.70 T. The combination of these two frequencies in this mode enables a very stable operation of the VENUS ECR ion source and is the preferred mode to use when the source is conditioned after maintenance. The optimum ratio of 28–18 GHz microwave power was found to be about 85% of 28 GHz to 15% of 18 GHz. If a higher percentage of 18 GHz power is coupled into the plasma, no performance improvements are observed, but the source plasma becomes slightly unstable.

Both modes of operation (single and double frequency) produce high intensity, high charge state ion beams. In fact, an identical high charge state performance can be achieved, but more microwave power is required for the double fre-

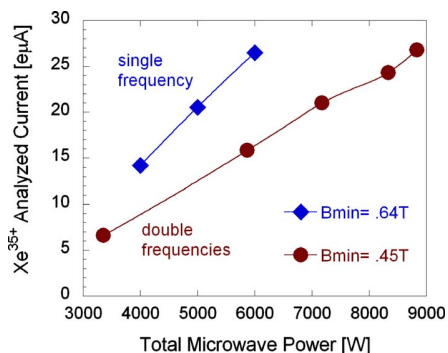


FIG. 8. (Color online) Comparison of the power dependence of  $\text{Xe}^{35+}$  production for a  $B_{\min}$  of 0.67 T (single frequency heating, 28 GHz) to a  $B_{\min}$  of 0.45 T (double frequency heating 28+18 GHz).

quency mode. For example, the same currents for  $\text{Xe}^{33+}$  to  $\text{Xe}^{39+}$  can be produced by using either 6 kW of 28 GHz microwave power in a single frequency mode (with  $B_{\text{ECR}}/B_{\min}=0.67$ ) or 7.5 kW of 28 GHz and 1.3 kW of 18 GHz power in a double frequency mode. As an illustration, Fig. 8 shows the dependence of  $\text{Xe}^{35+}$  with power for those two modes. As can be seen from the graphs, the source performance can be matched in each case, but more total power has to be used in the double frequency mode. If the x-ray energy spectra are compared for two tunes with identical high charge state, heavy ion currents, it is found that the numbers of counts in the low energy region of the spectra are very similar (Fig. 9). As expected (see Sec. IV), the x-ray spectrum extends up to much higher energies for the higher middle field. However, since lower energy electrons have the highest ionization cross section, the result suggests that a similar performance can be achieved if the warm electron density is matched in the two cases.

It is evident that in terms of power efficiency the gentle gradient is superior over the steep gradient double frequency mode. However, from an operational point of view, the double frequency mode with its steep gradient has clear advantages over the single frequency mode. Since the bremsstrahlung spectra for the steep gradient contain much fewer x-rays in the energy region above 400 keV (where the Ta shield around the plasma chamber is not effective), the re-

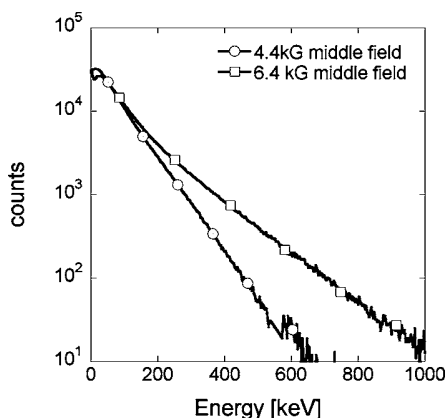


FIG. 9. The axial x-ray spectra for a  $B_{\min}$  of 0.44 T (8.8 kW power) in comparison to a  $B_{\min}$  field of 0.67 T (6 kW power). The Xe charge state distributions are nearly identical (Fig. 11).

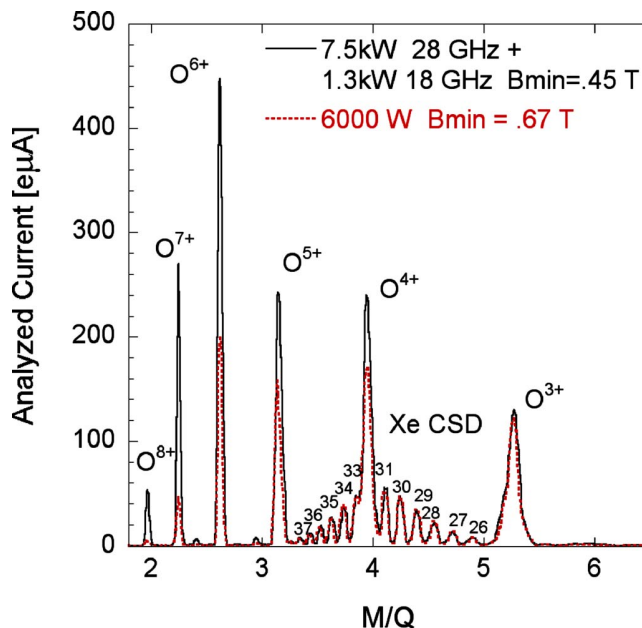


FIG. 10. (Color online) Charge state distribution (Xe+O) for the double frequency source and the single frequency heated source. The oxygen mixing gas charge state distribution is much more peaked toward the higher charge states for a  $B_{\min}$  of 0.45 T, which increases the total extracted current from the ECR source.

sulting heat load into the cryostat is much smaller (see Sec. VII). If the charge state distributions of the ion beams extracted for each mode are plotted on top of each other, the xenon spectra are remarkably similar (Fig. 10). However, the oxygen mixing gas spectra are very different for the two modes. In the double frequency mode, the oxygen spectra are clearly peaked on high charge states, while in the single frequency mode, the oxygen charge state distribution is much flatter. For example, in the case of oxygen 7+, only 40  $e\mu\text{A}$  are produced in the single frequency mode when the source is optimized for high charge state xenon ions, but 270  $e\mu\text{A}$  are produced in the double frequency mode. This shift in the mixing gas distribution is also reflected in an increase of total current when the source is switched from the single to the double frequency mode as the oxygen ions are shifted toward higher charge states. At the moment, we do not have an explanation for this phenomenon, but it has been experimentally observed for all heavy ions produced so far (Ar, Kr, Xe, and U).

## VII. HEAT LOAD INTO THE CRYOSTAT FROM BREMSSTRAHLUNG

The emitted bremsstrahlung, created by electron-ion collisions within the plasma volume and by electrons lost to the plasma chamber wall, adds a substantial heat load to the ion source cryostat. To better understand the amount of power absorbed in the cold mass under various tuning conditions, the heat load caused by x-ray absorption was measured in the VENUS source depending on coupled microwave power for the double and single frequency heated sources. The heat load was determined by comparing the temperature rise of the liquid helium when the helium reservoir was heated by a

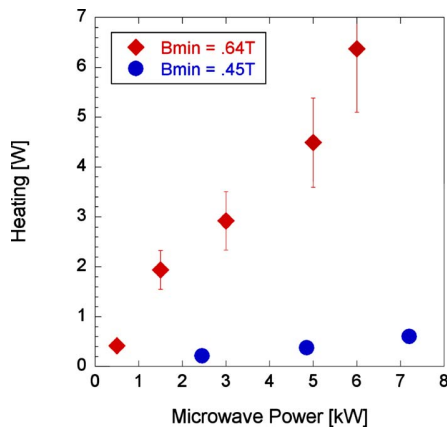


FIG. 11. (Color online) Heat load into the cryostat at minimum  $B$  fields of 0.64 and 0.45 T dependent on the injected microwave power. The error bar indicates the range of heat load depending on the discharge pressure and the accuracy of the measurement.

calibrated heater without plasma to the temperature rise observed when the source was operated at various microwave power levels. In Fig. 11, the heat load into the cryostat is plotted for a  $B_{\min}$  of 0.45 T and  $B_{\min}$  of 0.64 T. For a  $B_{\min}$  of 0.64 T, a heat load of about 1 W/kW was found, while for the double frequency heated source, the heat load was determined to be only 0.1 W/kW. The error bar indicates the range of heat load depending on the discharge pressure and the accuracy of the measurement. This big difference is caused by the high energy tail of the x rays present in the spectra for  $B_{\min}$  fields of 0.6 T and higher. Since the 2 mm Ta shield becomes transparent for x-ray energies above 400 keV, the shield loses its effectiveness at these energies, and the bulk of these x-rays produced is absorbed in the cold mass.

## VIII. CONCLUSION

A few conclusions can be drawn from the above measurements. A gentler magnetic field gradient at the resonant zone will result in a more efficient heating process and will lead to the generation of a hot electron tail in the electron energy distribution. This high energy tail is strongly affected by the ratio of  $B_{\min}/B_{\text{ECR}}$  and by the heating frequency. As expected, an ECR plasma heated with 28 GHz microwaves produces more x-rays than a plasma heated with 18 GHz microwaves if scaled fields are used and the mean electron temperature increases with frequency.

The high energy x-ray produced by 28 GHz heating using gentle magnetic field gradients at the resonant zone can-

not be effectively shielded by a few millimeters of Ta or other heavy-metal x-ray shields. Therefore, they can penetrate into the cryostat, where they are absorbed by the cold mass and add a substantial heat leak to the cryostat system. As the comparison for 18 and 28 GHz spectra using scaled magnetic fields show, this problem can be expected to be worse for fourth generation sources using microwave frequencies greater than 28 GHz. On the other hand, generation of this high energy tail can be avoided using double frequency heated plasma and a combination of steep gradients for the main heating frequency (e.g., 28 GHz) and gentle gradients for the second frequency (e.g., 18 GHz). Using higher total power, the performance of the source for gentler heating gradients can be matched, but with a much reduced heat load into the cryostat.

## ACKNOWLEDGMENTS

This work was supported by the Office of Energy Research, Office of High Energy and Nuclear Physics, Nuclear Physics Division of the U.S. Department of Energy under Contract No. DE AC03-76SF00098.

- <sup>1</sup>D. Leitner, D. S. Todd, M. L. Galloway, and C. M. Lyneis, *Journal of HEP&NP*, Chinese Physical Society 31, 1 (2006).
- <sup>2</sup>D. Leitner, C. M. Lyneis, T. Loew, O. Tarvainen, D. S. Todd, and S. Visostek, *Rev. Sci. Instrum.* **77**, 03A303 (2006).
- <sup>3</sup>C. Barue, M. Lamoureux, P. Briand, A. Girard, and G. Melin, *J. Appl. Phys.* **76**, 2662 (1994).
- <sup>4</sup>A. Girard, *Rev. Sci. Instrum.* **63**, 2676 (1992).
- <sup>5</sup>K. Bernhardt and K. Wiesemann, *Plasma Phys.* **24**, 867 (1982).
- <sup>6</sup>C. M. Lyneis, D. Leitner, O. Tarvainen, D. Todd, S. Virostek, T. Loew, and A. Heinen, *Rev. Sci. Instrum.* **77**, 03A342 (2006).
- <sup>7</sup>T. Nakagawa, Y. Higurashi, M. Kidera, T. Aihara, M. Kase, A. Goto, and Y. Yano, *Rev. Sci. Instrum.* **77**, 03A304 (2006).
- <sup>8</sup>G. Ciavola, S. Gammino, L. Celona, L. Torrisi, S. Passarello, L. Andó, M. Cavenago, A. Galatà, P. Spaedtke, K. Tinschert, R. Lang, R. Iannucci, R. Leroy, C. Barue, D. Hitz, P. Seyfert, H. Koivisto, P. Suominen, O. Tarvainen, H. Beijers, S. Brandenburg, D. Vanrooyen, C. Hill, D. Kuchler, H. Homeyer, J. Röhrich, L. Schachter, and S. Dobrescu, *Rev. Sci. Instrum.* **77**, 03A303 (2006).
- <sup>9</sup>S. Agostinelli, J. Allison, K. Amako, J. Apostolakis, H. Araujo, P. Arce, M. Asai, D. Axen, S. Banerjee, and G. Barrand, *Nucl. Instrum. Methods Phys. Res. A* **506**, 250 (2003).
- <sup>10</sup>Y. Jongen, C. Pirate, and G. Ryckewaert, *Proceedings of the 6th International Workshop on ECR Ion Sources*, Lawrence Berkeley National Laboratory, LBNL (1985), pp. 238–255.
- <sup>11</sup>H. Koivisto, *Rev. Sci. Instrum.* **70**, 2979 (1999).
- <sup>12</sup>R. Geller, *Electron Cyclotron Resonance Ion Source and ECR Plasmas* (Institut for Physics, Bristol, 1996).
- <sup>13</sup>A. Girard, C. Pernot, G. Melin, and C. Lécot, *Phys. Rev. E* **62**, 1182 (2000).
- <sup>14</sup>D. Leitner and C. M. Lyneis, *Proceedings of the Particle Accelerator Conference PAC'05* (American Physics Society, IEEE, Knoxville, 2005).
- <sup>15</sup>D. Hitz, A. Girard, G. Melin, S. Gammino, G. Ciavola, and L. Celona, *Rev. Sci. Instrum.* **73**, 509 (2002).

## APPENDIX A.III



## Time Evolution of Endpoint Energy of Bremsstrahlung Spectra and Ion Production from an Electron Cyclotron Resonance Ion Source

T. Ropponen\*, P. Jones, T. Kalvas, H. Koivisto, P. Peura, JYFL  
 O. Tarvainen, Los Alamos National Laboratory  
 P. Suominen, Prizztech Ltd / Magnet technology centre

### Abstract

Electron cyclotron resonance ion sources (ECRIS) [1] are used to produce high charge state heavy ion beams for the use of nuclear and materials science, for instance. The most powerful ECR ion sources today are superconducting. One of the problems with superconducting ECR ion sources is the use of high radio frequency (RF) power which results in bremsstrahlung radiation adding an extra heat load to the cryostat. In order to understand the electron heating process and timescales in the ECR plasma, time evolution measurement of ECR bremsstrahlung was carried out. In the measurements JYFL 14 GHz ECRIS was operated in a pulsed mode and bremsstrahlung data from several hundred RF pulses was recorded. Time evolution of ion production was also studied and compared to one of the electron heating theories. To analyse the measurement data a C++ program was developed. Endpoint energies of the bremsstrahlung spectra as a function of axial magnetic field strength, pressure and RF power are presented and ion production timescales obtained from the measurements are compared to bremsstrahlung emission timescales and one of the stochastic heating theories.

### DATA ACQUISITION SYSTEM AND DATA ANALYSIS

In order to study the time evolution of bremsstrahlung radiation JYFL 14 GHz ECRIS was operated in pulsed mode. The trigger signal for the RF pulse (leading edge) was synchronized with the data acquisition system. The duration of RF pulses launched into the plasma chamber was set to 1.76 seconds with 5.92 seconds off-time between consecutive pulses. The TTL type reference signal controls the RF switch which has a switching time of 40 ns (0–100 %) and provides timing signal for both the digital oscilloscope (used to record ion beam currents) and the digital signal processing unit (TNT2) [2]. The RF switch controls the 14 GHz oscillator signal to the klystron and a germanium detector was used to measure the radial bremsstrahlung spectra. TNT2 unit generates the data in binary format and a computer is used to store the data. Energy resolution of the germanium detector was 4.2 keV at peak energy of 444 keV and 7.4 keV at 1048 keV of  $^{152}\text{Eu}$  (shaping time was set to 2.0  $\mu\text{s}$ ).

The effect of the lead shielding around the collimator was also studied. It was noticed [3] that while adding

shielding around the lead collimator changed the count rates and also the shape of the bremsstrahlung spectra the timescales remained the same. The size of the collimator hole (from 0.5 mm<sup>2</sup> to 4 mm<sup>2</sup>) was not affecting the spectra and had a insignificant effect on the count rate which means that most of the bremsstrahlung events do not come through the collimator but around it.

Data analysis was done with a self-written C++ program. While the TNT2 unit discarded ADC overflows on-the-fly everything else was left untouched in the raw data. Pile-up events are rejected during the data sorting. Typical measurement time per one set of ECR parameters was 90 minutes resulting in data from over 700 RF pulses. To analyze the data 680 RF pulses are used in every data set i.e. bremsstrahlung data of 680 different RF pulses are combined in order to obtain enough statistics. Data from a background measurement is used during the data processing and the background spectrum is subtracted from the measurement data. The data sorting code produces a significant amount of data files. Both “RF on” and “RF off” phases are analysed and, for example, spectrum data is written with 2 ms time step (if the first 1500 ms of the RF pulse is used 750 spectra are produced for both “RF on” and “RF off” phases) and total count rate data integrated over the whole energy spectrum (from 15 keV to 600 keV) is generated throughout the whole length of the RF pulse. Typically a 1 GB of ASCII data is sorted in about 30 seconds. However, because the code also generates figures of all the sorted data as well as gif animations (time evolution of the bremsstrahlung spectrum in 2 ms steps) the sorting time per one data set can be significantly increased. A typical time to sort all the 21 data sets that were recorded during the measurements is between 9 and 10 h (Intel C2D E6600, 3 GB RAM). Using parallel computing to analyze the data would be relatively easy, however, the creation of animations can take 3 GB of memory, or even more, depending on the settings of the analysing program meaning that a normal desktop computer does not have enough memory to run parallel data analysing. Rejection of “bad” RF pulses has also been coded into the analyse program. This ensures that possible incomplete or erroneous RF pulses are discarded from the final analyse. The code has been written for *Unix/Linux* environments and requires *Gnu Scientific Library (GSL)*, *Gnuplot* and *Convert* in order to generate the graphs and animations.

\*tommi.ropponen@phys.jyu.fi

## KEY ISSUES IN THE RADIAL BREMSSTRAHLUNG TIME EVOLUTION MEASUREMENTS

The radial bremsstrahlung measurement from a magnetic pole was chosen because information about the electron energies was wanted and the charged particle flux at the pole is much greater than between the poles (radial port to the chamber). If the detector would have been located between the radial magnetic field poles (or in axial direction) it is believed that the bremsstrahlung events would originate partially from the plasma (movement of the charged particles in the plasma chamber) due to the fact that there is only about 1.5 mm of aluminium between the plasma chamber and surrounding air. Additional measurements with better collimation, measurements between the poles and axial measurements are planned to take place in the future with JYFL 14 GHz ECRIS.

In the radial bremsstrahlung measurements there are quite a few issues that need to be addressed in order to obtain good results. Firstly, the angular distribution of bremsstrahlung events must be understood. In the non-relativistic energies the angular distribution of bremsstrahlung radiation is “double cone like” meaning that bremsstrahlung radiation is produced in both the direction of movement of the incident electron as well as in the opposite direction [4]. The intensity of the bremsstrahlung emission is larger in the direction of propagation of the incident electron than in the opposite direction. However, the bremsstrahlung cone in the opposite direction becomes meaningful when a vast amount of electrons collide with the plasma chamber walls. The angle of incidence between the electrons and the plasma chamber walls affects the spatial distribution of the bremsstrahlung radiation. In ECRIS plasmas the velocity vectors of high energy electrons are typically oriented almost perpendicularly with respect to the magnetic field. This causes the solid angle, into which bremsstrahlung is emitted, to be large on each magnetic pole. Secondly, the bremsstrahlung photons interact with the matter over a long distance (usually several tens of millimeters) and the scattering processes play an important role before the photon can be detected in the detector crystal. It is possible that a photon changes its path significantly in the media and loses therefore its energy. Because a typical ECRIS uses a sextupole structure for the radial magnetic field, it is understood that the bremsstrahlung radiation originating from all of the six magnetic poles contributes to the measurement that is done in the proximity of one of the six poles. Thirdly, the collimator in radial measurements should be located as close to the detector as possible or if the collimator is located close to the plasma chamber of an ECRIS it should cover basically the whole ECRIS surface which is in the solid angle of the detector.

In the measurements presented in this article a collimator close to the ECRIS was used. Lead plates were used to improve the shielding around the collimator. The amount of the shielding as well as the collimator opening was studied ECRIS Plasma Physics and Techniques

along with the time evolution of bremsstrahlung emission and ion production time measurements. The collimator aperture had an insignificant effect on the spectra: the count rate at the germanium detector was basically the same with open and closed collimator. The shielding around the collimator, however, plays an important role in the shape of the spectra. This can be seen from Figure 1 a) where the steady state spectra of argon plasma is presented with two shielding geometries (the original shielding had less lead plates than the latter shielding). There is a clearly visible “hump” at the energies of 175–375 keV in the spectrum that is recorded with the original collimator/shielding geometry. Presumably, the curve with the “hump” is closer to the real shape of the spectra than the curve without any “hump” because the high energy part of the spectra is not attenuated so much. Adding lead plates around the collimator absorbs the higher energy electron population. However, the lower energy part of the spectra is not affected very much while adding shielding next to the collimator as can be seen from Figure 1 a). This could be a result from a situation where the lower energy part of the spectra is coming through a thinner part of the lead plate shielding (on the edges of the shielding) or partly through the ECR coil structure and therefore remains relatively unchanged. The size of the “hump” for different source parameters (argon plasma) is presented in the subfigures b), c) and d) of Figure 1. In subfigure a) the upper curve at 250 keV represents the original shielding and collimator aperture and the lower curve represents the situation after the changes. In b) and d) at 250 keV: the uppermost curve – coil currents of 550/550 A or 690 W, the middle curve – 500/500 A or 500 W and the lowest curve – 470/470 A or 300 W. Changing the neutral gas pressure does not affect the steady state count rate very much and all the curves overlap (subfigure c). This means also that the “hump” remains unchanged while the pressure is varied from  $1.5 \cdot 10^{-7}$  mbar to  $3.5 \cdot 10^{-7}$  mbar. However changing the axial magnetic field strength (subfigure b) or RF power (subfigure d) affects the total count rate integrated over the energies from 15 keV to 600 keV. The height of the “hump” (in relative counts / 2 ms) can be compared to the maximum height of the spectra (lower characteristic lead peak). These values are presented in Table 1 from which it can be seen that increasing the axial magnetic field strength (lowering the gradient) increases the “hump”/max (H/M) relation by over 10 percent. While the RF power is increased the H/M relation increases again 10 percent. The “hump” is growing while magnetic field gradient is lowered or RF power is increased meaning that the amount of hot electrons is increased inside the ECRIS plasma chamber. It has been reported that the effect from increasing the magnetic field (decreasing the distance between the resonances) is comparable to increasing the RF power in terms of heating efficiency [5].

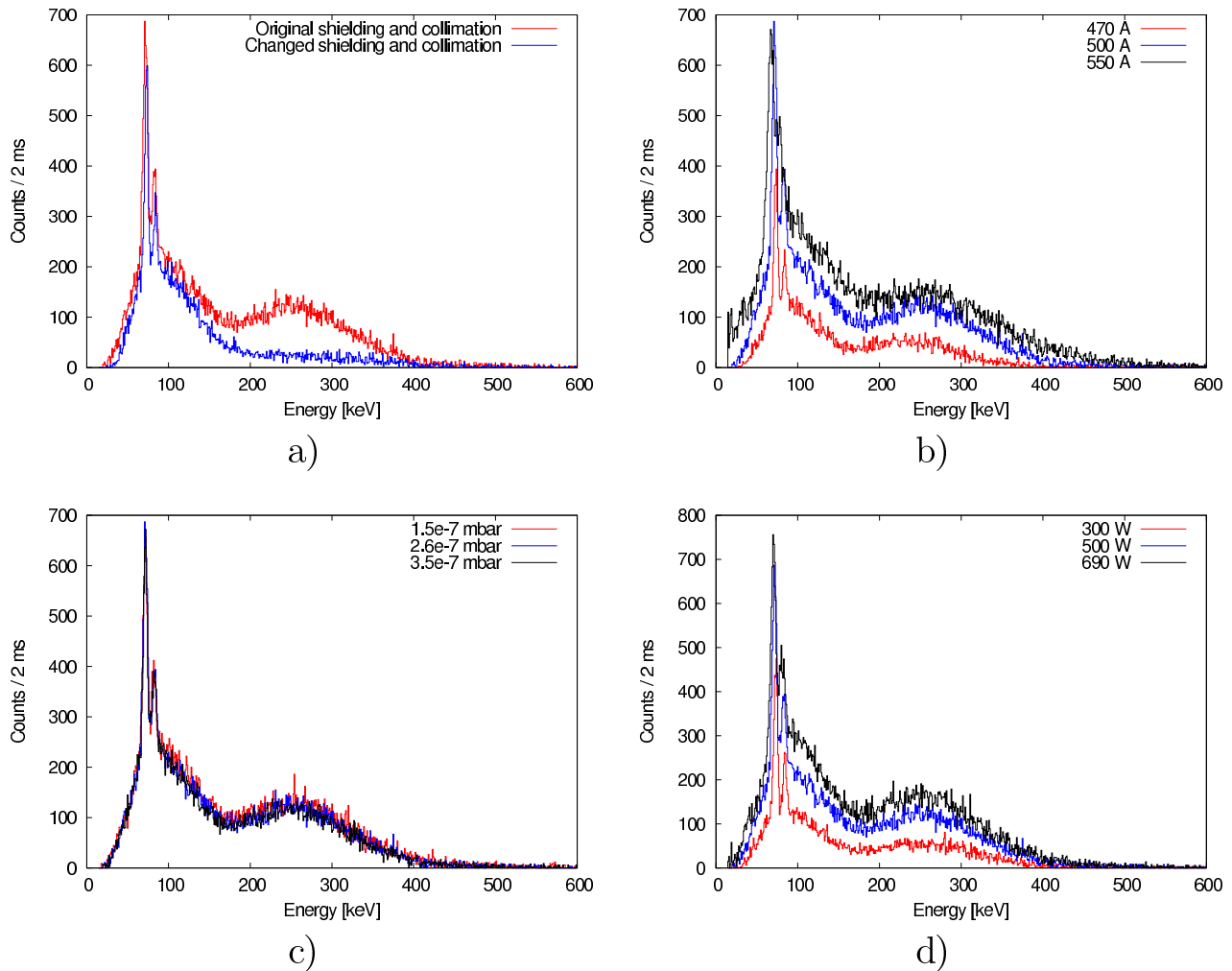


Figure 1: Steady state spectra of argon plasma in a time window of 1500–1502 ms from the leading edge of the RF pulse. a) different shielding and opening of the collimator, b) as a function of axial magnetic field strength, c) as a function of neutral gas pressure, d) as a function of RF power.

## EXPERIMENTAL RESULTS

The time evolution of ECR bremsstrahlung emission has been presented as a function of the axial magnetic field, neutral gas pressure and RF power in the references [3] and [6]. The latter includes also the time evolution of argon ion production from the beginning of the RF pulse with some argon charge states. In this section the time evolution of the endpoint energy of the bremsstrahlung emission spectra is presented as a function of the axial magnetic field strength, neutral gas pressure and RF power. The time evolution of oxygen and argon ion production is also presented during the whole RF pulse and the timescales are compared to the bremsstrahlung emission timescales.

ECRIS Plasma Physics and Techniques

### *Endpoint energy of the bremsstrahlung spectra as a function of axial magnetic field strength, neutral gas pressure and RF power*

Table 2 lists the endpoint energies with different ECRIS parameters for argon plasma. The endpoint energies in the steady state phase has been calculated using the following method: 5 % of the maximum count rate in the spectra (75 keV characteristic peak of lead) between times of 1500 and 1502 ms is used as a threshold value. When the average of nine consecutive count rates (each corresponding a single 1 keV energy window) in the aforementioned time window drops below the threshold the median energy corresponding to these nine count rates is defined as the endpoint energy of the spectrum. This is done in order to decrease the effect of statistical behaviour of the count rates.

With argon plasma the endpoint energy of the bremsstrahlung spectra is increasing rapidly when the axial magnetic field gradient is lowered.  $B_{\min}$  of 0.321 T results

Table 1: Relative count rate at the middle of the “hump” divided by the maximum count rate of the spectra (lower characteristic lead peak) with different ECRIS parameters. Steady state spectra at time window 1500-1502 ms are used (see Figure 1).

	470 A	500 A	550 A	300 W	500 W	690 W
Max / “hump”	13.5 %	18.2 %	23.7 %	12.2 %	18.0 %	22.5 %

Table 2: Endpoint energies of argon bremsstrahlung spectra between 1500–1502 ms from the RF power triggering (see Figure 1) with different JYFL 14 GHz ECRIS settings.

Argon plasma			
$B_{inj} / B_{ext}$	1.945/0.901 T	2.011/0.946 T	2.111/1.019 T
Endpoint energy	311 keV	364 keV	417 keV
Pressure	$1.5 \cdot 10^{-7}$ mbar	$2.6 \cdot 10^{-7}$ mbar	$3.5 \cdot 10^{-7}$ mbar
Endpoint energy	372 keV	364 keV	363 keV
RF power	300 W	500 W	690 W
Endpoint energy	338 keV	364 keV	375 keV

in 311 keV and endpoint energies of 364 keV and 417 keV are measured for  $B_{min}$  of 0.346 and 0.388 T, respectively. The total increase of the endpoint energy is roughly 34 % while the  $B_{min}$  increases less than 20 %.

Increased pressure of neutral argon gas has almost no effect on the endpoint energy. Corresponding endpoint energies are: 372 keV ( $1.5 \cdot 10^{-7}$  mbar), 364 keV ( $2.6 \cdot 10^{-7}$  mbar) and 363 keV ( $3.5 \cdot 10^{-7}$  mbar). The total decrease of the endpoint energy is about 2 % while the pressure is varied about 130 %.

Using an RF power of 300 W results in endpoint energy of 338 keV and energies of 364 and 375 keV are recorded with RF powers of 500 and 690 W, respectively. An increase of RF power by a factor of 2.3 results in an endpoint energy increase of about 11 %.

### Timescales of oxygen and argon ion production

Timescales of ion production were measured along with the bremsstrahlung emission with JYFL 14 GHz ECRIS. In the ion production measurements both oxygen and argon plasma were used and the results are presented here (for detailed time evolution of argon ion production see [6]). Operation parameters for the ECR for both oxygen and argon plasmas are presented in Table 3. During the measurements the ion source was tuned to  $O^{7+}$  (110  $\mu A$ ) or to  $Ar^{9+}$  (117  $\mu A$ ) in CW mode. The sampling rate of the oscilloscope (250 ks/sec) was too low in order to use averaging over the noise period and therefore, the ion current data is averaged over 20 consecutive measurement points in order to decrease the amount of noise which was observed at a frequency of 5 MHz (the source for this remained unknown).

Figure 2 illustrates the ion currents during the whole RF pulse. The curves at 1500 ms are the following: the uppermost curve – total count rate of bremsstrahlung events, the second highest curve –  $O^{7+}$ , the middle curve –  $O^{5+}$ , second lowest curve –  $O^{3+}$  and the lowest curve –  $O^{2+}$ . With charge states of 2+ and 3+ a so called preglow effect is seen during the first 4–7 ms. Maximum ion current of  $O^{2+}$  during the preglow peak is about 200  $\mu A$  while the steady state current is about 35  $\mu A$ . This means that during the preglow there is a boost of about 470 %. With  $O^{3+}$  the boost at the preglow maximum is 275 % (225  $\mu A$ ) compared to the steady state current of 60  $\mu A$ .

The steady state of bremsstrahlung emission is reached at around 600 ms (see the vertical line in Figure 2). If short RF pulses (around 4 to 7 ms) were used the production of lower charge states of oxygen ( $O^{2+}$ ,  $O^{3+}$ ) could be increased while the amount of bremsstrahlung radiation would still be lower than in steady state phase. From Figure 2 it is also seen that the lower charge states like  $O^{2+}$  and  $O^{3+}$  start to build up before  $O^{5+}$  and the highest charge state presented ( $O^{7+}$ ) reaches the steady state current around 500 ms.

Figure 3 illustrates the ion currents of the whole RF pulse can be seen in the case of argon plasma. A vertical line is located at 275 ms to mark the time when steady state of the bremsstrahlung production is reached. The following curves can be distinguished at 1500 ms: the uppermost curve – total bremsstrahlung count rate, the second highest curve –  $Ar^{10+}$ , the second lowest curve –  $Ar^{11+}$  and the lowest curve –  $Ar^{6+}$ . The lowest charge state ( $Ar^{6+}$ ) starts to rise at 5 ms and the maximum of the preglow peak is located around 8 ms (preglow peaks were also observed with argon charge states of 5+, 7+ and 8+ and the data for these is presented in [6]). The maximum of the ion current in the preglow peak of  $Ar^{6+}$  is about 75  $\mu A$  while the steady state ion current is 34  $\mu A$  (factor of 2.2 difference). The higher charge states (10+, 11+) start to rise when roughly 10 ms has elapsed from the launching the RF power into the plasma chamber. Preglow peak is not observed with these higher charge states because the ion source was tuned to

Table 3: Magnetic field strengths of the JYFL 14 GHz ECRIS in ion production measurements, the corresponding resonance lengths in axial direction, neutral gas pressures and RF powers.

Plasma	$B_{inj}$	$B_{min}$	$B_{ext}$	$\nabla B_{inj}^{res}$	$\nabla B_{ext}^{res}$	$d_{res}$	Pressure	RF power
Oxygen	2.026 T	0.353 T	0.962 T	6.038 T/m	5.663 T/m	112.6 mm	$4.3 \cdot 10^{-7}$ mbar	745 W
Argon	1.992 T	0.338 T	0.932 T	6.271 T/m	5.815 T/m	118.8 mm	$4.2 \cdot 10^{-7}$ mbar	515 W

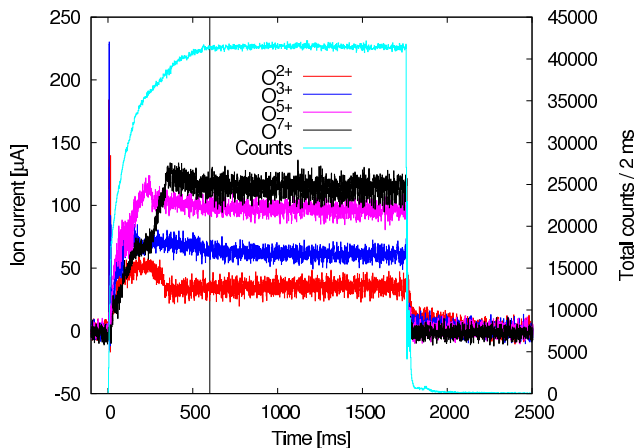


Figure 2: Time evolution of oxygen ions and bremsstrahlung count rate during the whole RF pulse.  $T=0$  corresponds to the leading edge of the RF pulse. A vertical line at 600 ms marks the time when the steady state of bremsstrahlung count rate is reached.

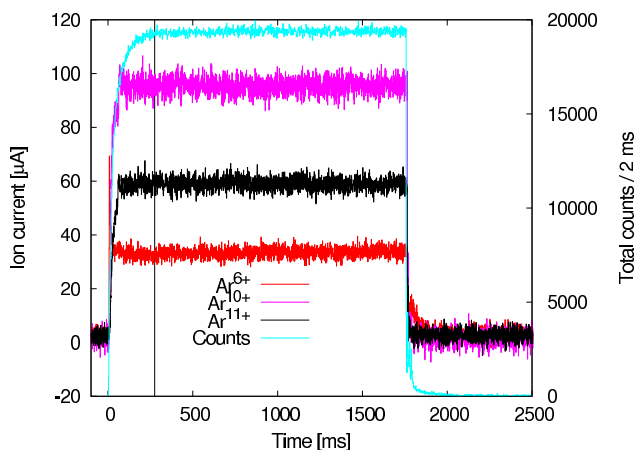


Figure 3: Time evolution of argon ions and bremsstrahlung count rate during the whole RF pulse. A vertical line at 275 ms marks the time when the steady state of bremsstrahlung count rate is reached.

$\text{Ar}^{9+}$ . Similar behaviour has been observed in [9].

With argon the ion currents have saturated well before the bremsstrahlung emission saturates. Ion saturation times are roughly 50 ms for  $\text{Ar}^{6+}$  and about 65 ms for the two higher charge states. The times are significantly lower for argon than oxygen plasma (hundreds of milliseconds, see Figure 2). With oxygen plasma the oxygen atoms can be

ECRIS Plasma Physics and Techniques

deposited on the plasma chamber walls and can be released during particle bombardment of the plasma and therefore the time to reach steady state with oxygen plasma could be longer than with argon plasma. However, this needs to be confirmed with additional measurements.

Ion production during the preglow pulse was also studied with argon plasma as a function of the RF power. In this measurement set JYFL 14 GHz ECRIS was tuned with same setting as in the previous measurement and the ion current of  $\text{Ar}^{6+}$  was observed while varying the RF power from 180 W to 690 W. The following steady state currents for different RF powers were measured:  $34 \mu\text{A}$  (180 W),  $33 \mu\text{A}$  (300 W),  $27 \mu\text{A}$  (500 W),  $26 \mu\text{A}$  (600 W) and  $29 \mu\text{A}$  (690 W). The time evolution of  $\text{Ar}^{6+}$  ion current for the first 20 ms is presented in Figure 4. At the “peak” the curves are: the lowest curve – 180 W, the second lowest – 300 W, the middle – 600 W, the second highest – 500 W and the highest curve – 690 W. The ion current starts to rise a bit after 4 ms with the two lowest RF powers and with the three highest RF power the rise starts approximately one millisecond later. Reason for this remains unknown. With 180 W there are not a clear maximum in the ion current but with higher RF powers the maximum is well defined. The steady state ion currents are relatively close to each other (from 34 to  $26 \mu\text{A}$ ), but the maximum of the preglow peak rises as the RF power is increased. Lowest “peak” current of less than  $45 \mu\text{A}$  is recorded with 180 W and the use of an RF power of 690 W results in the ion current of about  $95 \mu\text{A}$ . Changing the RF power with a factor of 3.8 changes the ion current maximum with a factor of 2.1. After about 20 ms the ion currents are in a steady state phase.

## TIMESCALE COMPARISON - MEASUREMENTS VERSUS STOCHASTIC HEATING THEORY

As shown, the steady state of bremsstrahlung count rates is reached in 275 ms with argon plasma and in 600 ms with oxygen plasma. A model by Sergeichev *et al.* [10] is used here to compare the observed timescales to the theory of stochastic electron heating. The model requires information about the magnetic field minimum ( $B_{min}$ ), microwave power (amplitude of electric field), microwave frequency and the bandwidth of the microwave. According to the heating model the transverse electron energy in the stochastic acceleration regime can be written as

$$W_{\perp}^0 [eV] = DE_0^{\frac{8}{7}} t^{\frac{2}{7}}, \quad (1)$$

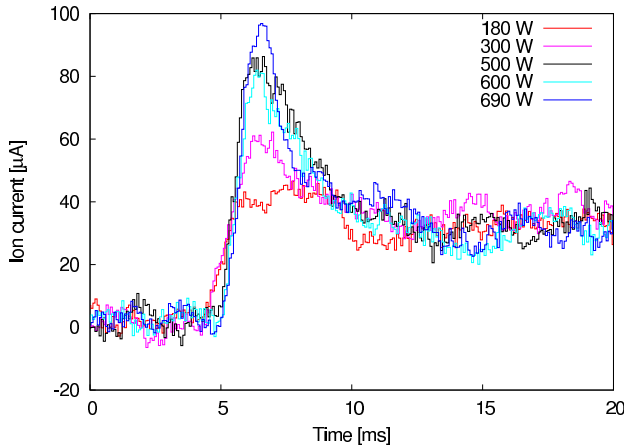


Figure 4: Time evolution of  $\text{Ar}^{6+}$  during the first 20 ms of the RF pulse with different RF powers.

where  $D$  is defined as

$$D = \left( \frac{\Delta\omega}{\omega_0} \frac{B_c}{B_c - B_0} \right)^{\frac{4}{7}} \left( \frac{2e}{m} \right)^{\frac{1}{7}} k^{-\frac{3}{7}} \pi^{-\frac{2}{7}}. \quad (2)$$

In these equations  $E_0$  is the electric field amplitude at the resonance,  $t$  time,  $\Delta\omega$  frequency bandwidth,  $\omega_0$  microwave frequency,  $B_c$  resonant magnetic field,  $B_0$  B-minimum and  $k$  is derived from the second order axial magnetic field approximation. In the case where the coil currents in JYFL 14 GHz ECRIS are 500/500 A  $B_0 = 0.35$  and  $k$  is about 147. The klystron of the 14 GHz ECRIS is tuned for a frequency of 14.1 GHz and the reported bandwidth according to the manual is at least 85 MHz. The RF power of 500 W is used thus, the amplitude of the electric field can be calculated approximately using Poynting vector to be about 9.1 kV/m in an empty chamber with plasma chamber quality factor of 1. The stochastic heating model of equation 2 does not explicitly take into account that the resonance field shifts to higher B field as the electrons gain energy (relativistic effect). This shortcome was treated by inserting the functional dependence of the resonance field on the electron energy i.e.  $B_c = B_c(W)$  into equation 2 and solving it numerically with a time step of 0.5 ms.

If the value of  $k$  is changed from 147 to 139 (corresponding to coil currents of 550/550 A) the maximum energy in stochastic heating according to Sergeichev ( $Q=1$ ) increases about 0.3 keV (from 14.4 to 14.7 keV). With  $Q=5$  (the amplitude of the electric field is multiplied by 5) the lower value of  $k$  (139) produces 1.8 keV higher energy (82.5 keV versus 80.7 keV) than the higher  $k$  value after 1500 ms of heating time. Therefore it can be stated that the value of  $k$  does not have a major impact on the final maximum energy.

Comparison of timescales between the theory (after Sergeichev) and measurements is presented in Figure 5. Just before 200 ms the lowest curve is after Sergeichev's theory with plasma chamber quality factor of 1, the second lowest curve is theory with  $Q=3$ , the middle curve is theory with  $Q=5$ , the second highest curve is endpoint en-

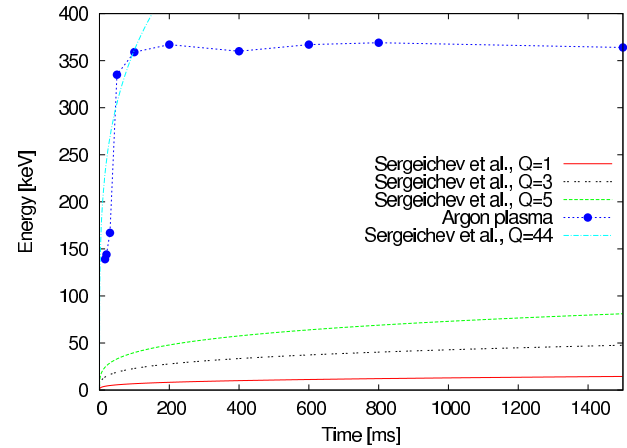


Figure 5: Comparison between the theory of stochastic heating and the endpoint energies measured with JYFL 14 GHz ECRIS. Theoretical curves plotted with different plasma chamber quality factors.

ergy data from measurements with argon (at given time) and the uppermost curve is calculated from the theory using  $Q=44$ . With this very high quality factor the first 100 ms seem to fit relatively well to the measured data, however, after that the  $Q=44$  curve overshoots the measurement values rapidly. This could be due to the fact that the theory does not take into account the limit of stochastic heating, which depends on the group velocity of the EM waves in the plasma. Therefore, the electron energy calculated from the theory does not exhibit saturation behaviour, clearly observed in the measurements, and quality factor  $Q=44$  becomes obsolete after the saturation has been reached. It is suggested that in an empty chamber the quality factor can be in the order of tens or hundreds of thousands [11] and after the plasma has been ignited the quality factor drops down and is around 3 [5]. During the plasma breakdown the quality factor changes rapidly as a function of plasma density (permittivity) but the timescales for this time evolution of quality factor remains unknown. However, another explanation must also be considered. The maximum value of radial magnetic field in the chamber walls of JYFL 14 GHz ECRIS is 0.85 T which corresponds to resonance field for electrons which have energy around 360 keV. The reached steady state behaviour, observed for example in Figure 5, could be a result from a fact that the resonance region has moved into plasma chamber walls and higher energy electrons do not have a resonance zone anymore inside the chamber.

Timescales can be roughly extracted from Figure 5 which presents the time evolution of endpoint energy for the measurement data. The electron energy after 200 ms is about 8 keV according to the stochastic heating theory with plasma chamber quality factor of 1. With  $Q=3$  the energy is 27 keV and with  $Q=5$  the energy is 48 keV at 200 ms. The endpoint energy for argon plasma, using the same 5 % threshold as before, is 367 keV at 200 ms. It

is clear that there are discrepancies between the theory and the measurements. If the quality factor  $Q$  is changed the energies according to the theory will increase. However, the timescales from the theory do not match with the measurements: saturation of the endpoint energies is much faster in the measurements than according to the theory where the energies do not saturate at all. Sergeichev's theory does not include any electron energy losses caused by the friction between neutral particles and electrons [10]. These phenomena will, however, decrease the electron energies and some other explanation is needed to explain the measured behaviour.

Different theoretical model for phase regime heating (the electron remains in the accelerating phase all the time) is also presented in [10]. This theory, as expected, generates very high energies in very short time periods. Using the operation parameters from JYFL 14 GHz ECRIS this phase regime theory generates over 1 MeV electrons in 10 ms. These timescales and energies imply that the stochastic heating model needs some corrections (distance between the resonance points, stochastic heating limit) to be accurate and consistent with the measurements and on the other hand rules out the possibility of phase regime heating in an ECR ion source if several resonance crossings are taken into account. This is supported by simulation results reported in reference [12].

## DISCUSSION

It is noticed that the steady states for endpoint energies are reached at around 200 ms with argon plasma (see Figure 5). Pressure of the neutral gas inside the ECRIS plasma chamber does not affect the endpoint energy very much. However, the highest endpoint energy (372 keV) is recorded with the lowest neutral gas pressure ( $1.5 \cdot 10^{-7}$  mbar). This could be a result from the collision frequency: with the lowest pressures the collision frequency between the particles in the plasma is lowest resulting in longer heating times of electrons before they are collided with other particles or scattered into the radial loss cone of the magnetic field. Changing the RF power from 300 W to 690 W results in an increase of 11 % in endpoint energy. The magnetic field gradient plays, however, an important role in the evolution of endpoint energies. Increasing the axial magnetic field strength (lowering the magnetic field gradient) results into significant changes in the endpoint energy: from 311 keV to 417 keV. Therefore it is stated that the endpoint energy of a bremsstrahlung spectra is dependent on the magnetic field configuration ( $B_{\min}$  and  $\text{grad}B$ ) while the effect of the neutral gas pressure and RF power is very small. It is worth of note that the magnetic field generated by the permanent magnets of the JYFL 14 GHz ECRIS is 0.85 T on the magnetic poles. As the electrons gain energy their resonance field shifts towards higher values. Magnetic field value of 0.85 T corresponds to an energy of about 360 keV, which is close to observed endpoint energy of the bremsstrahlung spectra (see e.g. Figure 5).

ECRIS Plasma Physics and Techniques

Therefore, it is plausible to claim that the magnetic field profile (and strength) in radial direction may limit the observed energies.

Production times of oxygen and argon ions were also studied and the time evolution of bremsstrahlung emission was compared to times to reach steady state ion currents. A so called preglow effect was observed with  $O^{2+}$  and  $O^{3+}$  ions. The maximum of the preglow peak ion current in the case of  $O^{2+}$  was about 5.7 times the steady state ion current, and with  $O^{3+}$  there was a difference by a factor of 3.75. With argon plasma the preglow was observed with  $Ar^{6+}$  (and with charge states 5+, 7+ and 8+, see reference [6]). Comparing the steady state of  $Ar^{6+}$  to the peak current there is a difference by a factor of 2.2. As expected, the higher charge states build up slower than the lower charge states with both oxygen and argon plasma. The differences in reaching the steady currents with oxygen and argon charge states might be due to more reactive oxygen which is deposited on the plasma chamber walls between the RF pulses and released by ion bombardment during the ignition of the plasma.

The preglow peaks appear several hundreds of milliseconds before the bremsstrahlung emission count rate reaches the steady state. This means that if short millisecond region RF pulses are used bremsstrahlung radiation levels could be decreased relatively more than the ion current, however this needs to be verified with measurements. Typical decay times for a bremsstrahlung spectra from JYFL 14 GHz ECRIS are around tens of milliseconds [3]. Therefore, using an ECR ion source to produce medium (or high, depending on the ECRIS tuning) charge states in a pulsed mode would require RF pulses with a duty factor around 20 % which is very low in terms of continuous ion beam.  $O^{2+}$  ion current saturates around 340 ms,  $O^{3+}$  and  $O^{5+}$  approximately at 700 ms and with  $O^{7+}$  it takes nearly 600 ms before the steady state current is reached. The bremsstrahlung count rate reaches the steady state around 600 ms meaning that the ion currents are reaching the steady state before or at same time as the bremsstrahlung emission saturates. With argon plasma the steady state time of the ion currents and the bremsstrahlung emission have a clear difference:  $Ar^{6+}$  saturates around 30 ms while  $Ar^{10+}$  and  $Ar^{11+}$  reaches the steady state ion current after about 70 ms has elapsed from the leading edge of the RF pulse and the bremsstrahlung emission saturates around 275 ms.

Similar behaviour for the ion current rise times with fast sputter sample and gas valve using neon, argon and gold ions have also been reported [13]. However, the ion rise times measured in [13] have been recorded while the ECRIS is in a steady state operation. Rise time for  $^{20}Ne^{2+}$  was 1.6 ms and for  $^{20}Ne^{8+}$  a rise time of 38.3 ms was measured at 407 W of RF power. In the ion production measurements presented in this article the rise time for  $O^{2+}$  is around 5 ms and for  $O^{7+}$  the rise time is roughly 20 ms. There are fundamental differences between the measurement setups used with JYFL 14 GHz ECRIS and with ATLAS ECR I (10 GHz). In the measurements presented in

this article, and in the references [3, 6], the ECR plasma was ignited during the RF pulse and turned off with the trailing edge of the RF pulse while the ATLAS ECR I was running in a steady state region with a buffer gas plasma and a fast gas valve or fast sputter sample was used.

When the argon ion production is studied as a function of the RF power it is observed that the maximum ion current of the preglow peak increases with the RF power while the steady state current of  $\text{Ar}^{6+}$  remained within a few microamperes. The preglow peak starts to rise after about 4 ms (180 W, 300 W) from the launching of the RF power and if higher RF powers (500 W, 600 W, 690 W) are used the rise point is moved to about 5 ms. No explanation for this behaviour has been found yet.

If the stochastic heating theory of Sergeichev *et al.* is compared to the time evolution of endpoint energies measured with JYFL 14 GHz ECRIS it is clear that the theory predicts (with  $Q=1$ ) energies that are several times lower than the measured endpoint energies are. If the value of  $Q$  is increased the energies predicted by the theory will increase but with relatively small  $Q$  values the theoretical curves lie at significantly lower energies than the measured values. If  $Q=44$  is used to calculate the electron energy from the theory the first 100 ms are in unison between the measured and theoretical values. After 100 ms the theoretical curve significantly overshoots the measured values. In addition, the timescales from the theory are significantly slower than the timescales obtained from the measurements when a reasonable value for  $Q$  is used. In a steady state region the endpoint energies extracted from argon plasma are about 360 keV. Because the timescales that the theory is predicting have a clear discrepancy to the measurement results, it seems that the theory needs some refinement like, for example, adding the stochastic heating limit into the theory.

## ACKNOWLEDGMENTS

This work has been supported by the EU 6th Framework programme "Integrating Infrastructure Initiative - Transnational Access", Contract Number: 506065 (EURONS), by the Academy of Finland under the Finnish Centre of Excellence Programme 2006-2011 (Nuclear and Accelerator Based Physics Programme at JYFL) and US Department of Energy under the contract DE-AC52-06NA25396. T. Ropponen would also like to acknowledge financial support from the Graduate School in Particle and Nuclear Physics. The gamma spectroscopy group of JYFL and the use of germanium detector from GAMMAPOOL resource is gratefully acknowledged.

## REFERENCES

- [1] R. Geller. *Electron cyclotron resonance ion sources and ECR plasmas*. Taylor & Francis, 1996.
- [2] L. Arnold, R. Baumann, E. Chambit, M. Filliger, C. Fuchs, C. Kieber, D. Klein, P. Medina, C. Parisel, M. Richer, ECRIS Plasma Physics and Techniques
- [3] C. Santos and C. Weber. TNT digital pulse processor. *IEEE Trans. Nucl. Sci.*, 53:723–728, 2006.
- [4] T. Ropponen, O. Tarvainen, P. Jones, P. Peura, T. Kalvas, P. Suominen and H. Koivisto. The effect of magnetic field strength on the time evolution of bremsstrahlung radiation created by an electron cyclotron resonance ion source. Submitted to *Nucl. Instr. and Meth. A*, 2008.
- [5] H. W. Koch and J. W. Motz. Bremsstrahlung cross-section formulas and related data. *National bureau of standards*, 31:920–956, 1959.
- [6] Y. Jongen. E.C.R. electron acceleration. In *Workshop on the Sixth International ECR Ion Source*, pages 238–255, Berkeley, California, 1985. Lawrence Berkeley Laboratory.
- [7] T. Ropponen, O. Tarvainen, P. Jones, P. Peura, T. Kalvas, P. Suominen and H. Koivisto. Time evolution of bremsstrahlung and ion production of an electron cyclotron resonance ion source. To be submitted.
- [8] V. M. Povyshev, A. A. Sadovoy, V. P. Shevelko, G. D. Shirkov, E. G. Vasina and V. V. Vatulin. Electron-impact ionization cross sections of H, He, N, O, Ar, Xe, Au, Pb atoms and their ions in the electron energy range from the threshold up to 200 keV. Communication of the Joint Institute for Nuclear Research, Dubna, 2001.
- [9] A. Li-Scholz *et al.*. *Atomic data and nuclear data tables*. 36, 1987.
- [10] T. Thuillier, T. Lamy, L. Latrasse, I.V. Izotov, A. V. Sidorov, V. A. Skalyga, V. G. Zorin and M. Marie-Jeanne. Study of pulsed electron cyclotron resonance ion source plasma near breakdown: The preglow. In *Proceedings of the 12<sup>th</sup> international conference on ion sources*, 79, 02A314. *Rev. Sci. Instr.*, 2008.
- [11] K. F. Sergeichev, D. M. Karfidov and N. A. Lukina. Electron cyclotron resonance acceleration of electrons to relativistic energies by a microwave field in a mirror trap. *Plasma Physics Reports*, 33:455–473, 2007.
- [12] F. Consoli, S. Barbarino, L. Celona, G. Ciavola, S. Gammino and D. Mascali. Investigation about the modes in the cylindrical cavity of an ECR ion source *Radiation Effects and Defects in Solids*, 160:467–475, 2005.
- [13] T. Ropponen, O. Tarvainen, P. Suominen, T. K. Koponen, T. Kalvas and H. Koivisto. Hybrid simulation of electron cyclotron resonance heating. *Nucl. Instr. and Meth. A*, 587:115–124, 2007.
- [14] R. C. Vondrasek, R. H. Scott, R. C. Pardo and D. Edgell. Techniques for the measurement of ionization times in ECR ion sources using a fast sputter sample and fast gas valve. *Rev. Sci. Instr.*, 73:548–551, 2002.

## APPENDIX A.IV





Contents lists available at ScienceDirect

# Nuclear Instruments and Methods in Physics Research A

journal homepage: [www.elsevier.com/locate/nima](http://www.elsevier.com/locate/nima)

## The effect of magnetic field strength on the time evolution of high energy bremsstrahlung radiation created by an electron cyclotron resonance ion source

T. Ropponen<sup>a,\*</sup>, O. Tarvainen<sup>b</sup>, P. Jones<sup>a</sup>, P. Peura<sup>a</sup>, T. Kalvas<sup>a</sup>, P. Suominen<sup>c</sup>, H. Koivisto<sup>a</sup>, J. Ärje<sup>a</sup><sup>a</sup> Department of Physics, University of Jyväskylä, P.O. Box 35, FI-40014, Finland<sup>b</sup> Los Alamos National Laboratory, Los Alamos, NM 87545, USA<sup>c</sup> Prizztech Ltd/Magnet Technology Centre, Tiedepuisto 4, FI-28600 Pori, Finland

### ARTICLE INFO

#### Article history:

Received 30 June 2008

Received in revised form

4 December 2008

Accepted 5 December 2008

Available online 24 December 2008

#### Keywords:

ECR

Bremsstrahlung time evolution

### ABSTRACT

An electron cyclotron resonance (ECR) ion source is one of the most used ion source types for high charge state heavy ion production. In ECR plasma the electrons are heated by radio frequency microwaves in order to provide ionization of neutral gases. As a consequence, ECR heating also generates very high electron energies (up to MeV region) which can produce a vast amount of bremsstrahlung radiation causing problems with radiation shielding and heating superconducting cryostat of an ECR ion source. To gain information about the time evolution of the electron energies in ECR plasma radial bremsstrahlung measurements were performed. JYFL 14 GHz ECR ion source was operated in pulsed mode and time evolution measurements were done with different axial magnetic field strengths with oxygen and argon plasmas. Bremsstrahlung data were analyzed with a time interval of 2 ms yielding information at unprecedented detail about the time evolution of high energy bremsstrahlung radiation from an ECR ion source. It was observed, for example, that reaching the steady state phase of the plasma bremsstrahlung requires several hundred milliseconds and the steady state time can be different with different gases.

© 2008 Elsevier B.V. All rights reserved.

### 1. Introduction

In an electron cyclotron resonance ion source (ECRIS) [1] bremsstrahlung radiation is generated in three distinctive processes: (1) in the plasma volume due to collisions between charged particles, (2) on the plasma chamber walls due to the interactions between the chamber wall material and the electrons escaping from the  $B$ -minimum structure and (3) in the plasma due to acceleration of charged particles. The resulting photons can penetrate through the plasma chamber wall causing radiation that requires heavy shielding around the ion source. In addition, in the case of superconducting ECR ion sources the bremsstrahlung radiation can substantially increase the heat load of the cryostat [2]. In order to be able to solve these problems it is essential to first try to understand the electron heating processes and ion source parameters affecting the electron energy and the photon flux. In addition, time evolution measurements of electron energies will give valuable input parameters for electron heating simulations.

Bremsstrahlung spectroscopy is a standard plasma diagnostics tool that has been widely applied to obtain information about the hot electron population of ECRIS plasmas [2–6]. The recorded spectra can be used, for example, for obtaining information of the spectral temperature of the high energy electron population, but the spectra should be cleaned especially from pile-ups which are causing severe distortion to the spectra at high count rates. However, unfolding the exact electron energy distribution function (EEDF) from the data is extremely difficult, if not impossible, due to the ion source geometry. The bremsstrahlung spectrum of an ECRIS is typically recorded in continuous (CW) operation mode yielding information about the steady state plasma properties. It has been reported [6] that the build-up of the bremsstrahlung spectrum takes tens of milliseconds while the decay time can be up to 100 ms (a simple mirror machine was operated in pulsed mode in the measurements). This observation is supported by electron cyclotron emission and diamagnetism measurements with an 18 GHz  $B$ -minimum ECRIS in pulsed mode [3] yielding corresponding timescales for build-up and decay of the hot electron population.

According to electron heating theories and experimental observations [2,4,7,8] low magnetic field gradient at the resonance zone results into high electron energies and high count rates of

\*Corresponding author. Tel.: +358 142 60 2456; fax: +358 142 60 2351.

E-mail address: [tommi.ropponen@phys.jyu.fi](mailto:tommi.ropponen@phys.jyu.fi) (T. Ropponen).

bremsstrahlung radiation. In order to gain understanding on the effect of the magnetic field strength on the hot electron population and bremsstrahlung build-up time the JYFL 14 GHz ECRIS was operated in pulsed mode. During the measurements ion beam was not extracted from the ion source (high voltages were not used) and the main focus was to obtain information about the timescales related to electron heating. The time evolution of the bremsstrahlung spectrum was measured as a function of time with three different axial magnetic field strengths, and photon counts at different energies was studied in detail with an analysis code developed for this purpose.

## 2. Experimental procedures

In this section the measurement setup for the bremsstrahlung experiments is presented and the analysis code written for the purpose of sorting the vast amount of collected data is described. Issues related to the shielding of the detector and corresponding effects on the recorded spectra are discussed.

### 2.1. Measurement setup

The measurement setup for the bremsstrahlung experiments with the JYFL 14 GHz ECRIS is presented in Fig. 1. A reference time signal was generated with an analog circuit providing a standard TTL signal as an output (TTL trigger in Fig. 1). In the experiments the pulse ratio (on/off time) of the circuit was fixed so that the RF power was launched into the ECRIS plasma chamber for 1.76 seconds while the power was off for 5.92 seconds between the consecutive pulses. Pulse length was selected in a way that the plasma would have sufficient amount of time to reach steady state phase (around 2 seconds), and it was also decided that there should be enough time between the RF pulses in order to have adequate time for the plasma breakdown (about three times the “on time” was selected). The TTL type trigger signal was then used to synchronize the measurement setup. A fast RF switch was employed to pulse the driver signal from the 14 GHz GUNN-type oscillator to the klystron. The rise time of the TTL controlled RF switch is specified to be 40 ns (0–100%) and 15 ns (10–90%). Due to the fast response time of the switch and the operational principle of the klystron (constant gain amplifier), it is reasonable to estimate that the RF power was launched into the plasma chamber some tens of nanoseconds after applying the TTL trigger

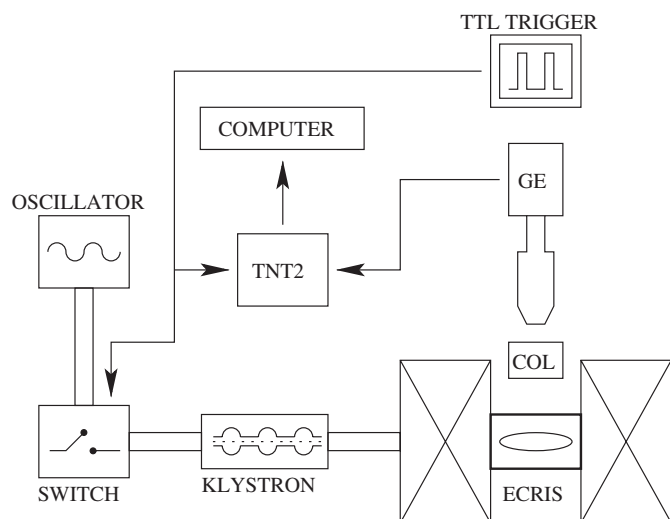


Fig. 1. Measurement setup in bremsstrahlung time evolution measurements.

pulse. The relevant timescales for ECR heating are on the order of milliseconds (up to few hundred milliseconds) and, therefore, the delays induced by the RF switch, klystron and wave propagation in the waveguide can be ignored. The gain of the klystron i.e. the position of the attenuator was adjusted manually in order to avoid any ripple of the applied power due to remote control system.

Much of the lead shielding around the ECRIS was removed to get a clear line of sight from the ECR chamber to the germanium detector (GE in Fig. 1). However, several tens of millimeters of material, including permanent magnets, was still in between the plasma chamber wall and the detector. This amount of material attenuates lower energy (less than 80 keV) part of the bremsstrahlung spectrum very efficiently (half-thickness of 80 keV photon e.g. in copper is 1 mm), and attenuation cannot be avoided in radial bremsstrahlung measurements. A collimator (COL in Fig. 1) was made out of lead bricks and two different size of openings were used— $0.5 \times 1.0$  and  $2.0 \times 2.0$  mm. The collimator consisted of two  $10 \times 10 \times 5$  cm lead bricks leaving quite a lot of unshielded surface into the solid angle seen by the detector. Therefore, lead plates were added around the collimator to absorb the bremsstrahlung radiation leaving only a small hole of the collimator unshielded. The Ge detector was located in the proximity of the ECRIS so that the crystal was aligned with one of the magnetic poles of the sextupole structure. Measured in axial direction, the collimator was located in the center of the plasma chamber. At this (axial) location the plasma flux is directed to all of the six magnetic poles. The placements of the detector mount with respect to the ECR plasma chamber are presented in Fig. 2.

Radial measurement from a magnetic pole was chosen for the first type of time evolution measurement instead of other measurement geometries for two reasons: (1) the electrons tend to follow the magnetic field lines and because of that the majority of collisions between the electrons and plasma chamber walls take place on a magnetic pole and (2) most of the low energy radiation detected through a radial port is generated by the plasma itself. The objective of this article was especially to study the evolution of high energy electrons which generate problems in the most powerful ECR ion sources, and therefore the measurements were performed at the location of the highest bremsstrahlung flux.

Signals recorded by the Ge detector were routed to the digital signal processing unit (TNT2 [9] in Fig. 1), which linked the data with the reference timing signal. The shaping time of the pulse was set to  $2.0 \mu\text{s}$  where both the rise time of the trapezoid and the flat top of the trapezoid were set to  $1.0 \mu\text{s}$ . Short shaping time was used in order to gain good timing resolution. Measured with  $^{152}\text{Eu}$  444 keV peak, the energy resolution was about 4.2 keV (FWHM) and about 7.4 keV with  $^{152}\text{Eu}$  1408 keV. A computer was used to collect and store all the data from the TNT2 unit.

During the measurements the collimator size and the shielding geometry around the ion source were varied in order to better understand where the measured bremsstrahlung is created and how substantial amount of the measured photons penetrated through the collimator setup. It was observed that while these changes in the geometry affected the count rate and the shape of the recorded spectra, the timescales required for obtaining a steady state remained unaffected. This is shown in Fig. 3 illustrating the number of total counts, integrated over all energies, as a function of time.

After experimenting with different lead shielding geometries it is understood that the recorded bremsstrahlung radiation in radial measurement is originating from all of the six magnetic poles. The lead shielding around the collimator was enhanced between the reported measurements with argon and oxygen. However, it is emphasized that the purpose of the measurements was to obtain

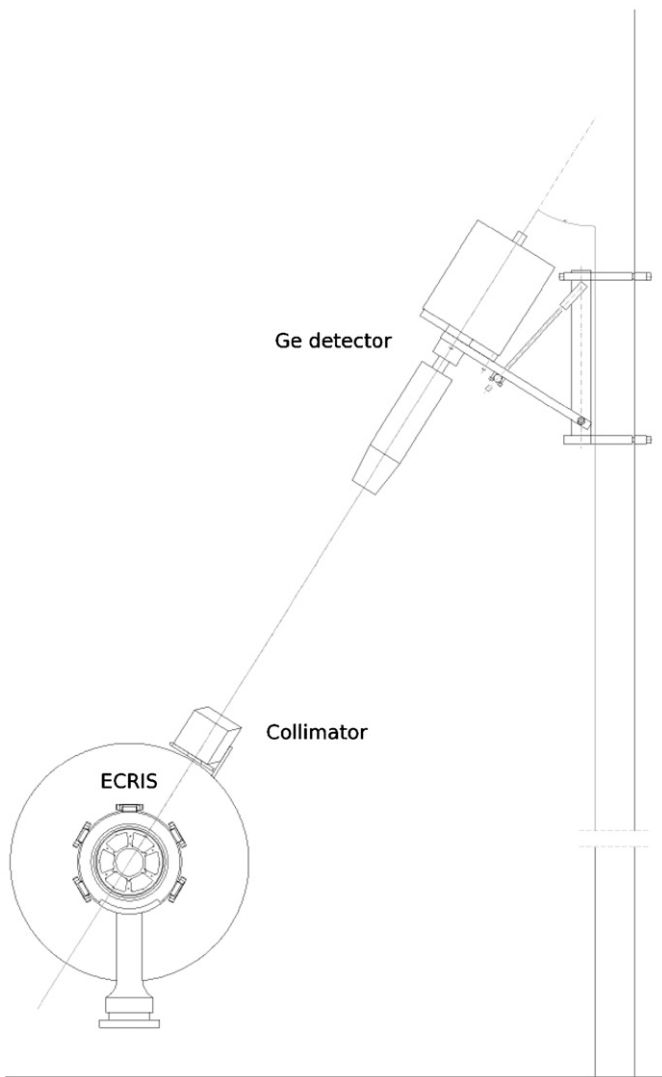


**Fig. 2.** The location of the detector in respect of the ECRIS. CAD drawing—radial cross-section. Germanium detector, collimator and ECRIS are labeled. Distance between the outer plasma chamber wall and the tip of the detector is about 990 mm.

information about the timescales of electron heating which are practically independent of shielding as demonstrated in Fig. 3. The effect of the lead shielding is seen on the measured spectra in the form of two characteristic lead peaks ( $k_{\alpha 1} = 74.9694$  keV and  $k_{\beta 1} = 84.393$  keV), which can be very dominant on the lower energy part of the spectra. It should also be noted that the measurement data are corrected by using a relative efficiency calibration for the germanium detector used in the setup. Due to complex measurement geometry and resulting material attenuation an absolute efficiency calibration was not done.

The wall bremsstrahlung from an ECRIS is an example of thick target bremsstrahlung at non-relativistic energies (energies that are smaller or comparable to the rest energy of the electron) [10]. Absorption of the bremsstrahlung photons in the target i.e. ECRIS plasma chamber walls is substantial. At these non-relativistic energies the angular distribution of the radiation intensity is widely spread being about the same order of magnitude at  $0^\circ$  and  $90^\circ$ , compared to the trajectory of the incident electron causing bremsstrahlung radiation [10].

In the ECR ion source plasma the electron energies vary from thermal (less than 1 eV) to MeV region meaning that the bremsstrahlung is generated by electrons with a wide range of

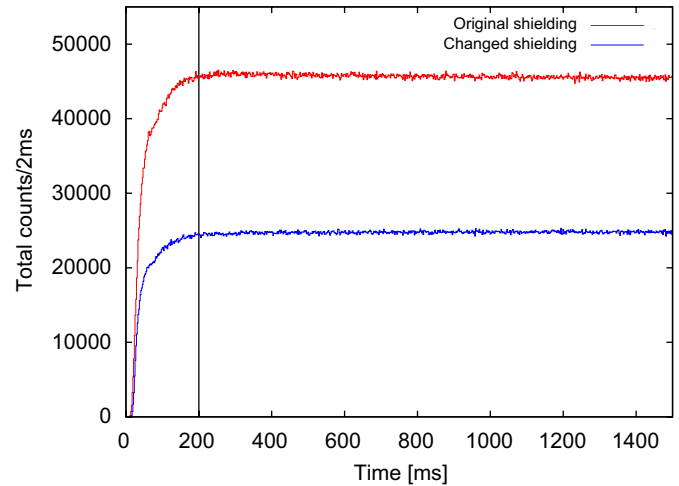


**Fig. 3.** Comparison of total counts with original (upper curve) and changed (lower curve; added lead plates) shielding around the collimator.  $T = 0$  corresponds to the leading edge of the trigger signal (RF power triggered “on”).  $B_{\text{ext}} 0.946$  T,  $B_{\text{min}} 0.346$  T,  $B_{\text{inj}} 2.011$  T, 500 W of RF power and neutral argon pressure of  $2.6 \times 10^{-7}$  mbar.

energies. On the other hand photons can scatter several times in the ECR structure (Al chamber, permanent magnets, etc.) before they are observed at the detector. The lower energy part of the bremsstrahlung spectrum is largely damped as the radiation penetrates into the ECRIS structure. Attenuation of the bremsstrahlung from an ECR ion source (at different energies) is difficult to correct due to complex geometry of the plasma chamber, cooling systems, magnets and outer casing. Compton tails from a bremsstrahlung event has a distinct effect on the shape of the bremsstrahlung spectrum. It is well known that unless the Compton tails are removed (unfolding of the spectra) the lower energy part of the bremsstrahlung spectrum is over-emphasized.

Separation of the bremsstrahlung events from each magnetic pole of an ECRIS is virtually impossible (sextupole structure). This affects the measured spectra due to unequal attenuation for photons originating from the different magnetic poles. It is also noteworthy that the electrons hitting the plasma chamber walls are in rotational motion around the magnetic field lines and a large portion of their energy is perpendicular to the magnetic field due to ECR heating processes. Therefore the angular distribution of the bremsstrahlung deviates from the ellipsoidal [10] cone. One has to also remember that the plasma chamber is not a point source. Bremsstrahlung is generated all the way along the permanent magnet poles (although the intensity changes along the magnetic pole) i.e. along a length of about 280 mm in the case of JYFL 14 GHz ECRIS (the electron losses at each magnetic pole also depend on the radial component of the solenoid field). Therefore, the bremsstrahlung processes are generating radiation basically in every direction around an ECR ion source.

## 2.2. Data analysis

During the experiments the raw data from the germanium detector are processed in the TNT2 unit in situ so that ADC overflows are rejected at once. Pile-up events and other unwanted phenomena are tagged by the TNT2 unit allowing them to be removed while sorting the measurement data at a later time. A single RF pulse does not produce enough statistics so that the analysis code combines data from several consecutive RF pulses. For example, the results presented in this article consist of data from 680 combined RF pulses corresponding a measurement time of 90 minutes for each ion source setting. Following this

procedure it is possible to illustrate bremsstrahlung spectra in time intervals of a few milliseconds, and have enough events in each spectrum to make reliable observations. The analysis code also monitors the data tags for the trigger signal and rejects possible erroneous RF pulses (such as undetected trigger on/off signal) before final data processing. The code uses recorded background spectrum (recorded while the ion source was shut-down) to correct the bremsstrahlung spectra i.e. remove the counts at each energy channel corresponding to average background count rates. The code also takes the relative efficiency correction for the germanium detector into account. It was noted that only energies over 15 keV should be processed due to the efficiency curve of the detector (the curve goes down rapidly at lower energies). If a time interval of 2 ms, for example, is used for processing a 1500 ms RF pulse, 750 spectra are created by the analysis code for the “RF on” period alone meaning that a vast amount of data in both “RF on” and “RF off” cases is produced with the sorting code giving a possibility of thoroughly studying the time evolution of the bremsstrahlung produced by an ECRIS.

### 3. Experimental results

In this section bremsstrahlung measurement data for both oxygen and argon plasmas is presented as a function of time with three axial magnetic field strengths. Detailed data from the beginning and the end of the RF pulse are presented in order to highlight the observed differences between varying source settings. During the measurements high voltages were not used and therefore ion beams were not extracted from JYFL 14 GHz ECRIS.

#### 3.1. Time evolution of bremsstrahlung radiation as a function of time with three magnetic field strengths

The magnetic field strengths at the injection ( $B_{inj}$ ), extraction ( $B_{ext}$ ) and  $B$  minimum ( $B_{min}$ ), corresponding to different coil currents used in the measurements, for JYFL 14 GHz ECRIS are given in Table 1. The axial gradients at the injection ( $\nabla B_{inj}^{res}$ ) and extraction ( $\nabla B_{ext}^{res}$ ) side resonances are also shown. Finally, the calculated axial distances ( $d_{res}$ ) between these resonance points ( $B_{res} = 0.504T$ ) are presented (a frequency of 14.1 GHz is used).

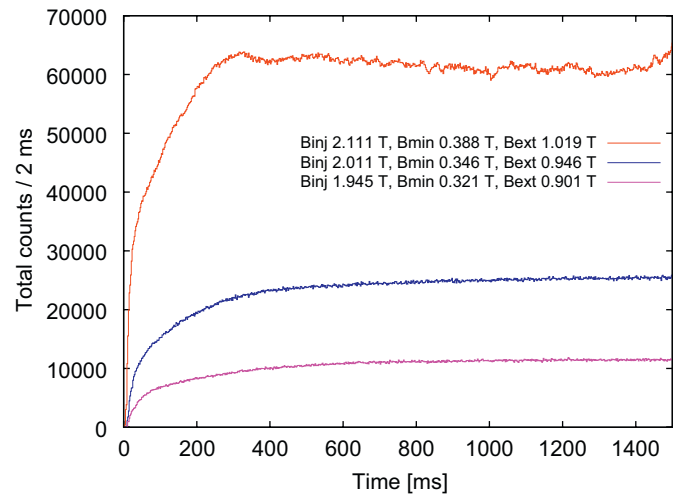
##### 3.1.1. Oxygen plasma

Fig. 4 shows the time evolution of total photon counts (integrated over the energy spectrum) measured with oxygen plasma for “RF on” period with different magnetic field strengths. The same data for the first 60 ms from the beginning of the RF pulse are presented in Fig. 5. This is done in order to highlight the difference in plasma ignition times observed with different magnetic field strengths. It should be noticed that the count rates in vertical axis in all of the figures presented in this article are not absolute—only a relative efficiency calibration of the germanium detector was performed. The plotted data curves in all

**Table 1**  
Magnetic field strengths of the JYFL 14 GHz ECRIS with different coil settings and the corresponding resonance length in axial direction.

Coils currents (inj/ext) (A)	$B_{inj}$	$B_{min}$	$B_{ext}$	$\nabla B_{inj}^{res}$ (T/m)	$\nabla B_{ext}^{res}$ (T/m)	$d_{res}$ (mm)
470/470	1.945	0.321	0.901	6.2	5.8	121
500/500	2.011	0.346	0.946	5.9	5.5	111
550/550	2.111	0.388	1.019	5.1	4.9	92

Magnetic field values are given in Tesla.



**Fig. 4.** Comparison of total counts during the RF-on period with different magnetic field strengths. Measured with oxygen plasma, 500 W of RF power and neutral gas pressure of  $2.6 \times 10^{-7}$  mbar.

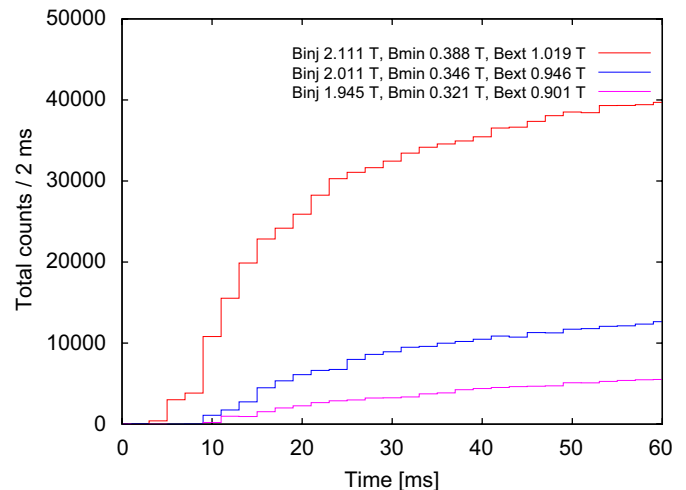


**Fig. 5.** First 60 ms of the data from Fig. 4.

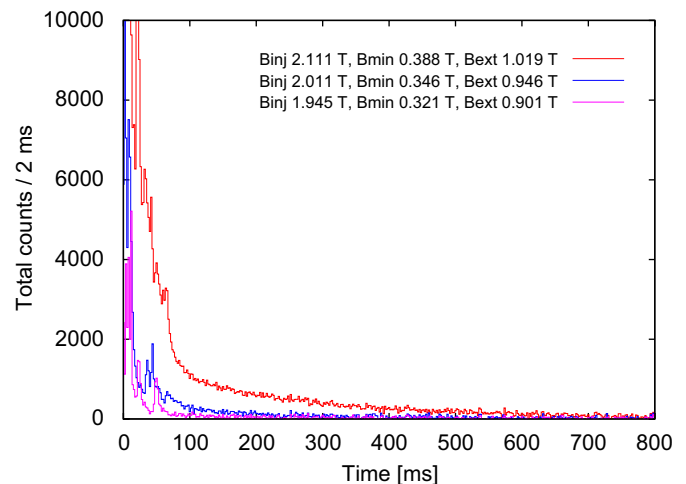


**Fig. 6.** Comparison of total counts during the first 800 ms of the RF-off period with different magnetic field strengths. Measured with oxygen plasma, 500 W of RF power and neutral gas pressure of  $2.6 \times 10^{-7}$  mbar.  $T = 0$  corresponds to the trailing edge of the RF pulse.

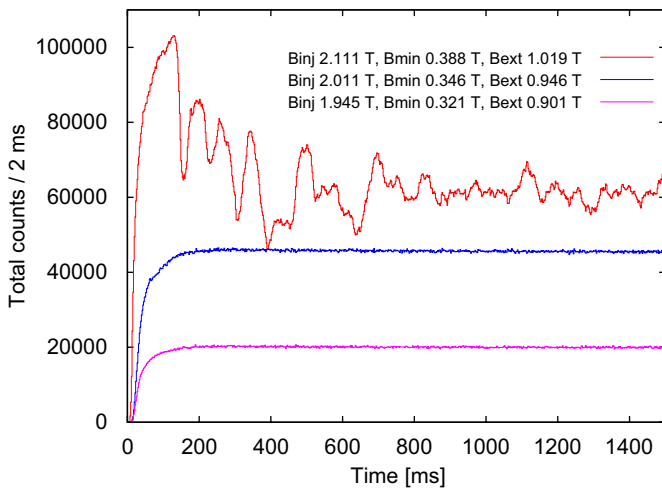


**Fig. 7.** Comparison of total counts during the RF-on period with different magnetic field strengths. Measured with argon plasma, 500 W of RF power and neutral gas pressure of  $2.6 \times 10^{-7}$  mbar.

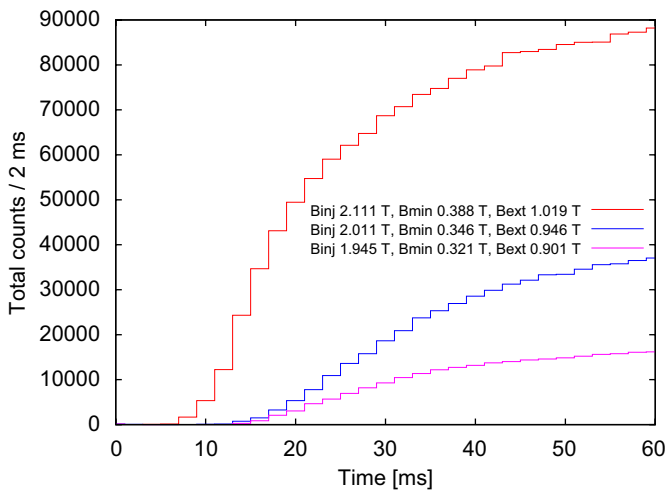


**Fig. 8.** First 60 ms of the data from Fig. 7.

forementioned pictures (as well as in Fig. 6) correspond to the following currents in both coils (for magnetic field values refer to Table 1): the uppermost curve/550 A, the middle curve/500 A and the lowest curve/470 A (this applies also to Figs. 7 and 8).

It was observed that the strongest axial magnetic field (lowest magnetic field gradient) yields the highest count rates and also significant instabilities in the bremsstrahlung count rates (see the oscillation of the uppermost curve in Fig. 4) are observed. The first counts at energies over 15 keV for coil currents of 550/550 A were observed 4–6 ms after switching on the RF power (see Fig. 5). With the lower coil currents it took around 10 ms for the first counts to appear. This difference in timescales could possibly arise from the more efficient heating usually connected to low magnetic field gradient at the resonance zone.

Fig. 6 shows the corresponding data for the first 800 ms of the “RF off” period starting at the end of the microwave pulse. The maximum count rate on the vertical axis in this figure is chosen to illustrate the observed differences in detail. Typical bremsstrahlung “decay times” are on the order of 300–400 ms for the two lowest  $B_{\min}$  values and around 700–800 ms for the highest  $B_{\min}$ . Some “peaks” can also be seen at the decay data. The reason for this behavior remains unknown. It is difficult to extract precise information about the decay times of the bremsstrahlung

radiation because the decay of the RF power in the klystron and, consequently, in the plasma chamber of an ECRIS are unknown. However, it seems that the decay of the bremsstrahlung in “RF off” phase is approximately as fast as the time to reach the steady state in “RF on” phase (see Figs. 4 and 6).

### 3.1.2. Argon plasma

The “RF on” data measured with argon plasma is presented in Figs. 7 and 8. The same coil currents as for oxygen plasmas were used. It can be seen from Fig. 7 that the instabilities in bremsstrahlung count rates observed with the strongest axial magnetic field (lowest gradient) are even more pronounced than with oxygen plasma. It is noted, as in the case of oxygen plasma, that the lower the gradB the higher the count rates. Fig. 8 shows that with coil settings of 550/550 A bremsstrahlung events above 15 keV starts to be produced after 8 ms from the leading edge of the RF pulse while with the lower coil current values this takes about 14 ms. The timescales are close to that observed with oxygen. This means that electron energies that are over one order of magnitude higher than required to produce highly charged ions (ionization potential e.g. for  $\text{Ar}^{8+}$  is about 144 eV [11]) are seen when the RF power has been launched into the plasma chamber for a time period of around 10 ms.

An interesting observation is that the timescales for reaching the steady state bremsstrahlung production are quite different for oxygen and argon. With argon the steady state is reached at around 200 ms while with oxygen it takes more than 600 ms to reach the steady state. The discrepancy could be explained by the fact that argon is a noble gas while oxygen is chemically reactive. It is possible that oxygen accumulates on the plasma chamber walls during the “RF off” period and is released due to the collisions of plasma particles during the beginning of the “RF on” period. This process can lead into varying neutral gas pressure for some hundreds of milliseconds.

### 3.2. Detailed time evolution of the measured bremsstrahlung spectra during the “RF on” period

In Section 3.1, the time-dependence of the count rates integrated over the whole energy spectrum for different elements and magnetic field settings was presented. Therefore, valuable information about the timescales required for the plasma ignition and reaching the steady state have been obtained. In this section a more detailed view of the time evolution of different energies that are present in the measured bremsstrahlung spectra will be presented. This is done in order to study the timescales of electrons to reach certain energies. In order to illustrate the time evolution of the bremsstrahlung spectra an example of a spectrum at different time intervals measured from the leading edge of the RF pulse will be presented. This example was measured with oxygen plasma using the following settings: RF power of 500 W, coil currents of 500/500 A and neutral gas pressure of  $2.6 \times 10^{-7}$  mbar.

Fig. 9 shows how the recorded bremsstrahlung spectrum evolves in time. Very few events are observed before 10 ms but during the time interval of 10–12 ms some events start to appear. The bremsstrahlung spectrum develops as follows: between 10 and 12 ms small characteristic lead peak at 75 keV can already be seen. Otherwise there are not many events on the spectrum; 12–14 ms: energies over 100 keV start to appear and the characteristic lead peaks (75 and 84 keV) are seen. The corresponding endpoint energy of the spectrum, reflecting the maximum electron energy, is about 150 keV while the maximum number of counts in this 2 ms interval is about 100 (maximum number of counts at the lower characteristic lead peak);

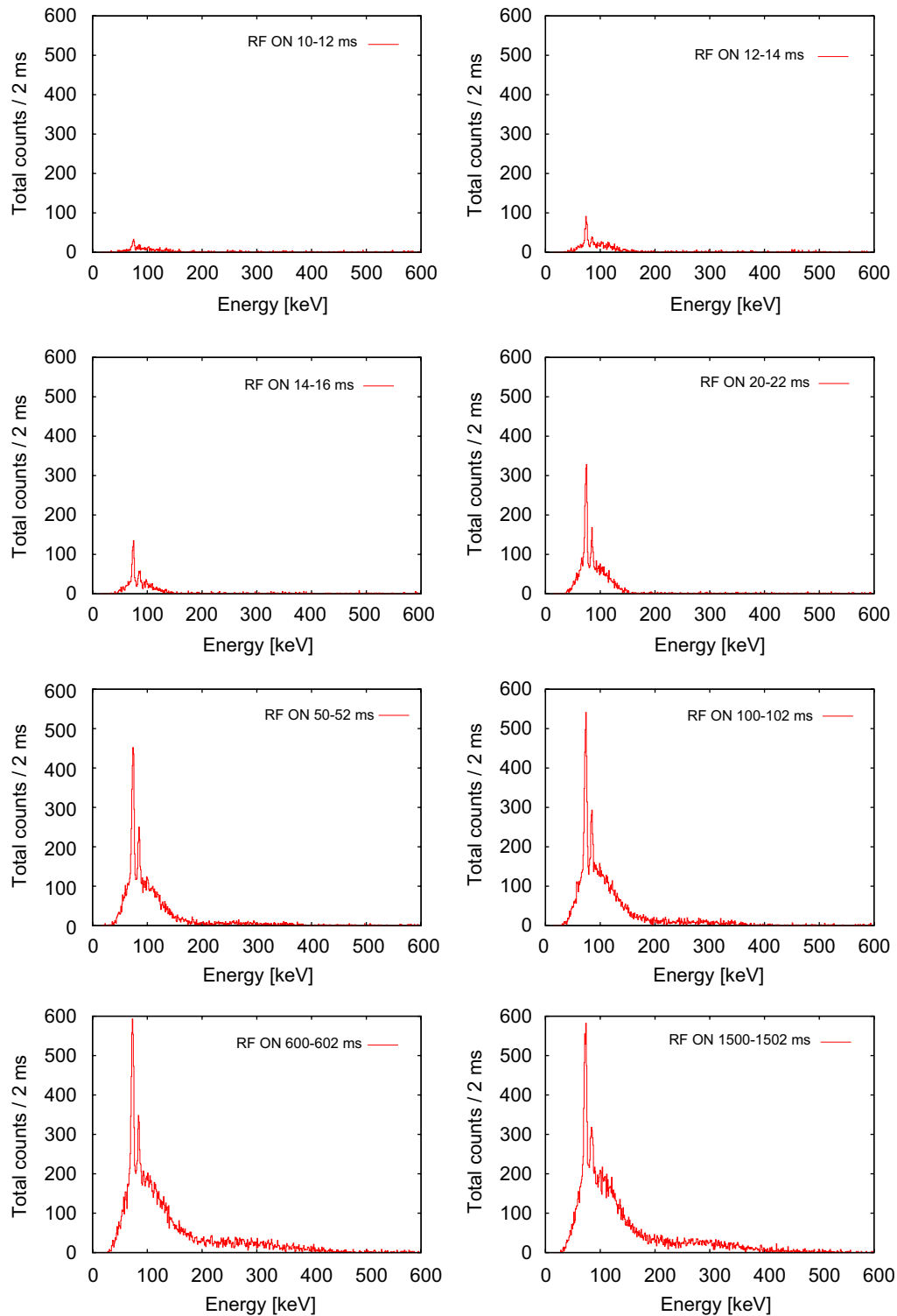


Fig. 9. Bremsstrahlung spectrum at different time intervals measured from the leading edge of the RF pulse. Oxygen plasma, 500 W, 500/500 A,  $2.6 \times 10^{-7}$  mbar.

14–16 ms: the count rate increases and the maximum number of events is roughly 140. At this point both of the characteristic lead peaks can be clearly observed. The endpoint energy is still around 150 keV; 20–22 ms: the count rate is increased again, now the maximum is around 330 events at the lower energy lead peak. Both lead peaks are very clearly visible while the endpoint energy is still around 150 keV; 50–52 ms: the maximum number of counts in one channel is about 450. At this point the higher energy part of the spectra starts to emerge. The endpoint energy has

shifted to over 350 keV and there is a “plateau” between energies from 200 to 300 keV. One possible explanation for this “plateau” can be a higher energy electron population which starts to build up after around 50 ms and continues to grow until the spectra reaches its steady state phase. This means that with the given ECRIS parameters it takes more than 20 ms and less than 50 ms to produce a visible amount of electrons in the spectra with energies exceeding 200 keV. 100–102 ms: the maximum count rate at this interval is around 550 and the endpoint energy is about 400 keV.

At this point the “plateau” between energies from 200 to 350 keV is even more pronounced. Proceeding a few hundred milliseconds forward it is seen that more counts are recorded between 600 and 602 ms than between 100 and 102 ms raising the whole spectrum up in the intensity scale. The endpoint energy is still around 400 keV. Comparing the spectra recorded at 1500–1502 and 600–602 ms reveals that a steady state is reached between 600 and 1500 ms after launching the RF power into the plasma chamber of JYFL 14 GHz ECRIS (steady state is actually reached at around 600 ms which can be confirmed from the time evolution animation of the spectra). The saturation of the total counts after 600 ms can also be verified from Fig. 4.

Another illustration of the time evolution of the bremsstrahlung is presented in Fig. 10 showing the time evolution of the count rates at different energies (1 keV windows around a given center) from the same data set used in Fig. 9. The ripple in the data, which is more pronounced at high energies, is related to the amount of statistics. However, from Fig. 10 it is seen that some electrons reach high energies very fast (a very low amount of high energy counts can be seen already after 12 ms). Therefore, counts, for example, at 300 keV appear soon after applying the RF power

but it takes several hundreds of milliseconds to reach the steady state at this energy. The steady state count rate was estimated at the figures and then the time to reach 50% and 90% of the steady state count rate was approximated from the figures. Table 2 lists approximate times to obtain the steady state phase for the energies considered in Fig. 10 with two different threshold values (50% and 90%).

From Table 2 it is seen that the time to reach the steady state with the energy of 75 keV is much shorter than with the other energies. Photons having energy over 75 keV can cause lead excitation which is released as characteristic lead radiation, thus the characteristic peak(s) of lead are strongly present and their time evolution is accelerated due to photons originating from the plasma. The 50% threshold time at 75 keV is 14 ms while threshold of 90% corresponds to a time of 44 ms. This means that the characteristic lead peak rises rapidly after the RF power has been launched into the plasma chamber. At the energy of 100 keV the times are 58 and 290 ms corresponding to thresholds of 50% and 90%, respectively. These times are significantly longer than the corresponding times for 75 keV. With both threshold values the steady state times are increasing as a function of energy, and

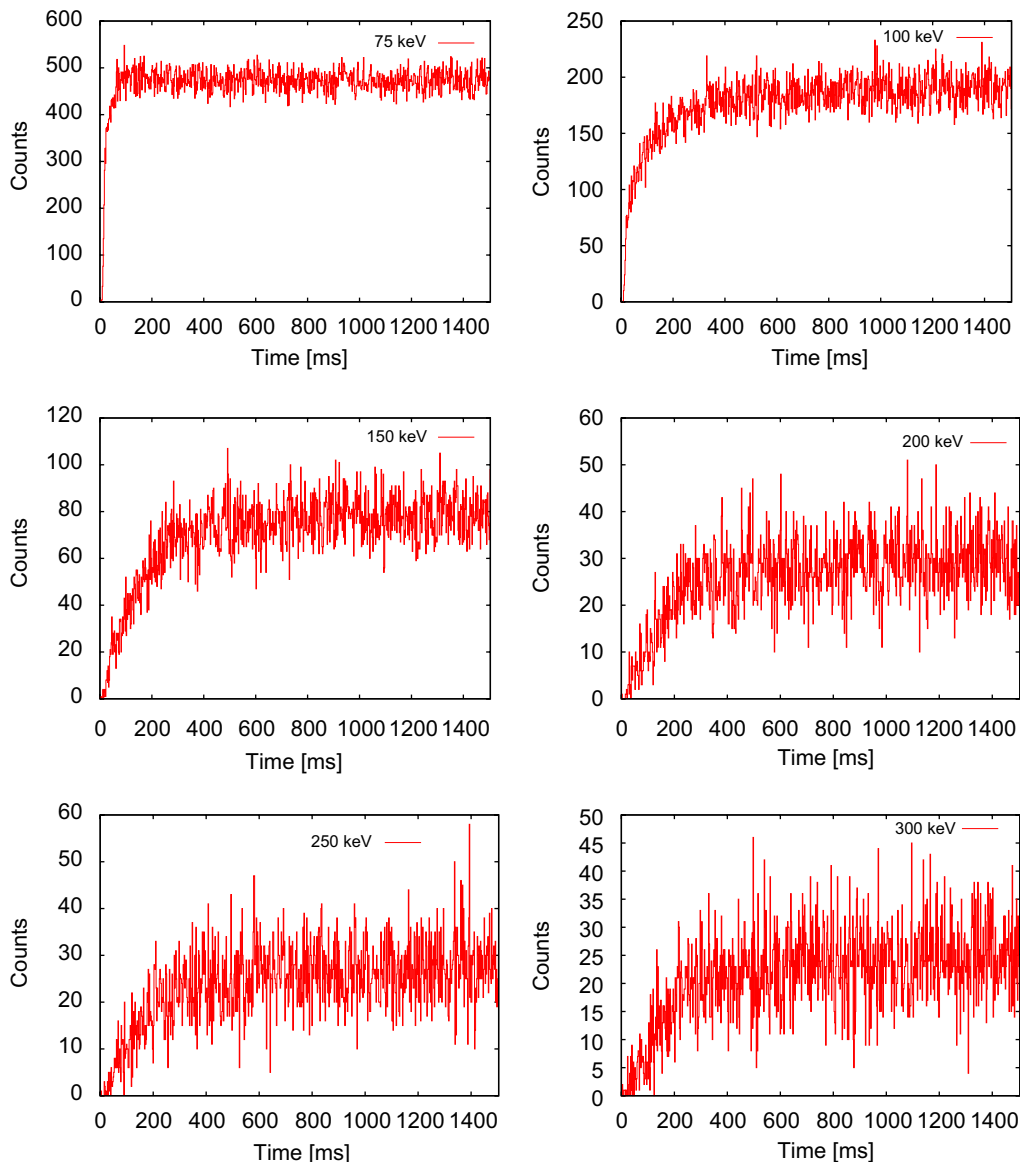


Fig. 10. Bremsstrahlung counts at different energies as a function of time, oxygen plasma, 500 W, 500/500 A,  $2.6 \times 10^{-7}$  mbar.

**Table 2**

Times to reach steady state phase with different energies and percentage thresholds from the steady state count rates presented in Fig. 10.

Energy (keV)	75	100	150	200	250	300
Steady state (ms) (TH: 50%)	16	58	110	127	150	172
Steady state (ms) (TH: 90%)	44	290	316	380	407	458

finally the steady state times are 172 ms (50%) and 458 ms (90%) at 300 keV. The steady state time of the total count rate extracted from Fig. 4 (the middle curve) with 90% threshold is about 340 ms which is in the same order of magnitude than the data in Table 2.

#### 4. Discussion and future prospects

The measurements described in this article reveal new information about the electron heating processes in an ECR ion source under different magnetic field strengths at unprecedented detail (time-resolving capability). Main focus of this article was to gain understanding about the electron heating timescales and energies at the plasma ignition and therefore, pulsed RF power was used. During the bremsstrahlung measurements ion beam was not extracted from the ion source.

In the experiments three arbitrarily chosen magnetic field configurations within the normal operation conditions were used. According to the measurements the lower magnetic field gradient resulted in significant increase in total bremsstrahlung emission count rates which can be seen in Figs. 4 and 7. With the two lowest coil settings the bremsstrahlung emission data are very stable, but with the highest coil currents the bremsstrahlung count rate is unstable throughout the RF pulse. There are at least three possible explanations for the increased count rate: (1) the gradient of the axial magnetic field, (2) concentration of electron losses into the radial loss cones possibly caused by the increased strength of the axial magnetic mirrors and (3) plasma instabilities. In the ECRIS plasma (1) and (3) can be connected because plasma instabilities are driven by the temperature gradients [1] which can arise from the changed magnetic field gradient. More efficient heating, caused by the lower magnetic field gradient, increases the electron energy (and  $v_{\perp}/v_{\parallel}$  ratio) faster than “high gradB” heating generating increasing temperature gradients in the plasma. Using higher coil currents decreases the distance between the axial resonance zones (see  $d_{res}$  values from Table 1) which can lead to increasing density gradients inside the plasma. It is also known that the density gradients in the ECR plasma can drive instabilities [1]. Thus, changing the axial magnetic field strength can affect the particle temperature and density gradients which can lead to instabilities.

The conventional definition of mirror ratio of a magnetic bottle is based on the relation of magnetic field strength at the maximum and at the minimum of the magnetic field ( $B_{max}/B_{min}$ ). However, it is assumed that the magnetic moment of electrons is conserved at the resonance which is not the case in the ECRIS plasma due to microwave heating. Therefore, it is reasonable to use the value  $B/B_{ecr}$  to describe “mirror ratios” in ECRIS plasmas (see also scaling laws from Ref. [1]). In the measurements described in this paper it is seen that  $B_{axial}/B_{ecr}$  is increasing in both injection and extraction sides as the coil currents are increased and the  $B_{radial}/B_{ecr}$  remains constant. Therefore, it is plausible to claim that increasing the strength of axial magnetic mirrors causes the electron losses to concentrate into radial direction (radial magnetic field on the poles is constant, 0.85 T). It is also noted that the value  $B_{radial}/B_{min}$  decreases as the coil currents are increased which could favor radial electron losses.

It remains unknown whether the instabilities observed in Figs. 4 and 7 could be avoided by slightly tuning the ion source magnetic field. The instabilities seen in the figures were found several weeks after the bremsstrahlung measurements when the data processing was completed. Therefore the authors did not have a chance to look into this subject more thoroughly during the measurements. Increased count rates were also observed as the magnetic field gradient was decreased (increasing  $B_{min}$ ) without increased instabilities in bremsstrahlung spectrum (see the two lowest curves in Figs. 4 and 7). Therefore it cannot be definitely concluded that the axial magnetic field gradient, concentration of electron losses into the radial loss cones or instabilities are solely responsible for the increased bremsstrahlung count rate, but it might be a combination of these phenomena.

According to the results the time required to reach the steady state phase of electron energies requires several hundred milliseconds and is different for oxygen and argon. Argon plasmas reached the steady state bremsstrahlung conditions in about one third of the time compared to oxygen plasmas (200 ms for argon, 600 ms for oxygen). There is at least one possible explanation for this: oxygen, as a more reactive gas than argon, will be deposited into the plasma chamber walls during the “RF off” period and is slowly released by the particle bombardment during the “RF on” period. The information about the bremsstrahlung time evolution in the moment of plasma ignition is very important in order to understand the heating process. This information can be used to write more realistic electron heating codes.

Studying the very beginning of the RF pulse revealed that energies over 15 keV start to appear in the ECRIS plasma chamber after a few milliseconds. These electron energies are probably present in the ECRIS plasma before this time but the electrons at these energies might not be scattered into the radial loss cones of the magnetic bottle until some time has elapsed (this time can be negligible, but is unknown at the moment). The lowest magnetic field gradients produced energies over 15 keV faster than the higher gradient values. Typical rise times for the first bremsstrahlung counts (over 15 keV energy) to appear with oxygen plasma are about 6 ms ( $B_{min}$  0.388 T) and 10 ms ( $B_{min}$  0.346 and 0.321 T). For argon plasma the corresponding numbers are 8 ms ( $B_{min}$  0.388 T) and 14 ms ( $B_{min}$  0.346 and 0.321 T). With the lowest magnetic field gradients the electron stays longer within the resonance volume and therefore can gain energy more efficiently. This can be seen as shorter rise times in the total count rate spectra.

From the time evolution of the bremsstrahlung spectra it is seen that it takes more than 20 ms and less than 50 ms to produce a visible amount of electrons with energies over 200 keV. After around 50 ms the “plateau”, which could be an evidence of the higher energy electron population, starts to grow at energies starting from 200 keV. It was observed that the steady state is reached at different times at different electron energies. The lower characteristic lead peak (at 75 keV) appears after 44 ms with 90% threshold. With the same threshold it takes about 250 ms longer to reach the steady state at the electron energy of 100 keV and additional 26 ms to reach the steady state at 150 keV. Times of 380, 407 and 458 ms are needed to reach the steady state with energies of 200, 250 and 300 keV, respectively.

This was the first attempt to measure the time evolution of bremsstrahlung emission from the plasma chamber of an ECR ion source. The time evolution experiments will be continued in the near future in order to receive new information about the ECRIS related plasma parameters. For example the time evolution of ion currents of different charge states with the time evolution of the bremsstrahlung and the effect of the microwave frequency on the bremsstrahlung time evolution has to be measured. It is also needed to take a more thorough look into the effect of magnetic

field by measuring the bremsstrahlung using several different coil currents in order to understand how the bremsstrahlung production becomes unstable and use longer RF pulses to see if the instabilities will be damped after a while. It is assumed that after comprehensive studies of ECR bremsstrahlung more realistic simulation codes can be developed and photon flux could be affected. In addition, the results can probably be used to decrease the radiation problems related especially to the superconducting ECR ion sources.

### Acknowledgments

This work has been supported by the EU 6th Framework programme “Integrating Infrastructure Initiative—Transnational Access”, Contract no. 506065 (EURONS), by the Academy of Finland under the Finnish Centre of Excellence Programme 2006–2011 (Nuclear and Accelerator Based Physics Programme at JYFL) and US Department of Energy contract DE-AC52-06NA25396. T. Ropponen would like to acknowledge financial support from the Graduate School in Particle and Nuclear Physics. The authors would also like to thank Dr. Daniela Leitner for

valuable discussions. The use of germanium detector from the GAMMAPOOL resource is gratefully acknowledged.

### References

- [1] R. Geller, *Electron Cyclotron Resonance Ion Sources and ECR Plasmas*, Taylor & Francis, London, 1996.
- [2] D. Leitner, J.Y. Benitez, C. Lyneis, D.S. Todd, T. Ropponen, J. Ropponen, H. Koivisto, S. Gammino, Measurement of the high energy component of the X-ray spectra in the venus ecr ion source, in: *Proceedings of the 12th International Conference on Ion Sources*, vol. 79, Article ID. 033302, Rev. Sci. Instrum. (2008).
- [3] C. Barue, M. Lamoureux, P. Briand, A. Girard, G. Melin, *J. Appl. Phys.* 76 (1994) 2662.
- [4] H. Koivisto, *Rev. Sci. Instrum.* 70 (1999) 2979.
- [5] A. Girard, *Rev. Sci. Instrum.* 63 (1992) 2676.
- [6] K. Bernhardt, K. Wiesemann, *Plasma Phys.* 24 (1981) 867.
- [7] Y. Jongen, E.C.R. electron acceleration, in: *Workshop on the Sixth International ECR Ion Source*, Lawrence Berkeley Laboratory, Berkeley, CA, 1985, pp. 238–255.
- [8] Y. Liu, H. Bilheux, Y. Kawai, F.W. Meyer, G.D. Alton, *Nucl. Instr. and Meth. B* 241 (2005) 965.
- [9] L. Arnold, R. Baumann, E. Chambit, M. Filliger, C. Fuchs, C. Kieber, D. Klein, P. Medina, C. Parisel, M. Richer, C. Santos, C. Weber, *IEEE Trans. Nucl. Sci.* NS-53 (2006) 723.
- [10] H.W. Koch, J.W. Motz, *Natl. Bur. Stand.* 31 (1959) 920.
- [11] D.R. Lide, *Handbook of Chemistry and Physics*, CRC Press, Boca Raton, 2004.



# APPENDIX A.V



# Plasma breakdown diagnostics with the biased disc of electron cyclotron resonance ion source

O Tarvainen, T Ropponen, V Toivanen, J Ärje and H Koivisto

University of Jyväskylä, Department of Physics, Accelerator Laboratory, PO Box 35 (YFL), 40500 Jyväskylä, Finland

E-mail: [olli.tarvainen@jyu.fi](mailto:olli.tarvainen@jyu.fi)

Received 6 March 2009, in final form 5 May 2009

Published 26 June 2009

Online at [stacks.iop.org/PSST/18/035018](http://stacks.iop.org/PSST/18/035018)

## Abstract

The electron cyclotron resonance ion sources at the JYFL (University of Jyväskylä, Department of Physics) accelerator laboratory have been operated in pulsed mode to study the time-resolved current signal from the biased discs of the ion sources. The purpose of the experiments is to gain an understanding of the ion source parameters affecting the time required for the transition from neutral gas to plasma. It was observed that the plasma breakdown time depends strongly on the neutral gas density, gas species and density of seed electrons. In particular, it was observed that a low power microwave signal at secondary frequency makes the breakdown time virtually independent of the neutral gas density. The results can be utilized for operation of ECR ion sources in the so-called preglow mode. A simple qualitative model, which is in good agreement with the experiments, has been developed to interpret the results.

(Some figures in this article are in colour only in the electronic version)

## 1. Introduction

The production of highly charged ions with electron cyclotron resonance ion sources (ECRIS) can be enhanced significantly by applying negative voltage to a biased disc, located at the injection end of the plasma chamber [1]. Practically all modern ECR ion sources are equipped with such a biased electrode with its voltage ranging typically from  $-20$  to  $-300$  V with respect to the source potential [2].

Several experiments have been performed to explain the beneficial effect of the biased disc. These include experiments with a movable disc [3], experiments with different sizes and shapes of the disc [4] and experiments with a pulsed voltage applied to the disc [5]. It is commonly understood that the negative voltage of the disc reduces the electron flux towards the injection end of the ion source followed by an increase in the electron density and a decrease in the plasma potential [6, 7]. To satisfy the condition for quasineutrality (current balance) the ion fluxes from the plasma have to decrease simultaneously [8] yielding a longer confinement time for ions. As a result the charge state distribution of the extracted ion beams shifts towards higher charges, which is often desired for beam injection into accelerators.

In this paper we present a study of plasma breakdown diagnostics with the biased disc of ECR ion source(s) in pulsed microwave power operation mode. The main purpose of the work is to understand the effects of different ion source parameters, such as microwave power, neutral gas density and magnetic confinement, on the time required for the plasma breakdown process to occur. Understanding this process is important for applications of ECR ion sources demanding fast ionization times, e.g. radioactive ion beam production in pulsed operation mode. The implications of the results on these applications are discussed in the last section of the paper.

## 2. Experimental setup and procedure

The plasma breakdown was studied with two different ECR ion sources (14 GHz and 6.4 GHz) at the JYFL accelerator laboratory [9, 10] (JYFL—University of Jyväskylä, Department of Physics). The main differences between these ion sources are the magnetic field strength and plasma chamber volume, 1.3 L for the 14 GHz source and 7.7 L for the 6.4 GHz source. The diameter of the biased disc is 21 mm in the case of JYFL 14 GHz ECRIS and 60 mm in the case of JYFL 6.4 GHz

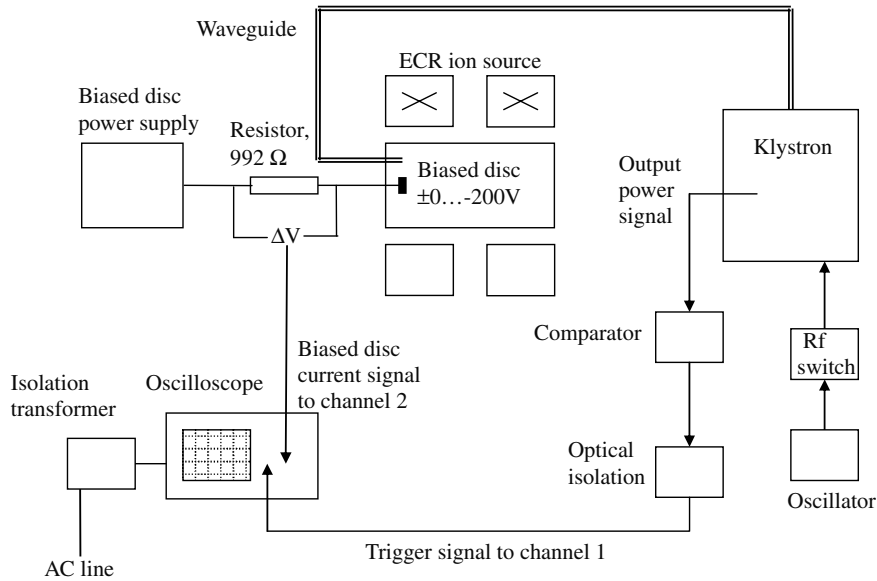


**Figure 1.** A schematic of the measurement setup.

ECRIS. The disc is located very close to the magnetic field maximum on the injection end of the plasma chamber (referred to as  $B_{inj}$  in this paper). Further details of the JYFL ion sources in their present configuration, including schematics, can be found from [10, 11]. For the experiments described in this paper the ion sources were operated in pulsed mode and the time-resolved current signal from the biased disc was recorded as a function of disc voltage, gas species, neutral gas pressure, microwave power, magnetic field strength and time between consecutive microwave pulses.

The output power of the klystron amplifier was controlled by pulsing the input signal from the oscillator. The gain (attenuator setting) of the klystron was kept constant during the pulsing. The microwave power was measured and the output signal from the klystron was directed to an oscilloscope to be used as a trigger signal ( $t = 0$  s) for the time-resolved measurement. The bias disc current was measured across a  $992 \Omega$  resistor connected directly between the biased disc power supply and the disc itself, which corresponds to a disc voltage drop of approximately  $1 \text{ V}/1 \text{ mA}$ . The voltage drop is negligible compared with typical biased disc voltage. As a consequence, the oscilloscope was floating on the biased disc voltage and the required optical isolation from the electronics of the klystron. Therefore, the output power signal (trigger) was directed through an optical isolation component (CNY66). The delay in the isolation circuit is on the order of microseconds and can be omitted in the following considerations. Due to a threshold voltage level of the optical isolation circuit, a voltage comparator was used to amplify the klystron output power signal (TTL level,  $0\text{--}5 \text{ V}$ ). This allowed measurements at microwave powers corresponding to the output signal level below the threshold of the optical isolation. The delay of the comparator was measured to be  $6 \mu\text{s}$  and is therefore negligible compared with the plasma breakdown time scales. Extraction voltage was not applied to the ion source during the bias disc current measurements. However, it was confirmed by measuring the time evolution of extracted beam currents (for

some ion source settings used in the biased disc measurement) that the extraction voltage does not affect the measured plasma breakdown times. It was also confirmed with different measurement resistors that the characteristics of the current signal from the biased disc are not due to the  $RC$  constant of the circuit but truly due to plasma phenomena. The possibility of the power supply voltage regulation affecting the data was excluded by comparing biased disc current signals measured with different power supplies (including a high current unit) yielding no observable difference. The neutral gas pressure in the plasma chamber was measured with a Penning ionization gauge adjacent to the chamber. The gauge reading was corrected for each element according to a calibration chart provided by the manufacturer. The subsequent error in neutral gas pressure values is within  $\pm 2\%$ . A schematic for the measurement setup is presented in figure 1. Figure 2 shows the biased disc of the JYFL 14 GHz ECRIS inside the plasma chamber.

### 3. Experimental results

#### 3.1. Time dependence of the bias disc current as a function of bias disc voltage

The studies of the plasma breakdown process were started by measuring the time-resolved current signals from the biased discs of the JYFL ECR ion sources as a function of the disc voltage. As an example, in figure 3, we present a family of curves measured for argon plasma with the JYFL 14 GHz ECRIS. The ion source settings were as follows: 14 GHz microwave power (pulsed)  $P = 500 \text{ W}$ , calibrated neutral gas pressure  $n_n = 3.8\text{E-}7 \text{ mbar}$ , magnetic field at injection  $B_{inj} = 2.02 \text{ T}$ , magnetic field at extraction  $B_{ext} = 0.95 \text{ T}$  and magnetic field minimum  $B_{min} = 0.35 \text{ T}$ . The axial distance from the resonance to the biased disc is approximately  $100 \text{ mm}$  under the given magnetic field settings. The radial magnetic field on the plasma chamber wall is  $0.85 \text{ T}$  (fixed for the JYFL

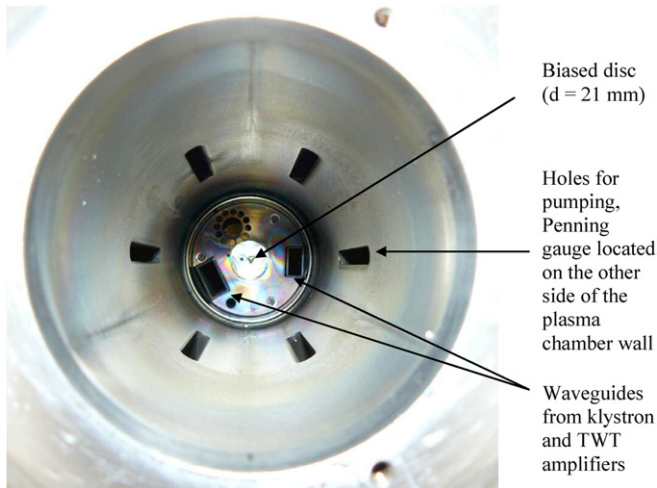


**Figure 2.** Biased disc of the JYFL 14 GHz ECRIS inside the plasma chamber (viewed from the extraction end). The triangular plasma loss pattern can be seen on the disc. Two rectangular waveguides from the klystron (WR62) and TWT (WR75) amplifiers are also visible. Penning ionization gauge is located adjacent to one of the pumping holes between the poles of the permanent magnet sextupole.

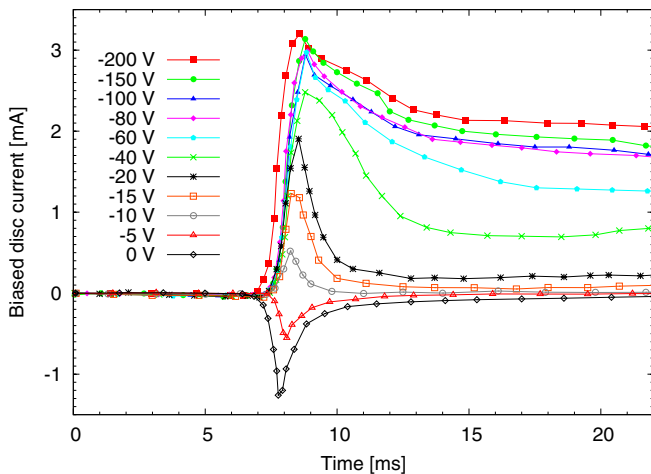


**Figure 3.** Time-resolved bias disc current of argon plasma as a function of biased disc voltage during the first 22 ms of the applied microwave pulse. JYFL 14 GHz ECRIS, neutral gas pressure  $3.8\text{E-}7$  mbar, pulsed microwave power of 500 W, magnetic field at injection of 2.02 T, magnetic field at extraction of 0.95 T and magnetic field minimum of 0.35 T.

14 GHz ECRIS). These settings are well within the range of typical values used for the beam production. The duration of the microwave pulses was about 6 s with off time greater than 30 s between consecutive pulses.

It is clear from the figure that the time required for the plasma breakdown to occur, namely 7–8 ms under the given ion source settings, is virtually independent of the biased disc voltage. By plasma breakdown we mean the fast transition from the undetectable current level to the mA level current. The biased disc current peaks between 8 and 9 ms with the maximum value depending on the applied voltage. The shape of the curve is determined by ‘neutral starvation’ and plasma sheath formation as a consequence of the proceeding step-wise

ionization. This was confirmed by studying time-resolved signal from the pressure gauge exhibiting a drop in the neutral gas pressure of 20–25 ms after switching on the microwave power and reaching saturation by 500 ms. Taking into account the diffusion time from the plasma chamber to the pressure gauge (few milliseconds), it is concluded that the peak in the biased disc current signal reflects the number of neutrals available for ionization. In the case of ECR ion sources peaks lasting for a few milliseconds have been observed on the extracted beam currents. The effect has been related to the formation of the steady-state charge state distribution (multiply charged ions) through step-wise ionization, and build-up of the plasma potential and electron energy distributions during the plasma breakdown [11].

The saturation current is reached after 0.5–1 s after the breakdown (not shown in figure 2). This suggests that the time required for the electron and ion densities and electron energy distribution function to reach their equilibrium is on the order of seconds. This observation is supported by time-resolved experiments [12] showing that the high energy (>30 keV) bremsstrahlung emission from the JYFL 14 GHz ion source reaches the steady state within similar time scale. Since the dependence of the bias disc current on the bias disc voltage has been thoroughly studied [6, 7] in cw mode, we do not discuss the saturation currents in this paper. It was shown with other gas species ( $\text{O}_2$ , He, Ne) that the time required for the breakdown is truly independent of the bias disc voltage for given element at fixed neutral gas pressure. This observation was confirmed with the JYFL 6.4 GHz ECRIS. By studying the bias disc current after switching off the microwave power it was observed that the (positive) signal decays from the saturation value to zero in 500–800 ms. This indicates that the electron confinement in ECRIS plasma is very strong.

In the case of the JYFL 14 GHz ECRIS the sign of the bias disc current changes at voltages between  $-5$  and  $-10$  V for argon plasma, i.e. electron flux towards the disc exceeds the ion flux. Since the biased disc can be considered as a primitive planar Langmuir probe, this indicates that the floating potential  $V_f$  (potential for which  $I_{\text{ion}} = I_{\text{electron}}$ ) lies between these values. For the JYFL 6.4 GHz ECRIS the floating potential for argon plasma was measured to be between 0 and  $-3$  V, suggesting that the plasma potential for the 6.4 GHz ion source is slightly higher compared with the 14 GHz ion source. This has been confirmed with dedicated plasma potential measurements performed with the JYFL ion sources [8, 13]. The electron densities cannot be deduced from the biased disc current signal (in comparison with typical Langmuir-probe diagnostics) due to the high energy electrons reaching the disc in spite of the retarding potential and due to the triangular shape of the particle flux (probe area  $\neq$  flux area)

### 3.2. Plasma breakdown time as a function of microwave power

The microwave power dependence of the plasma breakdown was studied with the JYFL 14 GHz ECRIS. The ion source settings were chosen as follows: calibrated neutral gas pressure of argon  $n_n = 3.4\text{E-}7$  mbar,  $B_{\text{inj}} = 2.02$  T,  $B_{\text{ext}} = 0.95$  T,

**Table 1.** Time measured from the leading edge of the microwave pulse required to reach 10% of the peak current,  $t_{10\%}$ , and the time required to reach the peak current,  $t_{\text{peak}}$ , for different microwave powers. Data measured for argon plasma (3.4E-7 mbar) with the JYFL 14 GHz ECRIS.

14 GHz microwave power (W)	$t_{10\%}$ (ms)	$t_{\text{peak}}$ (ms)
50	7.6 ( $\pm 0.5$ )	9.1 ( $\pm 0.5$ )
75	7.8 ( $\pm 0.5$ )	9.1 ( $\pm 0.5$ )
100	7.8 ( $\pm 0.5$ )	9.8 ( $\pm 0.5$ )
125	8.0 ( $\pm 0.5$ )	9.4 ( $\pm 0.5$ )
150	8.0 ( $\pm 0.5$ )	9.4 ( $\pm 0.5$ )
175	7.8 ( $\pm 0.5$ )	9.2 ( $\pm 0.5$ )
200	8.0 ( $\pm 0.5$ )	9.3 ( $\pm 0.5$ )
225	8.2 ( $\pm 0.5$ )	9.5 ( $\pm 0.5$ )
250	8.2 ( $\pm 0.5$ )	9.9 ( $\pm 0.5$ )
300	8.5 ( $\pm 0.5$ )	10.6 ( $\pm 0.5$ )
350	8.3 ( $\pm 0.5$ )	9.6 ( $\pm 0.5$ )
400	8.6 ( $\pm 0.5$ )	10.1 ( $\pm 0.5$ )
450	8.7 ( $\pm 0.5$ )	9.9 ( $\pm 0.5$ )
500	8.4 ( $\pm 0.5$ )	9.8 ( $\pm 0.5$ )
550	8.7 ( $\pm 0.5$ )	10.1 ( $\pm 0.5$ )
600	8.3 ( $\pm 0.5$ )	9.6 ( $\pm 0.5$ )
650	8.9 ( $\pm 0.5$ )	10.4 ( $\pm 0.5$ )
700	9.0 ( $\pm 0.5$ )	10.7 ( $\pm 0.5$ )

$B_{\text{min}} = 0.35$  T and bias disc voltage  $V_{\text{bd}} = -150$  V. The duration of the microwave pulses was about 2 s (enough to reach saturation current) with off time of 6 s between consecutive pulses. The results are presented in table 1 showing the time, measured from the leading edge of the microwave pulse, required to reach 10% of the peak current,  $t_{10\%}$ , and the time required to reach the peak current,  $t_{\text{peak}}$ , for different microwave powers. The error bars were determined by comparing ten consecutive pulses (average times shown in the table).

The data presented in the table suggest that the time required for plasma breakdown is almost independent of the applied microwave power. After the breakdown occurs, the peak current is reached very fast (within 1.5 ms). The saturation current is reached within 0.5–1 s. The ramp up time of the microwave power was measured to be on the order of microseconds. This cannot explain the delay between the applied microwave signal and plasma breakdown nor the current peak observed immediately after the breakdown.

### 3.3. Time dependence of the bias disc current as a function of neutral gas pressure and gas species

The neutral gas pressure of the plasma breakdown was studied with the JYFL 14 GHz ECRIS with all noble gases (helium, neon, argon, krypton and xenon) and oxygen ( $\text{O}_2$ ). The neutral gas pressures used for the measurements are within typical operational limits for ECR ion sources (E-7 to E-6 mbar). In these pressures the neutral gas is in the Knudsen regime, i.e. bulk properties vary significantly within a mean free path of neutrals. Enriched isotopic gases were not used for the measurement. The ion source settings were chosen as follows: (pulsed) microwave power  $P = 500$  W,  $B_{\text{inj}} = 2.02$  T,  $B_{\text{ext}} = 0.95$  T,  $B_{\text{min}} = 0.35$  T and bias disc voltage  $V_{\text{bd}} = -150$  V. The duration of the microwave pulses was about 5 s (enough

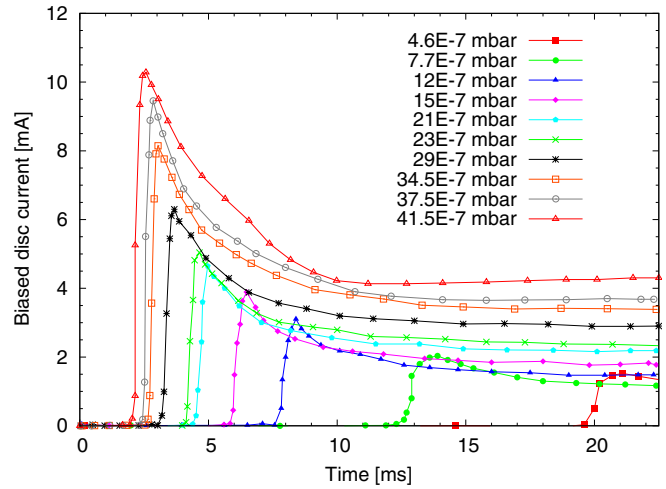


**Figure 4.** Time-resolved bias disc current of neon plasma as a function of neutral gas pressure during the first 22 ms of the applied microwave pulse. JYFL 14 GHz ECRIS, pulsed microwave power of 500 W, biased disc voltage of  $-150$  V, magnetic field at injection of 2.02 T, magnetic field at extraction of 0.95 T and magnetic field minimum of 0.35 T.

to reach saturation current) with off time greater than 30 s between consecutive pulses. As an example, figure 4 shows the time-resolved bias disc current signals measured at different neutral gas pressures of neon.

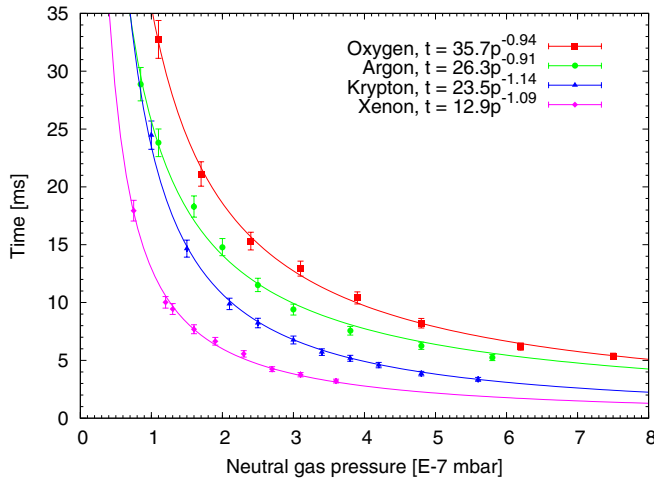
The figure shows that the time required for plasma breakdown depends strongly on the neutral gas density in the plasma chamber. The effect was further studied with different gas species as discussed below. The biased disc current increases with increasing neutral gas pressure indicating an increase in plasma density. However, by comparing the peak currents at each neutral gas pressure it can be deduced that the ionization degree of the plasma reduces with increasing neutral gas pressure degrading the gas efficiency of the ion source.

Figure 5 shows the time required to reach 10% of peak current,  $t_{10\%}$ , as a function of calibrated neutral gas pressure for oxygen, argon, krypton and xenon. The time is measured from the leading edge of the microwave pulse. Also a fit to the measured data is presented for each gas species. The equation describing the fit is presented in the data label with proper units. Similar data for helium and neon are presented in figure 6. The data are divided into two sets due to different order of magnitude in calibrated neutral gas pressures, which is a consequence of a vast difference in ionization probabilities of different gas species for a given electron energy distribution [14–16]. Note that error bars for  $t_{10\%}$  also depend on the neutral gas pressure.

The data in figures 5 and 6 show that the time required for the plasma breakdown (reaching 10% of the peak current) is almost inversely proportional to the neutral gas pressure for each gas species. The units in the equations for the data fits are ms for the time and E-7 mbar for the neutral gas pressure.

In order to explain the results we consider a simple model for the plasma breakdown. The volumetric rate of ionizing collisions  $f$  can be written as

$$f = \frac{dn_e}{dt} = n_e n_n \langle \sigma_{\text{ion}} v \rangle, \quad (1)$$



**Figure 5.** Time required for reaching 10% of peak biased disc current for oxygen, argon, krypton and xenon as a function of neutral gas pressure. JYFL 14 GHz ECRIS, pulsed microwave power of 500 W, biased disc voltage of  $-150$  V, magnetic field at injection of 2.02 T, magnetic field at extraction of 0.95 T and magnetic field minimum of 0.35 T. Fits for the experimental data are presented.

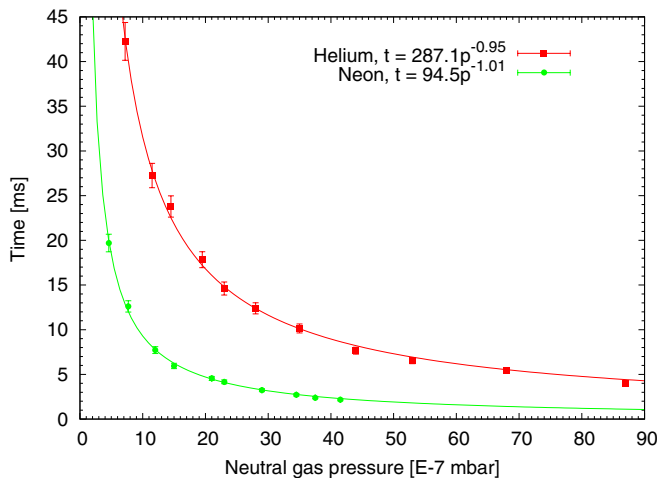


**Figure 6.** Time required to reach 10% of peak biased disc current for helium and neon as a function of neutral gas pressure. JYFL 14 GHz ECRIS, pulsed microwave power of 500 W, biased disc voltage of  $-150$  V, magnetic field at injection of 2.02 T, magnetic field at extraction of 0.95 T and magnetic field minimum of 0.35 T. Fits for the experimental data are presented.

where  $n_e$  is the electron density,  $n_n$  the neutral density,  $\sigma_{\text{ion}}$  the ionization cross section,  $v$  the relative velocity (electron and neutral particle) and  $\langle \rangle$  denotes the average over the velocity distribution. At the beginning of the plasma breakdown process we can assume that  $n_n$  is practically constant although the ionization degree reaches several tens of percent later during the microwave pulse. The validity of this assumption is supported by the fact that neutral gas density was observed to drop only after 20–25 ms from switching on the microwave power (this value contains the diffusion time of neutral gas from the plasma chamber to the pressure gauge). Furthermore, we impose a criterion for the plasma breakdown by stating that the breakdown occurs when the electron density reaches a critical value,  $n_{e,\text{critical}}$  sustaining the plasma and yielding

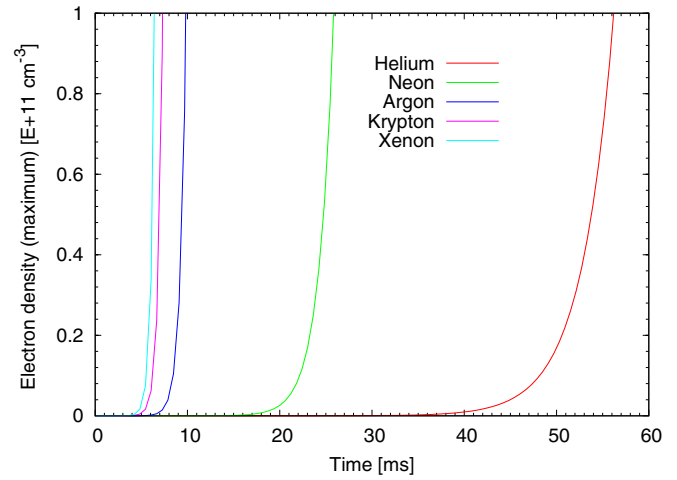


**Figure 7.** Calculated plasma electron density (maximum) for different gases from equation (2) as a function of time at 5 E-7 mbar neutral gas pressure. Cross section data from [14–16]. Decrease in the neutral gas density as a function of time is not taken into account.

measurable biased disc currents. Integrating the electron density in equation (1) from  $n_{e,0}$ , i.e. electron density in the plasma chamber at the beginning of the microwave pulse, to  $n_{e,\text{critical}}$  and time from  $t_0$  to  $t_{\text{breakdown}}$ , yields a characteristic time required for the breakdown:

$$t_{\text{breakdown}} = \frac{\ln(n_{e,\text{critical}}/n_{e,0})}{n_n \langle \sigma_{\text{ion}} v \rangle}. \quad (2)$$

For the integration we have assumed that  $\langle \sigma_{\text{ion}} v \rangle$  is independent of time, i.e. electron heating is not taken into account.

Equation (2) predicts that the time required for plasma breakdown is inversely proportional to neutral particle density as long as the other variables remain constant. The model is in good agreement with the results presented in figures 5 and 6. The exponent of the neutral gas pressure in the data fits ranges from  $-0.91$  to  $-1.14$  for the studied gas species ( $n_n \propto p$ ). The fact that the plasma breakdown is inversely proportional to  $\langle \sigma_{\text{ion}} v \rangle$  explains the difference in breakdown times (an order of magnitude) observed with different gas species at fixed neutral gas pressure. The extreme cases in this respect are helium and xenon whose ionization cross sections from neutral gas to 1+ ion differ approximately an order of magnitude at electron energies most relevant for the ionization of neutral gas [14–16]. Cross sections for all other gas species that were studied for this work fall within the range set by helium and xenon.

As an example, we calculate the (maximum) electron density as a function of time from equation (2) for all the noble gases at neutral gas pressure of 5 E-7 mbar. For the calculation we use maximum cross sections for ionizing collisions, i.e. optimum electron energy, and assume that ions are essentially stationary. Substituting cross section values from [14–16] into equation (2) and estimating that  $n_{e,\text{crit}}$  is  $10^7$  times greater than  $n_{e,0}$  yields the curves presented in figure 7. The corresponding (maximum) cross sections and (optimal) electron energies are as follows [14–16]: helium  $\sigma = 4.00$  E-17 cm<sup>2</sup>/E<sub>e</sub> = 100 eV, neon  $\sigma = 6.67$  E-17 cm<sup>2</sup>/E<sub>e</sub> = 170 eV, argon  $\sigma = 2.40$  E-16 cm<sup>2</sup>/E<sub>e</sub> = 90 eV, krypton

$\sigma = 5.61 \text{ E-}16 \text{ cm}^{-2}/E_e = 30 \text{ eV}$ , xenon  $\sigma = 4.90 \text{ E-}17 \text{ cm}^{-2}/E_e = 50 \text{ eV}$ . A more realistic calculation would require calculating  $\langle \sigma_{\text{ion}} v \rangle$  over the range most relevant for the plasma breakdown. However, the order of magnitude for  $t_{\text{breakdown}}$  remains unchanged even if this procedure is carried out. Our estimate of  $n_{e,0}$  assumes that the electric fields of the microwave modes excited to the cavity are capable of creating an electron density of  $10^4 \text{ cm}^{-3}$  by field ionization, which is plausible due to the extremely high Q factor of an empty cavity [17]. Therefore, the saturation electron density in our example is on the order of  $10^{11} \text{ cm}^{-3}$ , which is a commonly accepted value for ECR ion sources [18].

Figure 7 shows that the plasma breakdown times calculated from equation (2) are on the same order of magnitude as the experimental results. Moreover, the model can explain the difference between the elements. Studying the time evolution of the electron density, calculated from equation (2), also reveals that the observed abrupt rise in plasma density (within 1–2 ms from the breakdown) can be explained with the simple model. This is due to the exponential increase in the electron density as a function of time as long as the supply of neutrals remains sufficient, i.e. ‘neutral starvation’ does not take place. As long as the assumptions of the model hold, the availability of neutrals limits the peak density (biased disc current), which was also observed during the experiments (figures 4 and 9).

### 3.4. The effect of ‘seed electrons’ on the plasma breakdown time

According to our simple model the characteristic plasma breakdown time depends strongly on the electron density in the plasma chamber at the beginning of the microwave pulse,  $n_{e,0}$ . As a next step of the experiments this prediction was tested qualitatively.

It has been observed earlier that at the usual pressure regime of ECR discharge bremsstrahlung is detected even seconds after switching off the microwave power [19], i.e. electrons can remain confined in the minimum- $B$  structure of an ECRIS for relatively long times. Therefore, it can be expected that the microwave pulse repetition rate affects the plasma breakdown time if the off time is shorter than the confinement time. In this scenario the electrons from the previous microwave pulse would act as ‘seed electrons’ shortening the breakdown time for the consecutive microwave pulse. The effect of the microwave pulse separation was studied with the JYFL 6.4 GHz ECRIS. This ion source was chosen because the effect of the axial and radial magnetic field strength on the plasma breakdown time could be studied simultaneously. The Modified MultiPole Structure [20] of the JYFL 6.4 GHz ECRIS allows adjusting the radial sextupole magnetic field (in addition to adjusting the axial field), which makes this ion source more versatile for the experiment compared with the JYFL 14 GHz ECRIS with fixed sextupole strength.

The effect of the microwave pulse separation was studied with the following settings: (pulsed) microwave power  $P = 200 \text{ W}$ , neutral gas pressure of argon =  $3.2 \text{ E-}7 \text{ mbar}$ ,

**Table 2.** Time measured from the leading edge of the microwave pulse required to reach 10% of the peak current,  $t_{10\%}$ , for different microwave pulse separations. Data measured for argon plasma ( $3.2\text{E-}7 \text{ mbar}$ ) with the JYFL 6.4 GHz ECRIS.

Time between microwave pulses (s)	Plasma breakdown time, $t_{10\%}$ (ms)
1	7.5 ( $\pm 0.5$ )
2	8.5 ( $\pm 0.5$ )
3	10.5 ( $\pm 0.5$ )
5	12 ( $\pm 0.5$ )
10	17.5 ( $\pm 1$ )
15	22 ( $\pm 3$ )
30	21 ( $\pm 3$ )
60	36 ( $\pm 9$ )
120	28 ( $\pm 4$ )
180	26 ( $\pm 3$ )
300	34 ( $\pm 8$ )

$B_{\text{inj}} = 1.08 \text{ T}$ ,  $B_{\text{ext}} = 0.54 \text{ T}$ ,  $B_{\text{min}} = 0.17 \text{ T}$  and bias disc voltage  $V_{\text{bd}} = -50 \text{ V}$ . The duration of the microwave pulses was 5 s with variable off time between consecutive pulses. The plasma breakdown time as a function of microwave off time is presented in table 2.

The data presented in the table demonstrate that the time between microwave pulses indeed affects the plasma breakdown time, which increases almost linearly from 7.5 ms to 22 ms as the time between microwave pulses increases from 1 to 15 s. As the off time was further increased, the time required for the plasma breakdown became clearly more random, which is highlighted by the increase in the error margins. The effect was observed to be independent of the microwave power and was also observed with the JYFL 14 GHz ECRIS. The result indicates that some electrons from the previous microwave pulse are being confined up to 10–20 s. These electrons affect the plasma breakdown time for the consecutive pulse, as suggested by our model.

This conclusion was tested further by varying the magnetic field strength of the JYFL 6.4 GHz ECRIS at fixed off time between microwave pulses. Microwave power (pulsed) was set to  $P = 200 \text{ W}$ , neutral gas pressure of argon to  $3.2 \text{ E-}7 \text{ mbar}$ , bias disc voltage to  $V_{\text{bd}} = -50 \text{ V}$  and the time between microwave pulses to 5 s. Varying the magnetic field (axial and radial) affects the electron confinement and, consequently, the density of seed electrons from the previous microwave pulse,  $n_{e,0}$ . Figure 8 illustrates the plasma breakdown time ( $t_{10\%}$ ) as a function of the axial magnetic field strength for three different microwave pulse separations (off times). The solenoid field strength is compared with the maximum field that can be attained with the JYFL 6.4 GHz ECRIS (maximum coil currents). The highest possible magnetic field strengths with maximum coil currents are  $B_{\text{inj}} = 1.2 \text{ T}$ ,  $B_{\text{ext}} = 0.6 \text{ T}$ ,  $B_{\text{min}} = 0.19 \text{ T}$ , i.e. the field strength was varied as follows:  $B_{\text{inj}} = 1.2\text{--}0.96 \text{ T}$ ,  $B_{\text{ext}} = 0.6\text{--}0.48 \text{ T}$ ,  $B_{\text{min}} = 0.19\text{--}0.15 \text{ T}$ . The radial field strength was set with the MMPS structure to  $0.9 \text{ T}$ , measured on the wall of the plasma chamber at the magnetic pole.

The plot clearly shows that the time required for the plasma breakdown (measured from the leading edge of the microwave pulse) depends on the magnetic field strength and

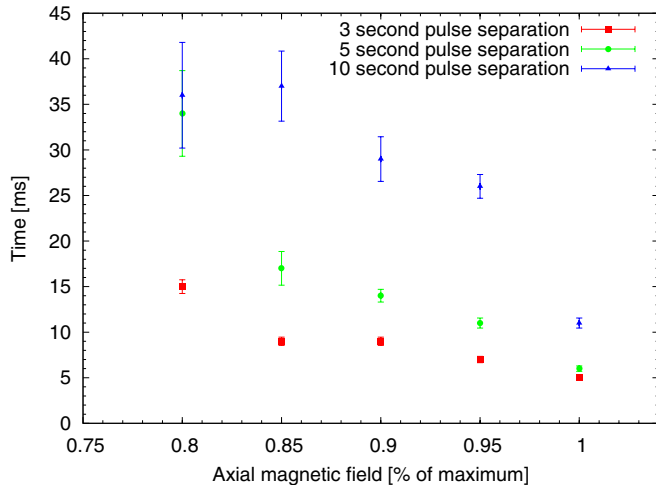


**Figure 8.** Time required to reach 10% of peak biased disc current a function of microwave pulse separation (time between consecutive pulses) and axial magnetic field strength. JYFL 6.4 GHz ECRIS, argon plasma, pulsed microwave power of 200 W, biased disc voltage of  $-50$  V.

microwave pulse separation. When the microwave pulse separation was increased further, it was observed that there was practically no difference in plasma breakdown times observed with different magnetic field strengths. This confirms that the effect displayed in figure 8 is indeed due to seed electrons from the previous pulse.

The effect of the radial confinement was studied by adjusting the MMPS structure. The sextupole field at the magnetic pole was lowered to 0.5 T. It was observed that the plasma breakdown time at given pulse separation (3, 5 and 10 s were used) increased approximately 10% compared with the situation at 0.9 T radial field. The effect of the radial confinement was therefore less pronounced as the effect of the axial confinement. This is supported by the observation [3] that in ECRIS minimum- $B$  structure electron losses are concentrated in the axial direction.

Finally, the role of seed electrons in the plasma breakdown time was studied with the JYFL 14 GHz ECRIS operated in double frequency mode. A very low power ( $<10$  W) secondary frequency of 11.56 GHz was launched into the plasma chamber by a travelling wave tube amplifier (TWTA) in continuous (cw) mode. This corresponds to only 2.5% of the full capacity of the TWTA at JYFL. In addition, 350 W of microwave power from the klystron was applied in pulsed mode. The pulse length was set to 5 s with spacing of 30 s between consecutive pulses. In fact, the TWTA is already sustaining a very low density plasma, which is illustrated by the offset of bias disc current before triggering the microwave pulse from the klystron ( $t = 0$ ). Therefore, by ‘plasma breakdown’ time we mean the time required to reach high density plasma after applying 350 W at 14 GHz. Figures 9 and 10 illustrate the effect of the seed electrons provided by the microwave power from the TWTA (5 W in this case). The experiment was carried out with helium since it was observed earlier that ignition of helium discharge takes most time at given pressure (lowest ionization cross section of noble gases). The magnetic field was set to

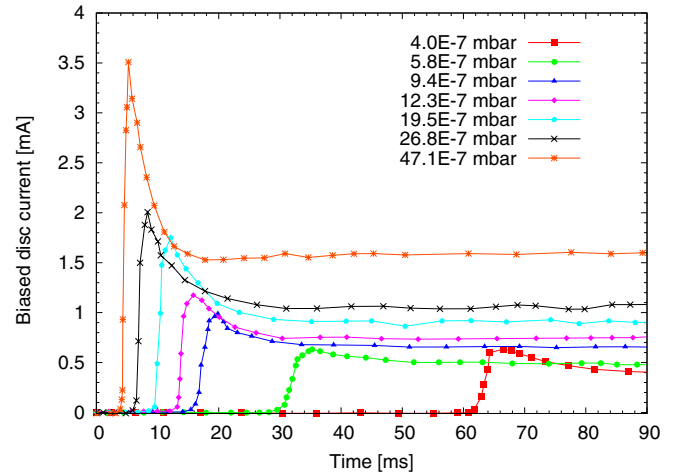


**Figure 9.** Time-resolved bias disc current of helium plasma as a function of neutral gas pressure during the first 90 ms of the applied microwave pulse. JYFL 14 GHz ECRIS, pulsed microwave power 350 W at 14 GHz, biased disc voltage of  $-70$  V, magnetic field at injection of 2.02 T, magnetic field at extraction of 0.95 T and magnetic field minimum of 0.35 T.

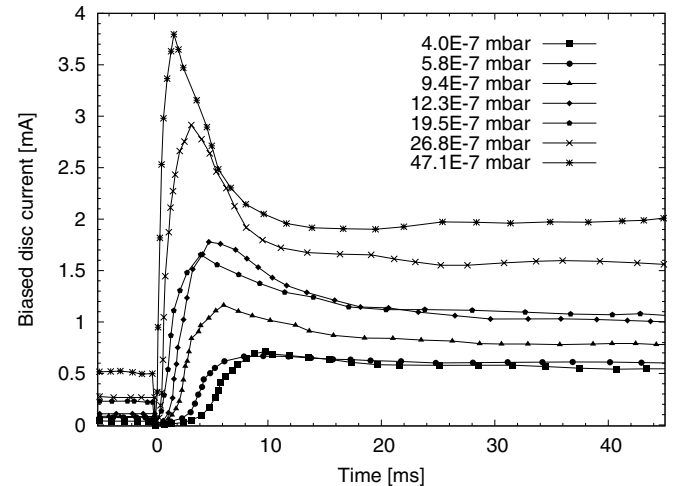


**Figure 10.** Time-resolved bias disc current of helium plasma as a function of neutral gas pressure during the first 45 ms of the applied microwave pulse. JYFL 14 GHz ECRIS, pulsed microwave power of 350 W at 14 GHz, cw microwave power of 5 W at 11.56 GHz, biased disc voltage of  $-70$  V, magnetic field at injection of 2.02 T, magnetic field at extraction of 0.95 T and magnetic field minimum 0.35 T.

$B_{\text{inj}} = 2.02$  T,  $B_{\text{ext}} = 0.95$  T,  $B_{\text{min}} = 0.35$  T and bias disc voltage to  $V_{\text{bd}} = -150$  V.

The figures demonstrate the remarkable effect of the seed electrons. The plasma breakdown time (time to reach 10% of maximum current) was reduced from 4–62 ms without the TWTA to 0.3–2.2 ms with the TWTA. The latter time range is practically equal to the confinement time (diffusion time) of ions from the core plasma to the biased disc [21]. The most outstanding result is that the breakdown time becomes almost independent of the neutral gas pressure. The implications of this result are discussed in the next section. The effect was observed already at cw power level of 2.5 launched from the TWTA (lowest possible). The current signal at  $t < 0$  ms in figure 7 is due to the seed plasma sustained by the TWTA.

The reason for the sudden drop in the biased disc current followed by application of the high power microwave signal is somewhat unknown. It is possible that this behaviour is due to higher mobility of electrons compared with ions, which causes the flux of electrons to override the flux of ions momentarily as the plasma density is increased by the additional microwave power. More experiments including a time-resolved plasma potential measurement will be carried out in the near term future to explain this behaviour. Equation (2) can be used to understand the shift of the rise time to the sub-millisecond time scale by substituting the known cross sections [14–16], neutral gas density and noticing that the steady-state electron density (with 350 W pulsed at 14 GHz + 5 W cw at 11.56 GHz) is higher by a factor of 3–10 to the electron density sustained by the TWTA (5 W cw at 11.56 GHz) at the given neutral gas pressure.

#### 4. Discussion

We have presented a consistent set of experimental results covering the effects of ECR ion source tuning parameters such as microwave power, neutral gas density, bias voltage, magnetic field strength etc, on the plasma breakdown time. It was observed that the plasma breakdown time is virtually independent of biased disc voltage and applied microwave power. During the initial phase of the breakdown the biased disc current (plasma) exhibits a transient peak. A similar transient has also been observed with other plasma devices such as inductively coupled rf ion sources [22] and helicon plasma generators [23] operated in MHz-range with orders of magnitude higher neutral gas pressures (0.1–100 mbar). In these cases the observed transient peak in plasma density has been associated with neutral depletion due to ‘ion pumping’ as the ions transfer energy to neutrals in collisions [23, 24]. In fact, neutral depletion presents a problem for inductively coupled rf ion sources suffering from inability to sustain high plasma densities when operated with long rf pulses (>1 ms) [22]. Our results suggest that a similar process (neutral depletion) could also take place in a very low pressure regime. The observation that microwave power had virtually no effect on the plasma breakdown time could be explained by the fact that electrons can gain energies far beyond the ionization potential of neutral atoms in single resonance crossing. This is due to very high electric field (high Q-value of the plasma chamber) [17] sustained even by low power microwaves before the plasma breakdown.

We have observed that the plasma breakdown time is inversely proportional with the neutral gas pressure. This result is in good agreement with a simple model derived from the volumetric rate of ionizing collisions in section 3.3. Similar dependence has been observed in microwave heated plasmas at higher pressures [25]. Our results extend the validity of this model into the very low pressure regime. Furthermore, the model predicts that the plasma breakdown time depends strongly on the density of ‘seed electrons’ whose role on the plasma breakdown characteristics was studied by varying the microwave pulse separation and magnetic field strength, presumably affecting the electron confinement times

and finally by igniting a low density plasma sustained by less than 10 W (in cw mode) of microwave power corresponding to the power level of cheap commercial TWT amplifiers.

It was observed that microwave pulse separation up to several seconds is required to erase the influence of the previous pulse. The conclusion is that hot electrons can remain confined in the magnetic field structure of a modern ECR ion source for several seconds after the ECR heating process is interrupted by switching off the microwave power. Cold electrons escape from the magnetic field immediately after the microwave power is switched off since they are no longer being actively removed from the loss cone by the ECR heating process increasing the velocity component perpendicular to the external magnetic field. This sudden leakage of charged particles from the magnetic field leads into a well-known afterglow transient at the end of the microwave pulse [26]. However, as the plasma density exhibits a fast decay, the collision frequency of the trapped hot electrons with  $v_{\perp} > v_{\parallel}$  is reduced leading presumably to hot electron confinement times on the order of seconds. As the cold electrons escape and hot electrons remain trapped, the electron energy distribution function shifts towards higher energies and the plasma becomes prone to instabilities, which have been detected (with JYFL 14 GHz ECRIS) during the afterglow.

Sustaining low density plasma with low level microwave power from the TWTA caused the plasma breakdown time to become very short (<1 ms) and virtually independent of the neutral gas pressure. This could be very important result for future operations of ECR ion sources in pulsed mode. It has been recently observed [11] that a fast transient peak in extracted ion currents of low and medium charge states occurs at the very beginning of the microwave pulse. This phenomenon has been named preglow as an explicit reference to the well-known afterglow transient. It has been suggested that the preglow transient could be utilized for the Beta Beam project [11] (neutrino physics) requiring fast and efficient ionization of radioactive  ${}^6\text{He}$  and  ${}^{18}\text{Ne}$  in pulsed operation for direct injection into a post accelerator LINAC. Seed electrons provided by low power microwaves from the TWTA could provide a cost-effective means to speed up the ionization process and minimize losses of radioactive ions. Moreover, this ‘forced preglow’ -technique could allow optimizing the charge state distribution of the extracted ion beams by varying the neutral gas pressure without simultaneously affecting the time required for the plasma breakdown (ionization time). This was confirmed with the JYFL 14 GHz ECRIS by measuring the extracted ion beam currents of helium and neon exhibiting the preglow transient. It was observed that the seed electrons cause the charge state distribution of the extracted ion beams to shift towards higher charges during the preglow, which is very practical taking into account the possible applications. Presenting these results in detail is out of the scope of this work focusing to plasma breakdown diagnostics with the biased disc. A similar technique, i.e. low power secondary frequency applied between high power pulses in order to ensure fast and repeatable plasma breakdown has been utilized earlier for the SNS (US Spallation Neutron Source) inductively

coupled rf ion source (MHz frequency range, orders of magnitude higher neutral gas pressure) intended for H<sup>-</sup> ion production [27].

## Acknowledgments

This work has been supported by the Academy of Finland under the Finnish Centre of Excellence Programme 2006–2011 (Nuclear and Accelerator Based Physics Programme at JYFL).

## References

- [1] Melin G *et al* 1990 *Proc. 10th Int. Workshop on ECR Ion Sources (Knoxville, TN) INS Report No Conf.-9011136* p 1
- [2] Drentje A G 2003 *Rev. Sci. Instrum.* **74** 2631
- [3] Gammino S, Sibring J and Drentje A G 1992 *Rev. Sci. Instrum.* **63** 2872
- [4] Biri S *et al* 1999 *Proc. 14th Int. Workshop on ECR Ion Sources (Geneva, Switzerland)* p 81
- [5] Stiebing K E, Hohn O, Runkel S, Schmidt L, Schmidt-Böcking H, Mironov V and Shirkov G 1999 *Phys. Rev. ST Accel. Beams* **2** 123501
- [6] Mironov V, Stiebing K E, Hohn O, Schmidt L, Schmidt-Böcking H, Runkel S, Schempp A, Shirkov G, Biri S and Kenez L 2002 *Rev. Sci. Instrum.* **73** 623
- [7] Tarvainen O, Suominen P and Koivisto H 2004 *Rev. Sci. Instrum.* **75** 3138
- [8] Drentje A G, Wolters U, Nadzeyka A, Meyer D and Wiesemann K 2002 *Rev. Sci. Instrum.* **73** 516
- [9] Koivisto H, Moisio M, Nieminen V, Suominen P and Liukkonen E 2003 *Nukleonika* **48** S81
- [10] Koivisto H, Heikkinen P, Hänninen V, Lassila A, Leinonen H, Nieminen V, Pakarinen J, Ranttila K, Ärje J and Liukkonen E 2001 *Nucl. Instrum. Methods Phys. Res. B* **174** 379
- [11] Izotov I V, Sidorov A V, Skalyga V A, Zorin V G, Lamy T, Latrasse L, Thuillier T 2008 *IEEE Trans. Plasma Sci. Part 2* **36** 1494
- [12] Ropponen T, Tarvainen O, Jones P, Peura P, Kalvas T, Suominen P, Koivisto H and Ärje J 2009 *Nucl. Instrum. Methods Phys. Res. A* **600** 525
- [13] Tarvainen O, Suominen P, Ropponen T, Kalvas T, Heikkinen P and Koivisto H 2005 *Rev. Sci. Instrum.* **76** 093304
- [14] Povyshev V M, Sadovoy A A, Shevelko V P, Shirkov G D, Vasina E G and Vatulin V V 2001 *Communication of the Joint Institute for Nuclear Research E9-2001-148*, Dubna
- [15] Phillippov A, Povyshev V M, Sadovoy A A, Shevelko V P, Shirkov G D, Vasina E G and Vatulin V V 2002 *Communication of the Joint Institute for Nuclear Research E9-2002-5*, Dubna
- [16] Almeida D P, Fontes A C and Godinho C F L 1995 *J. Phys. B: At. Mol. Opt. Phys.* **28** 3335
- [17] Consoli F, Celona L, Ciavola G, Gammino S, Maimone F, Barbarino S, Catalano R S and Mascali D 2008 *Rev. Sci. Instrum.* **79** 02A308
- [18] Girard A, Hitz D, Melin G and Serebrennikov K 2004 *Rev. Sci. Instrum.* **75** 1381
- [19] Wiesemann K 2009 private communication
- [20] Suominen P, Tarvainen O and Koivisto H 2006 *Rev. Sci. Instrum.* **77** 03A332
- [21] Mironov V and Beijers J P M [arXiv:0811.2865v1](https://arxiv.org/abs/0811.2865v1) [physics.atom-ph]
- [22] Welton R F, Stockli M P, Murray S N, Kang Y and Peters J 2006 *Rev. Sci. Instrum.* **77** 03A508
- [23] Clarenbach B, Lorenz B, Krämer M and Sadeghi N 2003 *Plasma Sources Sci. Technol.* **12** 345
- [24] Chen F F, Sudit I D and Light M 1996 *Plasma Sources Sci. Technol.* **5** 173
- [25] Yadav V K, Sathyanarayana K and Bora D 2008 *Pramana J. Phys., Indian Acad. Sci.* **70** 487
- [26] Geller R 1996 *Electron Cyclotron Resonance Ion Sources and ECR Plasmas* (London: Institute of Physics Publishing) ISBN 0740301074
- [27] Schenkel T, Staples J W, Thomae R W, Reijonen J, Gough R, Leung K N, Keller R, Welton R and Stockli M 2002 *Rev. Sci. Instrum.* **73** 1017



## APPENDIX A.VI



# Time Evolution of High-Energy Bremsstrahlung and Argon Ion Production in Electron Cyclotron Resonance Ion-Source Plasma

Tommi Ropponen, Olli Tarvainen, Pete Jones, Pauli Peura, Taneli Kalvas, Pekka Suominen, and Hannu A. Koivisto

**Abstract**—Bremsstrahlung radiation measurement is one of the most commonly used plasma-diagnostics methods. Most of the bremsstrahlung measurements with electron cyclotron resonance ion sources (ECRISs) have been performed in continuous-operation mode yielding information only on the steady-state bremsstrahlung emission. This paper describes results of bremsstrahlung and argon ion-current measurements with the JYFL 14-GHz ECRIS operated in a pulsed mode. The bremsstrahlung radiation was studied as a function of neutral-gas pressure and radio frequency power. The timescale of ECRIS bremsstrahlung production is compared to ion-production timescale for different charge states of argon for the first time. It was observed, for example, that the ion currents of different charge states reach the steady state before the bremsstrahlung emission rate saturates.

**Index Terms**—Bremsstrahlung time evolution, electron cyclotron resonance (ECR), preglow.

## I. INTRODUCTION

ELECTRON cyclotron resonance ion sources (ECRISs) [1] with solenoid and sextupole confinement have commonly been used to produce highly charged ions from heavy elements since the 1980s. Despite of the dedicated experiments on bremsstrahlung emission from magnetized ECR heated plasmas (see, e.g., [2], [3]) and all the operational experience with modern ECRISs (with sextupole structure), the details of the electron heating mechanism in ECRIS plasmas are still not completely understood. Therefore, more information about the effects of different ion-source parameters on the electron energy distribution is needed. This information could eventually help to mitigate radiation and cryostat heating problems often related to high-performance fully superconducting

third-generation ECR ion-source technology utilizing 28-GHz radio frequencies. Large-scale nuclear physics infrastructures and programs, such as RIBF at RIKEN, will need ion-beam intensities beyond the performance of the best third-generation ECRISs. Consequently, next-generation ECRISs using 50–60-GHz microwave frequencies has to be developed. The heating of cryostat of such an ion source will be a considerable problem.

In order to understand the stochastic ECR heating process, time-resolved measurements of the bremsstrahlung radiation under a variety of ion-source plasma conditions have been performed with the JYFL 14-GHz ECRIS [4]. The goal of the experiments has been to measure the timescale needed for production of high-energy (over 30 keV) electrons and link this information with ion-beam production times. This paper completes the experiments with different ion-source parameters (data on the effect of the magnetic field gradient on the time evolution of bremsstrahlung have been presented in [5]) and connects the ion-production times for different charge states of argon to the time evolution of the electron energies. The measurement setup and the data-analysis code have been thoroughly described in [5]. Thus, the measurement setup is discussed only briefly in this paper.

It has been observed [6] that the ion currents (low and medium charge states) extracted from an ECRIS plasma exhibit a repeatable transient current peak occurring at the very beginning of the plasma breakdown. This phenomenon has been named preglow as an explicit reference to the well-known afterglow transient at the end of the microwave pulse. The experiments at 18 and 28 GHz have demonstrated that the preglow effect occurs within a few milliseconds from the beginning of the microwave pulse. A theoretical model describing the preglow effect has also been developed [6], being in relatively good agreement with the experimental results. During the preglow transient, the ion currents of low and medium charge states are typically two to five times higher compared to steady state [6]. It has been proposed that the preglow transient could be used in ion production in Beta Beam Project [7], for example.

In this paper, the results of the time-resolved plasma diagnostics of the hot-electron population in modern ECRIS with solenoid and sextupole confinement are combined with the data on the ion currents (preglow effect) for the first time. The time dependence of high-charge-state argon ion-beam currents, not exhibiting the preglow behavior, is also briefly discussed.

Manuscript received January 16, 2009; revised March 18, 2009 and August 3, 2009. First published September 25, 2009; current version published November 11, 2009. This work was supported by the Academy of Finland under the Finnish Centre of Excellence Program 2006–2011 (Nuclear and Accelerator Based Physics Program at JYFL). The work of T. Ropponen was supported by the Graduate School in Particle and Nuclear Physics.

T. Ropponen, O. Tarvainen, P. Jones, P. Peura, T. Kalvas, and H. A. Koivisto are with the Department of Physics, University of Jyväskylä, 40014 Jyväskylä, Finland (e-mail: tommy.ropponen@jyu.fi; olli.tarvainen@jyu.fi; pete.jones@phys.jyu.fi; pauli.peura@jyu.fi; taneli.kalvas@jyu.fi; hannu.koivisto@phys.jyu.fi).

P. Suominen is with the Magnet Technology Centre, Prizztech Ltd., 28600 Pori, Finland (e-mail: pekka.suominen@gmail.com).

Color versions of one or more of the figures in this paper are available online at <http://ieeexplore.ieee.org>.

Digital Object Identifier 10.1109/TPS.2009.2030412

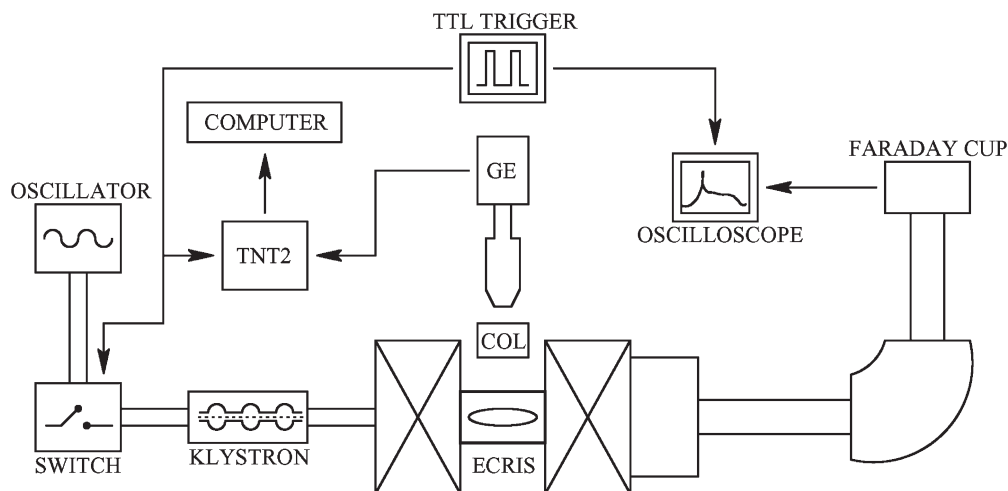


Fig. 1. Measurement setup of the bremsstrahlung time evolution and the preglow measurements. Germanium detector marked with “GE,” collimator marked with “COL,” and “TNT2” is the digital signal processing unit.

## II. MEASUREMENT SETUP AND THE DATA ANALYSIS

A capability for the ion-beam current measurement in pulsed operation was added to the setup described in detail in [5]. The main components of the setup are a fast RF switch, digital signal processing unit (TNT2 [8]), and a germanium detector. The schematic drawing of the setup is shown in Fig. 1.

The timing signal from the TTL trigger is used to synchronize the pulsing of the microwave power, the data processing in the digital signal processing unit, and the triggering in the oscilloscope. This allows the marking of both the leading and the trailing edge of the RF pulse into the raw measurement data. Signal from the 14-GHz GUNN-type oscillator is pulsed with the RF switch resulting in a pulsed RF power launched into the plasma chamber. Inside the ECRIS chamber, bremsstrahlung events are generated, and after collimation, the photons are detected at the germanium detector. Digital signal processing is used to record and time-stamp the raw measurement data, and finally, the preprocessed data are stored to a computer hard drive. A digital oscilloscope (Tektronix DPO4104) connected to a Faraday cup located downstream from the bending magnet was used for the time-resolved ion-beam current measurements of different charge states. The voltage signal corresponding to extracted ion current was recorded from the Faraday cup with a sample rate of 250 ks/s, i.e., 430 ks/RF pulse (1.76-s pulses with a duty factor of 22.9% were used). An extraction voltage of 10 kV was applied whenever ion-beam currents were recorded. When the bremsstrahlung was studied as a function of neutral-gas pressure or RF power, extraction voltage was not applied (as in the measurements described in [5]).

Due to the nature of the klystron amplifier (constant gain) and the fast rise time of the RF switch (specified rise time of 40 ns), the error due to the RF control circuit is negligible. The ion time-of-flight from the plasma to the Faraday cup ranges roughly from  $7.2 \mu\text{s}$  ( $\text{Ar}^{5+}$ ) to  $4.7 \mu\text{s}$  ( $\text{Ar}^{12+}$ ) with an extraction voltage of 10 kV. This is approximately three orders of magnitude less than the timescale of interest (in millisecond) and is omitted in the following considerations.

Bremsstrahlung data from 680 RF pulses are combined in the C++ analyzing code in order to gain enough statistics when sorting the bremsstrahlung data. The counts caused by background radiation and pile-up events are subtracted from the data. The preglow ion-current measurement data are averaged over 20 consecutive data points to decrease the noise. Only the relative efficiency calibration of the Ge detector was performed, and subsequently, the count rates are not absolute. Shaping time of the signal created in the Ge detector was set to  $2 \mu\text{s}$ , and a time step of 2 ms was used while generating the time evolution of bremsstrahlung spectra and the total count rate. The detector crystal was located about 990 mm away from the outer plasma chamber wall of the JYFL 14-GHz ECRIS [5].

By measuring the amplified RF signal from the klystron, it was also observed that there is a transient peak in the beginning of the RF pulse. A short power peak (600 W) with a duration of about  $50 \mu\text{s}$  is observed immediately after the RF oscillator signal is launched into the klystron. This peak drops rapidly, and the RF power reaches the preset RF power value after about  $600 \mu\text{s}$ .

The bremsstrahlung radiation is measured radially from one of the magnetic field poles of the JYFL 14-GHz ECRIS. The detector was located between the solenoids in axial direction. The bremsstrahlung observed by the Ge detector is consequently a mixture of thick target (wall) and plasma bremsstrahlung. In the ECR ion-source plasma, the location of the resonance zone depends on the electron energy due to relativistic effects. As a consequence, it is impossible to determine the relative location of the resonance zone, and the detector in a unique manner as the high-energy electrons (subject of this paper) are accelerated in a large volume. Moreover, the angular distribution of the thick target bremsstrahlung is a function of electron energy (for pinhole images showing the radial locations where bremsstrahlung events are generated in a typical 14-GHz ECRIS plasma, see [9]).

Typical photon energies in the bremsstrahlung spectra recorded from the JYFL 14-GHz ECRIS with the Ge detector are between 30 keV (close to the detector threshold) and 400 keV.

TABLE I

MAGNETIC FIELD STRENGTHS OF THE JYFL 14-GHz ECRIS WITH DIFFERENT COIL SETTINGS AND THE CORRESPONDING RESONANCE LENGTH IN AXIAL DIRECTION. SUBSCRIPT "INJ" REFERS TO INJECTION SIDE OF THE ECRIS, "EXT" EXTRACTION, "MIN" MINIMUM OF THE MAGNETIC FIELD LOCATED AT THE CENTER OF THE PLASMA CHAMBER, AND SUPERScript "RES" REFERS TO RESONANCE. RESONANCE POINTS CALCULATED FOR AN ELECTRON WITH NO KINETIC ENERGY

Magnetic field setting	$B_{inj}$	$B_{min}$	$B_{ext}$	$\nabla B_{inj}^{res}$	$\nabla B_{ext}^{res}$	$d_{res}$
#1 (500/500 A)	2.011 T	0.346 T	0.946 T	5.9 T/m	5.5 T/m	111 mm
#2 (491/491 A)	1.992 T	0.338 T	0.932 T	6.0 T/m	5.6 T/m	114 mm

Usually, it takes about 10–15 ms before the bremsstrahlung counts start to appear in the spectra, and the bremsstrahlung spectra become time independent as soon as the total count rate data saturate (for a typical radially measured time-evolution animation of JYFL 14-GHz ECRIS bremsstrahlung spectra and time evolution of different photon energies, see [5]).

### III. EXPERIMENTAL RESULTS

In the measurements presented in this paper, two different axial magnetic field settings (different solenoid currents) of the JYFL 14-GHz ECRIS were used. Details of these magnetic field values can be found at Table I. A biased disk voltage of  $-150$  V, which is typical for ECRIS operation, was used throughout the measurements reported in this paper. Argon and oxygen plasmas were studied.

#### A. Time Evolution of the Bremsstrahlung Radiation as a Function of the Neutral-Gas Pressure

The presented neutral-gas pressure readings for argon and oxygen plasmas were calibrated with calibration factors indicated in a Balzer's Penning gauge manual. Gas feed rate was adjusted to correspond a given pressure reading with magnetic field setting #1 (magnetic field has a slight effect on the gauge reading), and the RF power was kept off during the gas feed adjustments. After each measurement, the neutral-gas pressure reading was verified in order to ensure that the pressure remained constant during the experiment. The data for argon and oxygen are measured using magnetic field setting #1 and RF power of 500 W. Due to similar behavior, only data from argon plasma bremsstrahlung are presented in this paper. Measurements with oxygen plasma are discussed. In the following figures,  $T = 0$  corresponds to the leading edge of the RF pulse.

The time evolution of bremsstrahlung counts integrated over the energy spectrum (plotted from 15 to 600 keV) is shown in Figs. 2 and 3 for argon plasma with different neutral-gas pressures. In Fig. 2, the lowest, middle, and uppermost curves at a time of 1000 ms correspond to the neutral-gas pressures of  $3.5 \cdot 10^{-7}$ ,  $2.6 \cdot 10^{-7}$ , and  $1.5 \cdot 10^{-7}$  mbar, respectively. The highest count rate was produced with the lowest pressure, which is likely to yield the lowest plasma density. The steady-state count rates are reached between 200 and 300 ms depending on the neutral argon gas pressure inside the ECRIS plasma chamber.

The drain current indicating total amount of extracted ions from the JYFL 14-GHz ECRIS is typically lower at low neutral-gas pressures, supporting the assumption that the plasma den-

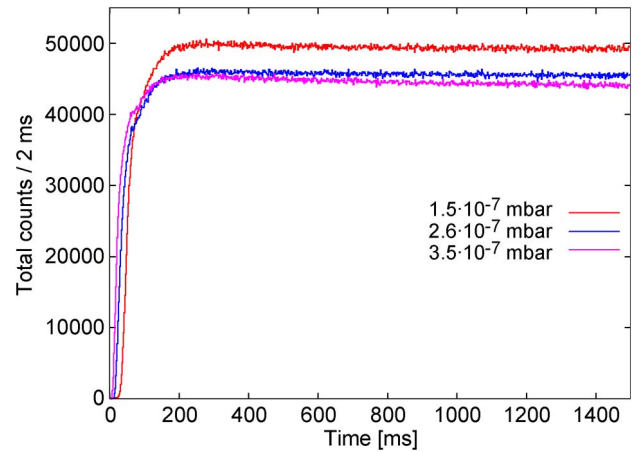


Fig. 2. Comparison of the bremsstrahlung counts during the "RF on" period with different neutral-gas pressures. Measured with argon plasma, 500 W of RF power, and magnetic field setting #1.

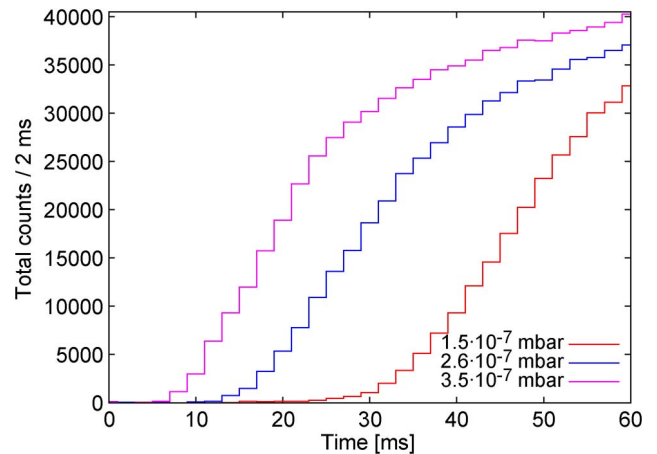


Fig. 3. First 60 ms of the data from Fig. 2.

sity is affected by the pressure. This is also confirmed by measuring current from the biased disk at  $-150$  V at steady-state conditions. The observation (high count rate at low pressure) can be explained by the frequency of collisions in the plasma. In a dense plasma, collisions between plasma particles ( $e-e$ ,  $e-i$ ) are more frequent than in low-density plasma. Due to reduced collision rate in low-density plasma, the number of high-energy electrons increases, resulting in an increased amount of bremsstrahlung radiation at energies over 30 keV. In addition, the electric field of the microwaves is damped less in the case of low plasma density, which means that the electric field strength on the resonance could be higher, resulting in higher energy gain in a single resonance crossing [10].

From Fig. 3, showing the first 60 ms, it is shown that the slopes of data curves are practically independent of the neutral-gas pressure for a duration of 15–20 ms after the count rate has started to build up. The lower the pressure, the later the bremsstrahlung emission starts. Changing the argon pressure from  $3.5 \cdot 10^{-7}$  to  $1.5 \cdot 10^{-7}$  mbar changes the time of plasma breakdown from 8 to around 20 ms. With  $2.6 \cdot 10^{-7}$  mbar, the plasma breaks down at 14 ms. This suggests that the plasma breakdown takes longer due to lower frequency of ionizing collisions depending on the density of neutrals.

Measurements with oxygen plasma yielded similar results as in the case of argon plasma. The highest count rates were observed at the lowest pressure. Plasma-breakdown times from 8 to 10 ms are recorded with pressures  $2.6 \cdot 10^{-7}$  and  $3.5 \cdot 10^{-7}$  mbar. With  $1.5 \cdot 10^{-7}$  mbar, it takes about 20 ms before photons are detected in the germanium crystal.

A clear steady state with pure O<sub>2</sub> gas feed is reached only with the neutral-gas pressure of  $1.5 \cdot 10^{-7}$  mbar (at around 600 ms) but no definite saturation of count rates can be observed with  $2.6 \cdot 10^{-7}$ - and  $3.5 \cdot 10^{-7}$ -mbar neutral-gas pressures, although the count rate increase is very slow after 600 ms. This observation could be explained by the fact that oxygen is chemically reactive. It can accumulate on the walls of the plasma chamber during the “RF off” period and becomes partially released by out-gassing due to plasma heating during the “RF on” period. This additional source of neutral gas affects the plasma properties. In the case of low gas feed rate, the accumulation rate of oxygen on the surface of the plasma chamber between the RF pulses is lower. Therefore, it takes less time to burn off the oxygen layer which could presumably lead to faster times for reaching an equilibrium.

The timescale for the plasma-breakdown process seems to be roughly similar for both gases (Ar and O<sub>2</sub>) at given neutral-gas pressures. This can be explained with almost similar ionization probabilities for the first ionization for the electrons between 10 eV and 10 keV (for cross sections, see [11]).

### B. Time Evolution of the Bremsstrahlung Radiation as a Function of the RF Power

The time evolution of total counts integrated over the energy spectrum measured with different RF powers in the case of argon plasma is shown in Figs. 4 and 5. The uppermost curve in the figures corresponds to RF power of 690 W, the middle curve 500 W, and the lowest curve 300 W. These power levels, which are typical for the JYFL 14-GHz ECRIS operation, are measured at the output of the klystron amplifier and do not take into account the losses in the waveguide. Estimated power losses are on the order of 20%–30%.

As expected, the higher the RF power, the higher the amount of steady-state bremsstrahlung (see Fig. 4). With 300- and 500-W RF powers, the steady state is reached at about 200 ms, but with the RF power of 690 W, the maximum of the bremsstrahlung count rate is observed at 200 ms, reducing slightly until the steady state is reached around 600 ms.

Times when the first bremsstrahlung counts are observed are very close to each other (around 10 ms). The increase of the count rate with increasing RF power is most probably due to faster heating process. This can be observed from the slopes shown in Fig. 5. In the beginning of the RF pulse, the most pronounced difference between the curves measured at different power levels is the variation of the slope, i.e., heating rate. It has been observed earlier that, above a certain threshold (few tens of watts), increasing the RF power does not affect the spectral temperature of the bremsstrahlung spectrum [12].

As in the case of argon plasma, the plasma breakdown in oxygen plasma takes place at 10 ms with all the RF powers. The steady state is reached at around 300 ms with the lowest

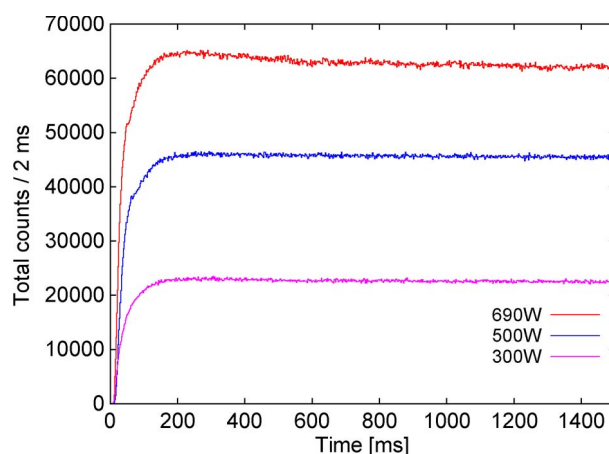


Fig. 4. Comparison of the bremsstrahlung counts during the “RF on” period with different RF powers. Measured with argon plasma, neutral-gas pressure of  $2.6 \cdot 10^{-7}$  mbar, and magnetic field setting #1.

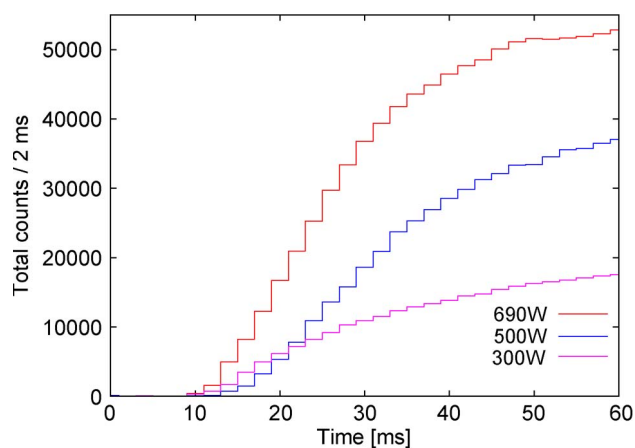


Fig. 5. First 60 ms of the data from Fig. 4.

RF power (300 W), but the steady state is not observed during the pulse (1.76 s) for the higher RF powers (500 W, 680 W). It seems that the time required for reaching the steady state increases with the RF power in oxygen plasma. Higher RF power levels lead into increased heat load onto the plasma chamber walls, which increases the “out-gassing area” adjacent to the plasma flux due to heat conduction. Thus, the observation does not contradict the assumption of the chemical reactivity of oxygen explaining the difference between the results measured with oxygen and argon.

Increased electron heating rate results to increased bremsstrahlung emission rate as long as the confinement time of electrons remains unchanged (constant magnetic field). The timescale for bremsstrahlung generation at the beginning of the RF pulse is similar for all of the RF powers used in the experiments. There is virtually no difference in times of detection of the first photons (above the detector threshold) as the RF power is varied.

### C. Comparison of the Argon Ion Production and Bremsstrahlung Emission Timescales

In order to gain understanding how the electron energies in the ECRIS plasma affect the ion production, the time

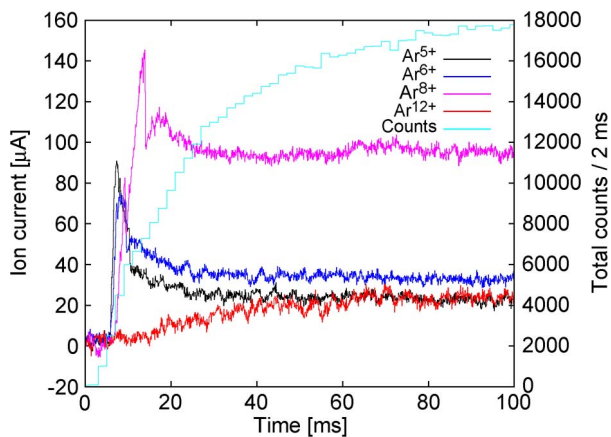


Fig. 6. Measured time evolution of the ion currents for different charge states of argon and corresponding bremsstrahlung counts integrated over the whole energy range—first 100 ms. At 30 ms: the uppermost curve “counts,” the second curve from the top “Ar<sup>8+</sup>,” the middle curve “Ar<sup>6+</sup>,” the second lowest curve “Ar<sup>5+</sup>,” and the lowest curve “Ar<sup>12+</sup>.” The two lowest curves are overlapping each other after 65 ms.

dependence of extracted ion-beam currents of different argon charge states was measured simultaneously with the bremsstrahlung. Special attention was paid into studying the preglow transient. The source was tuned (B field, neutral-gas pressure, and RF power) for maximum beam current of Ar<sup>9+</sup> (roughly 110  $\mu$ A) in continuous-operation mode before switching into pulsed mode. The source settings were as follows: extraction voltage of 10 kV, RF power of 515 W, neutral argon pressure of  $4.3 \cdot 10^{-7}$  mbar, and magnetic field setting #2. In this case, the preglow effect was clearly detected with charge states of Ar<sup>5+</sup> and Ar<sup>6+</sup>. Ion-beam currents of the lower charge states were not measured because the dipole magnet in the beam line of the JYFL 14-GHz ECRIS cannot bend ion beams with  $M/Q < 8$  to the Faraday cup at given extraction voltage (10 kV). Reducing the extraction voltage would have caused the drain current and, subsequently, plasma potential to change (see [13]). This kind of variations in the plasma conditions are to be avoided in order to compare bremsstrahlung radiation and ion production under identical ion-source plasma parameters. In addition, at extraction voltages less than 10 kV, space charge limits the extracted ion current (Child–Langmuir law,  $I \propto V^{3/2}/d^2$ ) instead of the plasma density. The comparison between steady-state and preglow peak ion currents would have been impossible under space-charge-limited conditions.

Fig. 6 shows the time evolution of the ion currents of selected charge states and bremsstrahlung for a period of 100 ms. It is seen that the low (Ar<sup>5+</sup>, Ar<sup>6+</sup>) and the medium (Ar<sup>8+</sup>) charge state ion currents reach steady-state conditions in less than 40 ms. However, Ar<sup>12+</sup> ion current rises until about 65 ms. While studying the count rate of bremsstrahlung emission, it is noticed that the count rate increases long after the ion currents have reached their steady state. The bremsstrahlung emission reaches the steady state after 320 ms, the steady-state count rate being around 19.000 counts/2 ms. This means that the argon beam currents (at least up to charge state Ar<sup>12+</sup>) saturate much faster than the bremsstrahlung emission. This result supports the conclusion that the most energetic electrons are useless from ionization point of view. However, in order to confirm this, the

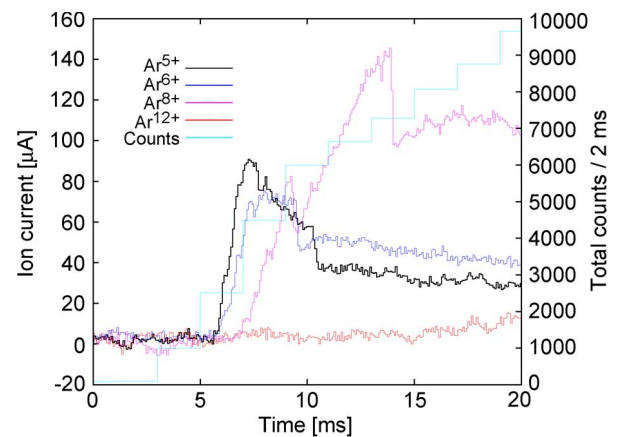


Fig. 7. Measured time evolution of the ion currents for different charge states of argon and corresponding bremsstrahlung counts integrated over the whole energy range—first 20 ms. At 20 ms: the uppermost curve “counts,” the second curve from the top “Ar<sup>8+</sup>,” the middle curve “Ar<sup>6+</sup>,” the second curve from the bottom “Ar<sup>5+</sup>,” and the lowest curve “Ar<sup>12+</sup>.”

time evolution of very high charge state of argon, like Ar<sup>16+</sup>, has to be studied using the most powerful ECRISs such as VENUS [14].

Fig. 7 shows the details of measured ion currents for selected charge states during the first 20 ms of the RF pulse and the corresponding bremsstrahlung counts integrated over the whole energy spectrum. With the lowest charge states (5+, 6+), the preglow effect is clearly observed, yielding peak currents of 1.4–4.1 times the steady-state current. Ar<sup>5+</sup> and Ar<sup>6+</sup> ion currents starts to rise after 5.8 ms from the leading edge of the RF pulse. Sharp peak in the ion current of Ar<sup>5+</sup> is reached at 7.3 ms while a wider peak of Ar<sup>6+</sup> is observed between 7.3 and 9.5 ms. The preglow peak of Ar<sup>8+</sup>, which starts to rise at 7 ms, is deformed: Two distinctive peaks are observed in the ion current. The first is seen at 9.5 ms and another at 13.8 ms. This behavior was observed to be repeatable but the reason for “double peak” observations is not known and needs to be studied further. With the charge states higher than Ar<sup>8+</sup>, preglow transient was not observed. The ion current of Ar<sup>12+</sup> appears slightly after 15 ms and reaches saturation at 65 ms.

The observations can be explained by stepwise ionization process. The lower charge states build up first and after that “feed” the higher charge states. This has been observed by Vondrasek *et al.* [15] with fast sputter sample and pulsed gas valve in a steady-state buffer gas plasma. When the ion currents start to rise, there is already a significant amount of high-energy bremsstrahlung, suggesting that the maximum electron energy is at higher energies than required for the ionization processes (ionization thresholds for Ar<sup>5+</sup> and Ar<sup>12+</sup> are 75 and 618.5 eV [11], respectively).

#### IV. CONCLUSION

In this paper, the time evolution of the bremsstrahlung radiation from an ECRIS is studied as a function of neutral-gas pressure and RF power. In particular, a comparison of the bremsstrahlung radiation and the ion-production times of different argon charge state is performed for the first time.

With argon plasma, the steady-state conditions are reached between 200 and 300 ms with all the neutral-gas pressures used in the measurements. The first bremsstrahlung counts appear between 8 and 20 ms. At the pressure of  $1.5 \cdot 10^{-7}$  mbar, there is a noticeable delay before the bremsstrahlung production starts (see Fig. 3). The total count rate slopes are however very similar between the different pressures. With oxygen plasma, it takes about 600 ms to reach the steady-state conditions at low neutral-gas pressure. If the pressure is increased, a definite steady state is not observed during the first 1500 ms from the leading edge of the RF pulse. The bremsstrahlung counts above 30 keV start to appear, as in the case of argon, between 8 and 20 ms, depending on the neutral-gas pressure. It is assumed that the difference between reaching the steady-state values with argon and oxygen plasmas can be explained by the out-gassing effect.

The high-energy bremsstrahlung from argon plasma reaches steady state around 200 ms at 300 and 500 W. The highest RF power (690 W) yields steady state around 600 ms. The bremsstrahlung production starts at 10 ms with all the RF powers, but there are significant differences between the total count rate slopes. The highest RF power produces a very steep slope in total count rate while the slope produced by the lowest RF power is quite gentle. Bremsstrahlung emission from oxygen plasma reaches steady state after 300 ms with the lowest RF power (300 W). With higher RF powers (500 W, 680 W), the steady state is not observed during the RF pulse. Similarly to argon, bremsstrahlung starts to be observed when 10 ms have elapsed from the leading edge of the RF pulse.

It is observed that the so-called preglow effect takes place with low and medium charge states. The preglow pulses for medium charge states (5+, 6+) start after about 5.8 ms from RF triggering. Ion current of  $\text{Ar}^{8+}$  appeared after 7 ms. Duration of the preglow pulses ranged from 2.8 ms ( $\text{Ar}^{6+}$ ) to 7.1 ms ( $\text{Ar}^{8+}$ ), and the beam current during the transient is 1.4–4.1 fold as compared to the steady-state current. No ions were detected roughly before 6 ms measured from the leading edge of the pulse. Similar behavior has been recorded by Thuillier *et al.* [6] who associated the observation with a superadiabatic electron energy distribution function (EEDF) and plasma-potential behavior during the plasma breakdown (for details, see [7]).

Typically, with the low and the medium charge states, the steady state is reached in less than 40 ms. Charge states higher than 9+ were observed to slowly (in few tens of milliseconds) reach the steady state without exhibiting any preglow behavior. From the ion-current measurements, it can also be seen that the time required to reach the leading edge of the ion-current pulse increases with increasing charge state of argon. This can be explained by the stepwise ionization process in the ECRIS plasma.

When the high-energy bremsstrahlung count rate is compared to the ion-current time evolution, it is noticed that the ion currents saturate well before the bremsstrahlung count rate reaches steady-state conditions. The saturation times are less than 65 ms for ion currents and 320 ms for bremsstrahlung count rate. This means that the EEDF continues to shift toward higher energies long after the ion currents have saturated.

Photon energies ranging from 50 to 150 keV (see, e.g., [5]) are detected at time interval of 14–16 ms. Therefore, it can be deduced that a significant amount of electrons have energies well over 1 keV at the time when a high charge state, like ( $\text{Ar}^{12+}$ ), ion current starts to rise.

The results have demonstrated that neutral-gas pressure does not affect the bremsstrahlung count rate significantly. The RF power has a remarkable effect on the count rate, as expected. Argon ions are produced in much faster timescale than is required for the electron energy distribution to reach a steady state. This is due to the fact that high-energy electrons (several tens of kiloelectronvolts and higher) are less important to the ionization process than lower energy electrons on the order of a few kiloelectronvolts. On the contrary, they create problems in the form of excessive bremsstrahlung radiation that requires heavy shielding for personnel safety and adds a significant heat load on the cryostat of superconducting ECRISs. These results open up an interesting possibility of controlling the electron energy in ECRIS plasmas by pulsing the RF power with very short pulses and high repetition rate after attaining the optimal electron energy distribution function for the production of desired charge state. Parallel to optimized ion production, the amount of bremsstrahlung could be conceivably reduced. Since it is questionable whether such a technique would work at all, this issue will be a subject of future investigations with the JYFL 14-GHz ECRIS. One of the most important aspects of the results presented in this paper is that they can be utilized for developing and benchmarking electron heating simulation (e.g., [10]) and ion-production (e.g., [16]) codes for ECRIS plasmas in order to understand what are the meaningful physical processes and how they work in a modern high-performance ECRIS.

#### ACKNOWLEDGMENT

The use of a germanium detector from GAMMAPOOL resource is gratefully acknowledged.

#### REFERENCES

- [1] R. Geller, *Electron Cyclotron Resonance Ion Sources and ECR Plasmas*. New York: Taylor & Francis, 1996.
- [2] T. J. Fessenden, "Pulsed electron-cyclotron resonance discharge experiment," MIT, Cambridge, MA, Tech. Rep. MIT-3221-19, Mar. 1966.
- [3] K. Bernhardt and K. Wiesemann, "X-ray bremsstrahlung measurements on an ECR-discharge in a magnetic mirror," *Plasma Phys.*, vol. 24, no. 8, pp. 867–884, Aug. 1982.
- [4] H. Koivisto, P. Heikkinen, V. Hänninen, A. Lassila, H. Leinonen, V. Nieminen, J. Pakarinen, K. Ranttila, J. Ärje, and E. Liukkonen, "The first results with the new JYFL 14 GHz ECR ion source," *Nucl. Instrum. Methods Phys. Res. B, Beam Interact. Mater. At.*, vol. 174, no. 3, pp. 379–384, Nov. 2001.
- [5] T. Ropponen, O. Tarvainen, P. Jones, P. Peura, T. Kalvas, P. Suominen, H. Koivisto, and J. Ärje, "The effect of magnetic field strength on the time evolution of high energy bremsstrahlung radiation created by an electron cyclotron resonance ion source," *Nucl. Instrum. Methods Phys. Res. A, Accel. Spectrom. Detect. Assoc. Equip.*, vol. 600, no. 3, pp. 525–533, Mar. 2009.
- [6] T. Thuillier, T. Lamy, L. Latrasse, I. V. Izotov, A. V. Sidorov, V. A. Skalyga, V. G. Zorin, and M. Marie-Jeanne, "Study of pulsed electron cyclotron resonance ion source plasma near breakdown: The preglow," *Proc. 12th Int. Conf. Ion Sources*, vol. 79, no. 2, Rev. Sci. Instrum., p. 02A 314, Feb. 2008.
- [7] I. V. Izotov, T. Lamy, L. Latrassel, A. V. Sidorov, V. A. Skalyga, T. Thuillier, and V. G. Zorin, "Experimental and theoretical investigation

of the preglow in ECRIS," *IEEE Trans. Plasma Sci.*, vol. 36, no. 4, pp. 1494–1501, Aug. 2008.

- [8] L. Arnold, R. Baumann, E. Chambit, M. Filliger, C. Fuchs, C. Kieber, D. Klein, P. Medina, C. Parisel, M. R. C. Santos, and C. Weber, "TNT digital pulse processor," *IEEE Trans. Nucl. Sci.*, vol. 53, no. 3, pp. 723–728, Jun. 2006.
- [9] S. Biri, A. Valek, T. Suta, E. Takács, C. Szabó, L. T. Hudson, B. Radics, J. Imrek, B. Juhász, and J. Pálkás, "Imaging of ECR plasmas with a pinhole X-ray camera," *Rev. Sci. Instrum.*, vol. 75, no. 5, pp. 1420–1422, May 2004.
- [10] T. Ropponen, O. Tarvainen, P. Suominen, T. K. Koponen, T. Kalvas, and H. Koivisto, "Hybrid simulation of electron cyclotron resonance heating," *Nucl. Instrum. Methods Phys. Res. A, Accel. Spectrom. Detect. Assoc. Equip.*, vol. 587, no. 1, pp. 115–124, Mar. 2008.
- [11] V. M. Povyshev, A. A. Sadovoy, V. P. Shevelko, G. D. Shirkov, E. G. Vasina, and V. V. Vatulin, "Electron-impact ionization cross sections of H, He, N, O, Ar, Xe, Au, Pb atoms and their ions in the electron energy range from the threshold up to 200 keV," *Communication of the Joint Institute for Nuclear Research*, 2001.
- [12] D. Leitner, J. Y. Benitez, C. Lyneis, D. S. Todd, T. Ropponen, J. Ropponen, H. Koivisto, and S. Gammino, "Measurement of the high energy component of the X-ray spectra in the VENUS ECR ion source," *Proc. 12th Int. Conf. Ion Sources*, vol. 79, no. 3, Rev. Sci. Instrum., p. 033 302, Mar. 2008.
- [13] O. Tarvainen, P. Suominen, and H. Koivisto, "A new plasma potential measurement instrument for plasma ion sources," *Rev. Sci. Instrum.*, vol. 75, no. 10, pp. 3138–3145, Oct. 2004.
- [14] D. Leitner, C. M. Lyneis, T. Loew, D. S. Todd, S. Virostek, and O. Tarvainen, "Status report of the 28 GHz superconducting electron cyclotron resonance ion source VENUS," *Rev. Sci. Instrum.*, vol. 77, no. 3, p. 03A 302, Feb. 2006.
- [15] R. C. Vondrasek, R. H. Scott, R. C. Pardo, and D. Edgell, "Techniques for the measurement of ionization times in ECR ion sources using a fast sputter sample and fast gas valve," *Rev. Sci. Instrum.*, vol. 73, no. 2, pp. 548–551, Feb. 2002.
- [16] V. Mironov and J. P. M. Beijers, "Three-dimensional simulations of ion dynamics in the plasma of an electron cyclotron resonance ion source," *Phys. Rev. ST Accel. Beams*, vol. 12, no. 7, p. 073 501, Jul. 2008. [Online]. Available: <http://www.citebase.org/abstract?id=oai:arXiv.org:0811.2865>



**Tommi Ropponen** was born in Leppävirta, Finland, in 1981. He received the M.Sc. degree in physics with a thesis focusing on the plasma potential and ambipolar diffusion of the ECR plasma from the Department of Physics, University of Jyväskylä, Jyväskylä, Finland, in 2005, where he is currently working toward the Ph.D. degree in the ECR Ion Source Group.

His current research interests are focused on the ECR plasma physics and main publications include

studies of electron heating in ECR plasma and ion-beam-current time evolution.



**Olli Tarvainen** was born in Joensuu, Finland, in 1979. He received the Ph.D. degree in physics, devoted to plasma physics of electron cyclotron resonance ion sources, from the University of Jyväskylä, Jyväskylä, Finland, in 2005.

From 2006 to 2009, he was a Postdoctoral Researcher with Los Alamos National Laboratory, where he conducted research and development on negative ion sources and helicon plasma generators. He is currently a Researcher with the Ion Source Group of the Department of Physics, University of

Jyväskylä. His current research interests include plasma physics of ion sources and their applications. His main publications include "The Effects of Cesium Equilibrium on  $H^-$  Ion Beam Production with LANSCE Surface Converter Ion Source" (Nuclear Instruments and Methods in Physics Research Section A: Accelerators, Spectrometers, Detectors and Associated Equipment, 2009) and "Plasma Breakdown Diagnostics with the Biased Disc of Electron Cyclotron Resonance Ion Source" (Plasma Sources Science and Technology, 2009).



**Pete Jones** was born in Wordsley, U.K., in 1970. He received the Ph.D. degree in nuclear structure physics from the University of Liverpool, Liverpool, U.K., in 1995.

Since then, he has been a Senior Researcher with the Department of Physics, University of Jyväskylä, Jyväskylä, Finland. He is the author or coauthor of about 150 scientific articles in nuclear physics. His current research interests are gamma-ray and electron spectroscopy, detector instrumentation and associated electronics, data acquisition and general

research, training, and supervision.



**Pauli Peura** was born in Saarijärvi, Finland, in 1981. He received the M.Sc. degree in physics from the University of Jyväskylä, Jyväskylä, Finland, in 2005, where he is currently working toward the Ph.D. degree in the Nuclear Spectroscopy Group of the Department of Physics.

He has been concentrating on the development and instrumentation of the TNT2 digital signal processing system for the JUROGAM II spectrometer. His current research interests include the neutron-deficient nuclei near the  $Z = 82$  shell gap, measured

with the recoil decay tagging and the recoil distance Doppler shift methods.



**Taneli Kalvas** was born in Tampere, Finland, in 1981. He received the M.Sc. degree in physics from the Department of Physics, University of Jyväskylä, Jyväskylä, Finland, in 2004, where he is currently working toward the Ph.D. degree in the Industrial Applications Group.

From 2004 to 2006, he was a Researcher with the Plasma and Ion Source Technology Group of Lawrence Berkeley National Laboratory, where he was developing radio-frequency ion sources for neutron generators and other applications. His current

research interests include the numerical modeling of ion optics and plasma extraction and the applications of ion sources.



**Pekka Suominen** was born in Pori, Finland, in 1979. He received the M.Sc. and Ph.D. degrees in accelerator/ion source physics from the University of Jyväskylä, Jyväskylä, Finland, in 2002 and 2006, respectively.

He is currently a Senior Consultant with the Magnet Technology Center, Priztech Ltd., Pori, where he is responsible for projects involving superconducting magnets. His main publications are about ECR ion sources (ECRISs), emittance measurements, plasma potential measurements, operation

with multiple frequencies, magnetic field simulations (Ph.D. thesis about "Modified Multipole Structure"), and ECRIS with arc-shaped coils (ARC-ECRIS).



**Hannu A. Koivisto** was born in Alajärvi, Finland. He received the Ph.D. degree in physics from the Department of Physics, University of Jyväskylä (JYFL), Jyväskylä, Finland, in 1998.

In 1998–1999, he had a Postdoctoral position with NSCL/MSU. He then returned to his home laboratory, where he is presently the Leader of the Ion Source Group of the Department of Physics, JYFL. He is the author or coauthor of about 70 articles in ion-source-related physics. The main research work has been done for developing the MIVOC method,

designing and constructing ECR ion sources, developing metal ion-beam production, and studying the ECR heated plasma and ion-beam production.



## APPENDIX A.VII



# The effect of RF pulse pattern on bremsstrahlung and ion current time evolution of an ECRIS\*

T. Ropponen,<sup>†</sup> O. Tarvainen, V. Toivanen, P. Peura, P. Jones, T. Kalvas, and H. Koivisto  
*University of Jyväskylä, Department of physics, Jyväskylä, Finland*

J. Noland and D. Leitner  
*Lawrence Berkeley National Laboratory, Berkeley, USA*

Time-resolved helium ion production and bremsstrahlung emission from JYFL 14 GHz ECRIS is presented with different radio frequency pulse lengths. RF on times are varied from 5 ms to 50 ms and RF off times from 10 ms to 1000 ms between different measurement sets. It is observed that the plasma breakdown occurs a few milliseconds after launching the RF power into the plasma chamber, and in the beginning of the RF pulses a preglow transient is seen. During this transient the ion beam currents are increased by several factors compared to a steady state situation. By adjusting the RF pulse separation the maximum ion beam currents can be maintained during the so-called preglow regime while the amount of bremsstrahlung radiation is significantly decreased.

## I. INTRODUCTION

Bremsstrahlung emission is considered as a standard plasma diagnostics tool used to study electron cyclotron resonance (ECR) heated plasmas [1, 2]. Bremsstrahlung emission has recently been studied with modern ECR ion sources [3–5] in order to understand the influence of various source parameters (frequency, magnetic field strength etc.) on the bremsstrahlung flux and energy. The time evolution of the bremsstrahlung spectra has been studied in pulsed operation mode and compared to extracted ion beam currents. It has been observed that the extracted ion beam currents attain their final values well before the bremsstrahlung emission reaches a steady-state. In particular, the so-called preglow transient, exhibited by low and medium charge states in the beginning of the RF pulse, occurs well before the bremsstrahlung count rate saturates to its maximum value. It has been suggested that the preglow could be utilized for applications requiring fast and efficient ionization of radioactive ion beams and their further injection into circular accelerator or storage ring [6, 7]. During the preglow the ion beam currents exceed their final steady-state value by a factor of 2–9. The characteristics, such as peak current and plasma breakdown time, associated with this transient, are strongly affected by the RF pulse duration and repetition rate. In order to explain this observation, the bremsstrahlung emission and preglow transient with various RF pulse patterns with pulse duration ranging from 5 to 50 ms and pulse separation from 10 to 1000 ms have been studied. The study presented in this article completes the set of time-resolved measurements comparing time scales of bremsstrahlung generation and ion beam

production with the JYFL 14 GHz ECRIS (see references [3–5]).

## II. MEASUREMENT SETUP AND EXPERIMENTAL RESULTS

The measurement setup has been thoroughly introduced in references [4] and [5]. A TTL signal is used to synchronize the digital signal processing system with the RF switch controlling the input signal from an oscillator into the klystron. Photons (bremsstrahlung) are detected with a germanium detector in radial direction with respect of the ion source plasma chamber. The detector set-up restricts the recorded bremsstrahlung spectra to energies above 30 keV. Time-resolved bremsstrahlung spectra and integrated count rates are obtained after data analysis with 50  $\mu$ s time step. The experiments described in this article were performed with helium plasma. The bremsstrahlung data are corrected with a relative efficiency calibration. The collimator structure used during the measurements described in this article is presented in figure 1. Openings of the collimator were chosen in order to reach suitable count rates at the detector. During the measurements the count rates ranged from a few kHz to 7 kHz.

### A. Helium ion and bremsstrahlung production with different duty factors

Figure 2 shows time-resolved ion beam currents of He<sup>+</sup> and He<sup>2+</sup> together with the integrated bremsstrahlung emission count rates for various RF pulse patterns at a fixed power of 350 W at a frequency of 14.1 GHz (helium partial pressure of  $1.8 \cdot 10^{-7}$  mbar). During the measurements the source conditions were not optimized for maximum ion beam currents of helium. It should be noted that ECRIS settings such as magnetic field, RF power and neutral gas pressure affect the bremsstrahlung emis-

---

\*Contributed paper, published as part of the Proceedings of the 13th International Conference on Ion Sources, Gatlinburg, Tennessee, USA, September 2009.

<sup>†</sup>Electronic address: [tommi.ropponen@jyu.fi](mailto:tommi.ropponen@jyu.fi)

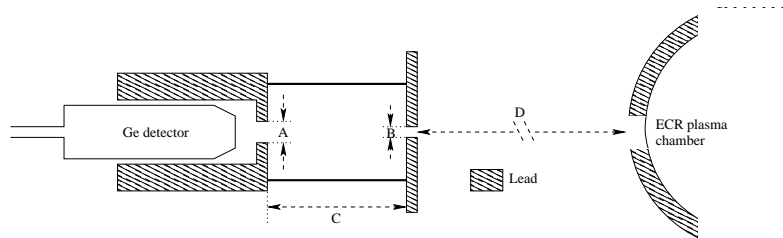


FIG. 1: Schematic drawing of the collimator and the detector. Distances marked in the figure are A: 20 mm, B: 10 mm, C: 163 mm and D: 1170 mm.

sion and ion beam current timescales as discussed in detail in references [4, 5, 8, 9].

Subfigure a) shows that with 5/1000 ms (on/off times) RF pulses the delay between the leading edge of the RF pulse and first observation of extracted ion beam ( $\text{He}^+$ ) is about 2.5 ms.  $\text{He}^{2+}$  appears about 1 ms later reflecting the stepwise nature of the ionization process. Bremsstrahlung count rate starts to increase about 1 ms before ion currents are detected, which could indicate that the diffusion time of ions from the ECR zone, where the plasma breakdown avalanche takes off, to extraction is on the order of ms (see e.g. [10]). In comparison, the time-of-flight from the ion source to the Faraday cup at 10 kV extraction potential is roughly  $10 \mu\text{s}$  i.e. orders of magnitude less. With the given RF pulse pattern (short on time and long off time) the preglow is heavily concentrated on  $\text{He}^+$  reaching the maximum in 4 to 5 ms from the leading edge of the RF pulse. In addition, after the RF has been switched off,  $\text{He}^+$  ion beam current is still detected for tens of milliseconds. This could be due to slow plasma decay due to well-confined hot electrons and diffusion times of ions. It has been shown previously [8] that some electrons can stay confined and affect the plasma breakdown of the consecutive pulse up to several seconds (between the RF pulses). In subfigure b) the RF pulse duration has been increased to 50 ms while the off time is kept at 1000 ms. The most interesting feature of subfigure b) is the fact that a clearly visible dip of bremsstrahlung count rate occurs after the bremsstrahlung count rate has started to build up. It has been suggested [6] that in the very beginning of the RF pulse the density of electrons is low and the RF power is sufficient to heat essentially all free electrons until they reach the stochastic heating limit. This situation corresponds to a so-called superadiabatic electron energy distribution function. As the plasma density increases by ionization, the RF power becomes insufficient to support the existing energy distribution, which is followed by a collapse of average electron energy. The observation i.e. dip in count rate coinciding with rapid increase of plasma density provides experimental support for this model. As soon as the preglow transient fades away, the bremsstrahlung count rate continues to increase almost linearly. It was confirmed from the bremsstrahlung data (not shown here) that the saturation is typically reached after 200–300 ms. Afterglow instabilities are observed

following the switch-off of the RF with both diagnostics (count rate and beam current). It can be seen that the beam current of  $\text{He}^+$  is decaying slower than the beam current of  $\text{He}^{2+}$ . This is presumably due to high density of neutrals causing charge exchange reactions in the low density plasma. In subfigure c) the RF on time is 5 ms while the off time is reduced to 20 ms. It is obvious that the plasma does not decay between the pulses. The breakdown is immediate and both charge states exhibit a preglow transient with maximum between 1–2 ms. The effect of so-called “seed electrons” on the plasma breakdown time (becoming shorter) has been studied earlier with the JYFL 14 GHz ECRIS [8, 9]. In those measurements the seed electrons were provided by a continuous low power signal at secondary frequency. It was observed that seed electrons shift the charge state distribution during the preglow transient towards higher charge states. Shortening the RF off period yields similar result. In this case the seed electrons originate from the (low density) plasma remaining confined from the previous pulse.

In subfigures d)-f) the RF on time is kept at 5 ms and the RF off time is varied. The RF off time affects the plasma breakdown time and time to reach the maximum of the preglow peak due to variation of seed electron density. The bremsstrahlung count rate is also affected, i.e. the longer the off time, the lower the count rate during the RF on period. This is believed to be caused by the amount of seed electrons which decreases as the time between the RF pulses increases. As the off time is increased from 10 ms to 40 ms the bremsstrahlung count rate decreases about 30 %. When the off time is increased to 100 ms the bremsstrahlung count rate drops yet another 30 %. However, the variation of the preglow peak currents is not as pronounced as the variation of the bremsstrahlung count rates.

### III. DISCUSSION

From figure 2 it can be seen that the times when ion currents start to rise and reach their maximum values are strongly affected by the RF pulse pattern, and plasma breakdown can be decreased by shortening the RF pulse separation. If the RF off time is kept short enough, sufficient amount of seed electrons are kept confined in the magnetic bottle and feed the ionization avalanche im-

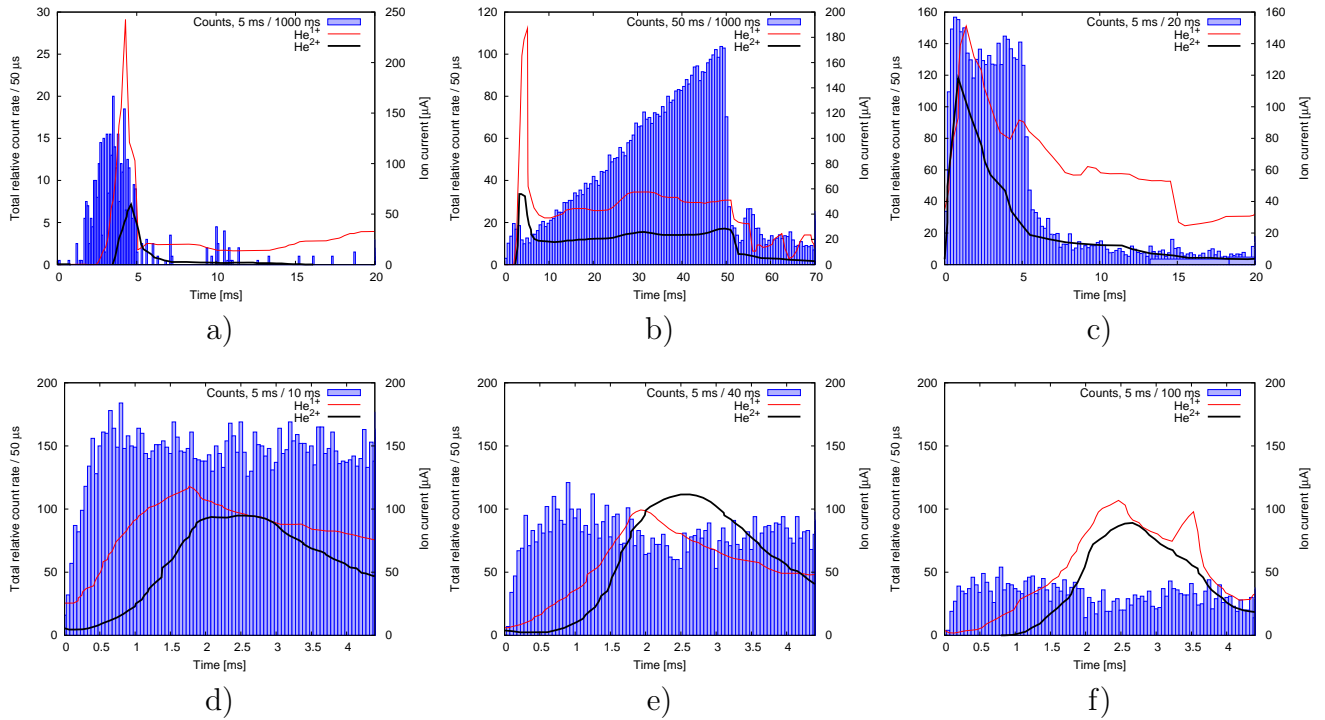


FIG. 2: Time-resolved bremsstrahlung count rate and ion beam currents of helium with different RF pulse patterns (ON/OFF): a) 5 ms/1000 ms duty factor 0.5 %, b) 50 ms/1000 ms duty factor 4.8 %, c) 5 ms/20 ms duty factor 20.0 %, d) 5 ms/10 ms duty factor 33.3 %, e) 5 ms/40 ms duty factor 11.1 % and f) 5 ms/100 ms duty factor 4.8 %. In subfigures a)-c) RF phases are illustrated completely (RF on) and in part (RF off). In Subfigures d)-f) detailed data from the first milliseconds of the RF pulse is presented. Bremsstrahlung count rates are projected on the left-hand y-axis and ion currents on the right-hand y-axis.  $T = 0$  denotes the leading edge of the RF pulse. Bremsstrahlung data are averaged over 616 RF pulses.

mediately after turning on the RF again. The observed bremsstrahlung count rates with short pulses (less than 100 ms) are considerably smaller than in continuous operation mode of the ECRIS. It seems that ECR ion sources operated in pulsed mode utilizing the preglow transient can produce ion beam intensities well over the steady state values with less problems due to bremsstrahlung and heat load to the cryostat (in the case of superconducting ion sources). However, extensive studies with multiply charged ECR plasmas are needed in order to confirm these results.

#### IV. ACKNOWLEDGMENTS

This work has been supported by the Academy of Finland under the Finnish Centre of Excellence Programme 2006–2011 (Nuclear and Accelerator Based Physics Programme at JYFL). T. Ropponen would like to acknowledge financial support from the Graduate School in Particle and Nuclear Physics and Magnus Ehrnrooth foundation. The use of a germanium detector from GAMMAPOOL resource is gratefully acknowledged.

- 
- [1] T. J. Fessenden, *Tech. Rep. MIT-3221-19*, Massachusetts Institute of Technology (1966).
  - [2] K. Bernhardt and K. Wiesemann, *Plasma physics* 24, 867 (1982).
  - [3] D. Leitner, J. Y. Benitez, C. Lyneis, D. S. Todd, T. Ropponen, J. Ropponen, H. Koivisto, and S. Gammino, *Rev. Sci. Instr.* 79, 033302 (2008).
  - [4] T. Ropponen, O. Tarvainen, P. Jones, P. Peura, T. Kalvas, P. Suominen, H. Koivisto, and J. Ärje, *Nucl. Instr. and Meth. A* 600, 525 (2009).
  - [5] T. Ropponen, O. Tarvainen, P. Jones, P. Peura, T. Kalvas, P. Suominen, and H. Koivisto (2009), *accepted to be published in IEEE Trans. Plasma Sci.*
  - [6] I. V. Izotov, T. Lamy, L. Latrassel, A. V. Sidorov, V. A. Skalyga, T. Thuillier, and V. G. Zorin, *IEEE Trans. Plasma Sci.* 36, 1494 (2008).
  - [7] The Beta Beam project, <http://beta-beam.web.cern.ch/beta-beam/task/index.asp>
  - [8] O. Tarvainen, T. Ropponen, V. Toivanen, J. Ärje, and H. Koivisto, *Plasma Sources Sci. Technol.* 18, 035018 (2009).
  - [9] O. Tarvainen, T. Ropponen, T. Thuillier, J. Noland, V. Toivanen, T. Kalvas, and H. Koivisto, *to be published in*

*the Proceedings of the 13<sup>th</sup> international conference on ion sources.*

*Beams* 12, 073501 (2009).

[10] V. Mironov and J. P. M. Beijers, *Phys. Rev. ST Accel.*